Spinal muscular atrophy : Evidence of a multi-system disease

Marc-Olivier Deguise

This thesis is submitted as a partial fulfillment of the Ph.D. program in Cellular and Molecular Medicine of the University of Ottawa

September 6th 2019

Department of Cellular and Molecular Medicine

Faculty of Medicine

University of Ottawa

© Marc-Olivier Deguise, Ottawa, Canada, 2020

Authorization

The content of this document consists of Marc-Olivier Deguise's original work. All previously published work as produced by Marc-Olivier Deguise & *al.* obtained permissions from the publishers for publication within this document, whether unaltered or modified. Licenses are provided below.

1. **Deguise M.O.** & *al*. (20XX) Myopathic phenotype precedes neuronal phenotype in a new mild mouse model of spinal muscular atrophy (Not yet submitted)
2. **Deguise M.O**. & *al.* (20XX). Spinal muscular atrophy: providing a novel framework to elucidate NAFLD molecular pathogenesis (Not yet submitted).
3. Marc-Olivier Deguise & *al.* (2019) Low fat diets increase survival of a mouse model of spinal muscular atrophy. *Ann Clin Transl Neurol (IF: 4.656)*. DOI : 10.1002/acn3.50920

This is an open access article under the terms of the Creative Commons Attribution-NonCommercial-NoDerivs License (https://creativecommons.org/licenses/by-nc-nd/4.0/), which permits use and distribution in any medium, provided the original work is properly cited, the use is non-commercial and no modifications or adaptations are made. If you remix, transform or build upon the material, you may not distribute the modified material. This work has been altered as part of the thesis.

4. **Deguise M.O.** & *al*. (2019) Abnormal fatty acid metabolism is a core component of spinal muscular atrophy. *Ann Clin Transl Neurol (IF: 4.656)*. DOI : 10.1002/acn3.50855

This is an open access article under the terms of the Creative Commons Attribution-NonCommercial-NoDerivs License (https://creativecommons.org/licenses/by-nc-nd/4.0/), which permits use and distribution in any medium, provided the original work is properly cited, the use is non-commercial and no modifications or adaptations are made. If you remix, transform or build upon the material, you may not distribute the modified material. This work has been altered as part of the thesis.

5. **Deguise M.O.** & Kothary R. (2019) Chapter 2: Spinal muscular atrophy. Chromatin signalling and Neurological disorders. Edited by Olivier Binda, Elsevier

The license number of this permission to reproduce this work is 4718220143434 and the terms and conditions can be found here.

6. **Deguise M.O.** and Kothary R. (2017) New insights into SMA pathogenesis: Immune dysfunction and neuroinflammation. *Ann Clin Transl Neurol (IF: 4.656).* **4**(7):522-530 Doi:10.1002/acn3.423

This is an open access article under the terms of the Creative Commons Attribution-NonCommercial-NoDerivs License (https://creativecommons.org/licenses/by-nc-nd/4.0/),

which permits use and distribution in any medium, provided the original work is properly cited, the use is non-commercial and no modifications or adaptations are made. If you remix, transform or build upon the material, you may not distribute the modified material. This work has been altered as part of the thesis.

7. **Deguise M.O.** & *al*. (2017) Immune dysregulation may contribute to disease pathogenesis in spinal muscular atrophy mice. *Human molecular genetics (IF: 5.689).* **26**(4):801-819. doi: 10.1093/hmg/ddw434

Oxford University Press Rights department: "As part of your copyright agreement with Oxford University Press you have retained the right, after publication, to use all or part of the article and abstract, in the preparation of derivative works, extension of the article into a booklength work, in a thesis/dissertation, or in another works collection, provided that a full acknowledgement is made to the original publication in the journal. As a result, you should not require direct permission from Oxford University Press to reuse your article."

8. **Deguise M.O.** & *al*. (2017) Chapter 10: Contributions of different cell types to SMA pathogenesis. Spinal Muscular Atrophy: Disease Mechanisms and Therapy, Edited by: C. J. Sumner, S. Paushkin and C.-P. Ko, Elsevier, ISBN: 978-0-12-803685-3

The license number of this permission to reproduce this work is 4621921478892 and the terms and conditions can be found here.

9. **Deguise M.O.** *& al*. (2016) Differential induction of muscle atrophy pathways in two mouse models of spinal muscular atrophy. *Scientific Reports (IF: 4.259)*. **6**:28846 | DOI: 10.1038/srep28846

This work is licensed under a Creative Commons Attribution 4.0 International License. The images or other third-party material in this article are included in the article's Creative Commons license, unless indicated otherwise in the credit line; if the material is not included under the Creative Commons license, users will need to obtain permission from the license holder to reproduce the material. To view a copy of this license, visit http://creativecommons.org/licenses/by/4.0/

Abstract

Spinal muscular atrophy (SMA) is a devastating recessive neurological disorder thought to be affecting primarily the motor neurons. As such, paralysis, motor weakness and death ensue. While SMA is most commonly seen in infants and children, it can span all ages. Its genetic etiology revolves around the homozygous deletion or mutation of the *SMN1* gene, whose product (SMN protein) has critical and ubiquitous roles in mRNA splicing, amongst various other functions in mRNA metabolism. As such, SMN depletion in other non-neuronal cells type is likely to have physiological repercussions, and perhaps modulate the SMA phenotype. Herein, we identify the molecular pathways of atrophy in skeletal and cardiac muscle of two mouse models of SMA and their therapeutic modulation via the histone deacetylase inhibitor trichostatin A. We also identify dramatic changes in immune organs in mouse models of SMA, which could impact susceptibility to infections. Furthermore, we establish the presence of important defects in fatty acid homeostasis in the liver and plasma seen in both mouse models and SMA patients. Finally, we provide the first mild mouse model of SMA that reliably reproduces canonical features of SMA, permitting aging studies. This model presents with a prominent myopathic phenotype prior to motor neuron death, without extra-neuronal involvement during the course of its lifespan. Overall, our work shows multiple potentially clinically relevant defects in extra-neuronal organs, provides ways to abrogate them and provides a framework to study them over the course of aging.

List of tables

List of figures

List of Abbreviations

↑: increase

4-PBA: Sodium phenyl-butyrate

AA: amino acids

AGC: automatic gain control

Akt: protein kinase B

ALP: alkaline phosphatase

ALS: amyotrophic lateral sclerosis

ALT: alanine aminotransferase

APCs: antigen presenting cells

ASD: atrial septal defect

ASO: antisense oligonucleotides

AST: aspartate aminotransferase

ATF4: activating transcription factor 4

Bax: BCL2 associated X protein

BCAA: branched-chain amino acid

BIN1: bridging integrator 1

Bip: Heat shock protein family A (Hsp70) member 5

BMD: bone mineral density

Bnip3: BCL2/adenovirus E1B 19 kDa protein-interacting protein 3

Bp: base pairs

Cas1: caspase 1

Casp2: Caspase 2

Casp8: Caspase 8

ChAT: Choline acetyltransferase

CHOP: DNA damage inducible transcript 3

CIHR: Canadian Institutes of Health Research

cKO: Conditional knockout

CMAP: compound motor action potential

CNS: central nervous system

D: days

DAVID: Database for Annotation, Visualization and Integrated Discovery

DMD: Duchenne muscular dystrophy

DMSO: dimethyl sulfoxide

DN: double negative

DNM2: dynamin 2

DP: double positive

ER: endoplasmic reticulum

ES: enrichment score

FasR: Fas receptor

FDA: U.S food and Drug Administration

FDR: false discovery rate

FMRP: Fragile X Mental Retardation Retardation Protein 1

FoxO: Forkhead box protein O

FTSA: fast skeletal muscle troponin activator

Gabarapl1: GABA(A) Receptor-Associated Protein Like 1

GC: glucocorticoid

GDNF: glial cell derived neurotrophic factor

GI: Gastrointestinal

GLT1: solute carrier family 1 member 2

GRP94: Heat shock protein 90 beta family member 1

Hamp: Hepcidin antimicrobial peptide

HbA_{1C}: glycated hemoglobin

HCC: Hepatocellular carcinoma

HDAC: histone deacetylase

HDACi: histone deacetylase inhibitor

HDL: high density lipoprotein

H&E: Hematoxylin and eosin

HFD: high fat diet

HFMSE: Hammersmith functional motor scale – expanded

HLHS: hypoplastic left heart syndrome

hnRNP-R: heterogeneous nuclear ribonucleoprotein R

HR: heart rate

HSA: human skeletal actin

HSD: high sucrose diet

HuD: ELAV Like RNA binding protein 4

IGF1: Insulin-like growth factor 1

IGF1R: insulin-like growth factor 1 receptor

IGFals: insulin-like growth factor binding protein acid labile subunit

IGfbp1: insulin-like growth factor binding protein 1

IMP1: Insulin-like growth factor 2 mRNA binding protein 1

IPA: ingenuity pathway analysis

iPSC: induced pluripotent stem cells

IVS: interventricular septum

KLF15: Krüppel-life Factor 15

KO: Knockout

KSRP: KH-type splicing regulatory protein

LC3: microtubule-associated protein light chain 3 beta

LC-MS: liquid chromatography-mass spectrometry

LDL: low density lipoprotein

LFD: low fat diet

LN: lymph nodes

M: months

MAFbx: Atrogin-1

MALT: mucosal associated lymphoid tissues

MCL: Markov Clustering Algorithm

MiR: MicroRNA

MN: Motor neurons

MTM1: myotubularin 1

mTOR: mammalian Target of Rapamycin

MuRF1: Muscle Ring Finger 1

MUSA1: muscle ubiquitin ligase of the SCF complex in atrophy-1

Myf-5: myogenic factor 5

MyHC: Myosin Heavy Chain

MyoD: Myogenic Differentiation 1

MyoG: Myogenin

N/A: Not available

N.A.: not assessed

NAFLD: non-alcoholic fatty liver disease

NASH: non-alcoholic steatohepatitis

N.C. – no change

NC: normal chow

NEFA: non-esterified fatty acids

NMJ: neuromuscular junction

OGTT: oral glucose tolerance test

P: postnatal day

P21: cyclin dependent kinase inhibitor 1A

P53: tumor protein p53

P62: sequestosome-1

PALS: periarteriolar lymphoid sheath

Pax7: Paired box 7

PBS: phosphate-buffered saline

PrP: Prion Promoter

QOL: quality of life

RBPs: RNA binding proteins

Ref: references

Rip1k: receptor interacting protein 1 kinase

Rip3k: receptor interacting protein 3 kinase

ROS: reactive oxygen species

RyR1: ryanodine receptor 1

SBMA: Spinal and bulbar atrophy

SC: spinal cord

SCI: Spinal cord injury

Serca1a: sarcoplasmic reticulum Ca2+ ATPase

SMA: spinal muscular atrophy

SMART: specific of muscle atrophy and regulated by transcription

SMN: survival motor neuron

SmnΔ7: $Smn^{-/-};SMN2^{+/+};Smn\Delta7^{+/+}$

SMUP: single motor unit potentials

snRNP: small nuclear ribonucleoprotein

SP: single positive

TA: tibialis anterior

TC: Total cholesterol

TCR: T-cell antigen receptor

TEAB: tetraethylammonium bromide

TG: triglycerides

TMT: Tandem Mass Tagging

TNFR1: TNF receptor superfamily member 1A

TSA: trichostatin A

TTN: titin

TUNEL: Terminal deoxynucleotidyl transferase dUTP nick end labeling

VPA: valproic acid

VLDL: very low density lipoprotein

VSD: ventricular septal defect

WAT: white adipose tissue

Y: years

Acknowledgements

My personal, emotional, and scientific growth through this training path has been inspired and supported by many of my close ones. I will cherish forever their constant encouragements, advices and support.

First, I can't express how grateful I am to have crossed path with Dr. Rashmi Kothary, who has been my supervisor since 2012. From the beginning, as a research embryo with little to no experience, he has provided me with innumerable opportunities and all the necessary tools to flourish and ultimately become an independent researcher. I will never forget how I first started working on SMA. On my first day, Dr. Kothary told me: "There are 3 projects in the lab, go around, see what interests you and start working on it". This liberty and freedom that Rashmi has allowed me to have on day one and subsequently throughout my training has sparked in me a scientific creativity I never thought I would develop. I am more than thankful for his constant availability, given my many impromptu office meetings to discuss ideas and his measured responses which have elevated my critical thinking. Needless to say, Dr. Kothary has served as the prime example of outstanding thesis supervisor and act as role model in building my (hopefully) own research program and mentoring students. Over the years, we have created a good friendship and one I hope will continue despite my transient divergence in my training path.

During my time in the laboratory, I was extremely lucky to be surrounded by such incredible minds. I am thankful for Dr. Justin Boyer, who took me under his wing when I

had everything to learn, and relentlessly taught me something new every day in the laboratory. In hindsight, his work ethic, perseverance and hard work have shown me that this is the only way research success can be attained. I am beyond grateful for the incredible support of Emily McFall, Yves De Repentigny, Ariane Beauvais who I have work closely on the projects within this thesis and have made my work in the lab extremely smooth, efficient, productive. They have supported me through my craziest ideas without doubts/questions and without them, these projects would not have been nearly as successful. Similarly, I extend my gratitude to Sabrina Gagnon, My Tran Trung, and Rebecca Yaworski, who have always ensured that the laboratory runs smoothly. I have had the pleasure to have many fruitful discussions and feedback with my fellow lab mates Sarah Cummings, Samantha Kornfeld, Anisha Lynch-Godrei, Mehdi Eshraghi, and Dr. Lyndsay Murray. They have diversified my views on the path forward. I have special thanks to give to my students (Nicole Auclair, Britanny Paul, Alexandra Tierney, and Lucia Chehade) I had the chance to mentor. They taught me important lessons in how to best teach concepts, how to spark their curiosity, develop excitement towards research, and how to become a better mentor. I can't go without thanking "the boys", comprised of Dr. Justin Boyer, Armin Yazdani, Dr Andrew Ferrier, Dr John-Paul Michalski, and Dr Ryan O'Meara, who have been there only for a short time after my arrival in the lab but made it an incredibly fun place to work.

I want to thank my advisory committee members Dr. Jodi Warman, Dr Jeff Dilworth and Dr. Alex Mackenzie for challenging me throughout my training, redirecting me towards important dilemma/questions, and supporting my learning. In a similar manner,

my innumerable collaborators for their advice, insightful discussions and contributions to my research.

Much of this work would not have been possible without the numerous funding agencies who have put their trust in Dr. Kothary's research (Canadian Institutes of Health Research, Muscular Dystrophy Association, and CureSMA) and myself (Canadian Institutes of Health Research, Department of Cellular and Molecular Medicine at the University of Ottawa, the Ottawa Hospital, The Canadian Medical Hall of Fame, and The Audrey J. Boyce family).

The name of my family members should figure on the first page of this thesis given their unconditional support in my hardships, successes, and dilemmas throughout this journey. First, my parents, Sylvie De Blois Deguise and Jean-Claude Deguise, who are one of the biggest inspirations I have. They have and continue to give everything they can to ensure my success, whether academically, emotionally, or on a personal level. They are the most dedicated persons I know. I am beyond thankful for their presence in my journey and their understanding in my pursuit of a very demanding career, which limits the time I can spend with them. Naomi Niznick, my better half, who has been by my side all along and never stopped believing in me throughout this long and strenuous path, even though this meant that I would be nearly absent in our relationship at times. She has provided me with a happy place to come home to. She has had a huge implication in maintaining my wellness and sanity. With her help, she makes me reach new heights and allows me to better myself everyday as a partner, person, researcher and clinician. Lastly, our new addition to the

family, our dog Eddie, who makes sure to remind me that every day is happy day as long as we have each other.

None of this work would have been possible without them. As it is often said: “it takes a village to raise a child”, it also takes a village to attain personal goals, excel and reach beyond our limits of our chosen field. For that, I am forever thankful.

Chapter 1 : General introduction

Contribution

This section comprises some parts directly taken from the following three manuscripts:

Marc-Olivier Deguise, Teresa N. Patitucci, Allison D. Ebert and Christian L. Lorson and Rashmi Kothary. (2017) Chapter 10: Contributions of different cell types to SMA pathogenesis. Spinal Muscular Atrophy: Disease Mechanisms and Therapy, Edited by: Charlotte J. Sumner, Sergey Paushkin and Chien-Ping Ko, Elsevier, ISBN: 978-0-12-803685-3

My Contribution: ~70% (Wrote the majority of the manuscript)

Authors contributions: TNP, ADE, CLL, RK wrote manuscript and critically reviewed it.

Marc-Olivier Deguise and Rashmi Kothary (2017) New insights into SMA pathogenesis: Immune dysfunction and neuroinflammation. *Annals of Clinical and Translational Neurology (IF: 3.901).* Doi:10.1002/acn3.423

My Contribution: ~85% (Wrote the majority of the manuscript)

Authors contributions: RK wrote manuscript and critically reviewed it.

Marc-Olivier Deguise & Rashmi Kothary (2019) Chapter 2: Spinal muscular atrophy. Chromatin signalling and Neurological disorders. Edited by Olivier Binda, Elsevier

My contribution: 85% (Wrote the majority of the manuscript)

Authors contributions: RK wrote manuscript and critically reviewed it.

Spinal Muscular Atrophy: Prevalence, genetic basis and clinical features

Spinal muscular atrophy (SMA) is a devastating neurological disease that can affect individuals of any age, most commonly diagnosed in babies and young infants. In the latter, it is considered as the most common genetic disorder leading to death after cystic fibrosis. In fact, 1 in 11,000 live births will be diagnosed with SMA, the consequent result of a homozygous mutation or deletion in the *Survival Motor Neuron 1* (*SMN1*) gene (1, 2). The carrier frequency for deleterious *SMN1* mutations is relatively high, albeit variable between ethnicities, ranging from 1 in 40 to 1 in 125 (2, 3). *SMN1* is found on chromosome 5q13, a region deemed unstable (4). Over the course of evolution, two distinct genetic events had particular importance for the disease. First, a duplication event in the chimpanzee lead to a 500 Kb inverted repeat element containing a second copy of the *SMN* gene, termed *Survival Motor Neuron 2* (*SMN2*) (5). Second, a single nucleotide (c.C680T) substitution arose in the duplicated *SMN2* gene, a characteristic unique to *Homo sapiens* (5). While this nucleotide substitution is translationally silent, it is not without consequences. Indeed, the substitution is found in a splicing enhancer region of exon 7, which favours exon 7 exclusion in ~90% of the transcripts from *SMN2* (6). Consequently, the protein product from this gene is truncated, unstable and rapidly degraded, leading to a production of low amounts of functional SMN protein (6, 7). Therefore, SMA is a disease of low levels of SMN rather than complete absence, due to the loss of *SMN1* but presence of the intact *SMN2* gene. In fact, complete depletion of SMN is incompatible with life (8). In the same manner, the *SMN2* copy number modulates disease severity, where high copy number leads to more SMN protein and consequently a milder disease outcome (9, 10). Therefore, *SMN2* acts as natural disease modifier in the context of SMA.

Traditionally, SMA is characterized as a motor neuron disorder, because of the preferential susceptibility of alpha motor neurons, which ultimately results in paralysis and muscle weakness to a varying degree. This weakness is more prominent in the proximal muscle, more so in the legs than in the arms. The clinical spectrum of SMA disease in mainly divided into 4 types (4). SMA type I (also known as Werdnig-Hoffmann disease) patients have generally two *SMN2* copies (9), and are diagnosed before 6 months of age. They show the most severe phenotype, with babies not reaching most motor milestones, including sitting (4). Without supportive therapy, or the newly U.S Food and Drug Administration (FDA) approved drugs (Spinraza and Zolgensma), the patients usually succumb to disease before their second year of life due to respiratory distress. However, supportive therapy offers significant lifespan extension in severe SMA patients (11). While SMA type I patients represent about 50% of diagnosed cases, they make up for a small proportion of the SMA population (12%) given the fatality of their symptoms (4). SMA type II (also known as Dubowitz disease) patients generally have three copies of *SMN2* and are diagnosed between 6 to 18 months of age (9). These children usually gain an ability to sit independently but most will not walk (4). Unlike SMA type I patients, they are more prone to developing scoliosis, which may result in respiratory compromise. Patients afflicted with SMA type II are the most prevalent (52%) given their less severe clinical presentation (4). SMA type III (also known as Kugelberg-Welander disease) patients have three to four copies of *SMN2*, and are diagnosed at the age of 18 months or older (4, 9). They account for 36% of SMA patients (4, 9). These infants will be able to walk independently but may lose this ability later in life (4). Type IV SMA patients have the least severe symptoms. The disease manifests after 21 years of age and progresses very

slowly (4). These patients will have a normal life expectancy due to the presence of more than four copies of *SMN2*, but will eventually develop muscle weakness and may require walking assistance or even wheelchairs (4).

The SMN protein: ubiquitous localization and functions

Since the discovery of the gene mutated in SMA in 1995, research may not have yielded a conclusive mechanism for the disease, but it has informed us greatly about SMN localization, structure and function. The SMN protein is relatively small and is composed of four main domains: a Gemin2-binding domain, a Tudor domain, a proline-rich domain and a YG domain (12). Many studies have established that the primary function of these domains mediates the interaction between SMN and its numerous binding partners (12). The SMN protein has a ubiquitous pattern of expression and is temporally regulated, prominently expressed in embryonic and neonatal period before weaning down to low levels into adulthood (13, 14). Within the cell, SMN shuttles from the cytoplasm to the nucleus, and vice-versa, and aggregates in nuclear structures called gems (15) and Cajal bodies (16). SMN is naturally found as part of a complex called the SMN complex, which includes SMN, Gemins2-8 and Unrip (12). The first, and most widely studied, function of SMN described the protein as essential for small nuclear ribonucleoprotein (snRNP) assembly, which are involved pre-mRNA splicing (12, 17). It has been hypothesized that SMN lead to pre-mRNA splicing of certain transcripts, which may be motor neuron specific or simply more deleterious in these cells, hence leading to the selective motor neuron loss (18-20). Nonetheless, it appears that the splicing defects are a relatively late

event in SMA pathogenesis and may not be sufficient to fully explain SMA pathogenesis (21).

Ever since, studies have implicated SMN in a growing array of mechanisms mediating RNA metabolism that extends from telomere synthesis to mRNA transport (22). The role of the SMN protein in mRNA transport and processing was attractive as it offered an explanation connecting SMN depletion to preferential motor neuron susceptibility. The presence of SMN in the axon (23, 24), without its usual Sm protein binding partners (25), but rather with associated to RNA binding proteins (RBPs) heterogeneous nuclear ribonucleoprotein R (hnRNP-R) (26), ELAV Like RNA Binding Protein 4 (HuD) (27), KH-Type Splicing Regulatory Protein (KSRP) (28), Fragile X Mental Retardation Retardation Protein 1 (FMRP) (29), Insulin Like Growth factor 2 mRNA Binding Protein 1 (IMP1) (30) as well as some classical SMN complex protein as Unrip (27), Gemin2 (27), Gemin3 (25), is thought to be responsible for mRNA transport, availability and potentially translation of major transcripts including β-actin (31), Cpg15 (32), and potentially many others (33). Consequently, SMN depletion leads to decreased availability of transcripts (27), many currently unknown. This event was hypothesized to lead to reduced axonal length and neurite outgrowth observed in SMN-depleted *in vitro* models (31, 34). The currently identified RBPs (HuD, KSRP, FMRP, IMP1) and mRNA (β-actin) affected by SMN depletion are unlikely to be the culprit as a single entity. Studies on knockouts of each individual proteins have not reported any significant motor function abnormalities or features in keeping with SMA pathology (34-39). Nevertheless, the combination of all of them could lead to SMA disease pathogenesis. Interestingly, studies on SMN as carrier of mRNA transcripts have not been studied in other cell types. As such, the search for a

disease mechanism that incorporates selective vulnerability of motor neurons remain an active goal of the SMA community.

To further complicate our understanding of SMA pathogenesis, SMN is also involved in histone mRNA 3' processing (40). Canonical histone (H2A, H2B, H3, H4 and H1) genes are replication-dependent (41). Unlike other mRNA, their transcripts do not contain any introns and do not harbour a poly-A tail but instead a stem loop on their 3' end (41). U7 snRNPs are responsible for the cleavage of the 3' end of the histone transcript. As with other snRNPs, a modified SMN complex, that includes Lsm10 and Lsm11 instead of SmD1 and SmD2 (42, 43), assist in the U7 snRNP assembly (40). SMN depletion leads to loss of U7 snRNP formation and consequently impairs histone mRNA 3' processing (40). This has tremendous effect on the histone expression and protein levels (40). It is possible that a minimal change in the pool of histones may lead to a significant change in proportion of canonical histone to non-canonical histone variants, a type of histone that is not replication dependent and processed as regular mRNA transcripts (41). As some histone variants regulate transcription (44), it could have fundamental effects on the expression of the rest of the genome. Furthermore, low levels of U7 snRNPs or abnormal levels of replication-dependent histones required to pack DNA following replication may have major consequences in cellular proliferation. Indeed, reducing U7 snRNP proteins or U7 snRNA is enough to slow the progression during cell cycle (45, 46), while low proliferative rates have been reported in SMN-depleted cells (18, 47). Interestingly, SMN is required during early development, a time marked by increased proliferation. Moreover, this mechanism could also explain pathological findings in SMA foetuses (48). Altogether, the ubiquitous functions of SMN, many still being uncovered, highlight the potential

importance of SMN in every cell. It strongly argues that depletion of SMN might lead to alterations in every cell type and their holistic consequences to disease phenotype is unclear.

Historical perspective: Skeletal muscle provide first evidence of extra-neuronal defects

The hunt for the defective cell type: Motor neurons vs. Skeletal muscles

Historically, upon discovery of the *SMN* gene, the notion that SMA might be a systemic, multi-organ disorder was not contemplated, despite some early evidence that it could be (49-53). Most of SMN's functions were yet to be uncovered. At the time, the main enigma relied on whether depletion of the causative gene product, SMN, lead to deficits in the skeletal muscles or the motor neuron. This was in part due to the clinical presentation of SMA and the close spatial and physiological relationship of the muscle and motor neuron. It was speculated that muscle defects could cause motor neuron death through detrimental signals or simply lack of neurotrophic factors (54, 55). On the other hand, motor neurons could develop lethal cell-autonomous dysfunction.

Cell culture: Separating the muscle from the motor neuron

The first few studies revealing possible muscle involvement focused mainly on the required interaction between muscles and motor neurons for proper motor neuron development and function. Human SMA patient muscle extract was shown to be inhibitory to neurite outgrowth (54). This suggested that the muscle was releasing factors that could be causing spinal neurons to malfunction, independent of the effect of muscle denervation

(54). Muscle defects were also identified using a nerve-muscle co-culture system, containing SMA patient muscle biopsy cells with healthy motor neurons. In this context, muscle cells were found to degenerate dependent on SMA disease severity, demonstrating that SMA muscles were not able to sustain proper function in the presence of healthy motor neurons (55). Furthermore, other potential players such as SMA fibroblasts did not significantly affect the co-culture system (56). This ultimately restricted the defects uniquely to muscle cells. Degeneration of the muscle cells was avoided when both control and SMA satellite cells were mixed, thus allowing for the formation of heteromyotubes (56).

Ultimately, these initial *in vitro* studies point to muscle being an affected cell type in SMA, which may interfere with proper communication between the muscle and the neuron, subsequently contributing to motor neuron degeneration. Neuromuscular junction (NMJ) studies now advocate for such an idea in the context of SMA, highlighting impaired NMJ maturation and signal transmission as an underlying primary cause of motor neuron death (57-59). Muscles are likely contributing to post-synaptic dysfunction at the NMJ, given that they are responsible for the production, localization, organization and maturation of acetylcholine receptors during development (60). In rodent models, there is a delay in gaining mature forms of the acetylcholine receptor (59). SMA type 1 patient myotubes have fewer nicotinic acetylcholine receptors, which fail to cluster when exposed to agrin, possibly interfering with NMJ development (61). Partial improvement of the NMJ function is witnessed upon SMN rescue targeted to myogenic factor 5 (Myf5) expressing progenitor muscle cells (62). Albeit, the authors do caution that this could also be secondary to

minimal SMN increased in the motor neurons (62). Altogether, SMN-depleted muscle may have consequences on all components of the motor unit.

Lessons on muscle defects from conditional mouse knockouts of SMN

The nerve-muscle co-culture studies gave valuable insights in muscle cell-autonomous defects. However, they did not clarify what the defects were or to what extent muscle defects contributed to SMA pathogenesis. Studies on localization and expression of SMN and its binding partners in muscle were increasingly reinforcing new potential intrinsic roles (63-65). More specifically, a novel surprising localization of SMN, with most of its complex, was found to be at the sarcomere of myofibrils both in heart and skeletal muscle, with potential binding interaction with alpha-actinin in both flies and mice (64, 65). This opens up the possibility that SMN plays a role in muscle extending beyond RNA metabolism and splicing, potentially being implicated in regulation of actin dynamics, sarcomere integrity, signalling, and myogenesis. Indeed, presence of such defects became clear in the first conditional knockout experiment. Muscle-specific knockout of SMN severely reduced lifespan and caused severe paralysis (66). The main feature of complete ablation of SMN in muscles was dystrophy, which is, to our knowledge, generally not seen in SMA patients or SMA preclinical models (66, 67). Therefore, the results from this early muscle-specific knockout should be interpreted carefully. SMA is characterized by low SMN protein rather than no SMN protein, making the conditional knockout not representative of true SMA muscles (67). In fact, any tissue fully depleted of SMN will show profound abnormalities, unlikely present in SMA patients (68). Despite this suboptimal modeling of the SMA muscle component, this study as well

as other muscle-specific SMN conditional knockouts (discussed in further detail below) have provided valuable information into the importance of SMN in muscle and the potential contributory role muscle plays in SMA disease pathogenesis.

Restoration of SMN in specific compartments confirm that all components of the motor unit, including muscles, are important

The first muscle-specific restoration of SMN in a mouse model of SMA argued against muscle being an important contributor to disease. Unlike the Prion Promoter (PrP) promoter-driven SMN mice, the human skeletal actin (HSA) promoter-driven mice displayed no lifespan extension or correction in myofiber size (69). The authors concluded that SMA muscles, therefore, had no contribution in SMA pathogenesis (69). However, it is noteworthy that the PrP driven muscle fiber size retained higher proportion of smaller fibers compared to control (69). This is in accordance with potential muscle autonomous defects that could have restricted full phenotypic rescue and could be representative of impaired muscle growth. Lastly, the HSA promoter may only increase SMN expression in myotubes and not in progenitor satellite cells. It is therefore likely that the lack of improvement in the HSA-SMN rescued mice reflects the lack of SMN expression in the satellite cells (70). Indeed, in subsequent work, the use of the Myogenic Differentiation 1 (MyoD) promoter to restore SMN in the muscle compartment lead to survival extension and improved motor behaviour similar to that observed with the choline acetyltransferase (ChAT) motor neuron specific promoter (71). Additionally, complete myofiber size rescue was unique to the MyoD inducible system, despite no NMJ amelioration (71). These results confer SMN a distinct role in muscle, particularly in muscle growth and myogenesis,

whether post-natal or embryonic (71). Recently, mouse models have been generated that diminish SMN exclusively in muscles to levels that are physiologically comparable to SMN levels in SMA tissue (unlike conditional knockouts described above) (72). Using Myf-5-Cre driver, it was shown that muscle SMN-reduction did not have an impact on survival and did not produce phenotypic abnormalities observed in SMA mice (72). Conversely, reintroducing SMN to muscle using the same driver in the SMA mouse model did not correct the phenotype (72). This reminds us that rescue of individual organs may not lead to beneficial changes. In fact, even rescue limited to the central nervous system (CNS) have poorer outcomes than systemic rescue (73). Thus, while the collective genetic studies in mice may not provide an absolute answer, the overall data available is suggestive that muscle contributes to SMA pathogenesis.

Skeletal muscle defects in SMA

Skeletal muscle is by far the non-neuronal tissue that has been the most extensively studied for the reasons mentioned above. Thirty years of research has yielded interesting findings at multiple levels. Over the years, the support for muscle contribution to SMA disease has waxed and waned. More recently, the muscle defects are being widely appreciated and a renewed view on their importance is steaming in the new therapeutic era of SMA. Our current knowledge is reviewed below.

Reduced SMN protein leads to embryonic and neonatal muscle growth impairment

SMN is particularly important early in life (74-77). This early temporal requirement of SMN makes it possible that embryonic and post-natal developmental delay could be at

play in SMA (74-77). Very little research has been done on the embryonic requirement of SMN in the context of SMA disease pathogenesis. One study reported smaller myotubes in SMA fetuses at all time points studied (78). SMA induced pluripotent stem cells (iPSC)-derived muscle progenitors and myotubes cultures displayed no specific defects in progenitor number or myotube formation (79). However, embryonic muscle fate is still understudied, and subtle defects could have significant consequences in the neonatal and post-natal periods and could provide an explanation for SMA post-natal findings (described in the following section).

Neonatal SMA muscles are small and do not appear to grow (80, 81). Even though other defects such as neurogenic atrophy eventually develop, motor neuron loss and consequently atrophy has been reported to occur late in the disease process in the *SmnΔ7* SMA mouse model (*Smn*$^{-/-}$;*SMN2*$^{+/+}$;*SmnΔ7*$^{+/+}$) (80). Other arguments for slow growth include the absence of fiber grouping in mouse models, a feature generally characteristic of chronic neurogenic atrophy, with rather uniformly smaller fiber pattern (80). Such observation is suggestive of a mechanism common to all fibers rather than denervated fibers. Furthermore, the embryonic isoform of muscle Myosin Heavy Chain (MyHC) continues to be expressed long after birth in SMA model mice (59, 82-84).

Potential modulators of post-natal muscle growth in SMA

Satellite stem cell dysfunction and impaired myogenesis

Building muscle comprises many steps and each step has a molecular signature orchestrated by strict temporal and differential expression pattern of transcription factors

(85). During post-natal development, the satellite stem cells are quiescent until they become committed, when they will be activated and will divide and increase to self-renew the stem cell pool or contribute to the regenerative process (85, 86). Once the conditions are right, the activated committed satellite cells (i.e. myoblasts) differentiate to become an elongated myotube that will eventually fused together to produce mature skeletal muscle (85).

Early work associated reduced SMN with aberrant Myf-5 expression in SMA patient muscle biopsy cultures (87). Such early disruption in the temporal regulation of an important myogenic factor was indicative of a snowball effect to the rest of the myogenic blueprint. Indeed, the fusion index was also impacted in SMA type I satellite cell cultures while SMA type II cells appeared relatively spared (87). Similarly, additional work in hypomorphic SMN knockdown C2C12 cells has shown that defects observed are SMN dose-dependent, resembling SMA clinical presentation (88). The hypomorphic C2C12 cell lines demonstrated decreased number of gems, low proliferative capacity, and major fusion abnormalities (88).

In early muscle conditional SMN knockout mice, satellite cells were also shown to be affected (89). These mice also had reduced lifespan and reduced satellite cell regenerative capacity, despite having characteristics of muscle dystrophy as stated earlier (89). Interestingly, the reduction in lifespan was absent in new conditional knockout mice in which SMN depletion was specifically targeted to mature skeletal muscle and not to satellite stem cells (70). Although, these latter mice lived much longer, they still showed a mild dystrophic feature with a slower progression, potentially due to the unaffected regenerative capacity of the satellite cells (70). Additional studies have also implicated

satellite cell abnormalities in SMA pathogenesis. Hayhurst & *al.* (2012) reported a higher number of Paired box 7 (Pax7)+/MyoD- and Pax7+/MyoD+ cells in pre-phenotype muscles from the *Smn*$^{-/-}$*;SMN2* mouse model (82). These satellite stem cells precociously expressed differentiation markers such as MyoD and Myogenin (MyoG) in culture (82). As previously reported, upon induced differentiation, the satellite cells had impaired fusion capacity and dysregulated pattern of MyHC expression (82). In accordance with the evidence implicating satellite cell dysfunction, Boyer & *al.* (2014) reported an increase in early onset central nucleation in skeletal muscle from two mouse models of SMA, namely *Smn*$^{-/-}$*;SMN2* and *Smn*$^{2B/-}$ (83). Central nucleation is indicative of active regeneration or presence of immature muscle fibers. In this context, active regeneration appears unlikely since muscle degeneration was not observed in these SMA mouse models (83). As such, the presence of the immature fibers is likely due to defective myogenesis. Indeed, myogenic factors such as Pax7, MyoD and MyoG were misregulated in both mouse models of SMA (83). Dysregulation of the myogenic gene expression program was also confirmed in primary cultures established from the mice (83). Collectively, there is now accumulating evidence for differentiation and fusion defects in SMN depleted muscle cells (61, 82-84, 87, 88).

Myogenic dysregulation in SMA has also been implicated by other studies. Bricceno & *al.* (2014) showed an altered regulation of microRNA (MiR) MiR206 and MiR486, two major muscle microRNAs (referred to as myoMirs) (84), in immortalized SMA mouse muscle cell lines. Importantly, the expression of embryonic and perinatal MyHC were greatly elevated (84). Furthermore, this study investigated possible mechanistic changes that could be inhibiting the proper fusion of the SMA muscle cells. A

reduced cleavage of talin was used to support the idea that cytoskeletal regulation was compromised, subsequently leading to cell migration and fusion defects (84).

Several studies have provided evidence that myogenesis is dysregulated in SMA model systems. Our understanding of SMN depletion in satellite cells remains limited. Functional studies could provide mechanistic insight into pathological events leading to myogenic defects and how this is relevant to SMA pathogenesis.

Anabolism and Catabolism in SMA

Muscle is highly active regarding protein production (anabolism) or degradation (catabolism). The balance/imbalance of these two processes can regulate skeletal muscle size. It is possible that a defective equilibrium in SMA leads to hypotrophic muscles, before atrophy fully initiates. Depending on the environment and stimulus, anabolism or catabolism can be rapidly induced. This is primarily controlled by the Insulin-like Growth Factor 1(IGF1)/Protein Kinase B (PKB or Akt) pathway (90). Akt is at the intersection of protein production, where it induces mammalian Target of Rapamycin (mTOR), and protein breakdown, where it inhibits the Forkhead box protein O (FoxO) transcriptional family of proteins (90). Other factors regulating this pathway include myostatin and follistatin (90).

Neurogenic atrophy is a well-accepted feature of SMA. This occurs when the muscles gradually get denervated because of the motor neuron loss. Since atrophy is secondary to motor neuron denervation, molecular pathways responsible have not been well studied in the context of SMA. The first (and only) study identified an upregulation of MyoG dependent high histone deacetylase (HDAC) 4 expression and activity (84).

These changes resulted in upregulation of Atrogin-1 (MAFbx) and Muscle Ring Finger 1 (MuRF1), commonly known as the atrogenes (91). Interestingly, similar results were obtained in patient samples (91). Use of the HDAC inhibitor trichostatin A (TSA) effectively reversed the atrogenes and MyoG aberrant expression in the preclinical model (91). In response to those findings, a mouse model of SMA (*SmnΔ7*) with a deleterious allele of MAFbx or MuRF1 was generated to understand whether reversal of atrophy could be beneficial (92). Unfortunately, the SMA mice did not display much improvement in body weight or survival (92). As expected, muscle fiber size increased but did not match that of control mice (92). Taken at face value, this study would imply that other atrophy pathways or atrophy-independent mechanisms, such as impaired myogenesis, act to produce the smaller SMA muscle fibers. As such, better characterization of molecular mechanisms of atrophy pathways and their therapeutic modulation is warranted.

SMA researchers have more extensively considered and experimented with stimulation of the anabolism pathways. It is well established that the use of myostatin, its inhibitor follistatin or IGF1 has shown beneficial effects on general muscle growth in mice (93-96). They have also shown promise in other mouse models of disease (97-99). Follistatin supplementation in SMA mice has provided modest results, with increased muscle mass and a slight improvement in motor function and survival (100). Similarly, myostatin knockout *SmnΔ7* mice did not show any improvement in motor behavior or in survival (101). These results were later reproduced (102). Transgenic overexpression of follistatin did not yield much beneficial effects (102). Thus, it appears that myostatin is not a critical player in muscle mass induction early postnatally and that the effect of follistatin,

if any, is mediated through other pathways (103). This is perhaps not surprising as myostatin is actually low in motor neuron disorders (104). In an attempt to understand potential therapeutic importance of stronger and larger muscles, an alternative pathway was utilized, in which they created SMA mouse models that overexpressed IGF1 solely in the muscles (105). While they observed an apparent increase in muscle weight associated with increased myofiber diameter, the lifespan was extended only modestly (4 days) with no motor improvements (105). In light of all these attempts to modulate muscle mass, relatively little information has been gleaned on the basal physiological levels of proteins involved in the IGF1-AKT pathway in SMA. A characterization of this pathway is warranted to help in better design of future therapeutic efforts focused around improving muscle growth in SMA.

Physiological defects in muscles of SMA mice

Muscles from mouse models of SMA can't function as well as wild type in electrophysiological tests (106). Muscles from *Smn*$^{-/-}$*;SMN2* mice at phenotypic stage had lower twitch force and lower tetanic force in an *ex vivo* study (106, 107). In addition, these muscles did not respond well to fatigue (106). The use of the *ex vivo* analysis allows one to negate all potential contribution of motor neurons, which could be affecting the muscles. Furthermore, pre-symptomatic *Smn*$^{-/-}$*;SMN2* and the *Smn*$^{2B/-}$ mice both present with muscle weakness, suggesting that the defect is independent from the motor neuron problems (106). To decipher what could internally cause weakness, investigation of sodium and calcium channels needed for proper contraction and relaxation were performed. Phenotypic *Smn*$^{-/-}$*;SMN2* and *Smn*$^{2B/-}$ mice had aberrant expression of ryanodine receptors (RyR1) and sodium channels proteins Nav1.4 and Nav1.5 while lower expression in sarcoplasmic

reticulum Ca2+ ATPase (Serca1a) was only observed in the more severe model mice (108). These abnormal expression patterns are highly indicative of cell-autonomous defects, ultimately leading to lower force production as most of these defects were not observed in experimentally denervated animals (106). Ling & *al.* (2010) reported similar findings negating that NMJ transmission failure provoked muscle weakness in *SmnΔ7* muscles (107). According to the authors, the decreased tension observed is attributable to small fiber size rather than contractility potential. Indeed, impaired myogenesis could be the muscle pathogenic trigger leading to multiple functional consequences including weakness (107). Therefore, it is likely that multiple mechanisms act synergistically to create the SMA muscle phenotype.

Multi-organ disease or motor neuron disease?

Even though SMN is ubiquitously expressed and has housekeeping functions (see previous sections), SMA has long been considered a motor neuron disorder. Much of the work has focused on motor neuron pathobiology while studies on non-neuronal entities concentrated on skeletal muscle (see previous sections). As intrinsic skeletal muscle defects were slowly being uncovered, studies identifying defects in other organ systems were surfacing. Other organs, including muscles, might not display an explicit phenotype or changes in commonly measured endpoints such as lifespan or weight. Importantly, while not as dramatic as the motor neuron phenotype, defects in other organs could potentially act synergistically and contribute to SMA pathogenesis, or at least modify it. Indeed, the SMA community seems to be shifting from the motor neuron-centric view to multi-organ

perspective when considering SMA pathogenesis (109, 110). In favour of the multi-organ involvement in SMA, it has been shown several times in pre-clinical models that systemic delivery of therapeutic compounds results in better outcome than neuronal-restricted delivery (111, 112). Moreover, Spinraza, an approved drug for SMA delivered intrathecally, does not completely rescue SMA disease (113). Altogether, this highlights the complex contribution of multiple organ systems in SMA and their importance for complete recovery.

Cardiac defects in SMA

Historically, a small but clinically identifiable sub-group of very severe SMA patients have presented with cardiac defects, including structural and functional deficits (reviewed in (114, 115)). The accumulation of case reports most commonly pointed towards increased susceptibility to atrial and ventricular septal defect (ASD and VSD, respectively) and hypoplastic left heart syndrome (HLHS) amongst others. Although limited to 4 patients, a report concluded that SMN is very likely to have some function in cardiogenesis, given that the predicted statistical occurrence of SMA (with 1 copy of SMN2) and septal defects together is much smaller than the occurrence reported in their findings (114). Consistent with this, several severe SMA mouse models present with structural and functional cardiac defects (116-119). Structural deficits included dilated cardiomyopathy, decreased wall and septal thickness, arterial changes, reduced cardiac fiber size and fibrosis while functional defects range from reduced cardiac output, bradycardia, and heart block (120-124). Interestingly, the bradycardic feature was

attributed to autonomic nervous system dysfunction and reduced cardiac innervation in SMA model mice (116, 117, 125). Strikingly, despite trial of gene therapy in these mice, some of these defects remained (120, 122). Autonomic cardiac alterations also appear to be present in a subset of the SMA population (reviewed in (121)). Molecular aetiologies have yet to be fully elucidated in mouse models of SMA.

Liver defects in SMA

Fatty acid metabolism studies were restricted to SMA patients and no extensive characterization has been performed in preclinical models. Patients show abnormal levels of esterified carnitine, dicarboxylic aciduria and diminished muscle mitochondrial β-oxidation proteins activity (49, 51, 126). A follow-up study found increased dodecanoic to tetradecanoic acid (C12:C14) ratio and development of ketonuria upon fasting (126). In addition, fatty acid filled vacuoles in the liver were reported at autopsy in SMA patients, an attribute commonly seen in patients with dysregulation of β-oxidation (51, 126, 127). More importantly, most of these observations were exclusive to SMA type 1 patients with a few exceptions in milder patients and were not reported in age-matched diseased controls (126). Altogether, SMN depletion is likely attributable to the observed defects, thought to be independent of muscle denervation (126). Significantly, other defects could be pinpointed directly to the liver. Liver restricted SMN ablation lead to embryonic lethality (68). Mutant embryo livers showed abnormal development, function and iron overload associated with misregulated expression of genes involved in iron homeostasis (68). SMA mice, which express low levels of SMN rather than complete depletion, show increased erythropoiesis, megakaryocyte and platelet production, together with mild iron storage

abnormalities (128). Other reports identified lower reduced hepatic expression of insulin like growth factor binding protein acid labile subunit (IGFals), an IGF1 binding partner capable of promoting its stability (73). In addition to these observations, mitotic defects, necrosis and inflammatory cell infiltration was evident in an anti-sense oligonucleotide-dependent SMA mouse model, which consequently lead to pronounced elevation of serum aspartate aminotransferase and alanine aminotransferase (129). The impact of these findings on overall metabolism and growth needs further work.

Pancreatic defects in SMA

Glucose metabolism defects have been reported in the context of SMA. The mild $Smn^{2B/-}$ mouse model displayed early onset fasting hyperglycemia and progressive glucose intolerance associated with important changes in cell composition of the pancreatic islets (130). This was defined by an increase in alpha glucagon producing cells and decrease of beta insulin producing cells (130). This resulted in hyperglucagonemia at all time points studied and hepatic insulin hypersensitivity in late stages of disease progression (130). Interestingly, analysis of patient autopsy material showed similar alterations in islet composition (130). To have a better understanding of the metabolic contribution to SMA pathogenesis, similar measures were investigated in SMN hypomorphic mice, which do not display any pathological hallmark of SMA (131). Glucose metabolism in one month old $Smn^{+/-}$ mice appeared to be normal (131). However, a high-fat diet regimen induced glucose tolerance problems, alpha cell mislocalization, hepatic insulin and glucagon hypersensitivity (131). Aging also triggered a different set of pancreatic abnormalities in SMN hypomorphic mice, which may become highly relevant when lifespan extension of

SMA patient becomes a reality (131). A small pilot cohort study revealed that almost all SMA patients displayed hyperinsulinemia and were considered resistant to insulin (132). Additionally, upon oral glucose tolerance test (OGTT), 3 of 6 patients had impaired glucose tolerance (132). Noteworthy, analysis of the patient's body composition ranked them all as obese (132). In another report, providing different diets have a significant effect on the survival of *SmnΔ7* mouse model of SMA (133), implying that modulation of intake could reduce the consequence of metabolic defects. In contrast with previous studies, the *SmnΔ7* mice were hypoglycemic and showed evidence of increased ketone production (133). Hypoglycemia and ketonuria were mentioned in two SMA patients (134). The variety of different metabolic phenotypes obtained in the different experimental settings increase the complexity of interpretation. It will be important to refine our knowledge on potential modulators of these metabolic defects because they can trigger dysfunction in all cell types as a consequence.

Gastro-intestinal defects

It is possible that the metabolic abnormalities observed in SMA are compensatory to primary gastro-intestinal malfunction causing sub-optimal absorption of nutrients. Gastrointestinal (GI) problems have been noted in SMA. In patients, gastroesophageal reflux, constipation and abdominal distention are often reported (135). Similarly, studies in mice showed constipation features, changes in fecal content distribution, delayed gastric emptying and slow liquid transit in the small intestines and colon despite normal activity, food and liquid intake (136). Interestingly, there are no apparent morphological changes or inflammation in the GI system (136). Impaired GI neuromuscular transmission appeared

to be responsible for some of these abnormalities (136). Whether impaired metabolism is linked to the GI system abnormalities remains to be determined.

Ultimately, although much of the work is still ahead of us, impaired metabolic functioning seems to be characteristic of the SMA phenotype and very likely contributory to disease onset and progression.

Defects in supportive neural cells

Within the neurological microenvironment, nearly all supportive neural cells have been implicated in neuronal dysfunction in one way or another. The altered relationship among these cells and the functional consequence remain largely unexplored. Nevertheless, their individual intrinsic defects are starting to be elucidated.

Astrocytes & Microglia

Increased astrogliosis is observed in necropsies of SMA patients (137-141) and in the *SmnΔ*7 mouse model at both pre-symptomatic and symptomatic stages (142, 143). SMA patients induced pluripotent stem cell-derived astrocytes revealed abnormal calcium regulation, decreased glial cell derived neurotrophic factor (GDNF) production but normal solute carrier family 1 member 2 (GLT1) expression(142). SMN restoration restricted to the astrocyte compartment significantly increased lifespan and motor behavior, but did not improve motor neuron survival (138). Interestingly, this may be due to altered direct contact interaction between astrocyte and motoneuron, which leads to reduction in synaptic formation and function (144). Mixed results have been published on the implications of

soluble factors (144, 145). One report identified astrocytic release of miR-146a as potential mediator of motor neuron survival and impaired neurite outgrowth (145). Microglial activation has also been observed in the *SmnΔ*7 mouse model but not in the more severe *Smn*$^{-/-}$*;SMN2* mice (107, 139, 140, 143). Nevertheless, characterization of molecular dysfunction has not been performed.

Schwann cells & Oligodendrocytes

Schwann cells appear susceptible to SMN depletion (146-148). In fact, myelination of certain peripheral nerves was reduced in two mouse models of SMA (147). SMA Schwann cells did not respond to myelination cues, initiated intrinsic apoptotic pathways and had diminished production of important extracellular matrix components (147). While re-introducing SMN only in Schwann cells reverts myelination defects and improves NMJ pathology, it does not improve survival, motor neuron counts or muscle fiber pathology (148). On the other hand, oligodendrocytes appeared unaffected (149). Their development as well as migration was untouched and myelination of the central nervous system was unaffected in the *Smn*$^{-/-}$*;SMN2* mice (149).

Consideration for therapy delivery and beyond

Spinraza, the newly-approved drug for SMA, is likely to provide benefits to SMA patients. Nonetheless, the drug does not completely revert SMA disease (113). Therefore, it is likely that type I SMA patients will transition into a less severe type III-IV phenotype once treated, giving them a longer or normal lifespan. In recent years, SMA is slowly being recognized as a multi-organ disorder (reviewed above and in (150), Fig. 1.1). The effect of

Smn depletion on various cell types and tissues in aging patients remains unknown. Importantly, there could be subclinical deficiencies, which, upon challenge, could cause overt problems. Supportive therapy in Duchenne muscular dystrophy (DMD) patients, leading to lifespan extension, has revealed cardiomyopathy as an important consideration in management of the disease (151). We could be facing a similar phenomenon with our Spinraza-treated SMA population, emphasizing the need for an appropriate SMA model for aging studies.

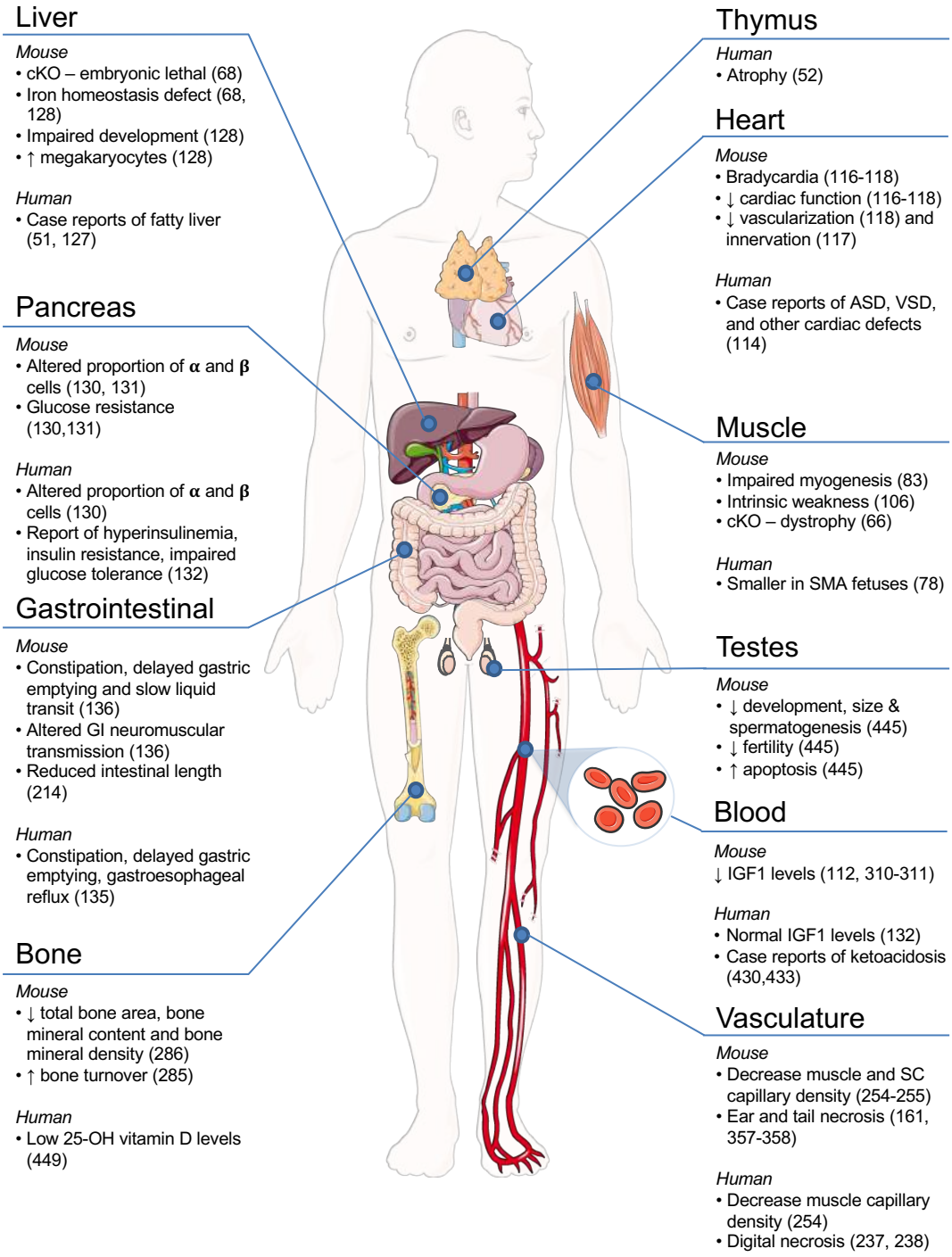

Figure 1.1 Contributions of non-neuronal organs in SMA pathology in mouse models and SMA patients. This schematic highlights the major findings of non-neuronal organs in mouse models and SMA patients up to 2016 (prior to full time PhD component). This

figure is by no means inclusive of all findings in the different systems but represent a good overview. Abbreviations - ASD: atrial septal defect, VSD: ventricular septal defect, cKO: conditional knockout, GI: gastrointestinal. Schematics component provided by Servier medical art.

SMA mouse models

Spinal muscular atrophy is heterogenous in its clinical presentation. Indeed, SMA patients can present with very severe symptoms, not reaching major motor milestones (Type I), to a normal lifespan with minor muscle weakness (Type IV) (reviewed above and in (4)). Reproducing the heterogeneity in mouse models of SMA has proven difficult (152). For example, the copy number of human *SMN2* in a mouse model does not result in similar severity as in human patients (152). For example, 4 copies of the *SMN2* gene leads to important motor deficits in humans (Type III) while very few defects are observed in the transgenic mice (152). Strangely, it appears that the window at which SMN depletion causes a SMA phenotype in mice is very narrow, with an almost all-or-nothing phenomenon, where mice are either very sick, or largely unaffected (152). The most common mouse models of SMA currently used include the severe mouse model *Smn*$^{-/-}$*;SMN2* (153), the "Taiwanese" mouse model (also *Smn*$^{-/-}$*;SMN2*) (154), the "delta7" model (*Smn*$^{-/-}$*;SMN2;SMN*$^{\Delta 7/\Delta 7}$) (155) and the *Smn*$^{2B/-}$ mice (156, 157) (Table 1.1). They are all considered severe mouse models, with the *Smn*$^{2B/-}$ mouse living the longest (survival - postnatal day (P25)) (157). Even though milder models have been generated (158-161), their use has been limited, potentially since some showed almost none of the universal

SMA features. Therefore, the less severe end of the clinical spectrum in SMA (Type III-IV) has never been extensively studied in preclinical models. At the moment, results obtained from severe models are the only information we have, with little information about molecular and pathological events in milder forms of SMA. Many reports have shown that molecular differences are present when comparing SMA mouse models or SMA patient tissues of varying severities (162, 163). In addition, current SMA mouse models do not allow for lengthy experimental framework given their short lifespan.

Table 1.1: Common mouse models of SMA

Name	Genotype	Total SMN protein (VS WT)	Median survival	Ref.
Severe	$Smn^{-/-}$;$SMN2^{Tg/Tg}$	~5-10%	5 days	(153)
Taiwanese	$Smn^{-/-}$;$SMN2^{Tg/Tg}$	~5-10%	10 days	(154)
SmnΔ7	$Smn^{-/-}$;$SMN2^{Tg/Tg}$;$SMN\Delta7^{Tg/Tg}$	~5-10%	14 days	(155)
Smn$^{2B/-}$	*$Smn^{2B/-}$*	~15%	25 days	(156, 157)

Rationale

From a biological perspective, it is important to understand the fundamental defects that lead to SMA development and how various tissues communicate with one another as SMA progresses. As therapeutics are developed and extend survival for a broad range of patients, it is plausible that underlying defects that were unrecognized or underappreciated will emerge. Recent work has demonstrated that SMA is a complex disorder that impacts a variety of tissues as reviewed above. Now that SMA-specific treatments have entered the clinic, it is even more imperative to fully comprehend the necessary cellular targets for an immediate as well as a sustained therapeutic impact.

Hypothesis

SMN depletion leads to widespread abnormalities in multiple non-neuronal organs, making SMA a multi-organ disorder.

Aims

1. Characterize molecular pathways underlying atrophy in SMA skeletal muscle and the effect of trichostatin A on these pathways
2. Investigate whether immune alterations are present in SMA
3. Investigate whether metabolic defects are present in SMA
4. Create a mild mouse model of SMA to identify SMN function in maintenance of neuronal and non-neuronal cell in aging.

Chapter 2: Differential induction of muscle atrophy pathways in two mouse models of spinal muscular atrophy

Differential induction of muscle atrophy pathways in two mouse models of spinal muscular atrophy

Marc-Olivier Deguise[1,2,3], Justin G. Boyer[1,2,4], Emily McFall[1], Armin Yazdani[1,2], Yves De Repentigny[1] and Rashmi Kothary[1,2,3,5,*]

[1]Regenerative Medicine Program, Ottawa Hospital Research Institute, Ottawa, Ontario, Canada K1H 8L6

[2]Department of Cellular and Molecular Medicine, University of Ottawa, Ottawa, Ontario, Canada K1H 8M5

[3]Centre for Neuromuscular Disease, University of Ottawa, Ottawa, Ontario, Canada K1H 8M5

[4]Present address: Cincinnati Children's Hospital Medical Center, Cincinnati, OH 45229, USA

[5]Department of Medicine, University of Ottawa, Ottawa, Ontario, Canada K1H 8M5

*Correspondence to: Rashmi Kothary; Ottawa Hospital Research Institute; 501 Smyth Road, Ottawa, Ontario, Canada K1H 8L6; Tel: (613) 737-8707; Fax: (613) 737-8803; Email: rkothary@ohri.ca

Published in Scientific Reports (IF: 4.259). **6**:28846 | DOI: 10.1038/srep28846

Author Contributions

M-O.D designed the study, performed experiments, prepared Figures 2.1, 2.2, 2.4-2.6, Supplementary Fig. S2.7-2.8, Supplementary Table S2.1, and wrote the manuscript. E.M performed experiments. Y.D.R performed electron microscopy and prepared Figure 2.3 and methods for electron microscopy. J.G.B was involved in the initial design of the study, performed some experiments and wrote the manuscript. A.Y helped with TSA treatment. R.K designed the study and wrote the manuscript. All authors reviewed the manuscript.

Abstract

Motor neuron loss and neurogenic atrophy are hallmarks of spinal muscular atrophy (SMA), a leading genetic cause of infant deaths. Previous studies have focused on deciphering disease pathogenesis in motor neurons. However, a systematic evaluation of atrophy pathways in muscles is lacking. Here, we show that these pathways are differentially activated depending on severity of disease in two different SMA model mice. Although proteasomal degradation is induced in skeletal muscle of both models, autophagosomal degradation is present only in *Smn*$^{2B/-}$ mice but not in the more severe *Smn*$^{-/-}$*;SMN2* mice. Expression of FoxO transcription factors, which regulate both proteasomal and autophagosomal degradation, is elevated in *Smn*$^{2B/-}$ muscle. Remarkably, administration of trichostatin A reversed all molecular changes associated with atrophy. Cardiac muscle also exhibits differential induction of atrophy between *Smn*$^{2B/-}$ and *Smn*$^{-/-}$*;SMN2* mice, albeit in the opposite direction to that of skeletal muscle. Altogether, our work highlights the importance of cautious analysis of different mouse models of SMA as distinct patterns of atrophy induction are at play depending on disease severity. We also revealed that one of the beneficial impacts of trichostatin A on SMA model mice is via attenuation of muscle atrophy through reduction of FoxO expression to normal levels.

Introduction

Spinal muscular atrophy (SMA) is a childhood neuromuscular genetic disease affecting 1 in 11,000 live births (2, 164, 165). SMA pathological hallmarks include motor neuron loss and severe muscle atrophy of the limb and trunk muscles. In 1995, the disease-causing gene, survival motor neuron 1 (*SMN1*), was identified (1). A mutation or deletion in the *SMN1* gene impairs SMN protein production. A second nearly identical copy of the gene, *SMN2*, is present at the same locus as *SMN1* (1). However, a single base pair substitution in *SMN2* profoundly limits its ability to produce full length SMN protein (6). Thus, increasing *SMN2* copy number leads to phenotypes of reduced severity that can be classified on a spectrum (reviewed in (166)).

The mouse only harbors a single *Smn* gene and homozygous loss is embryonically lethal (8). The addition of a human *SMN2* transgene to $Smn^{-/-}$ mice yielded the original mouse model of SMA ($Smn^{-/-}$;*SMN2*; also referred to as the severe model), which presents with a severe phenotype and lives to a maximum of postnatal day (P) 6 (153). Recently, mouse models of SMA with less severe phenotypes have been generated in an effort to uncover novel disease mechanisms and to test several therapeutic approaches. One of these is the $Smn^{2B/-}$ mouse model. Instead of incorporating the human *SMN2* transgene, this mouse harbours a 3 nucleotides substitution in the exonic splice enhancer of exon 7 (2B mutation) in one allele of the mouse *Smn* gene, while the other allele is null (156, 167). Consequently, the mice present with a phenotype associated with a longer life span (~P30) and enhanced motor function relative to the $Smn^{-/-}$;*SMN2* mouse model (156).

It has always been assumed that muscle defects observed in SMA were completely attributable to degenerating motor neurons. However, recent work on both the *Smn*$^{-/-}$*;SMN2* and *Smn*$^{2B/-}$ model mice revealed robust intrinsic muscle weakness prior to any overt motor neuron pathology (108). Muscle weakness in these models was attributed to impaired muscle development supported by the aberrant expression of several proteins involved in myogenesis (108, 168, 169). Atrophy, a direct consequence of motor neuron loss, is likely a contributing factor to muscle weakness, but it has not been systematically studied in SMA. Different atrophy initiating stimuli, such as fasting, denervation, and other systemic catabolic states activate common transcriptional changes in the atrogenes (170, 171). Myogenin (MyoG) is a transcription factor known to induce E3 ligases important in proteolytic sarcomere breakdown. However, the MyoG pathway becomes activated only in neurogenic atrophy (172, 173). This pathway has been previously investigated in the *SmnΔ7* model mice (*Smn*$^{-/-}$*;SMN2*$^{+/+}$*;SmnΔ7*$^{+/+}$) and SMA patients where increased myogenin expression correlated with increased expression of Muscle Ring Finger 1 (MuRF1, TRIM63) and Atrogin-1 (MAFbx, Fbxo32) in skeletal muscles (174). Importantly, myogenin-dependent increases in atrogene levels could be attenuated by treating *SmnΔ7* mice with the pan-histone deacetylase inhibitor trichostatin A (TSA), possibly due to its proposed effect on histone deacetylase 4 (HDAC4) (174). TSA has also been proposed to increase SMN expression through *SMN2* transcriptional modulation (175), which in turn could halt atrophy. However, other studies have suggested that the beneficial effects of TSA are not through SMN induction (176). Thus, it remains unclear whether TSA functions in a SMN-dependent or independent manner to reverse atrophy in the *SmnΔ7* model. Other studies have examined the contribution of MuRF1 and Atrogin-1

in SMA by crossing *SmnΔ7* mice with MuRF1 or Atrogin-1 null animals (177). The survival time and body weight of these mice matched the non-transgenic *SmnΔ7* mice control mice, suggesting MuRF1 or Atrogin-1 are not the only players in atrophy and that other pathways may be involved (177). Assessment of autophagy or other potential triggers to the degradation machinery have not been investigated in the context of SMA and might provide answers to this conflicting evidence.

Unlike MyoG, FoxO transcription factors are implicated in a much wider variety of atrophy types, including neurogenic atrophy, where it is thought to initiate but also maintain atrophy (171, 178). Additionally, FoxO proteins induce the expression of proteasomal genes, such as MuRF1 and Atrogin-1, as well as autophagic genes (178-180). This dual pathway control is important since autophagy has been reported to contribute to atrophy upon denervation (178-180). Hence, FoxO transcription factors are thought to control half of the genes identified in the molecular "common atrophy blueprint" present in different atrophy types (178, 179).

Here, we have investigated the potential contribution of autophagy and its regulation in the context of SMA. In addition, we have assessed whether or not SMA severity affects atrophy molecular profiles in two SMA model mice for which atrophy characterization is lacking. We were further interested in deciphering the mechanisms by which TSA protects against atrophy using the $Smn^{2B/-}$ model mice, which does not harbor the human *SMN2* transgene. Lastly, we extended our analysis to cardiac muscle, which has been previously described to have smaller caliber fibers(122).

Results

Atrophy in skeletal muscles from Smn$^{-/-}$;SMN2 *mice is marked by increased proteasomal degradation without signs of autophagosomal protein breakdown*

MuRF1 and Atrogin-1 are thought to be the main E3 ligases involved in proteasomal protein breakdown of muscles (181, 182). We decided to focus on the expression of these E3 ligase genes since atrophy is a transcription dependent process (178). Moreover, protein levels of E3 ligases and of autophagosome-lysosome related proteins are not always representative in wasting muscles (183). Assessment of the mRNA levels for these genes in pre-symptomatic P2 *Smn$^{-/-}$;SMN2* hindlimb muscles revealed no difference from control muscles (Figure 2.1a). In contrast, increase in transcripts for Atrogin-1 was observed in *Smn$^{-/-}$;SMN2* hindlimb muscles at P5 ($p = 0.021$) (Figure 2.1b), concordant with motor neuron pathology at this age (153). However, MuRF1 transcript expression was unchanged (Figure 2.1b). Interestingly, the temporal expression increase of MuRF1 mRNA is much slower and less drastic than Atrogin-1 in fully denervated muscles (171), which might explain the lack of a measured change in the partially denervated muscles from the *Smn$^{-/-}$;SMN2* mice. The main function of E3 ligases is ubiquitination of proteins to direct them for proteasomal degradation. We therefore investigated the ubiquitination status of proteins to confirm the biological relevance of the increased expression of Atrogin-1 transcripts. Accordingly, we observed a significant elevation in the level of ubiquitinated proteins in *Smn$^{-/-}$;SMN2* hindlimb muscles at P5 ($p = 0.0061$) (Figure 2.1d), but not at P2 (Figure 2.1c).

Autophagosomal and lysosomal processes have been reported in biopsies from patients that had been clinically diagnosed as having SMA (184, 185). However, autophagosomal implications in SMA preclinical models have not been established. We first investigated the expression of important contributors of these pathways and observed relatively unchanged mRNA levels for GABA(A) Receptor-Associated Protein Like 1 (Gabarapl1), CathepsinL and BCL2/adenovirus E1B 19 kDa protein-interacting protein 3 (Bnip3) in P2 and P5 hindlimb muscles when compared to controls (Figure 2.1e,f). We next examined protein levels of sequestosome-1 (sqstm1 or P62) and post-translational forms of microtubule-associated protein light chain 3 beta (MAP1LC3B or LC3). LC3 is the most commonly used measure to identify autophagosome formation (186). It is required for the elongation of the phagophore and LC3 lipidation from LC3-I to LC3-II is required for its function(187). P62 is important in mediating breakdown of protein aggregates by binding to LC3-II (187, 188). We observed that the double lipidated form of LC3 was not elevated in P2 or P5 *Smn*$^{-/-}$*;SMN2* hindlimb muscles (Figure 2.1g,h). Similarly, P62 was unchanged (Figure 2.1g,h). Altogether, these results confirm that proteasomal degradation is induced while autophagic processes are not contributing to atrophy in muscles of the severe *Smn*$^{-/-}$*;SMN2* model mice.

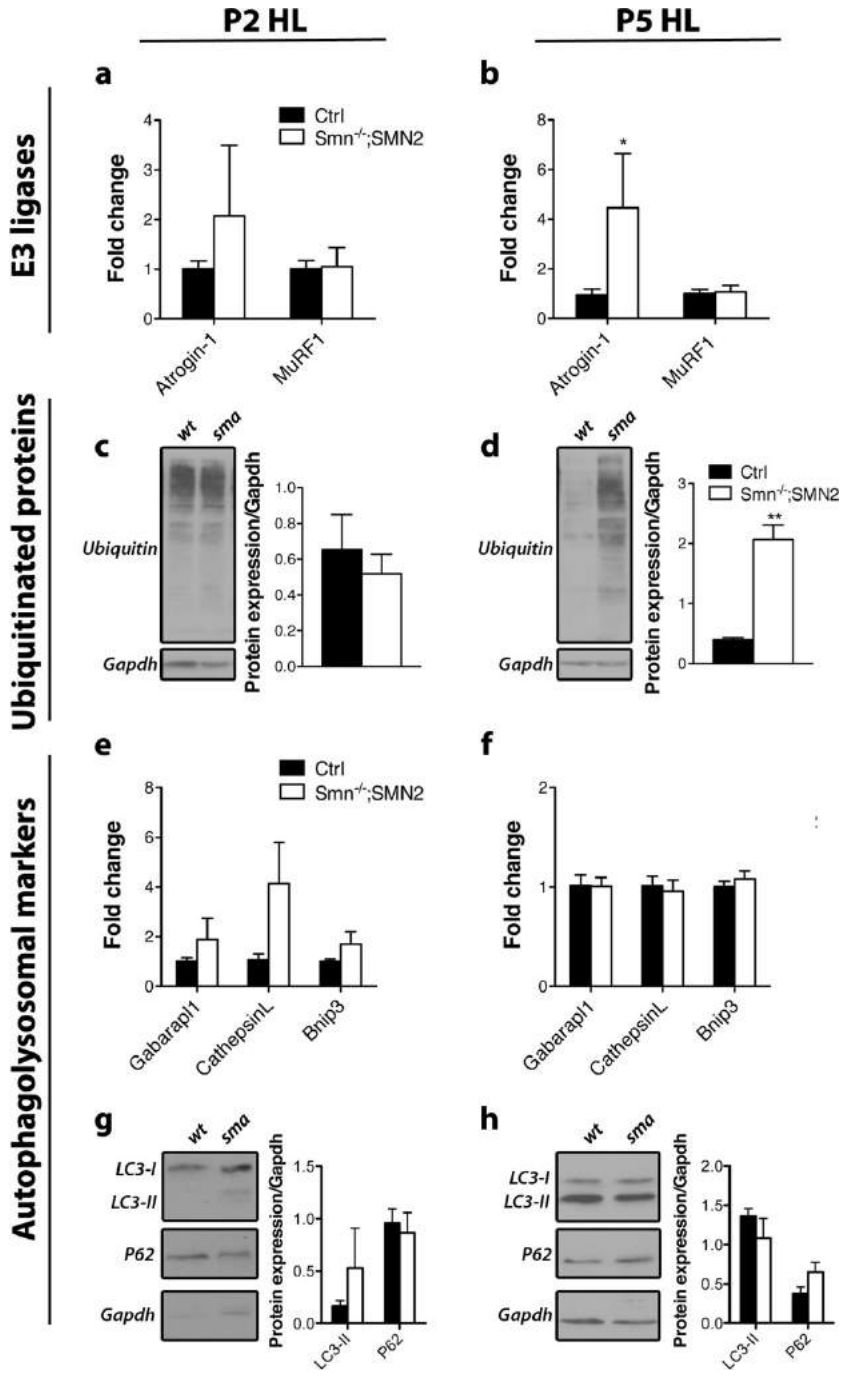

Figure 2.1. Characterization of the modes of skeletal muscle atrophy in *Smn$^{-/-}$;SMN2* mice. (a,b) Levels of Atrogin-1 and MuRF1 mRNA are not significantly changed at pre-symptomatic stage (P2) but Atrogin-1 is increased at symptomatic stage (P5) in the hindlimb (HL) of *Smn$^{-/-}$;SMN2* mice ($p = 0.021$). (c,d) Levels of ubiquitinated proteins are

unchanged at P2 but are significantly increased at P5 ($p = 0.0061$). (e,f) Gabarapl1, CathepsinL and Bnip3 transcript levels are unchanged at both P2 and P5 in muscles of *Smn$^{-/-}$;SMN2* mice. (g,h) No change was detected in LC3-II and P62 protein levels at both time points in hindlimb muscles of *Smn$^{-/-}$;SMN2* mice. (N=4 for a-g, N=3 for h; * $p \leq 0.05$).

Muscle atrophy in Smn$^{2B/-}$ *mice involves both proteasomal and autophagosomal protein breakdown*

The heterogeneity of severity in SMA could potentially have differing molecular underpinnings given the variability in onset of the disease and its progression. Noteworthy, other groups have reported that this is likely to occur but evidence has so far been lacking (163). Therefore, we analysed the less severe *Smn$^{2B/-}$* model to compare to the data from the *Smn$^{-/-}$;SMN2* mouse (see above). Interestingly, the *Smn$^{2B/-}$* mice showed a different molecular atrophy signature compared to the severe model. Atrogin-1 and MuRF1 mRNA levels showed a significant increase ($p = 0.05$ and 0.0067, respectively) in P21 post-symptomatic but not in P9 pre-symptomatic hindlimb muscles (Figure 2.2a,b). This increase of E3 ligases transcripts at P21 was accompanied by increased protein ubiquitination in hindlimb muscles of P21 *Smn$^{2B/-}$* mice ($p = 0.028$) (Figure 2.2c,d).

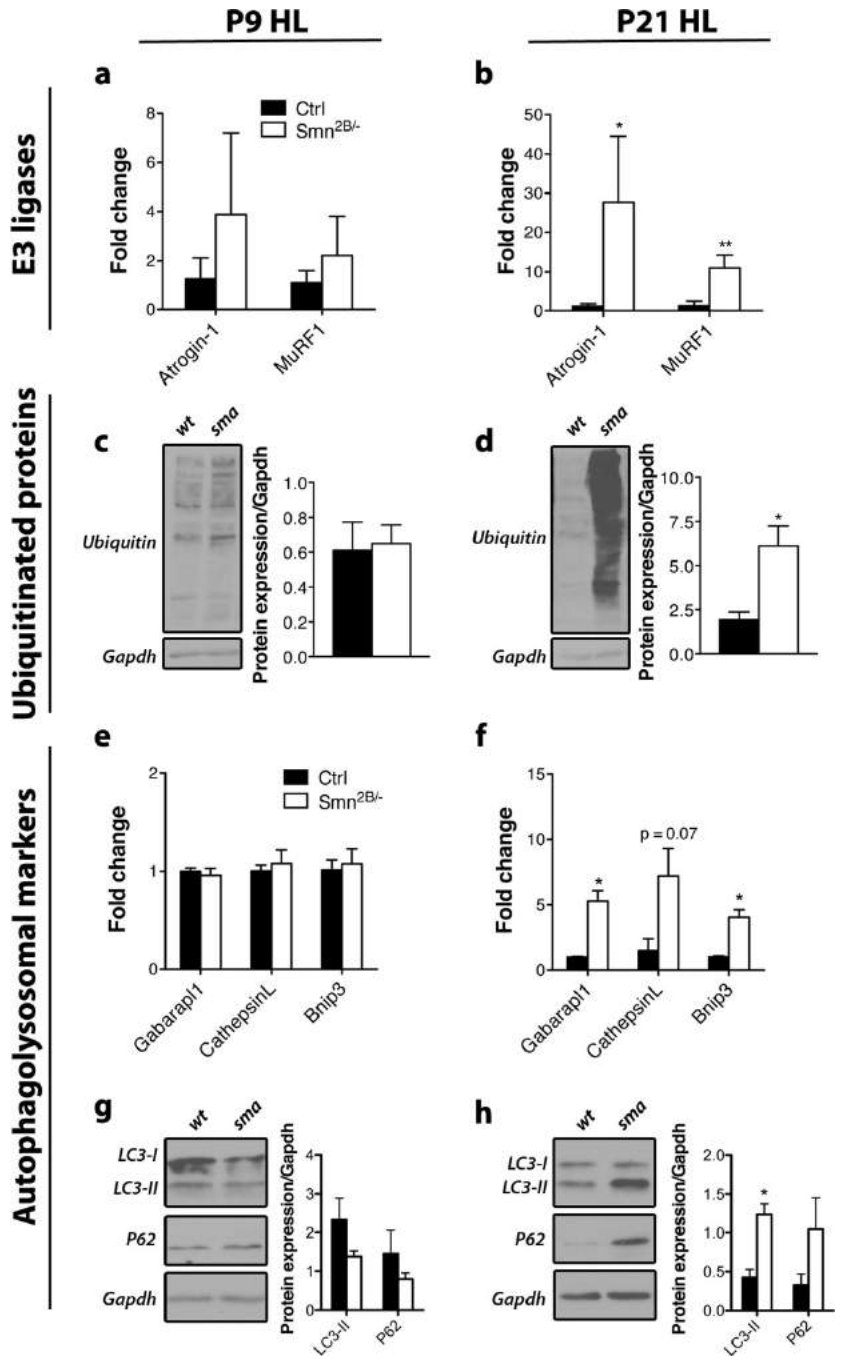

Figure 2.2. Characterization of the modes of skeletal muscle atrophy in *Smn*$^{2B/-}$ mice. (a,b) Levels of Atrogin-1 and MuRF1 mRNA are not significantly changed at pre-symptomatic stage (P9) but are increased at symptomatic stage (P21) in the hindlimb (HL) of *Smn*$^{2B/-}$ mice (p = 0.05 and 0.0067 respectively). (c,d) Levels of ubiquitinated proteins

are unchanged at P9 but are significantly increased at P21 ($p = 0.028$). (e,f) Gabarapl1, CathepsinL and Bnip3 transcript levels are unchanged at pre-symptomatic stage (P9) but are significantly elevated at P21 in hindlimb muscles ($p = 0.012$, 0.066, and 0.012, respectively). (g-h) Protein expression of LC3-II and P62 is relatively unchanged at pre-symptomatic stage and LC3-II is significantly increased at symptomatic stage in hindlimb muscles of *Smn*$^{2B/-}$ mice ($p = 0.011$). (N=4 for a-f, N=3 for g-h; $p \leq 0.05$ for * and $p \leq 0.01$ for **).

Next, we examined expression of the autophagosomal markers. Strikingly, Gabarapl1, CathepsinL and Bnip3 transcripts were all induced in hindlimb muscle at symptomatic stage ($p = 0.012$, 0.066, and 0.012 respectively) but not at pre-symptomatic stage (Figure 2.2e,f). These changes were accompanied by a significant increase in LC3-II protein levels only at P21 ($p = 0.011$) (Figure 2.2g,h). A trend toward increased P62 levels at P21 was also observed (Figure 2.2h). Even though levels of P62 usually increase when autophagic flux is blocked, it has also been observed during increased autophagic flux (186). The latter is more likely occurring in SMA atrophying muscle. Altogether, these results point towards participation of autophagic protein degradation in muscles of *Smn*$^{2B/-}$ mice but not *Smn*$^{-/-}$*;SMN2* mice.

To further confirm that autophagy is induced in the *Smn*$^{2B/-}$ model, we performed ultrastructural analysis of the tibialis anterior (TA) muscle. We analysed muscles from 3 individual mice, two of which showed more extensive vacuolization. We expected some variability since not all fibers are denervated in SMA muscles. Vacuoles were often observed containing degraded cytoplasmic content, mitochondria or electron dense

material, highly suggestive of autophagy-like processes (Figure 2.3). Moreover, structures observed closely resemble those seen in muscles co-transfected with constitutively active FoxO3 (180). Similar structures were also previously noted in ultrastructural analysis of clinically diagnosed SMA patient muscles (184, 185). We have also observed a large number of vacuoles that appear similar to fat droplets (e.g. see Figure 2.3h) (189). In association with the molecular data, we conclude that autophagy is playing a role in the atrophying muscles of $Smn^{2B/-}$ mice.

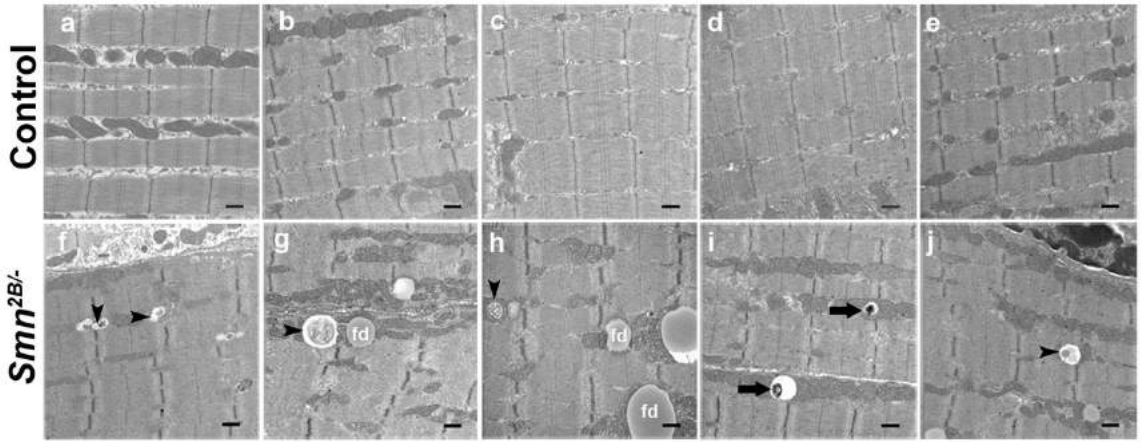

Figure 2.3. Ultrastructural analysis of TA muscles from *Smn*$^{2B/-}$ mice reveals an increase in autophagic vacuoles. (a-e) Representative micrographs (20,000x) of *Smn*$^{2B/+}$ TA muscles show that autophagic vacuoles (autophagosomes and autolysosomes) are not detectable. (f-j) Representative micrographs (20,000x) of *Smn*$^{2B/-}$ TA muscles show several examples of autophagic vacuoles with various degrading cellular structures (black arrowheads) or electron dense material (black arrows). These vacuoles of different size can be observed adjacent to Z-discs and mitochondria in skeletal muscle. A large number of fat droplets (fd) were also identified in the *Smn*$^{2B/-}$ TA muscles. (N=3 for all experiments). Scale bar = 500 nm.

TSA administration to $Smn^{2B/-}$ *mice reverses the expression of atrophic markers*

Trichostatin A, a pan HDAC inhibitor, has shown beneficial effects on atrophy in the *SmnΔ7* model mice (174). It is unclear whether this benefit was due to increased SMN protein, due to chromatin changes affecting other protective pathways, or both. Moreover, observations in the Bricceno & *al.* (2012) study (174) were limited to proteasomal degradation and overlooked autophagy. Here, we have used the $Smn^{2B/-}$ model, which does not contain the human *SMN2* transgene, to address these questions further. We treated the mice daily with either dimethyl sulfoxide (DMSO) or TSA (10 mg/kg) from P3 to P21. Strikingly, TSA administration effectively rescued all dysregulated parameters we had observed. TSA treated $Smn^{2B/-}$ mice had a significant increase in body weight compared to DMSO treated $Smn^{2B/-}$ mice ($p \leq 0.01$), although not quite comparable to DMSO treated control mice ($p \leq 0.001$), reminiscent of other studies (175, 176) (Figure 2.4a). Both Atrogin-1 and MuRF1 transcript levels at P21 were brought back to basal levels upon TSA treatment (Figure 2.4b). This was also associated with a decrease in the levels of ubiquitinated proteins (Figure 2.4c). The autophagosomal pathway was modulated in a similar fashion. The mRNA expression levels of Gabarapl1, CathepsinL and Bnip3 in muscles of TSA treated $Smn^{2B/-}$ mice were comparable to those of control mice (Figure 2.4d). Additionally, LC3 and P62 protein levels were back to normal (Figure 2.4e,f). These results are consistent with our previous published findings where TSA treatment rescued skeletal muscle fiber size (168, 176). Altogether, it suggests that the beneficial effect of TSA on $Smn^{2B/-}$ mice is likely occurring through a correction of the atrophy pathways in skeletal muscles, and is independent of SMN induction.

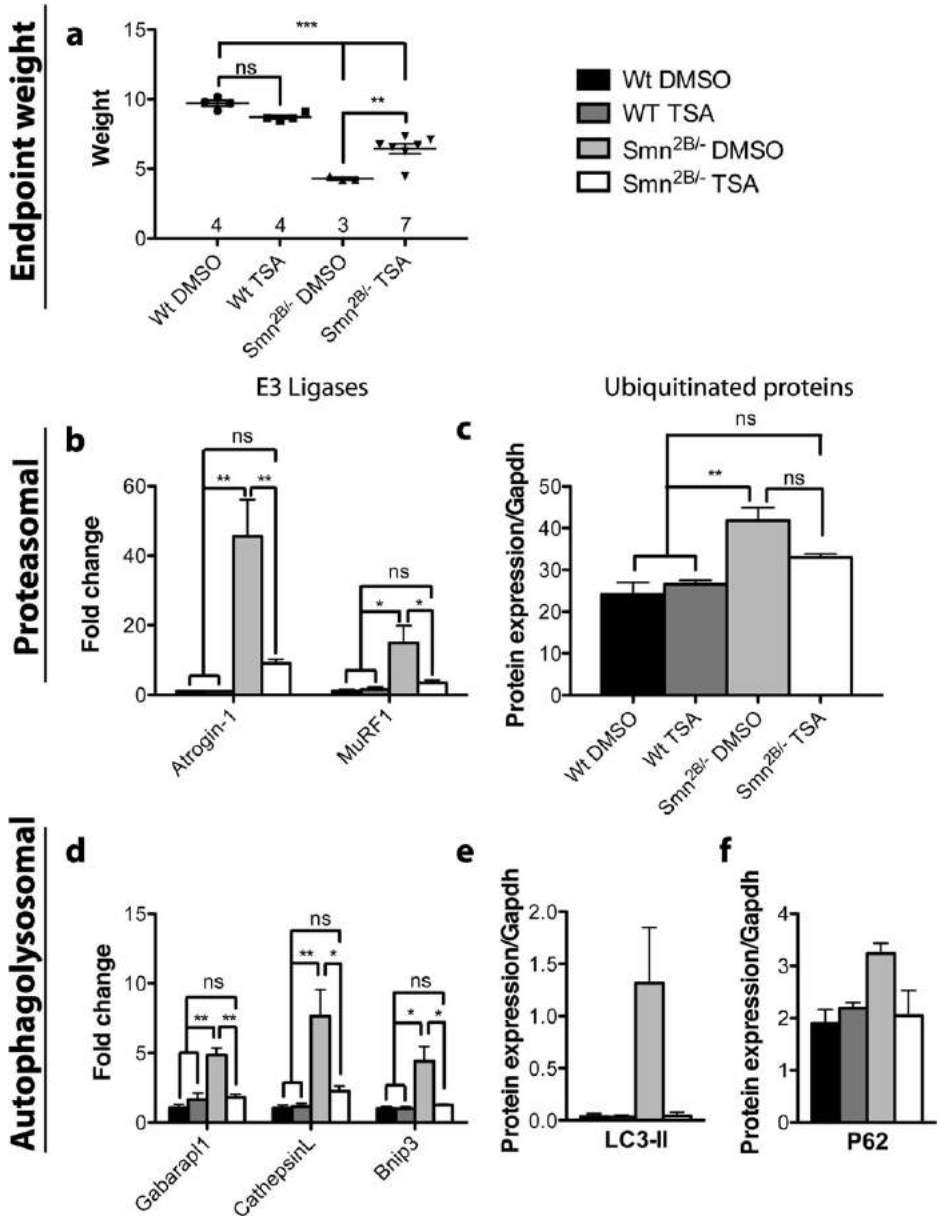

Figure 2.4. TSA administration in *Smn$^{2B/-}$* mice reversed both proteasomal and autophagosomal atrophy. (a) Mice were treated with either DMSO or TSA daily from P3 to P21, and then sacrificed for analysis. DMSO-treated *Smn$^{2B/-}$* mice were significantly smaller in weight compared to control mice ($p \leq 0.001$). TSA-treated mutant mice showed a significant increase in weight compared to DMSO-treated *Smn$^{2B/-}$* mice ($p \leq 0.01$), although they never reached the weight of controls animals. (b) Atrogin-1 and MuRF1 E3

ligase transcript levels were significantly higher in muscles from *Smn*$^{2B/-}$ mice compared to control counterparts ($p \leq 0.01$ and $p \leq 0.05$ respectively). However, this increase was attenuated in TSA-treated *Smn*$^{2B/-}$ mice ($p \leq 0.01$ and $p \leq 0.05$ respectively). (c) TSA treatment of *Smn*$^{2B/-}$ mice resulted in a decrease in the level of ubiquitinated proteins towards control levels. (d) Gabarapl1, CathepsinL and Bnip3 mRNA levels in muscles of *Smn*$^{2B/-}$ mice were restored to control levels upon TSA treatment. (e,f) LC3-II and P62 protein levels in *Smn*$^{2B/-}$ mice dropped to control levels upon TSA treatment. (N=3 for all experiments except c (*Smn*$^{2B/-}$ TSA N=4); $p \leq 0.05$ for *, $p \leq 0.01$ for ** and $p \leq 0.001$ for ***).

FoxO transcription factors are induced in muscles of Smn$^{2B/-}$ *mice*

Our observation of autophagosomal pathway involvement in muscles of *Smn*$^{2B/-}$ mice associated with its significant improvement upon TSA administration led us to investigate new potential regulators of atrophy in SMA. Overexpression of MyoG and its targets were previously shown to be corrected by TSA administration (174). However, MyoG does not regulate autophagosomal pathways and, thus, our results suggest at least one additional player in the control of atrophy in SMA. The FoxO transcription factor family of proteins are ideal candidates. They are part of the IGF1/PI3K/AKT pathway and they are capable of controlling both the proteasomal and autophagolysosomal genes in skeletal muscles (183). Increased transcription of these factors has previously been reported on numerous occasions following different atrophic stimuli (171, 190-192). Additionally, FoxO1 is transcriptionally regulated by itself and by FoxO3, while FoxO4 is transcriptionally regulated by FoxO3(193). Thus, we assessed mRNA levels of FoxO1,

FoxO3 and FoxO4 in both the *Smn*$^{-/-}$*;SMN2* and *Smn*$^{2B/-}$ model mice. We suspected that *Smn*$^{-/-}$*;SMN2* mice would not show any induction of these factors since autophagosomal transcriptional targets of FoxOs were not up-regulated in muscles of these mice (Figure 2.1e-h). We did not observe any changes in FoxO1 and FoxO4 transcript levels (Figure 2.5a,c). A small, but significant ($p = 0.016$), almost 2 fold increase in FoxO3 transcript levels in the symptomatic *Smn*$^{-/-}$*;SMN2* hindlimb muscles was observed (Figure 2.5b). In contrast, mRNA levels for FoxO1, FoxO3 and FoxO4 were significantly elevated by at least 3 folds in *Smn*$^{2B/-}$ hindlimbs at P21 ($p = 0.024$, 0.012, and 0.00032, respectively) (Figure 2.5d-f). Since we were able to rescue the autophagosomal abnormalities seen in the *Smn*$^{2B/-}$ model upon TSA administration, we assessed whether or not expression of FoxO transcripts would be similarly restored to normal levels. Indeed, transcript levels of all three FoxO transcription factors reverted back to control levels in TSA treated *Smn*$^{2B/-}$ hindlimb muscles (Figure 2.5g). Altogether, this data provides evidence that FoxO factors are induced to trigger autophagosomal degradation in muscles of *Smn*$^{2B/-}$ mice, and further that this induction can be reversed by TSA.

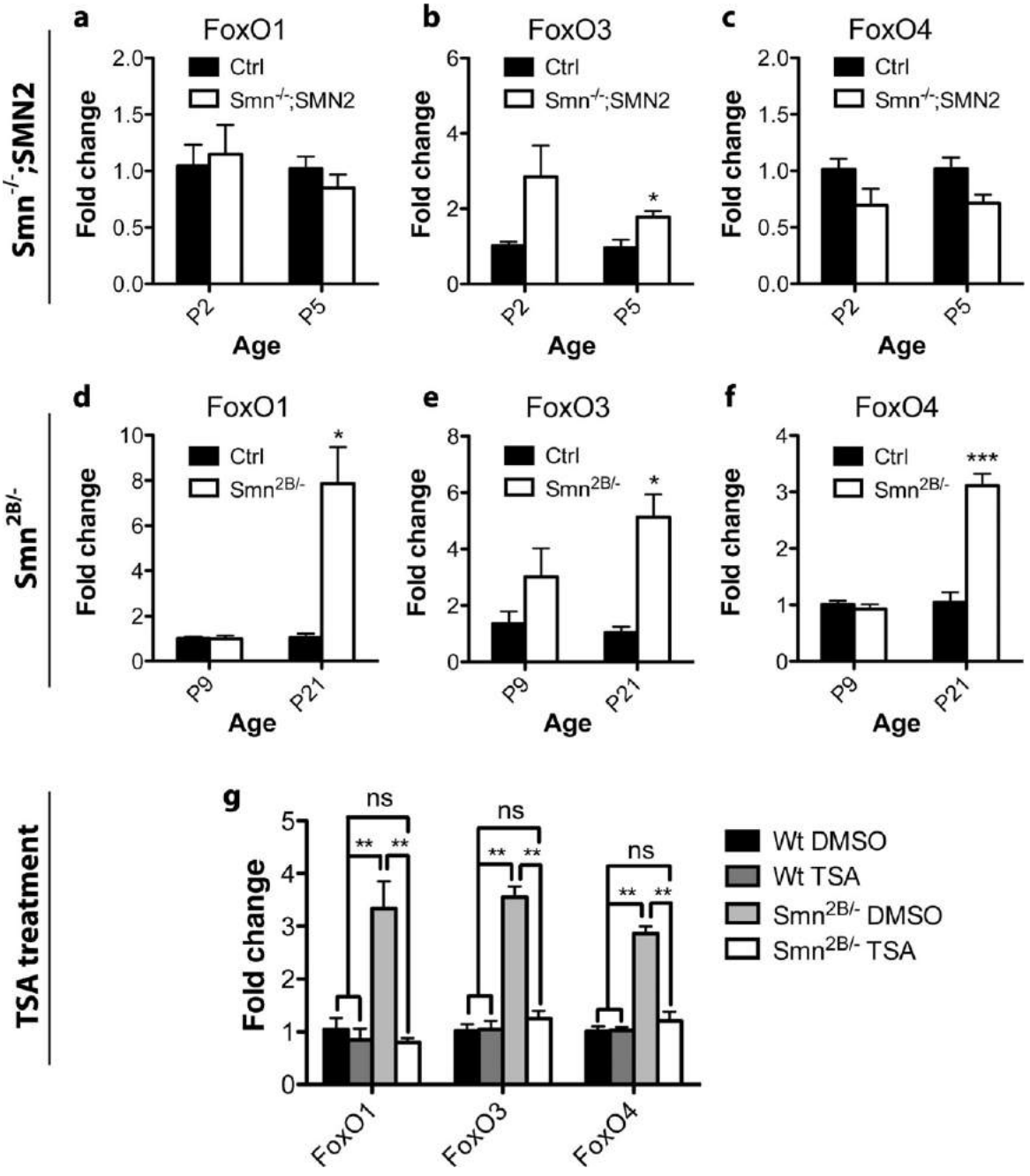

Figure 2.5. Alterations in the expression of the FoxO family of transcription factors are present in skeletal muscles of symptomatic stage *Smn$^{2B/-}$* mice and are reversed upon TSA treatment. (a-c) FoxO mRNA levels are generally not altered in muscles from

Smn$^{-/-}$*;SMN2* mice, except for FoxO3 which is slightly increased at symptomatic stage (P5). (d-f) In contrast, muscles from *Smn*$^{2B/-}$ mice show a significant increase in the levels of FoxO1, FoxO3 and FoxO4 transcripts at the symptomatic stage (P21) in comparison to controls ($p = 0.024$, 0.012, and 0.00032, respectively). (g) FoxO mRNA levels in muscles of *Smn*$^{2B/-}$ mice dropped to control levels upon TSA treatment. (N=4 for a-f, N=3 for g; $p \leq 0.05$ for *, $p \leq 0.01$ for **, and $p \leq 0.001$ for ***).

The FoxO pathway is induced in cardiac muscle of Smn$^{-/-}$;SMN2 *mice*

Unlike skeletal muscle, cardiac muscle is innervated by autonomic nerves. Thus, cardiac muscle should not experience denervation and consequently, should not undergo atrophy in the context of SMA. Nonetheless, the hearts of *SmnΔ7* mice display smaller fiber size, which likely contributes to cardiac remodeling (122). However, it remains unknown as to why this happens. Similar to skeletal muscles, FoxO transcription factors are also expressed in cardiac muscles (194). FoxO3 induces Atrogin-1 and MuRF1 transcription, and counteracts cardiac hypertrophy in multiple pathological settings (194). FoxO1 and FoxO3 also can induce autophagy in cardiac muscle (195). Additionally, mouse models with constitutively active FoxO3 show decreased heart weight explained by individual cardiomyocyte size reduction (196). Thus, we were intrigued whether atrophy processes in skeletal muscles analysed in this study might also be involved in cardiomyocyte fiber size reduction observed in SMA (122). We therefore repeated the same experiments for both *Smn*$^{-/-}$*;SMN2* and *Smn*$^{2B/-}$ whole hearts at symptomatic age.

Our analysis of the hearts of *Smn*$^{-/-}$*;SMN2* mice showed that Atrogin-1 mRNA levels were increased ($p = 0.018$) whereas those of MuRF1 were comparable to control mice (Figure 2.6a). This was not associated with elevation in the levels of ubiquitinated proteins (Figure 2.6c). This suggests that Atrogin-1 may have some other role in cardiac muscle. Furthermore, although we did not observe any changes in expression of the autophagosomal markers in the hindlimb muscles of *Smn*$^{-/-}$*;SMN2* mice, we did observe significant increased transcript levels of Gabarapl1, CathepsinL and Bnip3 in the heart ($p = 0.0076$, 0.033, and 0.0075, respectively) (Figure 2.6e). Further, we observed a trend toward increased protein levels for Bnip3 and Gabarapl1 in hearts from P5 *Smn*$^{-/-}$*;SMN2* mice (Figure 2.7). Lipidation of LC3-I to LC3-II was increased but did not reach statistical significance, and P62 remained relatively unchanged (Figure 2.6g). Finally, we noted that FoxO3 and FoxO4 transcript levels were significantly elevated ($p = 0.0069$ and 0.025, respectively) while FoxO1 transcript levels were elevated but did not reach statistical significance ($p = 0.079$) (Figure 2.6i). Together, these results suggest that some type of autophagy, whether contributing to atrophy or other unknown processes, might be occurring in the hearts of the severe mice and could be controlled by FoxO transcription factors.

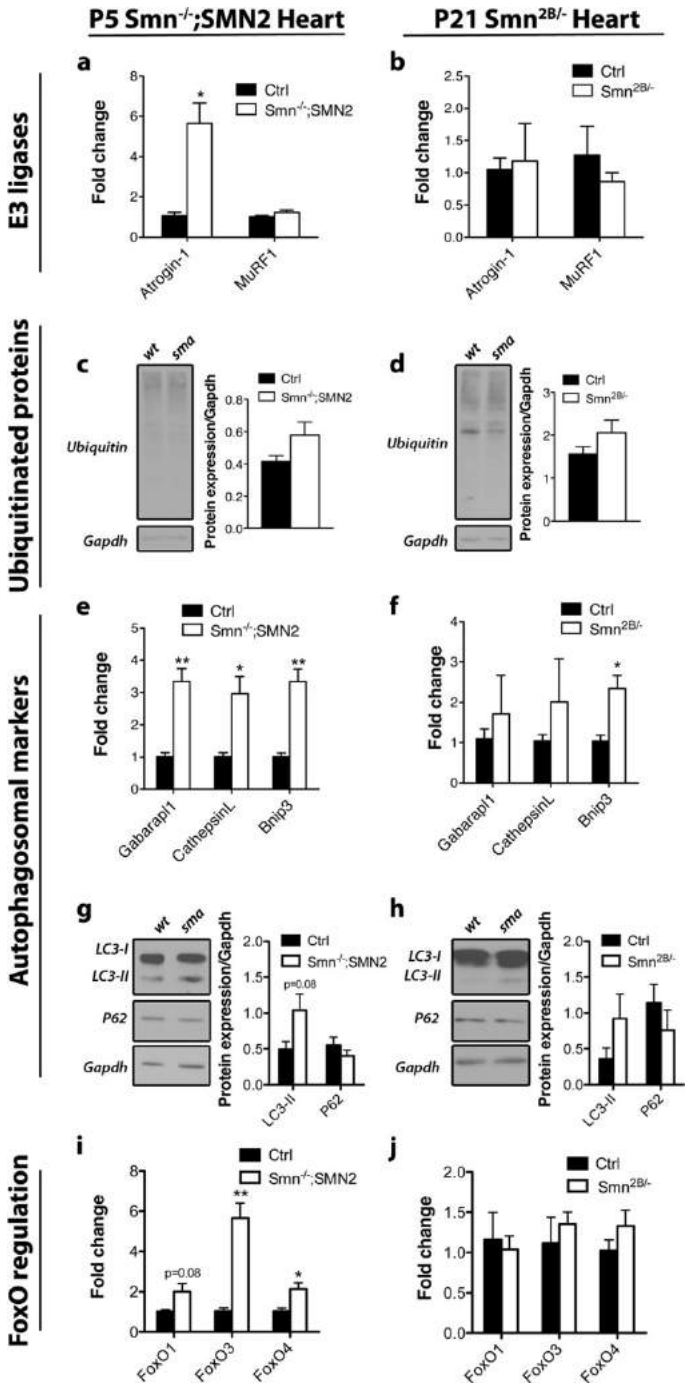

Figure 2.6. Alterations in the expression of the FoxO family of transcription factors and its targets in cardiac muscle of symptomatic stage SMA model mice are restricted to the severe *Smn$^{-/-}$;SMN2* strain. (a,c) Increased Atrogin-1 ($p = 0.018$), but not MuRF1, mRNA levels are observed in *Smn$^{-/-}$;SMN2* hearts at P5. However, this is not accompanied

by an increase in the level of ubiquitinated proteins. (b,d) The levels of Atrogin-1 and MuRF1 mRNA are not altered in hearts from P21 *Smn*$^{2B/-}$ mice. Similarly, there was no change in the level of ubiquitinated proteins. (e,f) Gabarapl1, CathepsinL and Bnip3 mRNA levels are elevated in P5 *Smn*$^{-/-}$*;SMN2* hearts (p = 0.0076, 0.033, and 0.0075, respectively) but not in P21 *Smn*$^{2B/-}$ hearts, although there was a trend towards an increase in all autophagosomal markers. (g,h) No change in LC3-II or P62 protein levels in the hearts of either model. (i,j) An increase in the mRNA level of some of the FoxO transcriptional factor family is observed in hearts from P5 *Smn*$^{-/-}$*;SMN2* mice (FoxO3, p = 0.0069 and FoxO4, p = 0.025) but not in hearts from P21 *Smn*$^{2B/-}$ mice. (N=4 for all experiments; p ≤ 0.05 for * and p ≤ 0.01 for **).

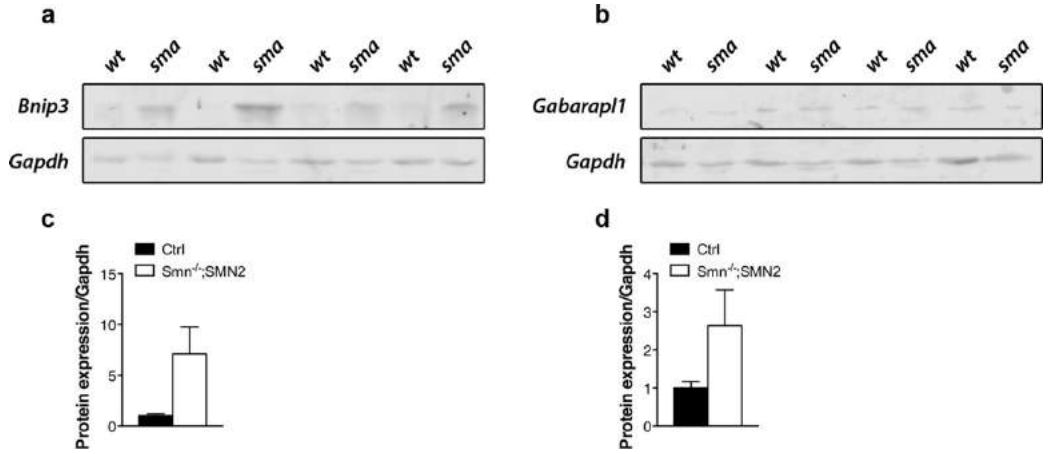

Figure 2.7 *Smn*$^{-/-}$*;SMN2* hearts show a trend toward increased Bnip3 and Gabarapl1 protein levels at P5. (a) Western blot of Bnip3. (b) Western blot of Gabarapl1. (c) Quantification of Bnip3 protein expression showing a trend toward elevated protein levels compared to control. (d) Quantification of Gabarapl1 protein expression showing a trend toward elevated protein levels compared to control. (N=4 for all experiments**)**

In marked contrast, the *Smn*$^{2B/-}$ mice exhibit a different molecular profile in cardiac muscles. Proteasomal E3 ligase Atrogin-1 and MuRF1 mRNA levels remained unchanged, which was associated with stable protein ubiquitination (Figure 2.6b,d). Interestingly, while the autophagosomal markers assessed in skeletal muscles provided solid evidence for autophagy, we only observed a trend towards induction for Bnip3, but not Gabarapl1 and CathepsinL, in P21 *Smn*$^{2B/-}$ hearts (Figure 2.6f). LC3-II and P62 were similar to control (Figure 2.6h). In addition, FoxO transcript levels remain unchanged (Figure 2.6j). Therefore, the *Smn*$^{2B/-}$ heart appears relatively spared in contrast to its *Smn*$^{-/-}$*;SMN2* counterpart. We further analysed the impact of TSA administration of *Smn*$^{2B/-}$ mice on hearts at P21, and its potential effect on Atrogin-1 and the autophagosomal markers. We observed no difference in mRNA expression in Atrogin-1, Gabarapl1 and CathepsinL in DMSO and TSA-treated control and *Smn*$^{2B/-}$ mice (Fig. 2.8). However, there was a significant increase in Bnip3 mRNA transcript levels in the hearts of DMSO-treated *Smn*$^{2B/-}$ mice compared to wild type (Fig. S2.8), which confirms the trend observed in our initial experiment. Reminiscent to the muscle, TSA treatment of symptomatic *Smn*$^{2B/-}$ mice restored Bnip3 transcripts back to control levels in the hearts of these mice (Fig. 2.8).

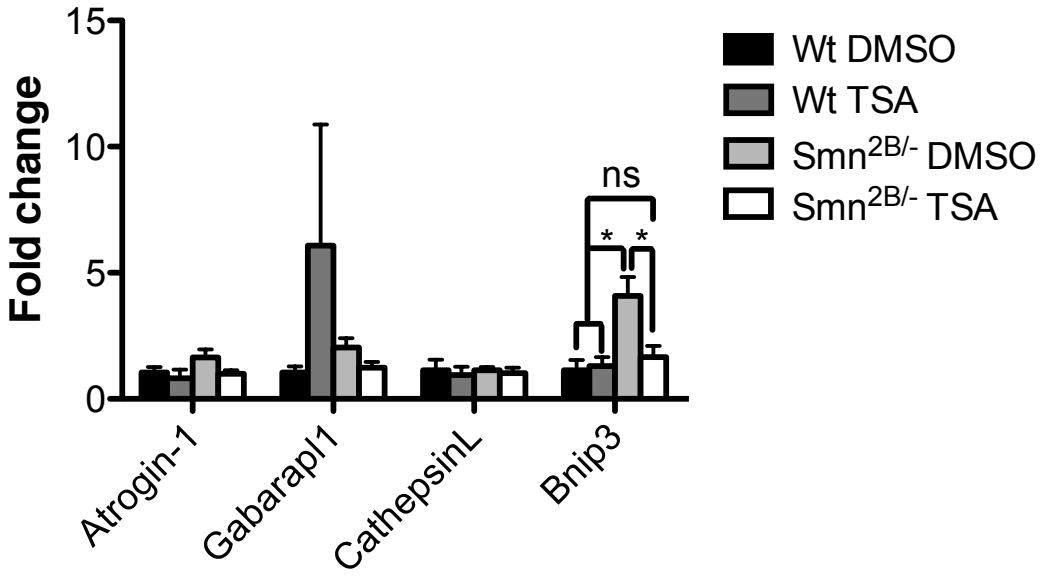

Figure 2.8 TSA administration to *Smn$^{2B/-}$* mice restores Bnip3 expression in hearts to normal levels. Atrogin-1, Gararapl1 and CathepsinL were unchanged as observed above. TSA treatment did not alter their expression. The increased expression of Bnip3 was effectively brought back to wild type control levels. (N=3 for all experiments; $p \leq 0.05$ for *)

Discussion

Atrophy is one of the pathological hallmarks of SMA. To date, a few studies have tried to elucidate the molecular mechanisms underlying the process of atrophy in SMA (174, 177). The focus of these studies has been mainly on MuRF1 and Atrogin-1 and their modulation by MyoG (174). MyoG-dependent induction of these two E3 ligases is unlikely to be solely responsible for all the atrophy processes occurring in SMA muscles. For example, myogenin or HDAC knockout mice provide only partial resistance to muscle atrophy and overexpression of MyoG is not sufficient to trigger atrophy (172). Additionally, the role of autophagolysosomal degradation in neurogenic atrophy is well established, but has not been studied in SMA (178, 180, 197).

Here, we have focused on the characterization of the FoxO pathway in muscles from SMA model mice. The FoxO transcription factors are critical players in muscle atrophy, being required for the induction of both proteasomal degradation and autophagosomal degradation in various catabolic states, including neurogenic atrophy (178-180, 197). Furthermore, in FoxO knockout mice, muscle tissue is partially spared following denervation-induced atrophy and completely spared following fasting-induced atrophy (178). Interestingly, both FoxO factors and many of their proteasomal-related and autophagosomal-related gene targets were induced post-symptomatically in skeletal muscles of $Smn^{2B/-}$ mice. In addition, the detection of autophagic and lysosomal vacuoles strongly supports the involvement of autophagy mediated by FoxO transcription factors in skeletal muscles of $Smn^{2B/-}$ mice. This does not preclude the role that MyoG may be playing in expression of the proteasomal E3 ligases MuRF1 and Atrogin-1 in $Smn^{2B/-}$ mice. With

respect to this, we have previously shown MyoG to be elevated in *Smn*$^{2B/-}$ mice at symptomatic age (168).

Identification of other catabolic mechanisms such as autophagy might offer an explanation for the inefficiency of MuRF1 and Atrogin-1 knockout *SmnΔ7* mouse models to gain weight or correct the muscle fiber size defect (177). Whether autophagy is present in the *SmnΔ7* model mice remains to be demonstrated. Nevertheless, the importance of other catabolic mechanisms in maintaining atrophy is very likely. In fact, muscle ubiquitin ligase of the SCF complex in atrophy-1 (MUSA1) and specific of muscle atrophy and regulated by transcription (SMART) are two new E3 ligases recently discovered that are under the control of FoxO family of transcription factors (178). These new E3 ligases contribute to fasting and neurogenic atrophy (178). Targeting a transcription factor, such as FoxO, that controls expression of multiple proteins involved in protein breakdown may yield a better outcome in preventing atrophy than targeting downstream effectors, such as Atrogin-1 and MuRF1. Furthermore, the traditional individual Atrogin-1 and MuRF1 knockout mice have incomplete sparing upon denervation and was subtle in the first 7 days after denervation (181). The short lifespan of the SMA models, including the *SmnΔ7* model (lifespan of ~14 days; loss of motor neurons at ~P9(155)), might not allow us to see the expected muscle sparing upon Atrogin-1 knockout. Indeed, this is what was observed by Iyer et al. (2014) (177). It should also be stressed that weight and fiber size as outcome measures in SMA might not be adequate or sufficient as it can't delineate between delayed myogenesis and atrophy that simultaneously occur in SMA muscles (48, 168, 174). Impaired myogenesis is likely a key player in reduced fiber size and mouse weight.

Consequently, it could mask or negate improvements that would be seen when modulating atrophy in SMA muscles.

The modulation of the IGF1 pathway as a means for possible therapy has also yielded modest results in the SMA field (105, 198, 199). The first attempts aimed at inhibiting modulators of the IGF1 pathway, myostatin and its antagonist follistatin, with the hope that it would correct muscle fiber mass in SMA. The use of multiple strategies to inhibit myostatin resulted in transient increase in muscle mass, modest increase in lifespan, and unclear results in motor function tests (198, 199). In addition, targeting directly IGF1 by muscle-specific overexpression mimicked closely the results of earlier studies on myostatin and follistatin, albeit with slightly better outcomes on increased fiber size (105).

Since SMA phenotype has a wide clinical heterogeneity, we took advantage of two mouse models to understand whether pathophysiologic mechanisms would be different. In fact, two variables may affect pathophysiology - the absolute level of SMN protein (severity-dependent) and the lifespan of the organism (time-dependent). While severe SMA mice (*Smn$^{-/-}$;SMN2)* do not have a long lifespan, the lower expressed SMN protein level may bring on different defects than milder SMA mice (*Smn$^{2B/-}$* mice). Contrastingly, mild SMA mouse models (such as the *Smn$^{2B/-}$* mice) have a longer lifespan that may allow sufficient time for some pathogenic features to arise. For example, we have previously obtained different molecular patterns of impaired myogenesis in the *Smn$^{-/-}$;SMN2* and *Smn$^{2B/-}$* mice that appeared to be time-dependent (168). Microarray data from a cohort of type 1 and type 3 patients also demonstrated differences in the molecular profile of

atrophy/hypertrophy (163). Here, we provide evidence that the severity of disease in the two mouse models presents with different molecular patterns of atrophy induction. Strikingly, we observed that only the symptomatic *Smn$^{2B/-}$* skeletal muscles induce expression of the autophagosomal markers while the symptomatic *Smn$^{-/-}$;SMN2* muscles do not. Consistent with this observation, FoxO transcription factor expression was induced in *Smn$^{2B/-}$* skeletal muscles but not in *Smn$^{-/-}$;SMN2* muscles. Given the lifespan difference between the *Smn$^{-/-}$;SMN2* and the *Smn$^{2B/-}$* mice, it is possible that *Smn$^{-/-}$;SMN2* mice don't live long enough for FoxO pathways to be induced. Indeed, the slight rise in FoxO3 transcripts in the *Smn$^{-/-}$;SMN2* muscles lead us to think that *Smn$^{-/-}$;SMN2* mice would potentially follow a similar protein degradation process if they could live longer. Interestingly, we also observe very different profiles in the atrophic markers of the heart tissues in the *Smn$^{-/-}$;SMN2* and *Smn$^{2B/-}$* mice. However, this time the difference is in the opposite direction and appears to be dependent on severity and not time. While we see alterations in the expression of Atrogin-1, autophagosomal genes and some FoxO genes in the hearts of *Smn$^{-/-}$;SMN2* mice, the *Smn$^{2B/-}$* hearts only display significant elevation of Bnip3. Interestingly, this altered expression in autophagosomal genes in *Smn$^{-/-}$;SMN2* hearts was not observed in *Smn$^{-/-}$;SMN2* skeletal muscles. In the same way, *Smn$^{2B/-}$* skeletal muscles displayed autophagic pathway induction while the *Smn$^{2B/-}$* heart muscles mostly did not. Therefore, cardiac muscle and skeletal muscle show rather divergent but intriguing pathologies in the context of SMA. Altogether, these results stress two important points: extrapolation of pathophysiology claims should be done cautiously between SMA animal models of differing severity, and as patients live longer because of new pharmacologic treatment strategies, new pathophysiologic problems may arise.

Utilization of the HDAC inhibitor TSA has shown beneficial effects in SMA preclinical studies (121, 168, 175, 176, 200). However, it is unclear whether TSA benefit is through transcriptional induction of the *SMN2* transgene or through the epigenetic regulation of other genes (175, 176, 201). Bricceno & *al.* (2012) showed that TSA could effectively reduce expression of E3 ligases MuRF1 and Atrogin-1 through HDAC4 inhibition in the *SmnΔ7* model mice (174). To elucidate TSA mechanisms on atrophy in our study, we used the $Smn^{2B/-}$ mouse, which doesn't harbour the *SMN2* transgene. In this mouse model, it was previously shown that SMN protein levels remained unchanged upon TSA treatment (176). Here, TSA reduced FoxOs transcripts with a consequent reduction in the expression of all downstream FoxO effectors. Therefore, we conclude that TSA benefit in $Smn^{2B/-}$ mice appears to be mediated by changes in the expression of genes other than SMN to alleviate atrophy in the mice. It is also possible that TSA has an effect on other cell types, such as neurons, which may negate atrophy at the earliest stages. However, the effect of TSA on motor neuron survival was negligible in two different mouse models of SMA (175, 176). In a recent study, TSA improved innervation status of denervated muscles, however, many endplates remained partially denervated or fully denervated (200). We also can't rule out the possibility that TSA could have a positive impact on FoxO repression. In fact, increased acetylation of FoxO3 results in cytosolic localization and inactivity, and this can be reversed by HDAC1 (191, 192, 202). Other studies have also shown that TSA treatment resulted in cytosolic FoxO1 and FoxO3 localization leading to reduce expression of FoxO-induced gene targets including Atrogin-1, MuRF1, and Lc3B (202).

The heart has received particular attention as a number of case studies reported cardiac defects in SMA patients (114, 115, 203). Preclinical studies have investigated SMA cardiac function and anatomy (120-123). Three main recurrent findings from these studies are small but proportionate heart size, bradycardia and abnormal heart remodelling (120-123). In our study, we identify induction of E3 ligase Atrogin-1 and multiple genes involved in autophagy in hearts from the severe *Smn*$^{-/-}$*;SMN2* mice but not in hearts from the less severe *Smn*$^{2B/-}$ mice. Interestingly, our data could bridge gaps in what has been previously identified in SMA hearts. Firstly, it is possible that the proteasomal and the autophagosomal systems both contribute to reduced fiber size of individual cardiomyocytes (122) and consequently to the smaller SMA hearts. Secondly, reminiscent to our study, the presentation of the thinner interventricular septum in the severe and *SmnΔ7* model is severity-dependent (123). In support of this, most case reports of cardiac defects in humans are in type I SMA patients and rarely in type II and III(114, 115, 203). Lastly, mice with constitutively active cardiac FoxO3 expression exhibit smaller hearts, reduced cardiomyocyte size, and reduced stroke volume and cardiac output (196). This resembles findings in SMA hearts (120, 122). Further research is warranted to delineate whether the increased expression of FoxO transcriptional factors and autophagic genes is pathological or protective in the context of SMA.

In summary, we demonstrate that different mouse models of SMA display different molecular signatures of atrophy induction in both skeletal and heart muscles. Further, we show that TSA likely alleviates atrophy in an SMN-independent manner by targeting

changes in expression of genes involved in the FoxO pathway. Finally, we show that hearts from severe SMA mice are potentially in a catabolic state, which may contribute to their abnormal functioning. Gaining a better comprehension of non-neuronal contributions, differences in commonly used mouse models, and the mode of action of HDAC inhibitors will help in advancing our understanding of SMA pathogenesis and the development of novel therapeutic strategies.

Materials and Methods

Mouse Models

The *Smn*$^{-/-}$*;SMN2* (Jackson Laboratory) and *Smn*$^{2B/-}$ mouse lines were housed at the University of Ottawa Animal Facility and cared for according to the Canadian Council on Animal Care. *Smn*$^{+/-}$ mice were crossed to *Smn*$^{2B/2B}$ mice to obtain *Smn*$^{2B/+}$ and *Smn*$^{2B/-}$ animals (156). Tissues were harvested from pre-symptomatic and symptomatic *Smn*$^{-/-}$*;SMN2* mice at P2 and P5, respectively. Pre-symptomatic tissues were collected at P9 while symptomatic tissues were dissected at P21 for the *Smn*$^{2B/-}$ mouse model.

TSA administration

TSA (10mg/kg) was administered daily as previously described (176). The treatment period was modified to P3-P21 to ensure maximal benefit (204). Mice were sacrificed and dissected after the last TSA/DMSO injection at P21.

Immunoblotting

Total protein lysate from SMA model mice and control animals was collected by either crushing liquid nitrogen frozen tissue with a pre-cooled mortar/pestle, and mixing muscle powder with RIPA lysis buffer (Cell Signaling) or homogenization in RIPA lysis buffer (Cell Signaling). Protein concentrations were determined using the Bradford method (Bio-Rad). Protein extracts were subjected to sodium dodecyl sulfate polyacrylamide gel electrophoresis and examined by immunoblot, as previously described (205). Primary

antibodies used were as follows: glyceraldehyde-3-phosphate dehydrogenase (Gapdh, Abcam: ab9485 - 1:2500 and ab8245 - 1:10000 or 1:12000), LC3B (Abcam: ab48394 - 1:1000), Ubiquitin (BioLegend (646301): Clone P4D1 - 1:1500), P62/Sqstm1 (Abcam: ab56416 - 1:1000), Bnip3 (Abcam: ab10433 - 1:1000), Gabarapl1 (ab86487 - 1:500). Secondary antibodies used were horseradish peroxidase (HRP)-conjugated anti-mouse immunoglobulin G (IgG, Bio-Rad) and HRP-conjugated anti-rabbit IgG (Bio-Rad) or IRDye 680 or 800 (Li-Cor). Signals were detected using enhanced chemiluminescence (Thermo) for standard western blotting, while fluorescence western blotting was performed with Odyssey CLx (Li-Cor). Densitometric analysis was performed using either ImageJ software or Image Studio 4.0 software. Results were normalized to Gapdh levels. LC3 protein levels were analysed as suggested by the guidelines to monitor autophagy (186).

RNA isolation and reverse transcription-quantitative polymerase chain reaction (RT-QPCR)

Total RNA was extracted from mouse models of SMA and wild type controls using RNeasy kit (Qiagen) according to the manufacturer's protocol. RNA concentrations were determined using a nanophotometer spectrophotometer (MBI Lab Equipment). RNA was reversed transcribed using the quantitect reverse-transcription kit (Qiagen) according to the manufacturer's protocol. QPCR was performed in triplicate for each sample using primers targeting Atrogin-1, MuRF1, FoxO1, FoxO3, FoxO4, Gabarapl1, CathepsinL, Bnip3 and Gapdh. A complete list of primers is available in the supplementary material (See Table 2.1). Each QPCR reaction contained 50 ng of cDNA, 2x SyBR Green JumpStart Taq ReadyMix for QPCR (Sigma Aldrich) or Evagreen SyBR (Biorad), RNase/DNase-free

water and appropriate primers (100-200 nM) in a final volume of 25 µl. Two negative controls were included in every QPCR plate and consisted of water in lieu of cDNA. QPCR results were quantified using $2^{-\Delta\Delta Ct}$ method. Results were normalized to Gapdh as an internal control.

Table 2.1: List of primers used in this study and their respective annealing temperatures.

Gene target	Forward primer	Reverse primer	Ta
Atrogin-1	CGTCTCACTTTCCCCTCAAG	GACTCCCAGCCATCCAATTAG	57
MuRF1	AGTGTCCATGTCTGGAGGTCGTTT	ACTGGAGCACTCCTGCTTGTAGAT	60
GabarapL1	CATCGTGGAGAAGGCTCCTA	ATACAGCTGGCCCATGGTAG	62
Bnip3	TTCCACTAGCACCTTCTGATGA	GAACACCGCATTTACAGAACAA	60
CathepsinL	GTGGACTGTTCTCACGCTCAAG	TCCGTCCTTCGCTTCATAGG	60
FoxO1	CAAAGTACACATACGGCCAATCC	CGTAACTTGATTTGCTGTCCTGAA	60
FoxO3	CCTCATCTCAAAGCTGGGTAC	GGTTTTCTCTGTAGGTCTTCCG	63
FoxO4	AAATGCCAGCCTCGGCCAGC	GGCATTCCTCCCAGTAACAG	60
GapDH	TCGGTGTGAACGGATTTG	GGTCTCGCTCCTGGAAGA	62

Transmission Electron Microscopy

P21 $Smn^{2B/+}$ and $Smn^{2B/-}$ mice were anaesthetized and perfused transcardially with 5 ml of phosphate-buffered saline (PBS) followed by 10 ml of Karnovsky's fixative (4% paraformaldehyde, 2% glutaraldehyde and 0.1 M sodium cacodylate in PBS, pH 7.4). TA muscles were collected and fixed overnight at 4ºC in Karnovsky's fixative. After fixation, each TA muscle was cut under a stereomicroscope into straight segments of 1 mm length. All segments were subsequently washed twice in 0.1 M sodium cacodylate buffer for 1 hour and once for overnight at room temperature. TA segments were post-fixed with 1% osmium tetroxide in 0.1 M sodium cacodylate buffer for 1 hour at room temperature. Segments were then washed in distilled water three times for 5 min. Specimens were dehydrated twice for 20 min for each step in a graded series of ethanol from water through 30%-50%-70%-85%-95% ethanol and twice for 30 minutes in 100% ethanol, followed by twice for 15 min in 50% ethanol/50% acetone and twice for 15 min in 100% acetone. TA segments were infiltrated in 30% Spurr resin/acetone for 20 min and once for 15 hours (overnight), then in 50% Spurr resin/acetone for 6 hours and in fresh 100% Spurr resin for overnight. Spurr resin was changed twice a day for three days at room temperature. All infiltration steps were performed on a nutator. Segments were embedded in fresh liquid Spurr resin and oriented inside the mould and then polymerized overnight at 70ºC. Ultrathin sections (80 nm) were collected onto 200-mesh copper grids and stained with 2% aqueous uranyl acetate and with Reynold's lead citrate. A little more than 130 electron micrographs per genotype were examined at different magnifications using a transmission electron microscope (Hitachi 7100).

Statistical analyses

All graphs represent means ± standard error of the mean. A two-tailed two sample Student's *t* test of unequal variance was performed using Microsoft Excel to compare the means of control and SMA groups. One-way ANOVA analysis was used to distinguish difference between treated and non-treated groups. The post-test used for the ANOVA was Bonferroni. Significance was set at $p \leq 0.05$ for *, $p \leq 0.01$ for ** and $p \leq 0.001$ for ***.

Acknowledgements

We would like to thank Sabrina Gibeault for assistance with experiments and all members of the Kothary laboratory for helpful discussions. This work was supported by grants from Cure SMA/Families of SMA Canada, Muscular Dystrophy Association (USA) (grant number 294568), Canadian Institutes of Health Research (CIHR) (grant number MOP–130279), and the E-Rare-2 program from the CIHR (grant number ERL-138414). J.G.B. was supported by a Frederick Banting and Charles Best CIHR Doctoral Research Award. M-O.D was supported by the Queen Elizabeth II Graduate Scholarship in Science and Technology and a Canadian Graduate Scholarship (Master's Program - CIHR). R.K. is a recipient of a University Health Research Chair from the University of Ottawa.

Additional Information

The authors declare no competing financial interest.

Chapter 3: Immune dysregulation may contribute to disease pathogenesis in spinal muscular atrophy mice

Immune dysregulation may contribute to disease pathogenesis in spinal muscular atrophy mice

Marc-Olivier Deguise[1,2,3], Yves De Repentigny[1,3,&], Emily McFall[1,3,&], Nicole Auclair[1,6], Subash Sad[4], and Rashmi Kothary[1,2,3,5,#]

[&] These authors contributed equally to the work.

[1]Regenerative Medicine Program, Ottawa Hospital Research Institute, Ottawa, Ontario, Canada K1H 8L6

[2]Department of Cellular and Molecular Medicine, University of Ottawa, Ottawa, Ontario, Canada K1H 8M5

[3]Centre for Neuromuscular Disease, University of Ottawa, Ottawa, Ontario, Canada K1H 8M5

[4]Department of Biochemistry, Microbiology, and Immunology, University of Ottawa, Ottawa, Ontario, Canada K1H 8M5

[5]Department of Medicine, University of Ottawa, Ottawa, Ontario, Canada K1H 8M5

[6]Faculty of Science, University of Ottawa, Ottawa, Ontario, Canada, K1N 9B4

#Correspondence to: Rashmi Kothary; Ottawa Hospital Research Institute; 501 Smyth Road, Ottawa, Ontario, Canada K1H 8L6; Tel: (613) 737-8707; Fax: (613) 737-8803; Email: rkothary@ohri.ca

*Published in Human Molecular Genetics 2017 Feb 15;26(**4**):801-819. Doi: 10.1093/hmg/ddw434*

Author Contributions

MOD designed the study, performed experiments, prepared Figures 3.1-3.4 & 3.8-3.27, all tables except 3.3 (done by Sabrina Gibeault), and wrote the manuscript. YDR provided supported for experiment and directly contributed to Figure 3.5-3.7 & 3.12. E.M provided support with experiments. NA performed experiments for figure 3.12. SS provided intellectual guidance for the project. RK designed the study and wrote the manuscript. All authors reviewed the manuscript.

Abstract

Spinal muscular atrophy (SMA) has long been solely considered a neurodegenerative disorder. However, recent work has highlighted defects in many other cell types that could contribute to disease aetiology. Interestingly, the immune system has never been extensively studied in SMA. Defects in lymphoid organs could exacerbate disease progression by neuroinflammation or immunodeficiency. Smn depletion led to severe alterations in the thymus and spleen of two different mouse models of SMA. The spleen from Smn depleted mice was dramatically smaller at a very young age and its histological architecture was marked by mislocalization of immune cells in the $Smn^{2B/-}$ model mice. In comparison, the thymus was relatively spared in gross morphology but showed many histological alterations including cortex thinning in both mouse models at symptomatic ages. Thymocyte development was also impaired as evidenced by abnormal population frequencies in the $Smn^{2B/-}$ thymus. Cytokine profiling revealed major changes in different tissues of both mouse models. Consistent with our observations, we found that survival motor neuron (Smn) protein levels were relatively high in lymphoid organs compared to skeletal muscle and spinal cord during postnatal development in wild type mice. Genetic introduction of one copy of the human *SMN2* transgene was enough to rescue splenic and thymic defects in $Smn^{2B/-}$ mice. Thus, Smn is required for the normal development of lymphoid organs, and altered immune function may contribute to SMA disease pathogenesis.

Introduction

Spinal muscular atrophy (SMA) is an inherited fatal neurological disease characterized by alpha motor neuron loss and neurogenic atrophy. The disease-causing gene is Survival Motor Neuron 1 (*SMN1*), which codes for a ubiquitously expressed protein (1, 15, 17). After close to 20 years of innovative research, a cure or treatment is still is not available to patients. In fact, although motor neurons are primary targets in SMA, the specific aetiology of disease pathogenesis remains uncertain. It is still unknown why motor neurons are particularly susceptible to depletion of the ubiquitously expressed SMN protein in comparison to other organs or cell types. As a result, the SMA field continues to debate whether or not SMA should be considered a motor neuron disease or a multi-organ disease (109, 166, 206).

Consequently, pre-clinical therapeutic endeavours aim at increasing levels of SMN through various approaches - either solely in the nervous system or systemically. Importantly, systemic delivery of antisense oligonucleotides (ASOs) to increase SMN levels results in a better outcome than administration solely in the central nervous system (112). Moreover, delivery of ASOs only in the periphery was sufficient to increase lifespan and improved motor functions in a mouse model of SMA (207). Such evidence highlights the importance of other cell types in SMA pathogenesis. This is consistent with studies showing that other cell types are also affected in SMA, albeit to a lesser extent than the motor neurons. Examples include cell types that have a close relationship with motor neurons, such as skeletal muscles and astrocytes, to cell types that are completely unrelated, such as the gastrointestinal system, heart, pancreas and liver (108, 120-123, 138, 142, 162,

168, 169, 208-214). Astrocytes of *Smn*Δ*7* (*Smn*$^{-/-}$;*SMN2*$^{+/+}$;*Smn*$^{\Delta 7/\Delta 7}$) model mice and SMA human iPSC-derived astrocytes show many signs of activation, with the latter also showing impaired calcium handling (142). Moreover, restoration of SMN uniquely in these cells significantly increases lifespan, weight, and motor functions in two mouse models of SMA (138). Similarly, several studies have shown intrinsic defects in skeletal muscles. SMA model mice have a delay in muscle growth highlighted by dysregulation of important myogenic transcription factors (168, 169). Consequently, differentiation and fusion of myoblasts is impaired (168, 169, 208, 209). Likewise, the hearts of SMA model mice display changes in functions on multiple levels. They are bradycardic, smaller and have a decreased ejection fraction indicative of possible cardiac insufficiency (120-123). Recently, elevation of the E3 ligase atrogin-1 and autophagy markers have been reported in the hearts of severe *Smn*$^{-/-}$;*SMN2* (*Smn*$^{-/-}$;*SMN2*$^{+/+}$) mice at symptomatic age, revealing potential intrinsic molecular underpinnings of these defects (162). Clinically, some patients with more severe presentation of SMA also have co-existing heart conditions (115, 215). Metabolically, both patients and mouse models have abnormal lipid and glucose profiles compared to controls (50, 210, 211, 216). Therefore, collectively it seems likely that SMA is the cumulative result of defects in multiple cell types.

The immune system has not been studied in the context of SMA. Yet, it is possible that immune dysregulation could make SMA patients more prone to infection or exacerbate their current disease state. The immune system is divided into two major branches, the innate and adaptive responses, which are each controlled by different populations of immune cells (217, 218). The adaptive (or acquired) immune response is mediated mainly

by lymphocytes such as T-cells and B-cells (217, 218). These cells develop in primary lymphoid organs, such as the bone marrow and the thymus. Unlike the B-cells, which exclusively develop in the bone marrow, the thymus is essential in T-cell development and maturation (217, 218). Fully mature B-cells and T-cells will migrate in the periphery and most will reside in secondary lymphoid organs such as the lymph nodes and the spleen (217, 218). The spleen is involved in a wider array of processes including blood filtration, hematopoiesis, iron metabolism and fighting infection, especially of encapsulated bacteria (219, 220). In the context of SMA, there has been one brief report indicating smaller thymus and spleen in the *Smn*$^{-/-}$*;SMN2* severe mouse model, likely due to increased apoptosis (139).

Here, we have characterized the gross morphology and basic tissue architecture of the spleen and thymus in both *Smn*$^{-/-}$*;SMN2* and *Smn*$^{2B/-}$ model mice. As well, we have characterized the lymph nodes in *Smn*$^{2B/-}$ mice. We further examined lymphocyte development in the thymus. Finally, we performed cytokine profiling in these organs and in the serum to understand any functional impairment. Altogether, we report important changes in both the spleen and thymus of two SMA model mice, which appear to initiate in secondary lymphoid organs. Overall, our work demonstrates that immune dysregulation is likely contributing to the overall clinical picture of SMA.

Results

The spleen is decreased in size in two mouse models of SMA

Based on initial observations during dissection, a thorough temporal examination of the abnormal gross morphology of the spleen in *Smn*$^{2B/-}$ and *Smn*$^{-/-}$*;SMN2* mice was performed. Different strategies of normalization (spleen length/mouse weight, spleen length/tibia length, spleen length/mouse length, spleen length/brain weight) all yielded similar results (Fig. 3.1A-D). Moreover, spleens from both male and female *Smn*$^{2B/-}$ mice showed similar results (Fig. 3.1). Therefore, data was normalized to mouse length and weight, and included both genders. The spleen gross morphology in *Smn*$^{2B/-}$ mice was compared to control littermates at various ages to better appreciate the progression of events. At postnatal day 0 (P0), changes to the size of spleens of *Smn*$^{2B/-}$ mice were not observed (Fig. 3.2A-C). Significant reductions were observed in both spleen weight/body weight and spleen length/total body length ratios at P19 (Fig. 3.2M-O), P14 (Fig. 3.2J-L), P9 (Fig. 3.2G-I), and P4 (Fig. 3.2D-F) in the *Smn*$^{2B/-}$ mice, albeit of diminishing severity at younger ages. Overall, the progression of changes in spleen size followed an inverse function with time (Fig. 3.2P). *Smn*$^{2B/-}$ spleens often appeared necrotic, likely due to splenic infarct. Quantification showed that spleens from P19 *Smn*$^{2B/-}$ mice are 2.26 times more likely to have an infarction compared to wild type but not *Smn*$^{2B/+}$ mice (Fig. 3.3). The infarct size was not graded, but there did not appear to be any appreciable difference based on qualitative assessment. To better understand the underlying pathology of living immune cells, necrotic spleens were not included in subsequent analysis.

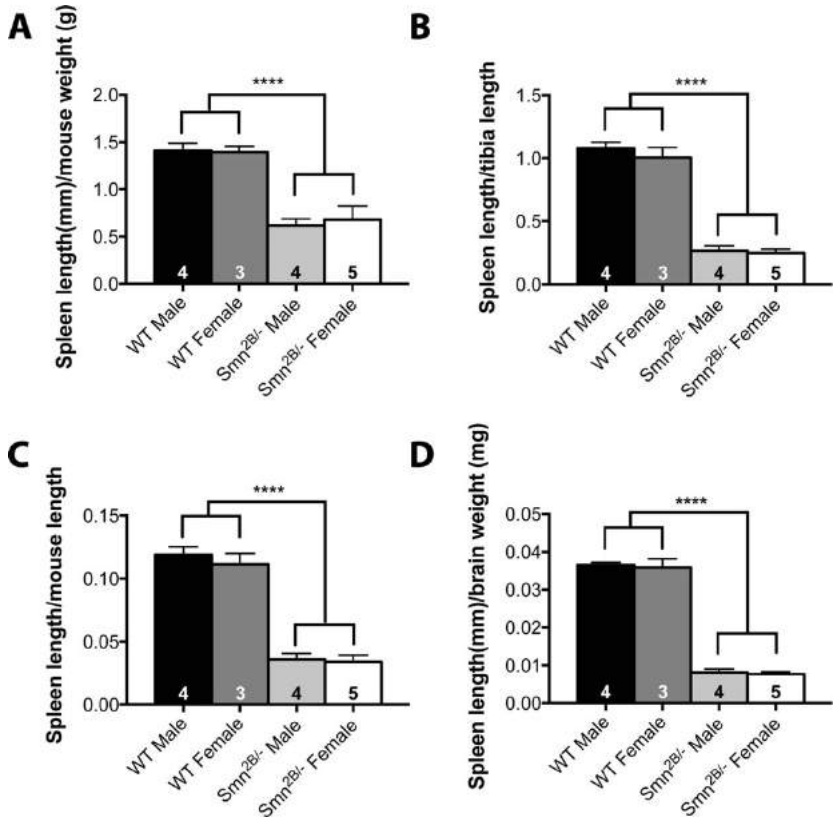

Figure 3.1. Different methods to normalize gross morphological defects in spleens yield similar results in both male and female mice. Normalization of spleen length/mouse weight (A), spleen length/tibia length (B), spleen length/mouse length (C), and spleen length/brain weight (D) all showed significantly reduced ratios in *Smn*$^{2B/-}$ male and female mice compared to wild type. (The n value for each experiment is as written in the graph bars, one-way ANOVA with bonferroni post-test, $P \leq 0.0001$ for ****).

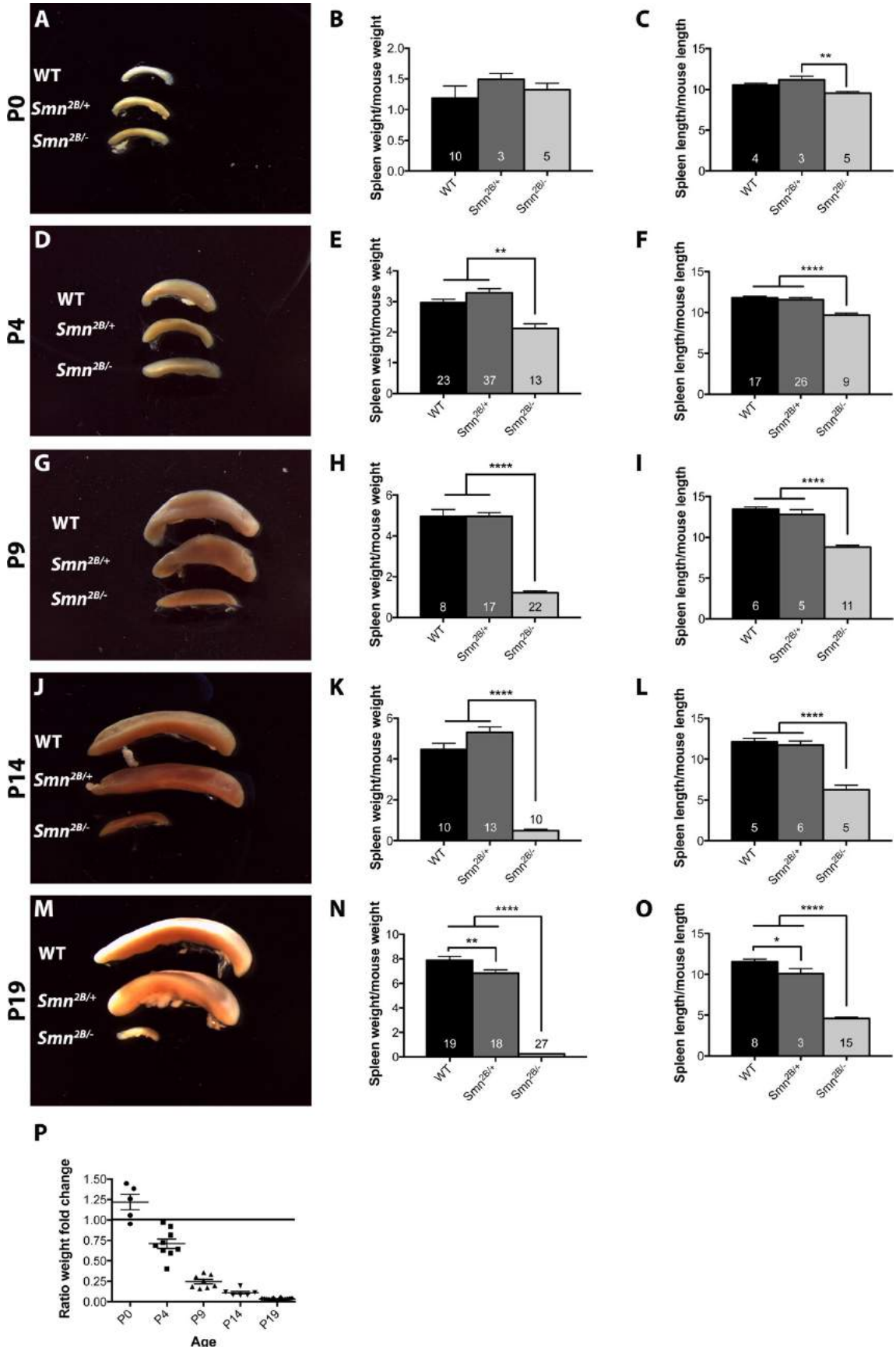
A
P0
WT
Smn2B/+
Smn2B/-
B
Spleen weight/mouse weight
10
3
5
C
Spleen length/mouse length
**
4
3
5
D
P4
E
**
23
37
13
F
****
17
26
9
G
P9
H
****
8
17
22
I
****
6
5
11
J
P14
K
****
10
13
10
L
****
5
6
5
M
P19
N
****
**
19
18
27
O
****
*
8
3
15
P
Ratio weight fold change
P0
P4
P9
P14
P19
Age

Figure 3.2. *Smn*$^{2B/-}$ mice have significantly smaller spleens beginning at a young age. Representative images and quantification of the weight and length ratios of the spleens from wild type, *Smn*$^{2B/+}$, and *Smn*$^{2B/-}$ mice at P0 (A-C), P4 (D-F), P9 (G-I), P14 (J-L), P19 (M-O). (P) Spleen size is inversely correlated with age. (The n value for each experiment is as written in the graph bars, one-way ANOVA with bonferroni post-test. $P \leq 0.05$ for *, $P \leq 0.01$ for **, $P \leq 0.001$ for *** and $P \leq 0.0001$ for ****).

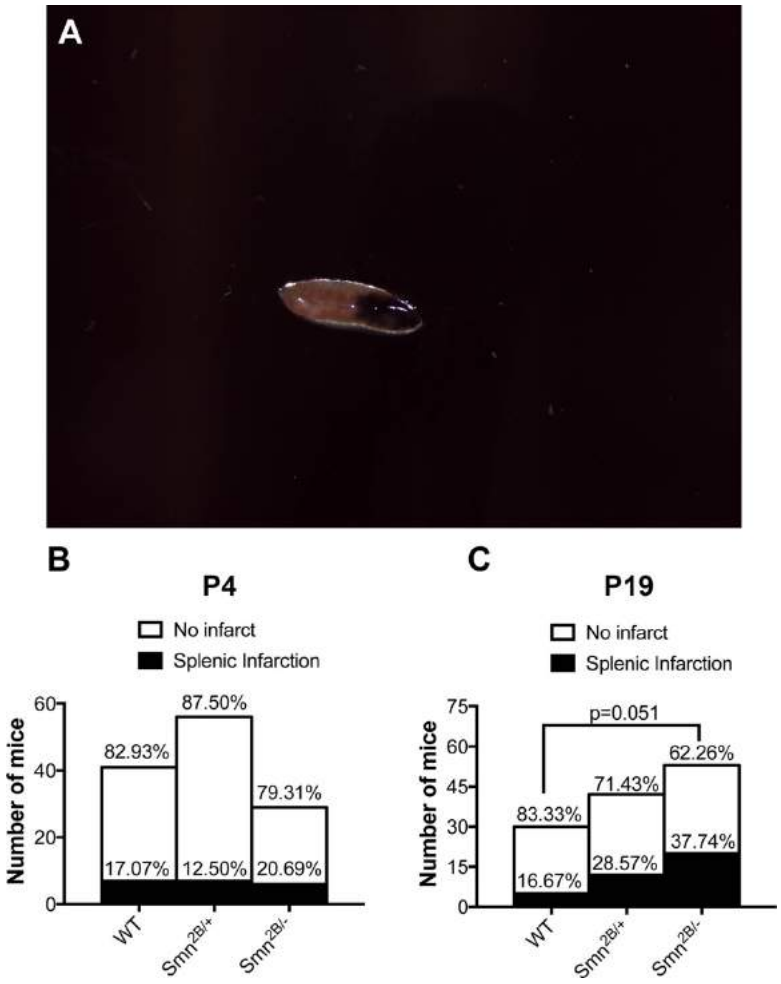

Figure 3.3. *Smn*$^{2B/-}$ spleens have a higher incidence of splenic infarct at P19. (A) Representative image of an infarct in P19 *Smn*$^{2B/-}$ spleen. (B) Quantification of the relative risk of splenic infarction. This was relatively similar in all genotypes at P4. (C) Quantification of relative risk of splenic infarction showed that P19 *Smn*$^{2B/-}$ spleens are approximately twice more likely to infarct than wild type spleens (relative risk = 2.26, 95% confidence interval 1.018 to 5.453, p = 0.0505) but not *Smn*$^{2B/+}$ mice (relative risk = 1.32, 95% confidence interval 0.7467 to 2.406, p = 0.388). (n=41, 56, 29 for WT, *Smn*$^{2B/+}$, *Smn*$^{2B/-}$ respectively at P4 and n=30, 42, 53 for WT, *Smn*$^{2B/+}$, *Smn*$^{2B/-}$ respectively at P19, Fischer's exact test and confidence interval calculated by Koopman asymptotic score).

Examination of spleens from the severe *Smn*$^{-/-}$*;SMN2* mice at P5 revealed a clear difference in both weight and length of the spleen compared to wild type and heterozygous mice (Fig. 3.4G-I), similar to previous reports (139). In addition, significant changes in both weight and length of the spleen were observed at P2 (Fig. 3.4D-F). Changes in spleen size were not observed at birth (P0) (Fig. 3.4A-C). Overall, the changes in size of *Smn*$^{-/-}$*;SMN2* spleens become progressively worse over time (Fig. 3.4J). Altogether, the spleens of SMA model mice are significantly smaller than those from control mice, and this defect is present before any overt motor neuron pathology(153, 157).

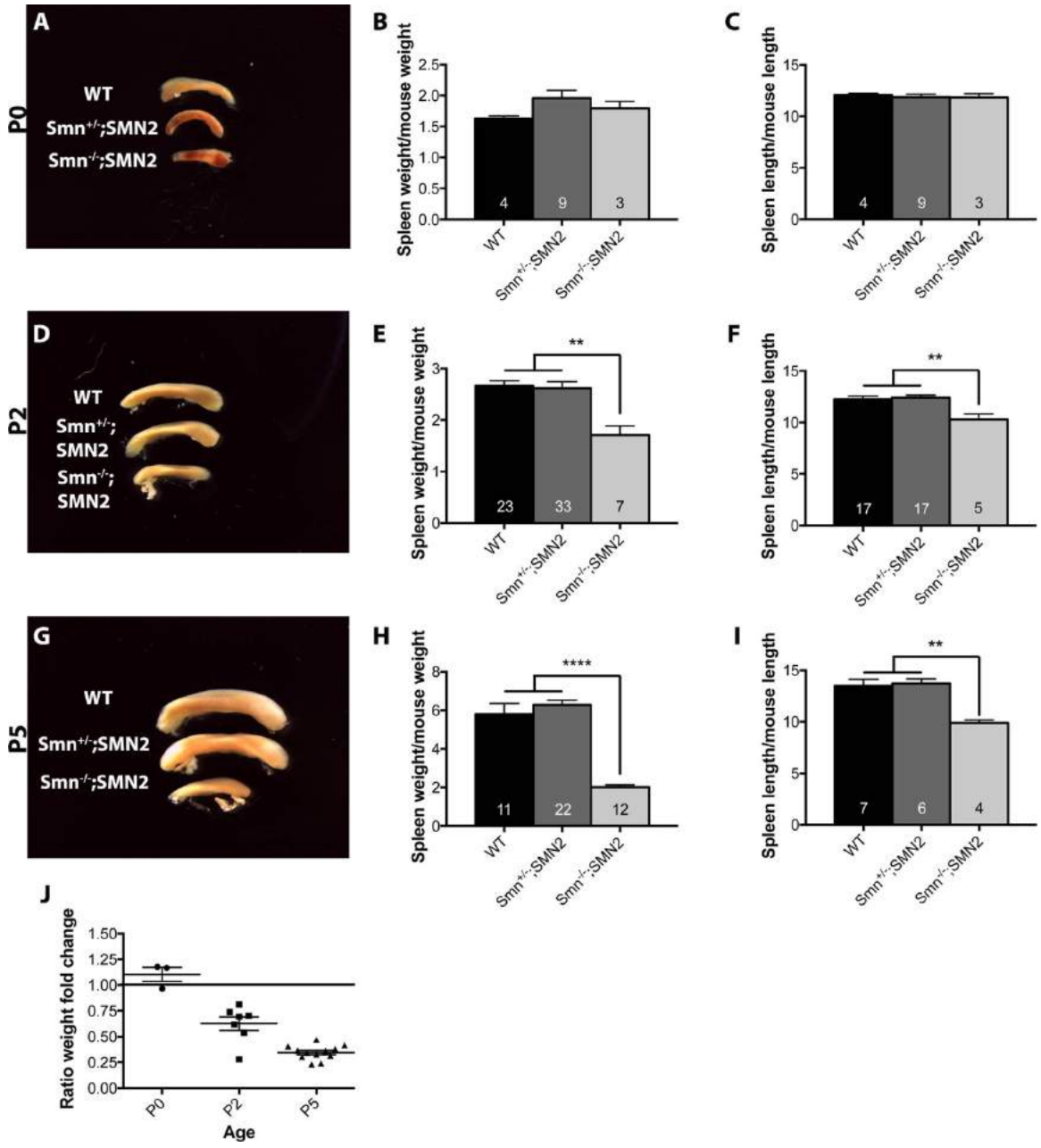

Figure 3.4. *Smn*$^{-/-}$*;SMN2* mice also have smaller spleens from a young age. Representative images and quantification of the weight and length ratios of the spleens from wild type, *Smn*$^{+/-}$*;SMN2*, and *Smn*$^{-/-}$*;SMN2* mice at P0 (A-C), P2 (D-F), P5 (G-I). (J) Spleen size is inversely correlated with age. (The n value for each experiment are as written in the graph bars, one-way ANOVA with bonferroni post-test, $P \leq 0.05$ for *, $P \leq 0.01$ for **, and $P \leq 0.0001$ for ****).

Architectural disorganization in the spleen is more prominent in the less severe $Smn^{2B/-}$ mice than in the severe $Smn^{-/-}$;SMN2 mice

The spleen histology is highly sophisticated with different regions harbouring different functions. The red pulp is a region where incoming blood from arteries is filtered(219). The white pulp contains mostly lymphoid cells such as B-cells and T-cells, which are segregated into two compartments of their own (219). The T-cells are present around the arteriole (often denoted as the periarteriolar lymphoid sheath - PALS) while the B-cells are distributed in follicles within the PALS (219). The red pulp and white pulp are separated by a marginal zone composed mainly of macrophages and marginal zone B-cells (219). Macrophages can also be found diffusely in the red pulp where they play an important role in iron metabolism (219). Hematoxylin and eosin (H&E) staining was performed on spleen sections at P0, P4, P9, P14 and P19 for the *$Smn^{2B/-}$* mice and at P2 and P5 for the *$Smn^{-/-}$;SMN2* mice (Fig. 3.5). The architecture of the spleen from *$Smn^{2B/-}$* mice was clearly disrupted with effacement of the clear margin of the white pulp at P19 in comparison to wild type mice (Fig. 3.5I,J). Additionally, all *$Smn^{2B/-}$* spleens analyzed appeared hyperchromatic with accumulation of fibrotic-like tissue and smooth muscle cells (Fig. 3.5J). This is possibly due to necrosis or apoptosis, which could explain their small size. Indeed, spleen stained for smooth muscle actin revealed altered localization with increased clumping of smooth muscles cells in contrast to wild type spleens at P19 (Fig. 3.6). When analysing earlier time points, namely P14, P9 and P4 (Fig. 3.5C-H), a similar characteristic loss of white pulp borders was observed. We primarily observed red pulp and no white pulp at P0 for both wild type and *$Smn^{2B/-}$* mice (Fig. 3.5A,B), consistent with

previous studies (221). Remarkably, the *Smn*$^{-/-}$*;SMN2* model mice did not have a disruption of the red and white pulp architecture at P2 or at P5 (Fig. 3.5M,N).

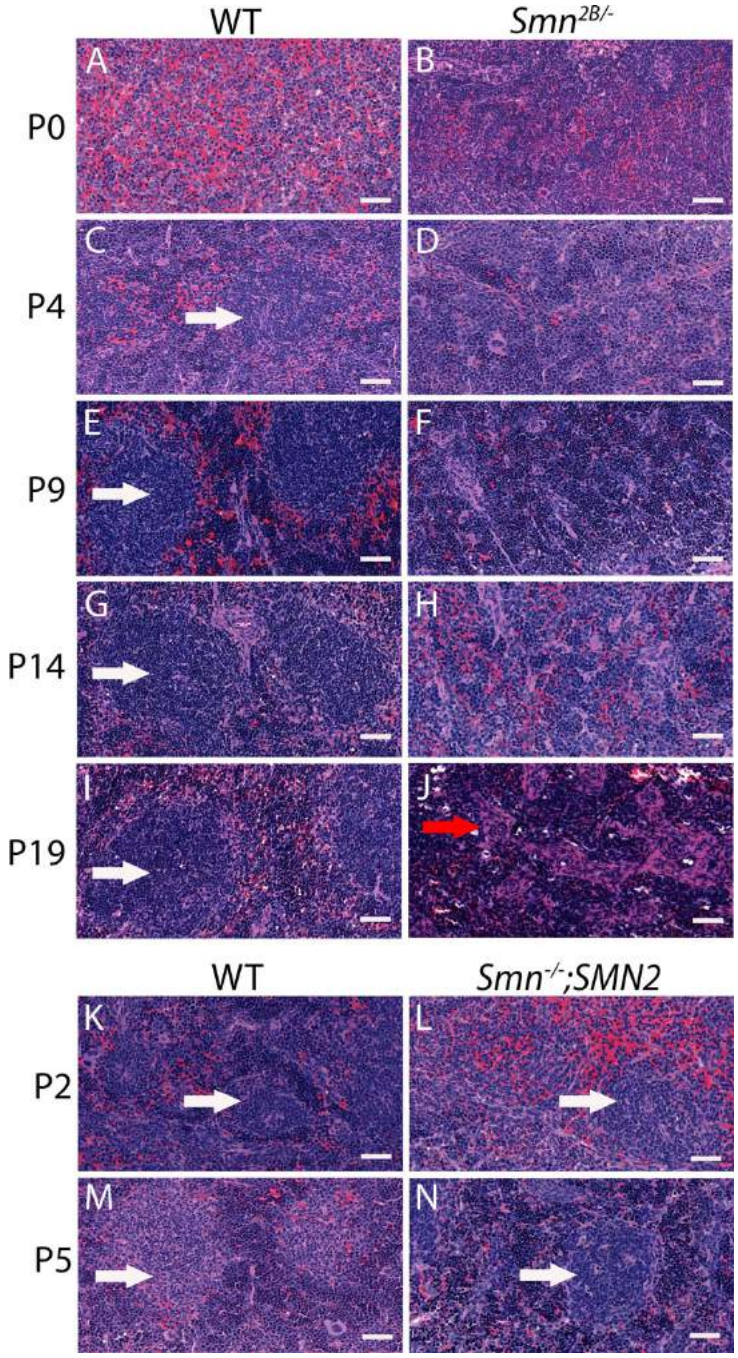

Figure 3.5. Abnormal spleen architecture in *Smn$^{2B/-}$* mice but not in *Smn$^{-/-}$;SMN2* mice. Representative 40X images of sections of spleen after H&E staining of wild type and *Smn$^{2B/-}$* mice at P0 (A,B), P4 (C,D), P9 (E,F), P14 (G,H), and P19 (I,J). Disruption of white pulp formation is apparent already at P4 in the spleens of *Smn$^{2B/-}$* mice. Accumulation of smooth muscle cells is apparent at P19 (J). Representative images of sections of spleen after H&E staining of wild type and *Smn$^{-/-}$;SMN2* mice at P2 (K,L) and P5 (M,N). White pulp was readily identifiable (white arrows). The red arrow identifies area of smooth muscle cell accumulation. Scale bar represent 50 µm. (n=3 for all samples except for P0 *Smn$^{2B/-}$* mice, where n=2 and P2, P5 *Smn$^{-/-}$;SMN2* mice, where n=4).

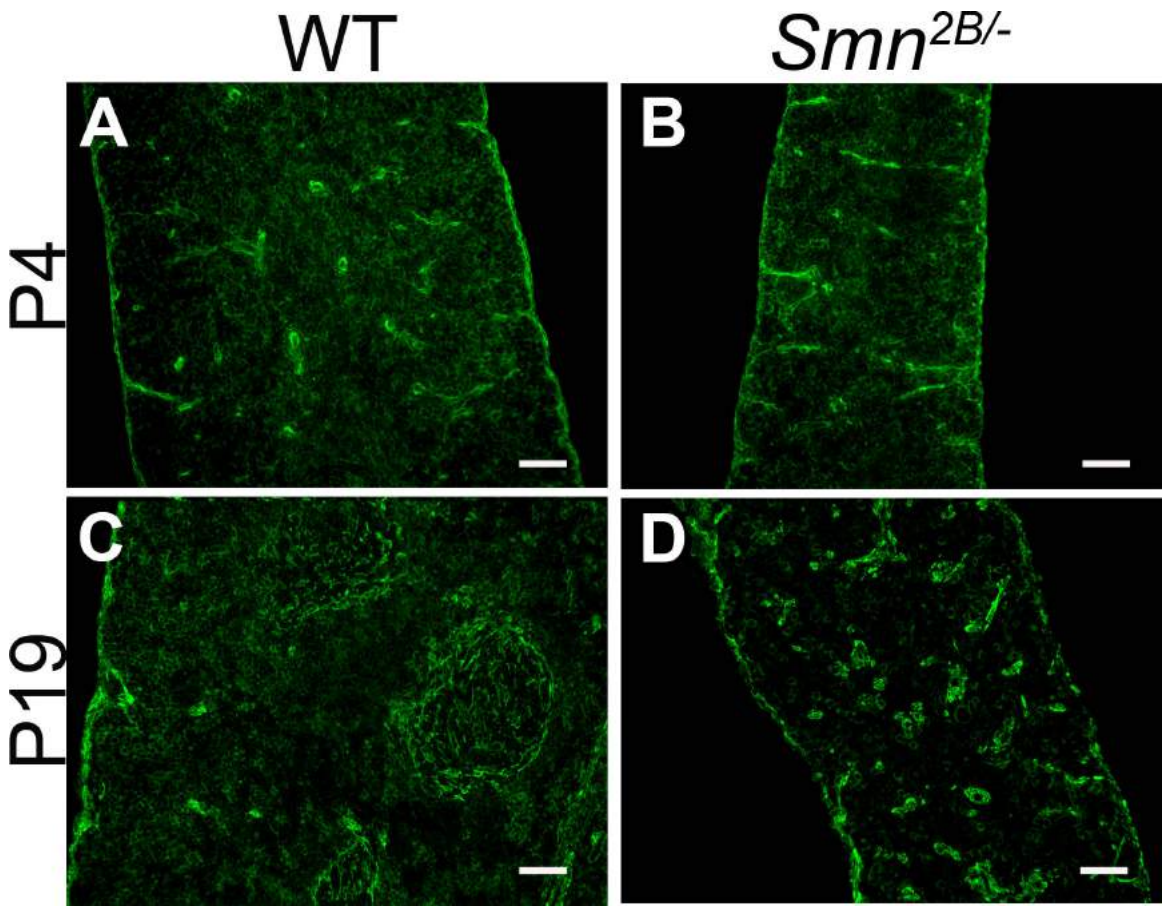

Figure 3.6. Smooth muscle cell accumulation in *Smn*$^{2B/-}$ spleens at P19 but not at P4. (A, B) Representative 20X images of smooth muscle actin immunostaining to label for smooth muscle cells at P4 reveal very similar staining patterns. (C-D) Representative 20X images of smooth muscle actin immunostaining at P19 reveal abnormal clumping of smooth muscles cells in *Smn*$^{2B/-}$ spleens. Scale bar represent 20 μm. (n=4 for P19, n=2 for P4 for all experiments).

Immune cells in the spleen are mislocalized in the Smn$^{2B/-}$ mice but not in the severe Smn$^{-/-}$;SMN2 mice

To better characterize the changes in architecture in the spleens of *Smn$^{2B/-}$* and *Smn$^{-/-}$;SMN2* mice, immunohistochemistry was performed to label T-cells, B-cells, and macrophages (Fig. 3.7). The analysis of P4 *Smn$^{2B/-}$* spleens clarified that white pulp are potentially still forming at this age in the mutant mice as shown by staining of the T-cell marker CD3 around blood vessels (Fig. 3.7B,F). This reflects the positioning of the T-cells in the PALS. However, the B-cell marker CD19 and the macrophage marker F4/80 staining was diffuse in P4 *Smn$^{2B/-}$* spleen and did not surround the PALS as in wild type (Fig. 3.7C,G and D,H respectively). This could indicate possible infiltration of both B-cells and macrophages into what should be the white pulp. At P19, staining of CD3, CD19 and F4/80 revealed a severe mislocalization of T-cells, B-cells and macrophages in *Smn$^{2B/-}$* spleens compared to control (Fig. 3.7B'-H'). Unlike wild type, T-cell marker CD3 staining (Fig. 3.7B'-F') in *Smn$^{2B/-}$* spleens showed very diffuse distribution with no clear white pulp conformation and PALS region, confirming the results from the H&E staining (Fig. 3.7A',E'). Similarly, B-cell marker CD19 and macrophage marker F4/80 staining did not show the marginal zone pattern in *Smn$^{2B/-}$* spleen in comparison to wild type (Fig. 3.7C',G' and D',H', respectively). However, some unclear oval-shaped regions with decreased density of CD19 staining were present in *Smn$^{2B/-}$* mice (Fig. 3.7G'). These might be attributed to the accumulation of smooth muscle identified on H&E staining and immunostaining since similar low density areas were observed in CD3 stained spleens (Fig. 3.7F'). Strikingly, the immunostaining assessment in the spleens from *Smn$^{-/-}$;SMN2* mice revealed that the structures were largely unaffected, similar to the results obtained from the

H&E staining (Fig. 3.7I-P and I'-P'). The difference between the two SMA mouse models at symptomatic ages is quite interesting. Such differences between models have previously been reported in other contexts in SMA and it is possible that such changes require time and/or other factors to present themselves (162, 168). Altogether, these results suggest a defective segregation of the white and red pulp in *Smn*$^{2B/-}$ spleens. Remarkably, the localization of these various immune cells confirms that the white pulp may be absent in the spleens of *Smn*$^{2B/-}$ mice, which could impair fundamental splenic functions. However, the progression of events leading to what appears to be a loss of white pulp formation remains to be determined.

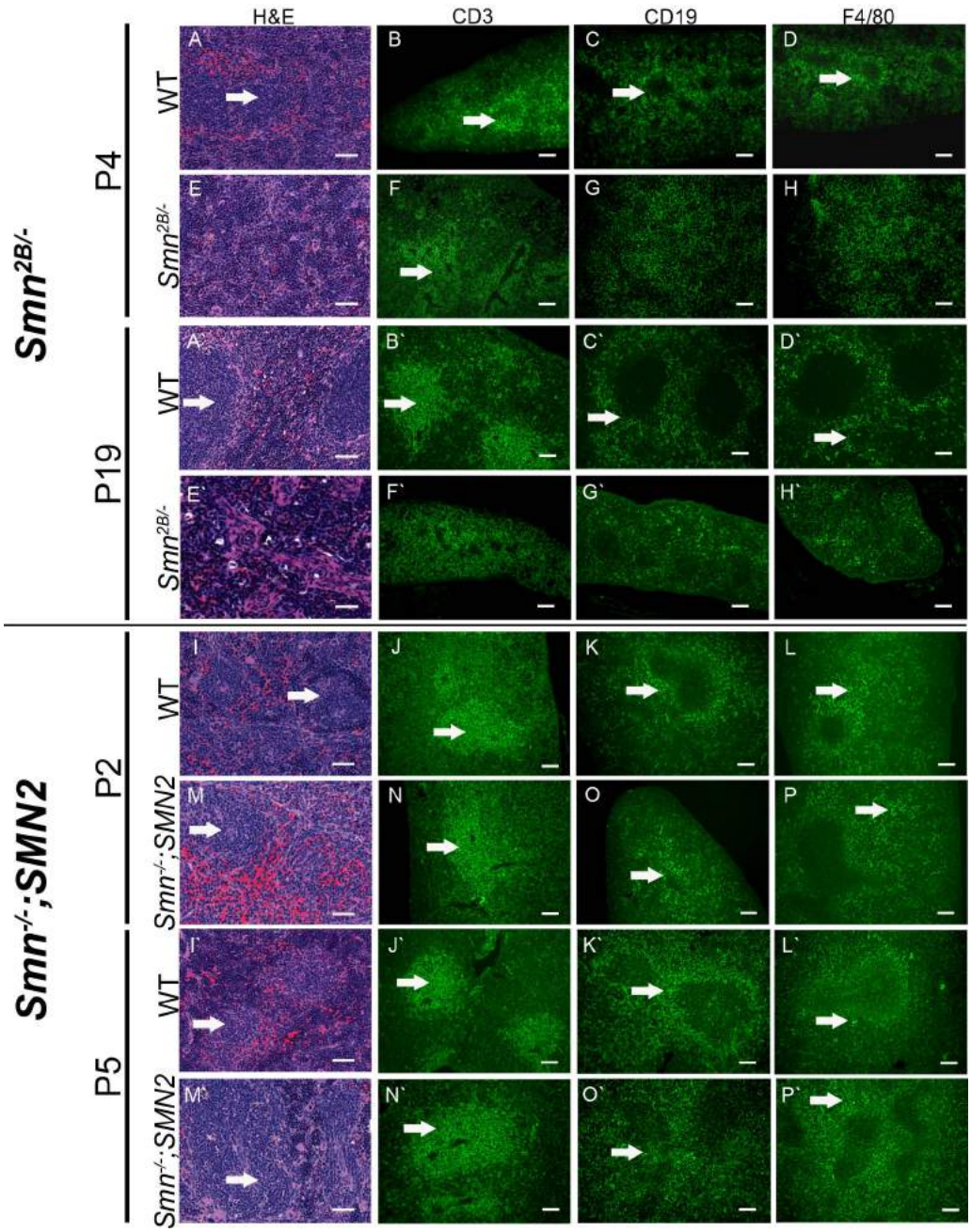

Figure 3.7. T-cells, B-cells and macrophages are mislocalized in the spleens of symptomatic *Smn$^{2B/-}$* mice but not of *Smn$^{-/-}$;SMN2* mice. Representative images of H&E, CD3, CD19, and F4/80 staining of wild type and *Smn$^{2B/-}$* spleen sections at P4 (A-H) and P19 (A'-H'). The T-cell marker CD3 staining was present in the PALS at P4 but was very diffuse at P19 in the *Smn$^{2B/-}$* samples. The staining patterns of the B-cell marker

CD19 and the macrophage marker F4/80 were diffuse at P4 and P19. Representative images of H&E, CD3, CD19, and F4/80 staining of wild type and *Smn*$^{-/-}$*;SMN2* spleen sections at P2 (I-P) and P5 (I'-P'). No mislocalization of immune cells at either time points was apparent in this mouse model. The white arrows identify areas where staining was expected. Scale bar represent 50 μm for H&E images and 20 μm for immunostaining images. (n=4 at P4, n=4 at P19, n=2 at P2, n=2 at P5).

The thymus is decreased in size in symptomatic Smn$^{2B/-}$ *mice but not in Smn*$^{-/-}$*;SMN2 mice*

Our comparison of the various organs had showed a trend towards a decrease in the ratio of the thymus weight over mouse weight in *Smn*$^{2B/-}$ mice at P19 (Fig. 3.8). An examination of the thymus at P4 and P19 showed that it was significantly smaller at P19 but not at P4 in *Smn*$^{2B/-}$ mice compared to *Smn*$^{2B/+}$ and wild type controls (Fig. 3.9A-D). We next compared these gross morphological changes in the spleen and thymus to other organs such as the liver and kidneys of some of the same animals. We did not observe similar decreases in relative size at P4 or P19 for liver and kidney (Fig. 3.8A,B), suggesting that the reduction in size is specific to lymphoid organs. Previous findings had indicated that *Smn*$^{-/-}$*;SMN2* mice had smaller thymus at P5 (139). Interestingly, we did not observe a decrease in thymus size in the *Smn*$^{-/-}$*;SMN2* mice at any stage (Fig. 3.9E-H), although there was a trend toward smaller thymus size at P5.

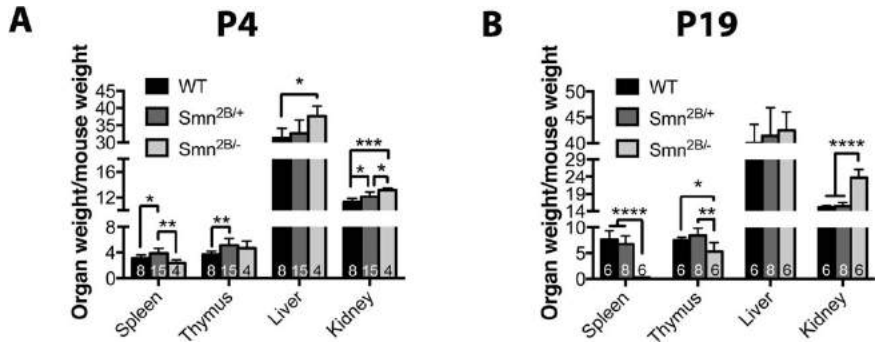

Figure 3.8. Organ size reduction is specific to lymphoid organs. (A) Organ weight ratio for spleen, thymus, liver and kidney showed that only *Smn*$^{2B/-}$ spleen is reduced at P4. *Smn*$^{2B/-}$ non-lymphoid organs (liver and kidney) showed trend toward increased weight ratio. (B) Organ weight ratio for spleen, thymus, liver and kidney showed that only *Smn*$^{2B/-}$ spleen and thymus are reduced at P19 but not the liver and kidney. (The n value for each experiment is as written in the graph bars, one-way ANOVA with bonferroni post-test, $P \leq 0.05$ for *, $P \leq 0.01$ for **, and $P \leq 0.001$ for *** $P \leq 0.0001$ for ****).

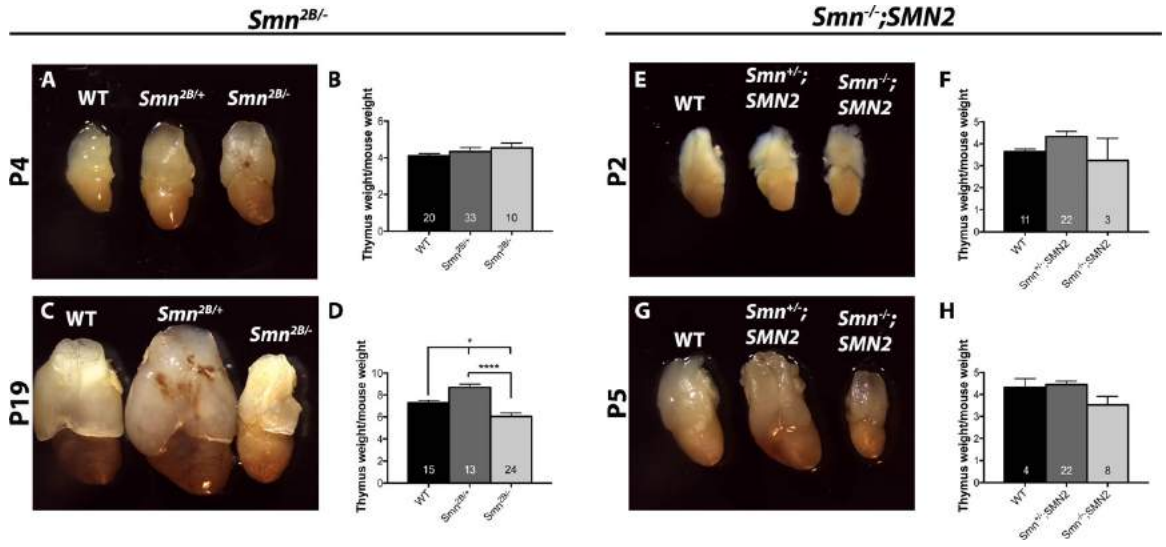

Figure 3.9. The thymus is smaller in symptomatic *Smn$^{2B/-}$* mice but not in *Smn$^{-/-}$;SMN2* mice. Representative images and quantification of the thymus weight to mouse weight ratios from *Smn$^{2B/-}$* mice at P4 (A,B) and P19 (C,D), and from *Smn$^{-/-}$;SMN2* mice at P2 (E,F) and P5 (G,H). (The n value for each experiment are as written in the graph bars, one-way ANOVA with bonferroni post-test, $P \leq 0.05$ for *, and $P \leq 0.0001$ for ****).

Architectural defects are also present in thymus of symptomatic $Smn^{2B/-}$ mice

The thymus is normally composed of the cortex (outer zone), where early development of T-cells occur (double negative - DN - $CD4^{-ve}$; $CD8^{-ve}$ and double positive - DP - $CD4^{+}$; $CD8^{+}$), and the medulla (inner zone), where final maturation of $CD4^{+}$ (CD4 single positive - SP) or $CD8^{+}$ (CD8 single positive - SP) cells occurs(222). At P19, striking abnormalities in sections of thymus from *$Smn^{2B/-}$* mice were apparent. There was clear reduction in cellularity and cortex thinning compared to wild type controls (Fig. 3.10G-L). An increase in the number of apoptotic bodies and tingible body macrophages was evident by the classical "starry-sky" appearance in the majority of the animals analysed (Fig. 3.10H,K)(223). The comparison of cross-sectional area of the lobe of the thymus confirmed the decreased size observed in morphological assessments (Fig. 3.10I). We next assessed whether such changes were also present in the thymus at P4, a time when we first observed spleen abnormalities. Interestingly, no significant changes were present at this age (Fig. 3.10A-F).

We next performed the same analysis on the thymus from the *$Smn^{-/-}$;SMN2* mice. The H&E staining of the *$Smn^{-/-}$;SMN2* thymus revealed a very similar pathology at late stage (P5) but not at early stage (P2), as we observed in the *$Smn^{2B/-}$* thymus (Fig. 3.11). However, these changes were of lesser severity, likely due to the shortened lifespan of the *$Smn^{-/-}$;SMN2* mice.

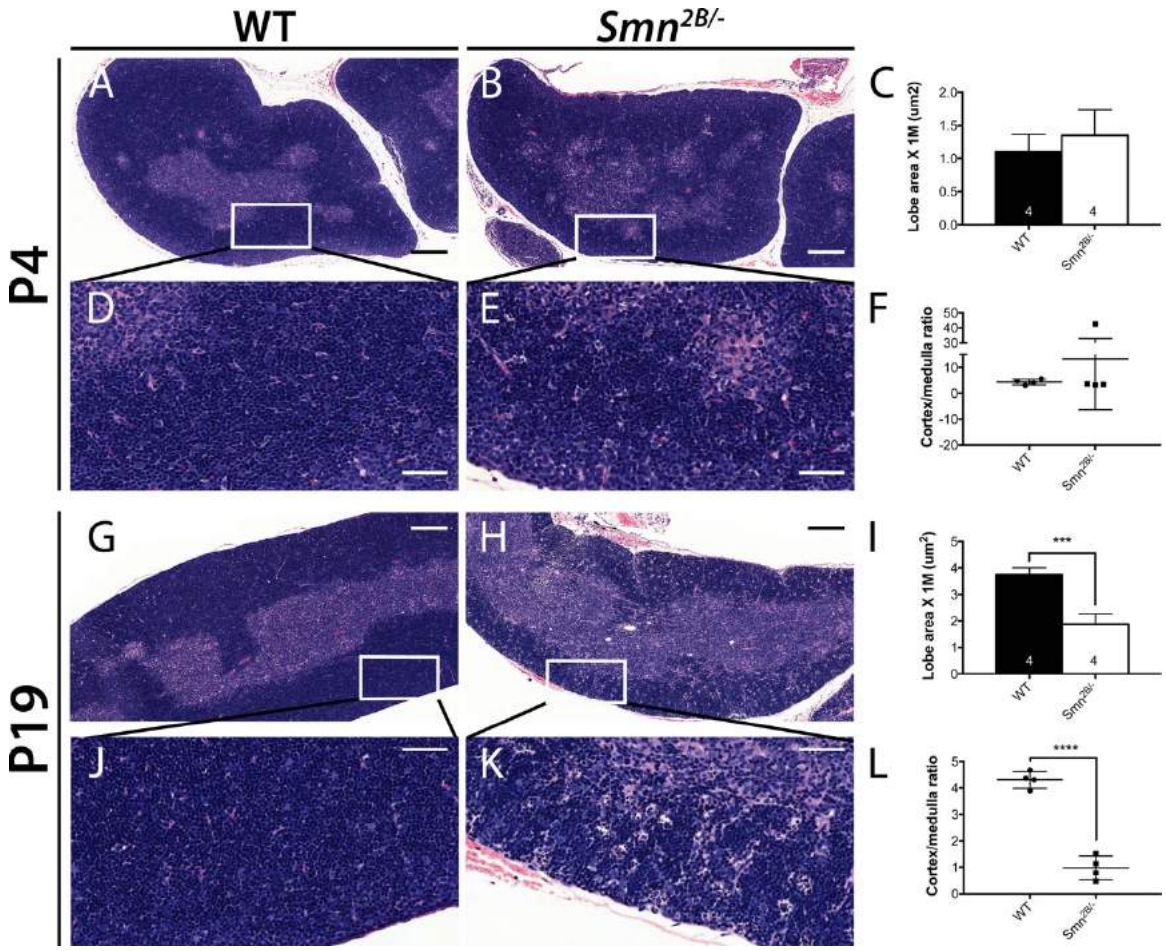

Figure 3.10. Abnormal thymic architecture in symptomatic *Smn$^{2B/-}$* mice. Representative 10X images of H&E stained sections of thymus showing the medulla and cortex in wild type and *Smn$^{2B/-}$* mice at P4 (A,B) and P19 (G,H). Representative 50X images of the cortex in the thymus of wild type and *Smn$^{2B/-}$* mice at P4 (D,E) and P19 (J,K). Quantification of the average thymic lobe area (C) and cortex/medullary area ratio (F) showed no difference between *Smn$^{2B/-}$* and wild type mice at P4. Quantification of the average thymic lobe area (I) and cortex/medullary area ratio (L) showed a decrease in *Smn$^{2B/-}$* thymus compared to wild type thymus at P19. Scale bar represent 200 μm in A,B,G,H and 50 μm in D,E,J,K. (n=4 for all experiments, two-tailed Student's *t* test, $P \leq 0.001$ for *** and $P \leq 0.0001$ for ****).

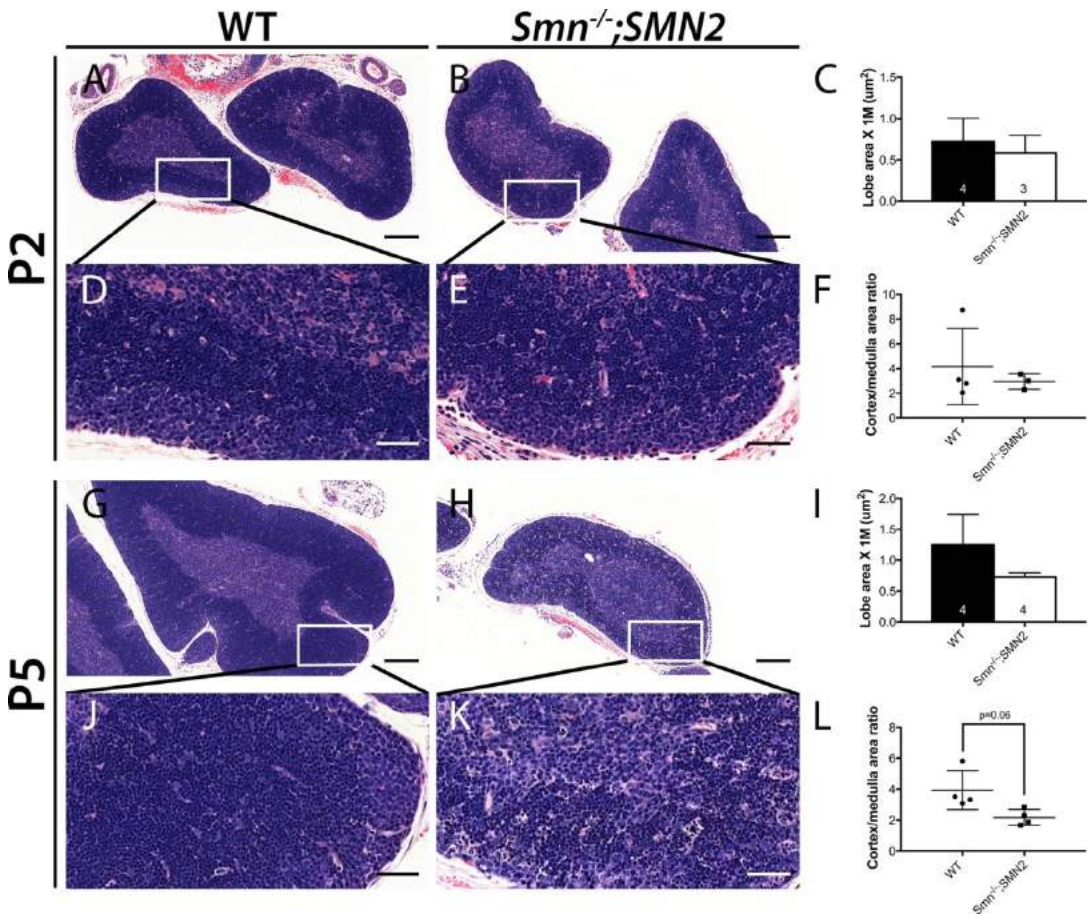

Figure 3.11. Abnormal thymic architecture in symptomatic *Smn$^{-/-}$;SMN2* mice. Representative 10X images of H&E stained sections of thymus showing the medulla and cortex in wild type and *Smn$^{-/-}$;SMN2* mice at P2 (A,B) and P5 (G,H). Representative 50X images of the cortex of the thymus of wild type and *Smn$^{-/-}$;SMN2* mice at P2 (D,E) and P5 (J,K). Quantification of the average thymic lobe area (C) and cortex/medullary area ratio (F) showed no difference between *Smn$^{-/-}$;SMN2* and wild type mice at P2. Quantification of the average thymic lobe area (I) and cortex/medullary area ratio (L) showed a trend towards a decrease in *Smn$^{-/-}$;SMN2* thymus compared to wild type at P5. Scale bar represent 200 µm in A,B,G,H and 50 µm in D,E,J,K. (n=4, for all experiments, except P2 *Smn$^{-/-}$;SMN2,* where n=3, two-tailed Student's *t* test).

To follow up on our observations on the apoptotic bodies in the thymus of *Smn*$^{2B/-}$ mice, a more thorough analysis was performed. Terminal deoxynucleotidyl transferase dUTP nick end labeling (TUNEL) and cleaved caspase 3 staining revealed increased positive punctae in P19 *Smn*$^{2B/-}$ thymus in comparison to wild type (Fig. 3.12A-F). Analysis of several pro (Bax, Caspase 2 (Casp2), Caspase 8 (Casp8), Fas receptor (FasR) and p53), anti-apoptotic (Bcl2), and autophagy markers (Bnip3, Gabarapl1 and CathepsinL) revealed a general trend in increase in transcripts levels in both pro-apoptotic and autophagy genes at P19 but did not reach significance, implying that cell death might have already occurred (Fig. 3.12H). At P4, a time where no pathology is observed in the *Smn*$^{2B/-}$ thymus, transcript expression levels were relatively unchanged with the exception of p53 (Fig. 3.12G). Interestingly, a similar profile was present in P5 *Smn*$^{-/-}$*;SMN2* thymus with the increase in the mRNA levels of several markers being statistically significant (Fig. 3.12J). Once again, at the earlier time point (P2), little change was observed in the *Smn*$^{-/-}$*;SMN2* thymus (Fig. 3.12J).

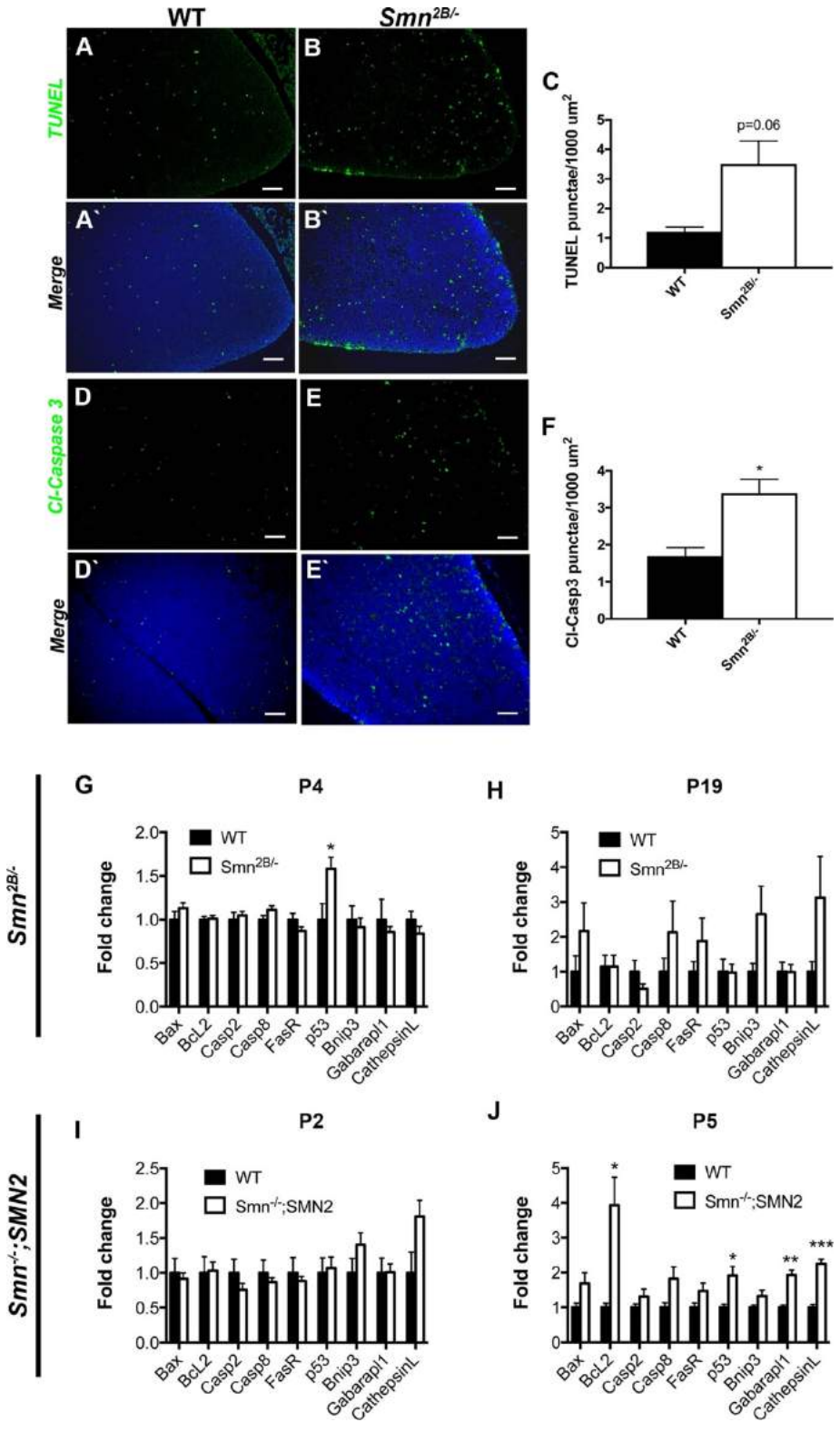

Figure 3.12. Increased cell death in P19 *Smn$^{2B/-}$* thymus. (A-C) TUNEL staining of P19 WT and *Smn$^{2B/-}$* thymus revealed increased TUNEL positive signals in *Smn$^{2B/-}$* thymus. (D-

F) Cleaved caspase 3 staining of P19 WT and *Smn*$^{2B/-}$ thymus revealed increased positive signals in *Smn*$^{2B/-}$ thymus. (G-H) Analysis of various pro, anti-apoptotic cell death and autophagy markers revealed a trend toward increased transcript levels in P19 *Smn*$^{2B/-}$ thymus but not in P4 *Smn*$^{2B/-}$ thymus. (I-J) Analysis of various pro, anti-apoptotic cell death and autophagy markers revealed a trend toward increased transcript levels in P5 *Smn*$^{-/-}$*;SMN2* thymus but not in P2 *Smn*$^{-/-}$*;SMN2* thymus. (n=4 for all experiments except for G where Bnip3, Gabarapl1 and CathepsinL n=3, two-tailed Student's *t* test, $P \leq 0.05$ for *, $P \leq 0.01$ for **, and $P \leq 0.001$ for ***).

T-cell development is misregulated only in symptomatic Smn$^{2B/-}$ *mice*

The spleen gross morphology changes in the SMA model mice may be a consequence of abnormal immune cell development given that both *Smn*$^{2B/-}$ and *Smn*$^{-/-}$*;SMN2* mouse models show thymic architectural abnormalities. Specifically, the progenitor cell may not get into the thymus as efficiently or get stalled in the thymus at any point in development, which would lead to fewer cells migrating to the spleen and therefore partly explaining its small size. We therefore decided to perform a systematic assessment of T-cell development in *Smn*$^{2B/-}$ mice. T-cell development is a complex multi-step process in which cells are passaged through different organs before becoming fully functional. First, hematopoietic cells migrate from the bone marrow to the thymus, where they commit to the T-cell lineage (DN1 - CD4^{-ve}; CD8^{-ve}, CD44^{+}, CD25^{-ve} and DN2 - CD4^{-ve}; CD8^{-ve}, CD44^{+}, CD25^{+}), gain and rearrange their T-cell antigen receptor (TCR) β before successfully pairing with pre-TCRα (DN3 - CD4^{-ve}; CD8^{-ve}, CD44^{-ve}, CD25^{+} and DN4 - CD4^{-ve}; CD8^{-ve}, CD44^{-ve}, CD25^{-ve}) (222, 224). They will then progress to CD4^{+}; CD8^{+} cells

(DP, bright - early stage, and dull - late stage) which are marked by reorganization of the α chain (222). The αβ TCR on the DP cells will be challenged for recognition to ensure that autoimmunity doesn't occur (a process known as central tolerance). T-cells that do not recognize self-antigen generally go through a mechanism known as "neglect" while T-cells that bind strongly to self-antigen will go through negative selection (apoptosis) or anergy where they become regulatory T-cells (222, 225). Therefore, only T-cells that have a receptor that have intermediate specificity to self-antigen will positively be selected (events described by co-expression of either CD5 and TCRβ or CD69 and TCRβ) and will be allowed to mature further (222). At this point, they will transiently go through $CD4^{+}$;$CD8^{lo}$ stage before becoming either CD8 SP or CD4 SP mature cells and migrate to the periphery and lymphoid organs, such as the spleen (222).

Flow cytometry analysis of the P19 *Smn*$^{2B/-}$ thymocytes reveals major abnormalities at multiple levels of development. There was a significantly larger proportion of DN, $CD4^{+}$;$CD8^{lo}$, mature CD8 SP, and CD4 SP cells, and a diminished proportion of DP cells in *Smn*$^{2B/-}$ mice compared to *Smn*$^{2B/+}$ mice (Fig. 3.13A-C). This means that more cells enter the thymus and more cells go through the maturation process or that T-cells get stalled in the DN stage and mature state of development. All the population subset frequencies in the *Smn*$^{2B/+}$ thymus were within normal ranges for normal rodents, except for the DN population, which was slightly lower (226). Examination of the various sub-stages in the DN population showed a significant increase in the proportion of DN3 with an approximately equal decrease in the DN4 sub-population (Fig. 3.13D-F). The positive selection process is characterized by pre-selection ($TCR\beta^{lo}$;$CD69^{-ve}$), TCR engagement

(TCRβ^{int};CD69^{+}), post-positive selection (TCRβ^{hi};CD69^{+}), mature positively selected SP (TCRβ^{hi};CD69^{-ve}) (222, 227). Interestingly, flow cytometric analysis of the positive selection process in P19 *Smn*$^{2B/-}$ thymocytes identified an increase in the proportion of cells going through TCR engagement, being positively selected and being more mature (Fig. 3.14A-C). The analysis of sub-populations of cells going through these events was mostly unremarkable, except for an increase in the proportion of DN cells appearing as mature TCRβ^{hi};CD69^{-ve} cells (Fig. 3.14D-O). Alternately, analysis of positive selection through CD5 and TCRβ surface marker expression yielded similar results (Fig. 3.15). These results point towards a precocious positive cell selection, potentially to increase mature naïve T-cell production.

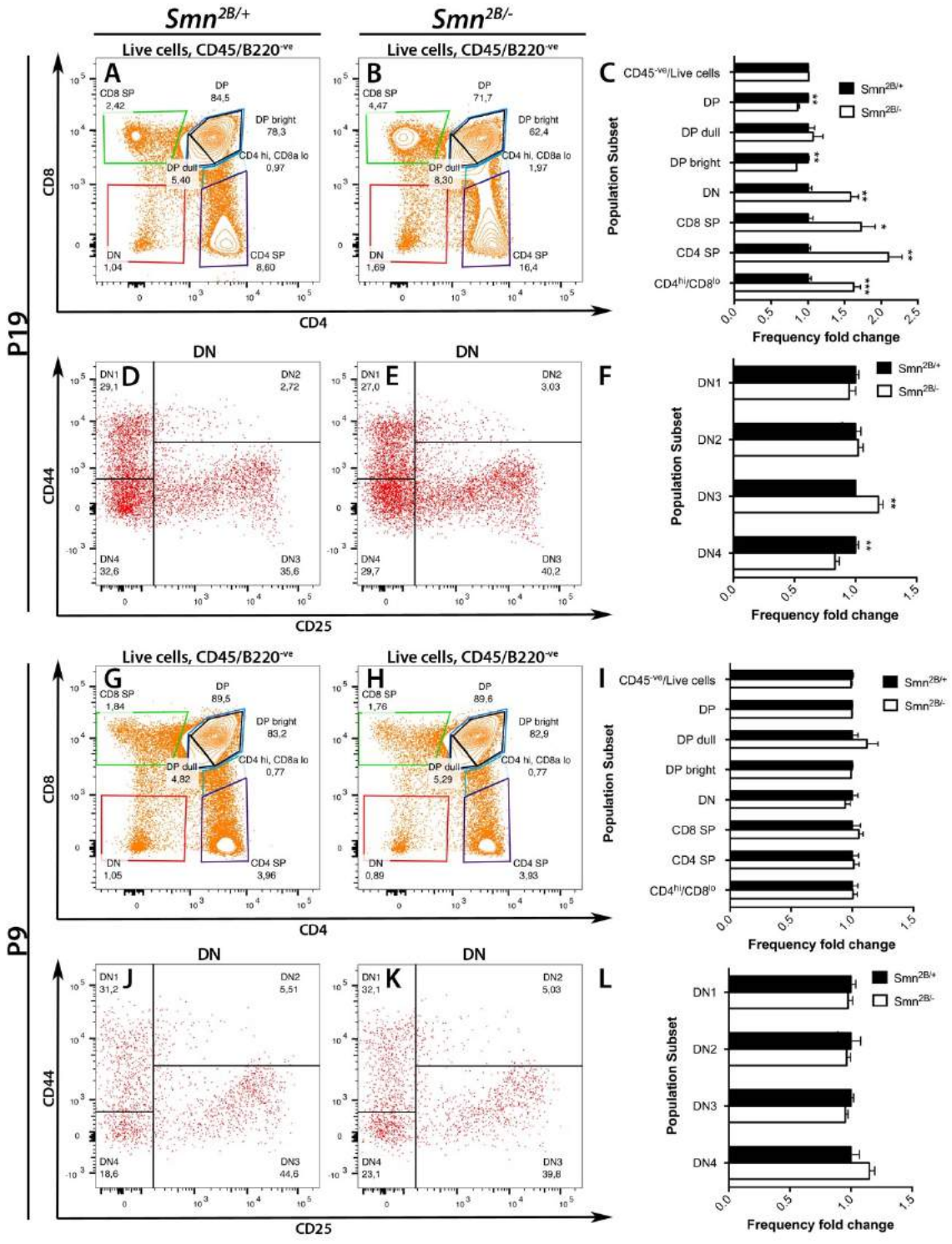

Figure 3.13. T-cell development is misregulated in P19 but not P9 thymus from *Smn*$^{2B/-}$ mice. Representative contour plots of thymocytes (gated on live cells, CD45/B220^{-ve}) in various stages of development based on CD4/CD8 immunophenotyping in *Smn*$^{2B/+}$

and $Smn^{2B/-}$ mice at P19 (A,B) and P9 (G,H). Quantification of population frequencies presented as a fold change revealed major abnormalities at P19 (C) but not at P9 (I). Representative contour plots of DN-gated thymocytes in the various DN sub-stages based on CD44/CD25 immunophenotyping in $Smn^{2B/+}$ and $Smn^{2B/-}$ mice at P19 (D,E) and P9 (J,K). Quantification of DN sub-population frequencies presented as a fold change showed significant difference in DN3 and DN4 populations at P19 (F) while no change was observed at P9 (L). (n=5 for P19, n=5 and 6 for $Smn^{2B/-}$ and $Smn^{2B/+}$ respectively, two-tailed Student's *t* test, $P \leq 0.05$ for *, $P \leq 0.01$ for **, and $P \leq 0.001$ for ***).

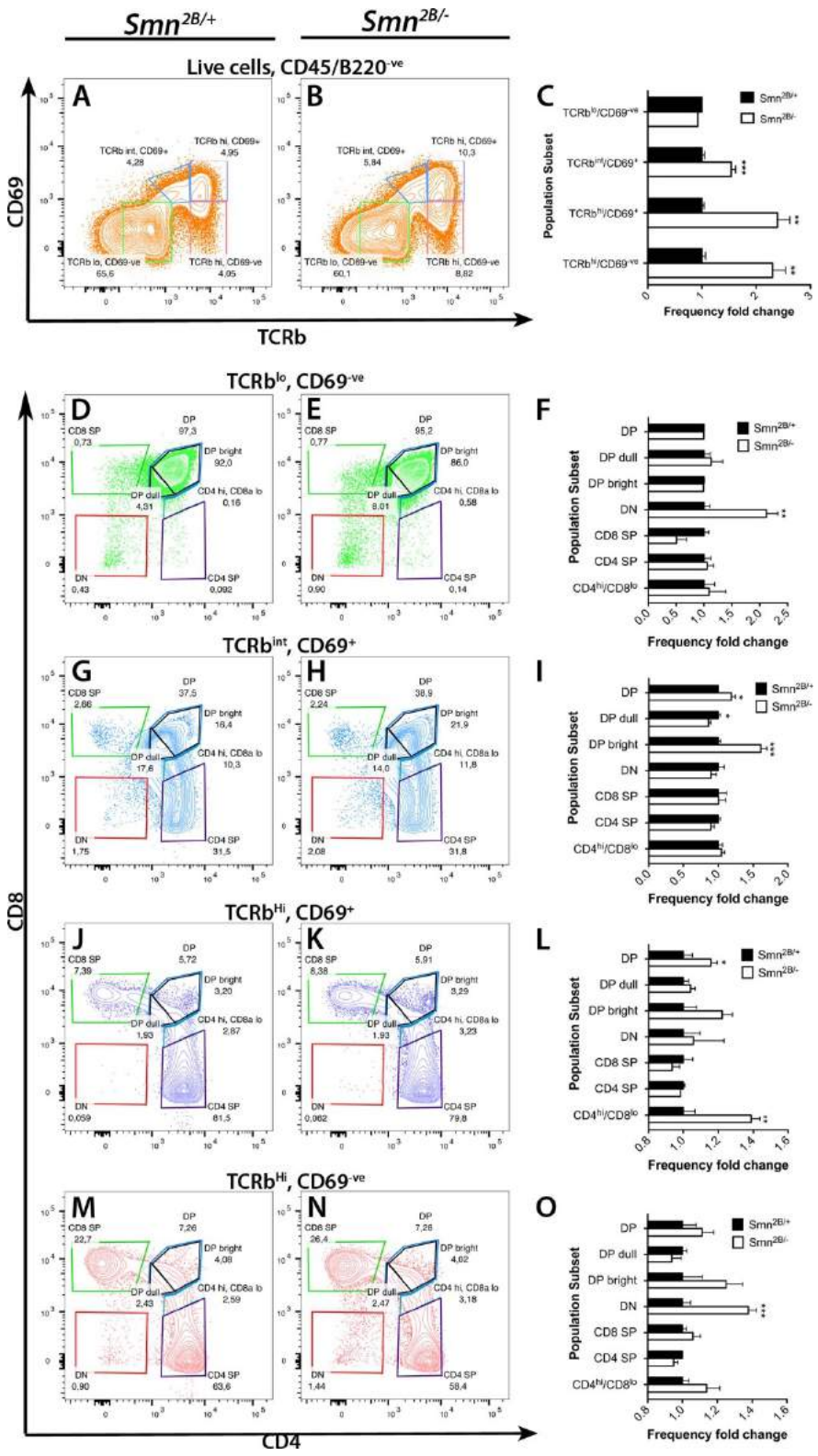

Figure 3.14. Precocious positive selection is present in the thymus of P19 *Smn$^{2B/-}$* mice.

Representative contour plots of thymocytes (gated on live cells, CD45/B220^{-ve}) in various

stages of positive selection based on CD69/TCRβ immunophenotyping in *Smn*$^{2B/+}$ and *Smn*$^{2B/-}$ mice at P19 (A,B). (C) Quantification of population frequency presented as a fold change demonstrates a significant increase in the proportion of cells going through TCR engagement (TCRβ^{int};CD69^{+}), post-positive selection (TCRβ^{hi};CD69^{+}), and mature positively selected SP (TCRβ^{hi};CD69^{-ve}). Representative contour plots and quantification of sub-populations present in each positive selection stages, namely TCRβ^{lo};CD69^{-ve} (D-F), TCRβ^{int};CD69^{+} (G-I), TCRβ^{hi};CD69^{+} (J-L), TCRβ^{hi};CD69^{-ve} (M-O), by immunophenotyping cells with CD4/CD8 shows an alteration in the proportion of the sub-populations. (n=5 for all experiments, two-tailed Student's *t* test, $P \leq 0.05$ for *, $P \leq 0.01$ for **, and $P \leq 0.001$ for ***).

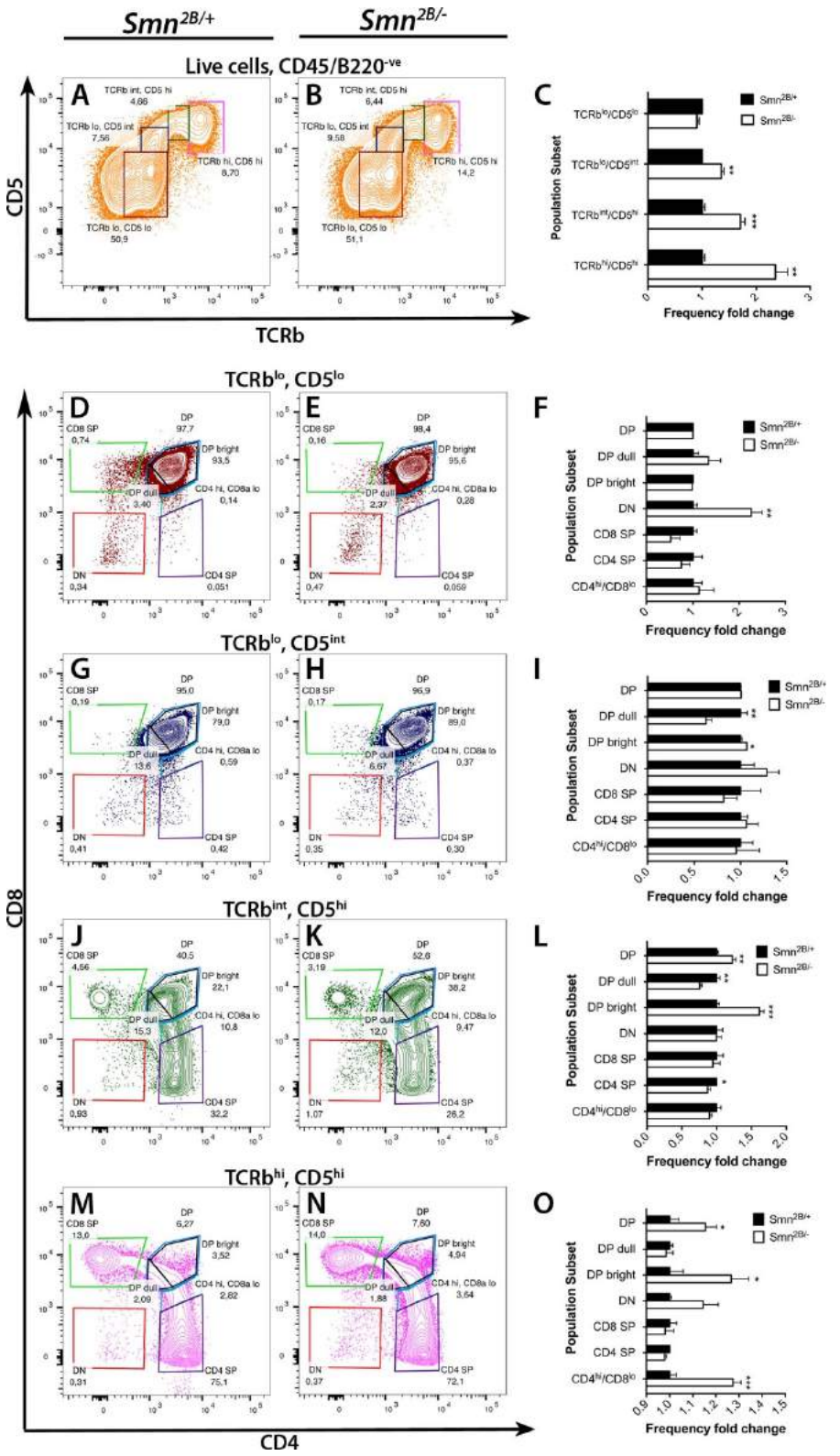
Smn2B/+
Smn2B/-
Live cells, CD45/B220-ve
A
B
C
TCRb int, CD5 hi
4,66
TCRb lo, CD5 int
7,56
TCRb hi, CD5 hi
8,70
TCRb lo, CD5 lo
50,9
TCRb int, CD5 hi
6,44
TCRb lo, CD5 int
9,58
TCRb hi, CD5 hi
14,2
TCRb lo, CD5 lo
51,1
CD5
TCRb
TCRblo/CD5lo
TCRblo/CD5int
TCRbint/CD5hi
TCRbhi/CD5hi
Population Subset
Frequency fold change
TCRblo, CD5lo
D
E
F
DP
97,7
DP bright
93,5
DP dull
3,40
CD4 hi, CD8a lo
0,14
CD8 SP
0,74
DN
0,34
CD4 SP
0,051
DP
98,4
DP bright
95,6
DP dull
2,37
CD4 hi, CD8a lo
0,28
CD8 SP
0,16
DN
0,47
CD4 SP
0,059
DP
DP dull
DP bright
DN
CD8 SP
CD4 SP
CD4hi/CD8lo
TCRblo, CD5int
G
H
I
DP
95,0
DP bright
79,0
DP dull
13,6
CD4 hi, CD8a lo
0,59
CD8 SP
0,19
DN
0,41
CD4 SP
0,42
DP
96,9
DP bright
89,0
DP dull
6,67
CD4 hi, CD8a lo
0,37
CD8 SP
0,17
DN
0,35
CD4 SP
0,30
TCRbint, CD5hi
J
K
L
DP
40,5
DP bright
22,1
DP dull
15,3
CD4 hi, CD8a lo
10,8
CD8 SP
4,56
DN
0,93
CD4 SP
32,2
DP
52,6
DP bright
38,2
DP dull
12,0
CD4 hi, CD8a lo
9,47
CD8 SP
3,19
DN
1,07
CD4 SP
26,2
TCRbhi, CD5hi
M
N
O
DP
6,27
DP bright
3,52
DP dull
2,09
CD4 hi, CD8a lo
2,82
CD8 SP
13,0
DN
0,91
CD4 SP
75,1
DP
7,60
DP bright
4,94
DP dull
1,88
CD4 hi, CD8a lo
3,64
CD8 SP
14,0
DN
0,37
CD4 SP
72,1
CD8
CD4

Figure 3.15. Precocious positive selection in P19 *Smn*$^{2B/-}$ mice is confirmed by CD5/TCR*β* immunophenotyping. Representative contour plots of thymocytes (gated on live cells, CD45/B220^{-ve}) in various stages of positive selection based on CD5/TCRβ immunophenotyping in *Smn*$^{2B/+}$ and *Smn*$^{2B/-}$ mice at P19 (A,B). (C) Quantification of population frequency presented as a fold change demonstrates a significant increase in the proportion of cells initiating positive selection (TCRβ^{lo};CD5^{int}), in the positive selection process (TCRβ^{int};CD5^{hi}), and mature positively selected SP (TCRβ^{hi};CD5^{hi}). Representative contour plots and quantification of sub-populations present in each positive selection stages, namely TCRβ^{lo};CD5^{lo} (D-F), TCRβ^{lo};CD5^{int} (G-I), TCRβ^{int};CD5^{hi} (J-L), TCRβ^{hi};CD5^{hi} (M-O), by immunophenotyping cells with CD4/CD8 shows an alteration in the proportion of sub-populations. (n=5 for all experiments, two-tailed Student's *t* test, $P \leq 0.05$ for *, $P \leq 0.01$ for **, and $P \leq 0.001$ for ***).

We next examined whether these changes occurred at an earlier time point. Surprisingly, flow cytometry analysis of P9 *Smn*$^{2B/-}$ thymocytes revealed no significant abnormalities in the proportion of sub-populations compared to *Smn*$^{2B/+}$ thymocytes (Fig. 3.13G-L). Similarly, very few changes were observed in the positive selection process analysed by TCRβ with either CD69 or CD5 (Fig. 3.16 & 3.17) Therefore, it appears that the changes in the thymocyte cell populations in P19 *Smn*$^{2B/-}$ mice are either independent to the spleen defects or a consequence in response to abnormalities in the periphery such as in the spleen. We attempted to perform a similar flow cytometry analysis to characterize immune sub-populations in spleens from P19 and P9 *Smn*$^{2B/-}$ mice but were unsuccessful in retrieving enough cells due to their small size.

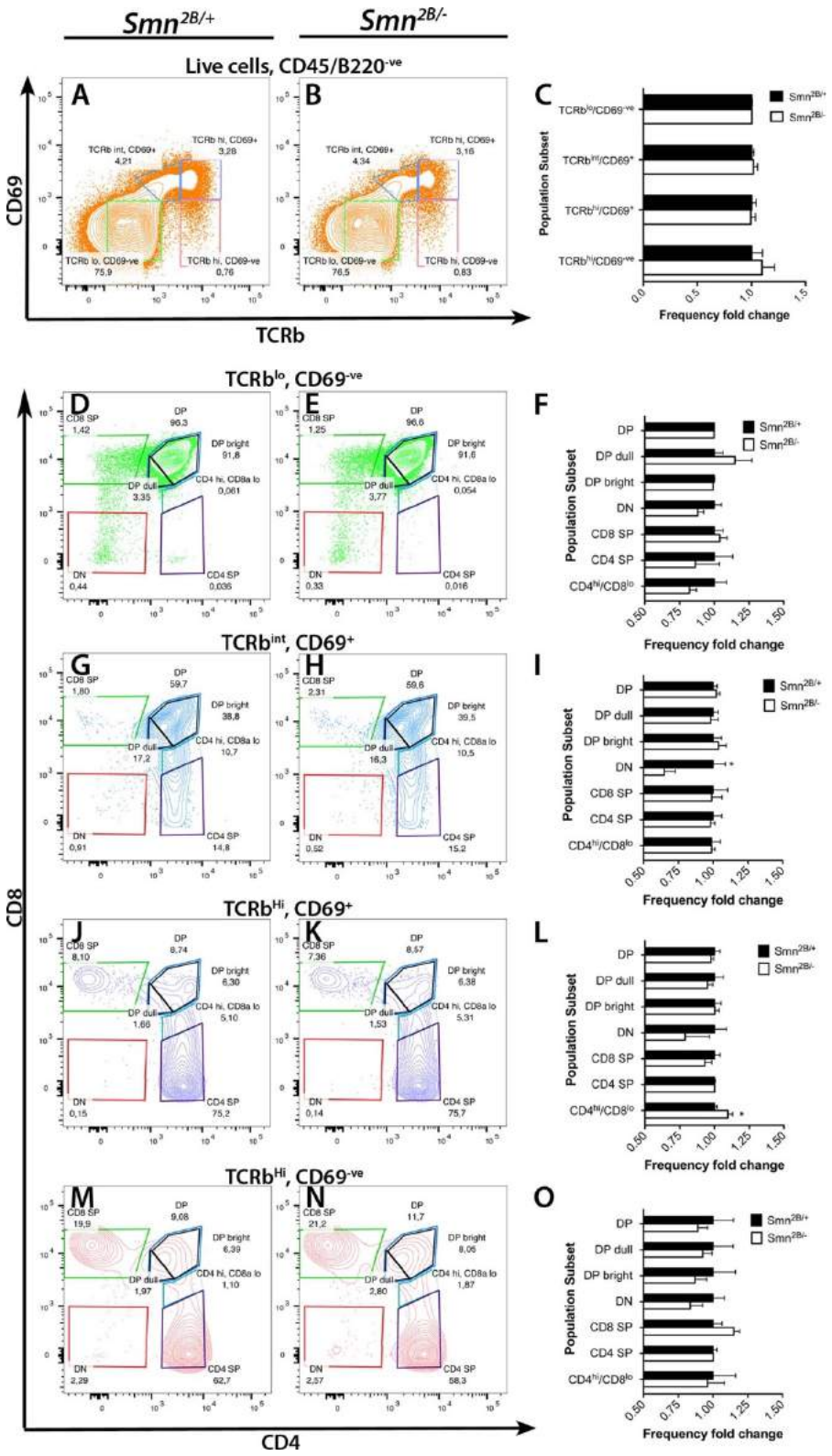
Smn2B/+
Smn2B/-
Live cells, CD45/B220-ve
A
B
C
CD69
TCRb
TCRb int, CD69+ 4,21
TCRb hi, CD69+ 3,28
TCRb lo, CD69-ve 75,9
TCRb hi, CD69-ve 0,76
TCRb int, CD69+ 4,34
TCRb hi, CD69+ 3,16
TCRb lo, CD69-ve 76,5
TCRb hi, CD69-ve 0,83
Population Subset
TCRblo/CD69-ve
TCRbint/CD69+
TCRbhi/CD69+
TCRbhi/CD69-ve
Frequency fold change
TCRblo, CD69-ve
D
E
F
CD8
CD4
CD8 SP 1,42
DP 90,3
DP bright 91,8
DP dull 3,35
CD4 hi, CD8a lo 0,061
DN 0,44
CD4 SP 0,035
CD8 SP 1,25
DP 96,6
DP bright 91,6
DP dull 3,77
CD4 hi, CD8a lo 0,054
DN 0,33
CD4 SP 0,016
DP
DP dull
DP bright
DN
CD8 SP
CD4 SP
CD4hi/CD8lo
TCRbint, CD69+
G
H
I
CD8 SP 1,80
DP 59,7
DP bright 38,8
DP dull 17,2
CD4 hi, CD8a lo 10,7
DN 0,91
CD4 SP 14,8
CD8 SP 2,31
DP 59,6
DP bright 39,5
DP dull 16,3
CD4 hi, CD8a lo 10,5
DN 0,52
CD4 SP 15,2
TCRbHi, CD69+
J
K
L
CD8 SP 8,10
DP 8,74
DP bright 6,30
DP dull 1,66
CD4 hi, CD8a lo 5,10
DN 0,15
CD4 SP 75,2
CD8 SP 7,36
DP 8,57
DP bright 6,38
DP dull 1,53
CD4 hi, CD8a lo 5,31
DN 0,14
CD4 SP 75,7
TCRbHi, CD69-ve
M
N
O
CD8 SP 19,9
DP 9,08
DP bright 6,39
DP dull 1,97
CD4 hi, CD8a lo 1,10
DN 2,29
CD4 SP 62,7
CD8 SP 21,2
DP 11,7
DP bright 8,06
DP dull 2,80
CD4 hi, CD8a lo 1,87
DN 2,57
CD4 SP 58,3

Figure 3.16. Positive selection assessed by CD69/TCRβ shows no impairment in the thymus of P9 *Smn$^{2B/-}$* mice. Representative contour plots of thymocytes (gated on live cells, CD45/B220^{-ve}) in various stages of positive selection based on CD69/TCRβ immunophenotyping in *Smn$^{2B/+}$* and *Smn$^{2B/-}$* mice at P9 (A,B). (C). Quantification of population frequency presented as a fold change demonstrates no difference in the proportion of cells going through the various stages. Representative contour plots and quantification of sub-populations present in each positive selection stages, namely TCRβ^{lo};CD69^{-ve} (D-F), TCRβ^{int};CD69^{+} (G-I), TCRβ^{hi};CD69^{+} (J-L), TCRβ^{hi};CD69^{-ve} (M-O), by immunophenotyping cells with CD4/CD8 show relatively unchanged proportions of sub-populations. (n=5 for *Smn$^{2B/-}$* mice and n=6 for *Smn$^{2B/+}$* mice for all experiments, two-tailed Student's *t* test, $P \leq 0.05$ for *).

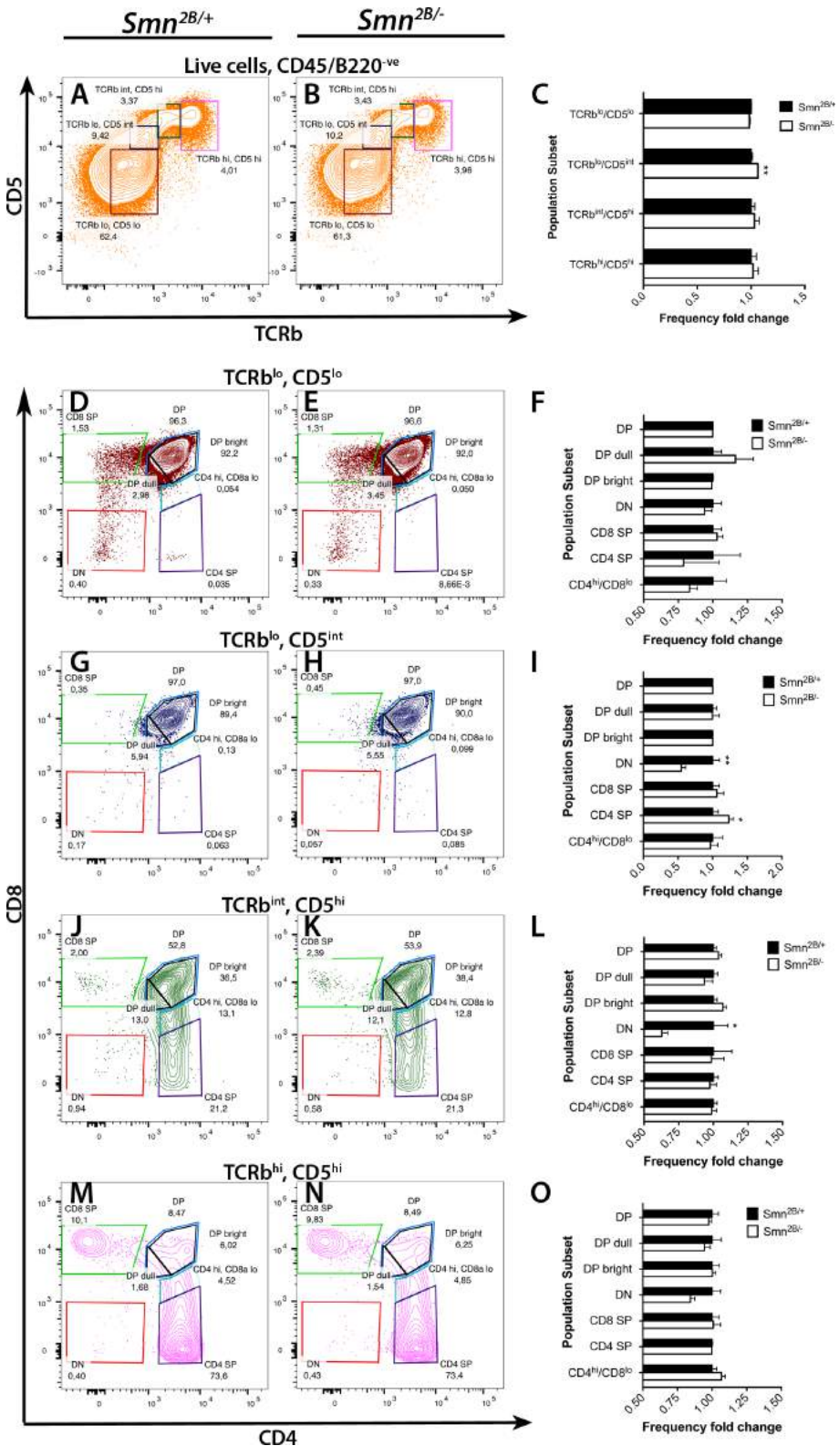
Smn2B/+
Smn2B/-
Live cells, CD45/B220-ve
A
B
C
TCRb int, CD5 hi
3,37
TCRb lo, CD5 int
9,42
TCRb hi, CD5 hi
4,01
TCRb lo, CD5 lo
82,4
TCRb int, CD5 hi
3,43
TCRb lo, CD5 int
10,2
TCRb hi, CD5 hi
3,96
TCRb lo, CD5 lo
81,3
CD5
TCRb
Population Subset
TCRblo/CD5lo
TCRblo/CD5int
TCRbint/CD5hi
TCRbhi/CD5hi
Frequency fold change
TCRblo, CD5lo
D
E
F
CD8 SP
1,53
DP
96,3
DP bright
92,2
DP dull
2,98
CD4 hi, CD8a lo
0,054
DN
0,40
CD4 SP
0,035
CD8 SP
1,31
DP
96,6
DP bright
92,0
DP dull
3,45
CD4 hi, CD8a lo
0,050
DN
0,33
CD4 SP
8,66E-3
DP
DP dull
DP bright
DN
CD8 SP
CD4 SP
CD4hi/CD8lo
TCRblo, CD5int
G
H
I
CD8 SP
0,35
DP
97,0
DP bright
89,4
DP dull
5,94
CD4 hi, CD8a lo
0,13
DN
0,17
CD4 SP
0,063
CD8 SP
0,45
DP
97,0
DP bright
90,0
DP dull
5,55
CD4 hi, CD8a lo
0,099
DN
0,057
CD4 SP
0,085
TCRbint, CD5hi
J
K
L
CD8 SP
2,00
DP
52,8
DP bright
36,5
DP dull
13,0
CD4 hi, CD8a lo
13,1
DN
0,94
CD4 SP
21,2
CD8 SP
2,39
DP
53,9
DP bright
38,4
DP dull
12,1
CD4 hi, CD8a lo
12,8
DN
0,58
CD4 SP
21,3
TCRbhi, CD5hi
M
N
O
CD8 SP
10,1
DP
8,47
DP bright
6,02
DP dull
1,68
CD4 hi, CD8a lo
4,52
DN
0,40
CD4 SP
73,6
CD8 SP
9,83
DP
8,49
DP bright
6,25
DP dull
1,54
CD4 hi, CD8a lo
4,85
DN
0,43
CD4 SP
73,4
CD8
CD4

Figure 3.17. Positive selection assessed by CD5/TCRβ shows no impairment in the thymus of P9 *Smn$^{2B/-}$* mice. Representative contour plots of thymocytes (gated on live cells, CD45/B220^{-ve}) in various stages of positive selection based on CD5/TCRβ immunophenotyping in *Smn$^{2B/+}$* and *Smn$^{2B/-}$* mice at P9 (A,B). (C) Quantification of population frequency presented as a fold change demonstrates no change in the proportion of cells going through the various stages. Representative contour plots and quantification of sub-populations present in each positive selection stages, namely TCRβ^{lo};CD5^{lo} (D-F), TCRβ^{lo};CD5^{int} (G-I), TCRβ^{int};CD5^{hi} (J-L), TCRβ^{hi};CD5^{hi} (M-O), by immunophenotyping cells with CD4/CD8 shows no alteration in the proportion of subpopulations. (n=5 for *Smn$^{2B/-}$* mice and n=6 for *Smn$^{2B/+}$* mice for all experiments, two-tailed Student's *t* test, $P \leq 0.05$ for *, $P \leq 0.01$ for **).

Cytokine profiling

To better understand the functional impairments and/or the aetiology of the defects observed in the lymphoid organs, a thorough cytokine screen in the thymus and spleen at P4 and P19, and in the serum at P19 was performed (Fig. 3.18). It is important to note that naïve cytokine levels are often very low, if even measurable. To our surprise, many changes were readily detected in every organ and time point analyzed. The greatest changes were observed in P19 thymus from *Smn$^{2B/-}$* mice, with almost a global increase of many of the cytokines screened (Fig. 3.18D). Interestingly, a very similar heat map profile was apparent in P4 thymus (Fig. 3.18C). Given the reduction in spleen size, we expected an inflammatory profile, indicative of cell death. However, none of the inflammatory cytokines (such as IL-1β, IL-6, and TNF-α) were significantly changed in both P4 and P19

Smn$^{2B/-}$ spleens (Fig. 3.18A,B). On the other hand, the thymus of P19 *Smn*$^{2B/-}$ mice showed significant induction of many inflammatory cytokines such as IL-1β, IL-6 and TNF-α (Fig. 3.18D). We also noticed that some cytokines appeared misregulated in more than one organ. Notably, eotaxin, IL-3, IL-6, IP-10, LIF, MIG were misregulated in spleen and thymus (Fig. 3.18A-D). Similar analysis of *Smn*$^{2B/-}$ P19 lymph nodes revealed that LIF levels were significantly changed (Fig. 3.19A). Changes in IL-2, M-CSF, VEGF, and TNF-α were also present (Fig. 3.19A). We also investigated the cytokine profile of spinal cord tissue (Fig. 3.19B). Once again, eotaxin and IP-10 expression was altered (Fig. 3.19B). A trend towards an inflammatory profile was present with a mild increase in IL-1β, MIP1α and TNF-α, however many did not reach significance (Fig. 3.19B).

The spleen and thymus of P5 *Smn*$^{-/-}$*;SMN2* mice was also subjected to cytokine profiling (Fig. 3.19C,D). Strikingly, eotaxin, IP-10 and MIG were misregulated in P5 *Smn*$^{-/-}$*;SMN2* spleens while IP-10, LIF, and MIG were significantly changed in the thymus (Fig. 3.19C,D). These changes, however, were not always in the same direction, once again highlighting the molecular complexities between different severities of disease. The P5 *Smn*$^{-/-}$*;SMN2* thymus and spleen also display common cytokine changes not displayed in the *Smn*$^{2B/-}$ model mice. More particularly, VEGF was increased compared to wild type in both spleen and thymus while IL-9 showed changes in the opposite direction (Fig. 3.19). Altogether, the extent of changes observed highlight the intense pathology in the lymphoid organs and the potential consequence it may have in overall immune function.

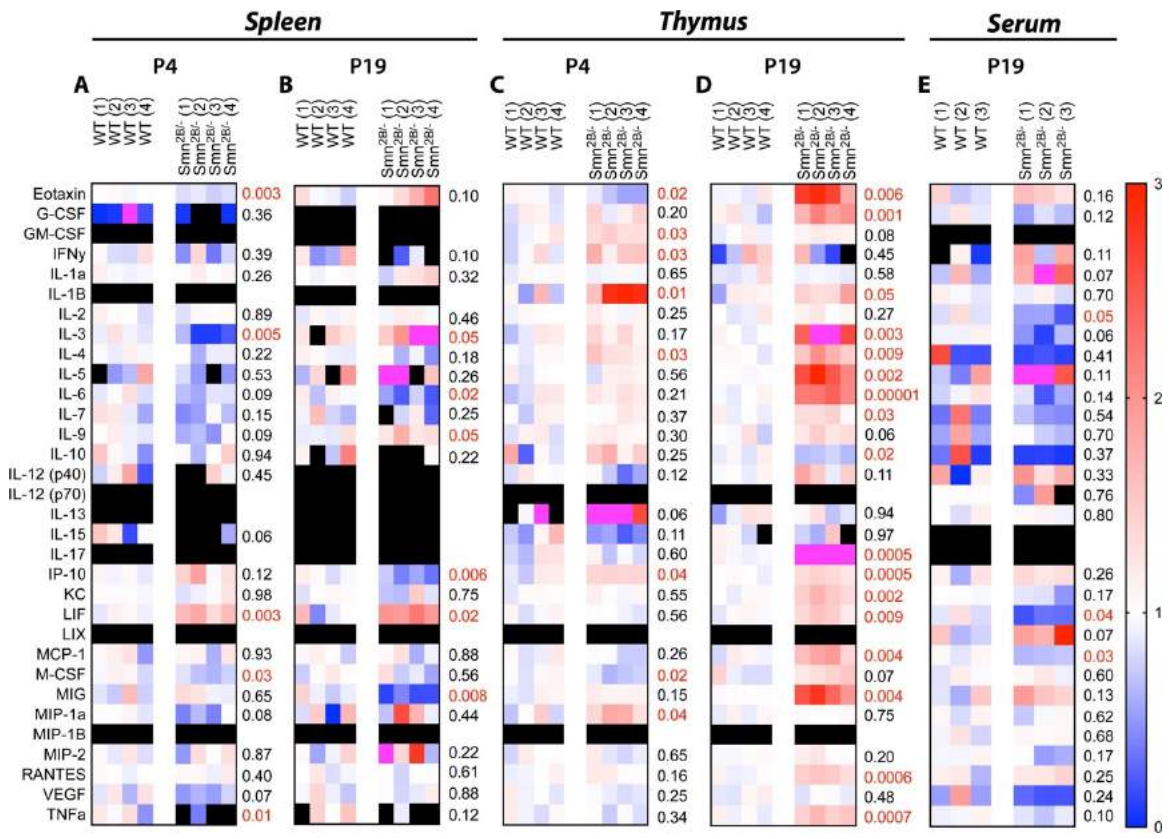

Figure 3.18. Cytokine profiling reveals altered protein levels in spleen and thymus from P4 and P19 *Smn*$^{2B/-}$ mice. Heat map of cytokine profiles in P4 (A) and P19 (B) *Smn*$^{2B/-}$ spleens exhibit various changes, with LIF and IL-3 being commonly misregulated at both time points. Heat map of cytokine profiles in P4 (C) and P19 (D) *Smn*$^{2B/-}$ thymus exhibit several changes, with eotaxin, IL-1B, IL-4 and IP-10 being commonly misregulated at both time points. (E) Heat map of cytokine profiles in serum of P19 *Smn*$^{2B/-}$ mice show down-regulation of IL-2, LIF, and MCP-1. Each box represents a fold change compared to wild type. Black boxes indicate cytokine levels too low to be sensitively recorded. Magenta boxes represent values of fold change higher than 3. The result from each individual sample is shown in the columns. (n=4 for each experiment other than serum where n=3, two-tailed Student's *t* test, the *P* values are indicated next to the heat maps).

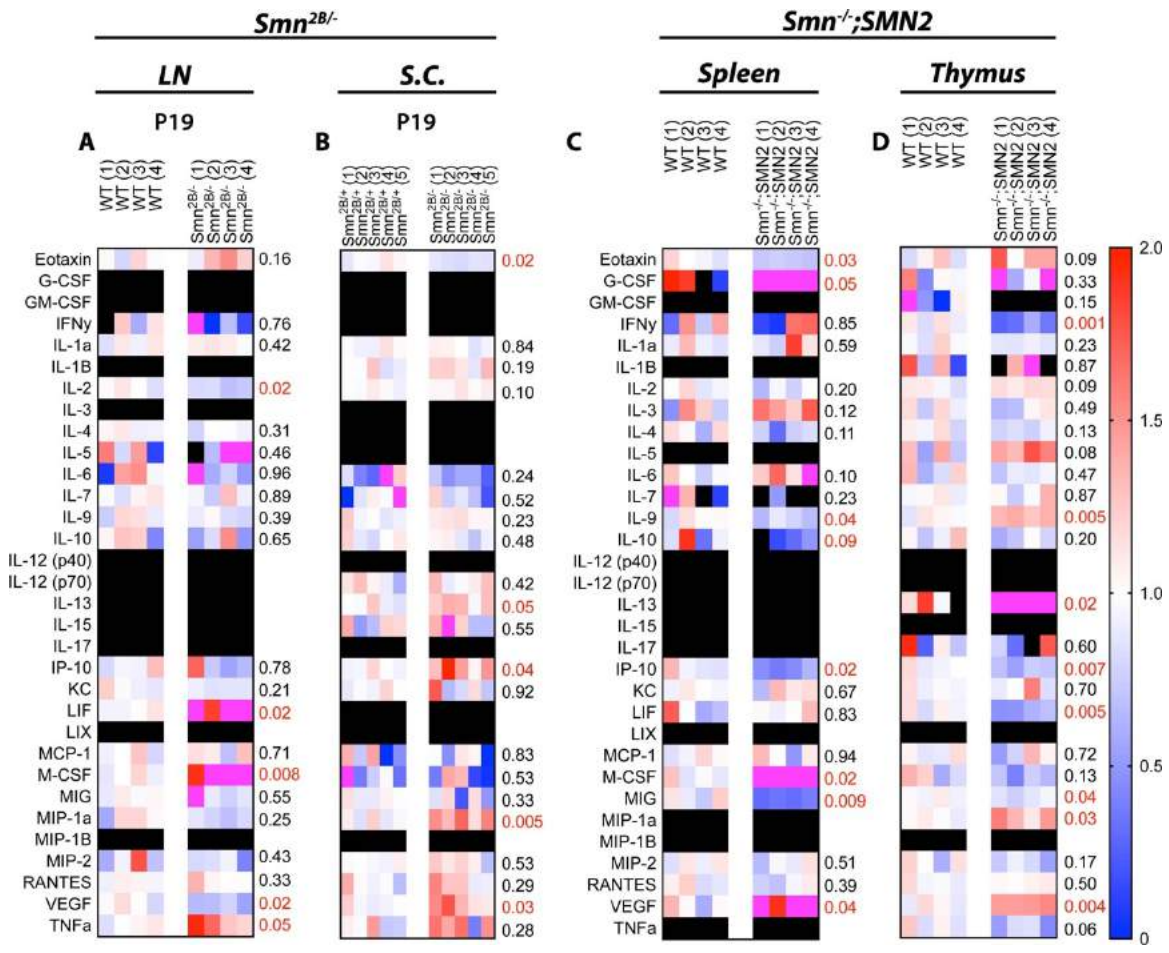

Figure 3.19. Cytokine profiling reveals altered protein levels in lymph nodes and spinal cord of P19 *Smn$^{2B/-}$* mice and in spleen and thymus from P5 *Smn$^{-/-}$;SMN2* mice. (A) Heat maps of cytokine profiles in P19 *Smn$^{2B/-}$* lymph nodes reveal several changes, notably, increased LIF and TNFα levels. (B) Heat map of cytokine profiles of P19 spinal cord (S.C.) revealed changes in eotaxin and MIP-10. An inflammatory profile was present (MIP-1a, TNFα, RANTES) but did not reach significance. Heat maps of cytokine profiles in P5 *Smn$^{-/-}$;SMN2* spleen (C) and thymus (D) show several alterations in cytokine levels, with IP-10, MIG and VEGF being commonly misregulated in both organs. Each box represents a fold change compared to wild type. Black boxes indicate cytokine levels too low to be sensitively recorded. Magenta boxes represent values of fold change higher than

3. The result from each individual sample is shown in the columns. (n=4 for each experiment other than B where n=5, two-tailed Student's *t* test, the *P* values are indicated next to the heat maps).

SMN expression in lymphoid organs

Smn expression in the lymphoid tissues of wild type mice was compared to other commonly affected tissues in SMA such as skeletal muscle and spinal cord. When compared to skeletal muscle, both thymus and spleen had strikingly higher Smn protein levels at P19 (Fig. 3.20A,B). Interestingly, Smn protein levels in the lymphoid tissues were even higher than in spinal cord (Fig. 3.20A,B). It is recognized that *Smn* levels are generally high embryonically and decrease gradually after birth in most tissues studied(13). Smn protein levels in wild type spleens were fairly similar from P0 to P14 with an increase P14 to P19 (Fig. 3.20C). Moreover, Smn levels closely followed the expression pattern of CD3 and CD19, which are T-cell and B-cell markers respectively. In the thymus, Smn protein levels were sustained from P0 to P19 (Fig. 3.20D). As expected, we observed significantly reduced levels of Smn protein in both $Smn^{2B/-}$ spleen and thymus in comparison to wild type (Fig. 3.20E).

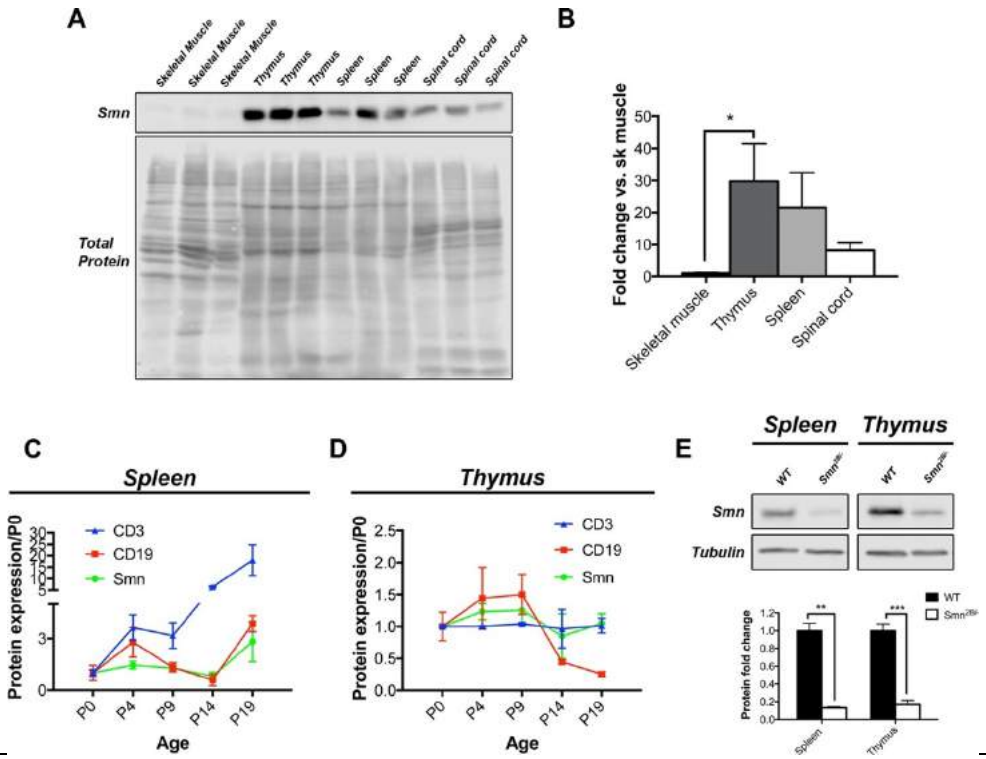

Figure 3.20. High levels of Smn protein in lymphoid organs during postnatal development. (A) Western blot analysis of Smn in different tissues of P19 wild type mice. The membrane stained for total protein is shown in the panel below. (B) Quantification of the western blot highlights the relatively high Smn protein expression in the thymus and in the spleen compared to skeletal muscle and spinal cord. (C) Quantification of western blot analysis of the temporal protein expression profile of CD3, CD19 and Smn in spleen from wild type mice shows a relatively sustained Smn expression that is similar to CD3 and CD19. (D) Quantification of western blot analysis of the temporal protein expression profile of CD3, CD19 and Smn in thymus from wild type mice shows sustained expression for all three proteins. (E) Smn levels in the $Smn^{2B/-}$ spleen and thymus were reduced as expected. (n=3 in A and B, n=2 for each time point in C and D, and n=4 for E. One-way ANOVA with bonferroni post-test for B and two-tailed Student's *t* test for E, $P \leq 0.05$ for *, $P \leq 0.01$ for **, and $P \leq 0.001$ for ***).

Genetic introduction of one copy of SMN2 rescues lymphoid organ defects in $Smn^{2B/-}$ mice

To determine whether lymphoid organ defects were directly caused by low levels of Smn protein, we crossed the $Smn^{2B/2B}$ mouse to a $Smn^{+/-};SMN2^{+/+}$ mouse. The progeny from this cross would contain $Smn^{2B/-};SMN2$ mice, allowing for a slight increase in SMN protein from the newly introduced human *SMN2* transgene. Surprisingly, we observed a complete rescue in the size of the spleen and the thymus on gross morphology assessment at P19 (Fig. 3.21A,D,G). In addition, the structure of the spleen was comparable to wild type mice on histology at this age, with multiple white pulp areas readily evident (Fig. 3.21B,C). H&E analysis of the thymus similarly showed no differences in the rescued mice when compared to wild type (Fig. 3.21E,F). Western blot analysis showed a modest increase in Smn protein levels in $Smn^{2B/-};SMN2$ mice compared to $Smn^{2B/-}$ mice (Fig. 3.21H).

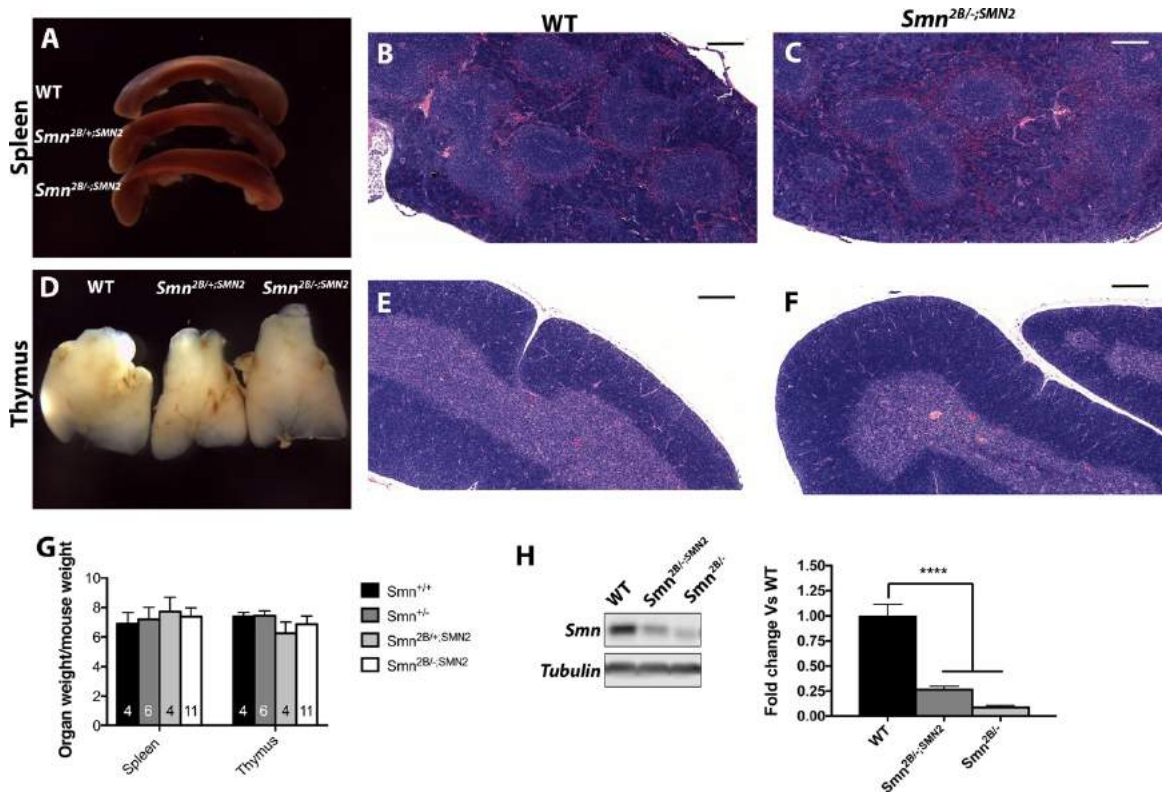

Figure 3.21. Genetic introduction of the human SMN2 transgene in the *Smn$^{2B/-}$* mice rescues the lymphoid organ defects. Gross morphology of the spleen and the thymus are rescued in the *Smn$^{2B/-}$;SMN2* mice at P19 (A,D,F). H&E staining of the *Smn$^{2B/-}$;SMN2* spleen shows structural integrity with the presence of white pulp comparable to wild type (B,C). H&E staining of the *Smn$^{2B/-}$;SMN2* thymus shows rescue of the cortex thinning (E,F). Smn protein levels in the spinal cord of the *Smn$^{2B/-}$;SMN2* mouse is modestly increased relative to Smn2B/-, but still lower than wild type (G). (The n value for A,D,F are as written in the graph bars of F, n=3 in B,C,E,F, and n=4 for G, one-way ANOVA with bonferroni post-test for F,G, $P \leq 0.0001$ for ****).

Discussion

The immune system has not been extensively studied in SMA, but defects in such cells could lead to immune deficiencies or enhance neuroinflammation. In fact, altered immune function in SMA patients could exacerbate disease progression and result in increased hospitalization rate, longer hospital stay, increased morbidity and mortality. However, given the compromised health status and the multiple interventions that SMA patients go through, it is likely that immune involvement, if present, has been historically considered part of the secondary effects and not attributed to disease pathogenesis per se. Here, we report smaller lymphoid organs in two mouse models of SMA. Tissue architectural abnormalities were observed in the thymus of both symptomatic *Smn*$^{2B/-}$ and *Smn*$^{-/-}$*;SMN2* mice and in the spleen in *Smn*$^{2B/-}$ mice. Importantly, we also report aberrations in T-cell development in P19 stage *Smn*$^{2B/-}$ mice, and cytokine level alterations in multiple contexts in both *Smn*$^{2B/-}$ and *Smn*$^{-/-}$*;SMN2* mice, which could have important functional consequences.

Neuroinflammation is a well-established contributor in neurodegenerative disorders (228). Peripheral immune alterations have surfaced in the amyotrophic lateral sclerosis (ALS) field. Interestingly, G93A SOD1 ALS mouse models showed reduced spleen size, architectural defects, and increase cell death of the splenic T-cells and B-cells (229). Moreover, healthy immune cell transplantation lead to better motor performance and survival (229). A new potential model for ALS, the C9orf72 knockout mouse, presented with splenomegaly and enlarged lymph nodes, marked by malfunctioning macrophages and microglia as early pathologic features (230). Subsequently, neuroinflammation

appeared with age and molecularly resemble, at the transcriptome level, that of C9-ALS human patients (230). Interestingly, T-cells appear to be an important player in the neuroprotection conferred by glial cells in ALS (231, 232). It is possible that the pre-symptomatic defects we observed in the spleen are caused by immune cell-autonomous defects. Thus, dysfunctional T-cells and potentially other cell types may limit the full neuroprotective potential of the glial system in the context of SMA. In a similar manner, the spleen size observed is likely to evoke an immune cell redistribution to the circulating system, which may have peripheral consequences.

Even though the thymus was relatively spared as evidenced from the morphological assessment, its architecture was abnormal in both mouse models of SMA, albeit to different degrees of severity. Interestingly, the thymus had the highest Smn protein expression compared to spleen, spinal cord and skeletal muscle, and this expression was relatively sustained over time. Moreover, the thymus from *Smn*$^{2B/-}$ mice showed severe cortico-medullary thinning in comparison to those from the *Smn*$^{-/-}$*;SMN2* mice. Interestingly, an increased proportion of apoptotic bodies and tingible body macrophages were also present in both mouse models of SMA, suggestive of active apoptotic or necrotic processes (223). This appears to be in accordance with a previous report showing increased cell death in *Smn*$^{-/-}$*;SMN2* thymocytes (139). In addition, we found increased proportion of mature SP thymocytes (residents of the medulla) and decreased proportion of DP thymocytes (residents of the cortex) on flow cytometry analysis, which nicely fits with the cortico-medullary thinning. Studies have shown that administration of glucocorticoids leads to similar changes in population proportions (233, 234). Additionally, increased

glucocorticoid levels could also be responsible for the increase in apoptotic bodies we observed in the cortex, more specifically in the DP population (223, 235). In addition to changes in population proportions, a higher proportion of *Smn*$^{2B/-}$ thymocytes were precociously going through the positive selection process. It is possible that this is in response to a loss of peripheral T-cell homeostasis. T-cells are going through precocious apoptosis in secondary lymphoid organs. Related to this, we have observed hyperchromaticity in P19 *Smn*$^{2B/-}$ spleens, which is generally a sign of apoptotic processes.

The triggering event that causes the spleen to become small and display an abnormal architecture remains to be determined. We hypothesized that the T-cells may be stalled in the thymus, consequently not migrating to the spleen. Our analysis of thymic histological changes and T-cell development revealed that these changes occur later (P19) than any defects in the spleen (P4). Autonomic dysfunction has been reported in SMA (120-123, 236-238). Importantly, spleen and thymus architecture may also be dependent on neuronal signals (239, 240). Autonomic dysfunction or denervation could be a potential cause for abnormal compartmentalization within the spleen in SMA. Chemokines have also been shown to be important for recent emigrant thymocytes to travel to secondary lymphoid organs (a process known as homing) (219, 241). For example, manipulating lymphotoxin α/β, CCL19 and CCL21 or their receptors lead to splenic architectural disruption (242-248). Altogether, examining the interaction between the primary and secondary lymphoid organs by studying the immune system as a whole will be crucial to understanding and correctly interpreting the abnormalities observed.

The architecture of the spleen is complex and highly organized to ensure efficiency of its multiple functions. The spleen can exert both innate and adaptive immune response in the presence of an unknown pathogen, especially if present in the blood (219). This is facilitated by the fact that most of the blood travels in the marginal zone, where different populations of macrophages, dendritic cells and B-cells reside (219). These macrophages are particularly important in the clearance of pathogens like *Mycobacterium tuberculosis*, *Streptococcus pneumoniae*, *Escherichia coli*, *Staphylococcus aureus*, and *Neisseria meningitidis* through the innate arm of the immune system (219, 249-252). On the other hand, the marginal zone B-cells can readily become antibody-producing cells if they come across a foreign antigen and migrate in the red pulp for fast antibody delivery into the bloodstream (219). They can also become antigen presenting cells (APCs) and migrate to the white pulp where they activate a T-cell dependent response as part of the adaptive immune system (219). A disruption of the splenic architecture as observed in the $Smn^{2B/-}$ mice is likely to impair some, if not many, of the processes described above. The loss of proper white pulp formation could have several possible consequences. For example, it is unknown whether the marginal zone is still present around the "absent" white pulp. Interestingly, we noticed that residents of this zone, namely the B-cells and macrophages, showed diffuse localization throughout the spleen. The T-cells were also found diffusely distributed across the whole spleen. The red pulp, an area where T-cells are generally not found, could be absent. The red pulp is responsible for clearance of old erythrocytes and for iron homeostasis (219). This could lead to haematological abnormalities. Future research is needed to better understand the defective architecture of the spleen and the

specific functional impairments of *Smn*$^{2B/-}$ mice by the characterization of the different populations of macrophages, dendritic cells, T-cells and B-cells.

The accumulation of smooth muscle cells in the P19 *Smn*$^{2B/-}$ spleens is rather intriguing. Smooth muscle cells are normally found around arteries and within organs. It is possible that abnormal blood vessel morphogenesis leads to less extensive artery and capillary network, and consequently results in higher probability of splenic infarct in the *Smn*$^{2B/-}$ mice. It is now evident that distal necrosis is a prominent feature of mouse models of SMA, especially when therapeutics allow for lifespan extension (154, 159, 207, 253). Some SMA patients also display similar features (237, 238). Moreover, blood vessel abnormalities have been shown in skeletal muscles, hearts and the spinal cord (123, 254, 255). Since the spleen is engorged with red blood cells, it is possible that a lower perfusion efficiency could explain the decreased spleen size, architectural abnormalities and the trend of higher incidence of splenic infarct.

The cytokine profiling revealed global immune dysregulation, which could have severe functional consequences. Surprisingly, despite the phenotype observed, the spleen of the *Smn*$^{2B/-}$ model mice did not show a very strong inflammatory profile as assessed by expression of inflammatory cytokines such as IL-1β, IL-6, and TNF-α (256). In marked contrast, the thymus showed marked inflammatory cytokine expression and a decrease in the anti-inflammatory cytokine IL-10. Interestingly, some of these changes were present in *Smn*$^{2B/-}$ P4 thymus. LIF, a cytokine in the IL-6 family, which is considered an inflammatory cytokine (256), is misregulated in multiple organs and time points. Even though very few

histological changes were observed in the P5 *Smn*$^{-/-}$*;SMN2* spleen, changes in G-CSF, GM-CSF seem to point towards increased hematopoiesis. This clear disruption in cytokine homeostasis accentuates the potential role of immune dysfunction in SMA pathogenesis. Altogether, we presented an array of abnormalities in various lymphoid organs in mouse models of SMA. Whether these alterations directly increase neuroinflammation or result in immune deficiencies, remains to be determined. Future research will focus on narrowing potential aetiologies of such defects and investigating functional impairments of defective lymphoid organs in the SMA context.

Materials and Methods

Mouse Models

The *Smn*$^{-/-}$*;SMN2* (Jackson Laboratory) and *Smn*$^{2B/-}$ (C57BL/6J background) (157) mouse lines were housed at the University of Ottawa Animal Facility and cared for according to the Canadian Council on Animal Care. *Smn*$^{+/-}$ mice (C57BL/6J) were crossed to *Smn*$^{2B/2B}$ mice (C57BL/6J) to obtain *Smn*$^{2B/+}$ and *Smn*$^{2B/-}$ animals. Similarly, *Smn*$^{+/-}$*;SMN2*$^{+/+}$ (FVB) mice were crossed to *Smn*$^{2B/2B}$ (FVB) mice to obtain *Smn*$^{2B/+}$*;SMN2* and *Smn*$^{2B/-}$*;SMN2* (FVB) animals (157). C57BL/6J and FVB wild type mice were bred separately. Spleen and thymus were harvested from pre-symptomatic (P0 and P2) and symptomatic (P5) *Smn*$^{-/-}$*;SMN2* mice. Tissues were collected at P0, P4 and P9 pre-symptomatic mice and from P14 and P19 symptomatic *Smn*$^{2B/-}$ and *Smn*$^{2B/-}$*;SMN2* mice.

Gross morphology

A 0.75X picture of the spleens and tibia were taken with a Leica M80 dissection microscope mounted with a camera (Leica IC80 HD). The lengths were measured using ImageJ. The mouse measurements for normalization were done prior to dissection using a ruler for the length of the mouse and a scale for its weight. Tissues were then fixed in 10% formalin for 24-48 h and transferred to 70% ethanol for long-term storage.

Tissue processing and H&E staining

Spleens, thymus and lymph nodes were fixed in formalin (1:10 dilution buffered, from Protocol, cat #245-684) for 24-48 h at 4ºC and then transferred in 70% ethanol at 4ºC until processing. All samples were processed at the University of Ottawa (Department of Pathology and Laboratory Medicine) and embedded in wax using a LOGOS microwave hybrid tissue processor. Paraffin block tissues were cut with a microtome at 3-4 μm of thickness and stained for H&E using a Leica autostainer XL Leica CV5030. Stained H&E samples were scanned with a MIRAX MIDI digital slide scanner (Zeiss). Images were acquired using 3DHISTECH Panoramic Viewer 1.15.4 at different magnifications. Quantification of the thymus area and the corticomedullary area ratio was performed by assessing area of 3 serially cut sections (slide 5, 10 and 15 or 17) using ImageJ. One or both lobes per slide were quantified depending whether both lobes were present on the slide.

Immunohistochemical staining

Tissues were processed, embedded and sectioned as described above. Slides were deparaffinized in 3 changes of xylene substitute HEMO-DE (Electron Microscopy Science, 23412-01) (or toluene) for 5 min each followed by 2 changes into a 50/50 mixture of absolute ethanol and HEMO-DE (or toluene) for 5 min each. Slides were gradually rehydrated in 100%-95%-70%-50%-0% ethanol. A heat-induced antigen retrieval step was performed when needed using Tris/EDTA buffer (10 mM Tris, 1 mM EDTA, 0.05% Tween 20, pH 9.0) or sodium citrate pH 6.0. Sections were permeabilized with 0.1%

Triton-X (Sigma) and then blocked for 1 h in 5-10% goat serum in PBS for 1 h. M.O.M kit (Vector, BMK-2202) was used as per the manufacturer's protocol to optimize staining condition of primary mouse antibodies on mouse primary tissue. Slides were incubated with primary antibodies for 90 min at room temperature at the following concentrations: CD3 (DAKO #2018-11 - 1:100), CD19 (Abcam, ab197895 or ab31947 - 1:100) and F4/80 (eBioscience ref 14-4801-81 - 1:100 or Abcam, ab6640 - 1:100) and cleaved caspase 3 (Cell signalling, 9664L - 1:300). For TUNEL (Roche, 11684795910) staining, manufacturer instructions were followed. Sections were washed and then incubated with secondary antibodies (Alexa Fluor-488, Alexa Fluor-555 or Alexa Fluor-647 from Invitrogen - 1:500) for 1 h at room temperature. Sections counterstained with 3`3`-diaminobenzidine (DAPI, Molecular Probes, D1306). Slides were mounted with fluorescent mounting medium (DAKO mounting media). Pictures were acquired using microscope Zeiss Axio Imager M1 mounted with a camera.

Immunoblotting

Total protein lysate was collected by homogenization of flash frozen spleen, thymus, lymph nodes, skeletal muscle, or spinal cord in RIPA lysis buffer (Cell Signaling). Protein concentrations were determined using the Bradford assay (Bio-Rad). Protein extracts were subjected to sodium dodecyl sulphate polyacrylamide gel electrophoresis and examined by immunoblot, as previously described (205) with modified blocking conditions where Odyssey blocking buffer (Li-Cor 927-40000) replaced 5% milk. Revert Total protein stain (Li-Cor 926-11010) was used as per the manufacturer's protocol. Primary antibodies used were as follows: Anti-Smn (BD Transduction, 610647 - 1:2000),

CD3 (DAKO #2018-11 - 1:1000), CD19 (Abcam, ab197895 - 1:1000) and alpha-tubulin (Abcam, ab4074 – 1:1000). Secondary antibodies used were IRDye 680 or 800 (Li-Cor - 1:10000 to 1:20000). Signals were detected with Odyssey CLx (Li-Cor). Results were normalized to total protein.

RNA isolation and reverse transcription-quantitative polymerase chain reaction (RT-QPCR)

Total RNA was extracted from mouse models of SMA and wild type controls using RNeasy kit (Qiagen) according to the manufacturer's protocol. RNA concentrations were determined using a Nanophotometer spectrophotometer (MBI Lab Equipment). RNA was reversed transcribed using the quantitect reverse-transcription kit (Qiagen) according to the manufacturer's protocol. QPCR was performed in triplicate. A complete list of primers are available in the supplementary material (Table 3.1). A standard curve was performed for each primer set to ensure their efficiency. Each QPCR reaction contained equal amount of cDNA, Ssofast Evagreen Supermix (Biorad), RNase/DNase-free water and appropriate primers (100-200 nM) in a final volume of 25 µl. Two negative controls were included in every QPCR plate and consisted of water in lieu of cDNA. QPCR results were analyzed using Biorad CFX manager 3.1. Results were normalized to two or three internal controls that were determined to have stable expression according to their M-value (below 0.5) and their coefficient variance (below 0.25). The internal controls for each experiment are as followed: P2 thymus (Cyclophilin A and PBGD), P5 thymus (PBGD and SDHA), P4 thymus (PolJ, Hprt1, PBGD), and P19 thymus (Ubiquitin C and Ywhaz).

Table 3.1. Primer sequences used in this study.

Gene and orientation	Sequence
Bax For	TGCAGAGGATGATTGCTGAC
Bax Rev	GATCAGCTCGGGCACTTTAG
BcL2 For	CTGCACCTGACGCCCTTCACC
BcL2 Rev	CACATGACCCCACCGAACTCAAAGA
Caspase 2 (casp2) For	GAGGCTGACTTCCTGTATGCTT
Caspase 2 (casp2) Rev	AACCACGACCCGTCCTTT
Caspase 8 (casp8) For	GGCCTCCATCTATGACCTGA
Caspase 8 (casp8) Rev	TGTGGTTCTGTTGCTCGAAG
Fas cell surface death receptor (FasR) For	TGTGAACATGGAACCCTTGA
Fas cell surface death receptor (FasR) Rev	TTCAGGGTCATCCTGTCTCC
TrP53 (p53) For	GCTTCTCCGAAGACTGGATG
TrP53 (p53) Rev	CTTCACTTGGGCCTTCAAAA
Bnip3 Forward	TTCCACTAGCACCTTCTGATGA
Bnip3 Reverse	GAACACCGCATTTACAGAACAA
Gabarapl1 Forward	CATCGTGGAGAAGGCTCCTA
Gabarapl1 Reverse	ATACAGCTGGCCCATGGTAG
Cathepsin L Forward	GTGGACTGTTCTCACGCTCAAG
Cathepsin L Reverse	TCCGTCCTTCGCTTCATAGG
Tyrosine 3-monooxygenase/tryptophan 5-monooxygenase activation protein, zeta polypeptide (Ywhaz) For	AAGACAGCACGCTAATAATGC
Tyrosine 3-monooxygenase/tryptophan 5-monooxygenase activation protein, zeta polypeptide (Ywhaz) Rev	TTGGAAGGCCGGTTAATTTTC
ubiquitin C (Ubc) For	GCCCAGTGTTACCACCAAGA
ubiquitin C (Ubc) Rev	CCCATCACACCCAAGAACA
Cyclophilin A (PPIA) For	ATCTTCTNGCTGGTCTTGCC
Cyclophilin A (PPIA) Rev	GTCTCCTTCGAGCTGNTTGC
Hypoxanthine Phosphoribosyltransferase 1 (Hprt1) For	CCCAGCGTCGTGATTAGTGATG
Hypoxanthine Phosphoribosyltransferase 1 (Hprt1) Rev	TTCAGTCCTGTCCATAATCAGTC
RNA Polymerase II Subunit J (PolJ) For	ACCACACTCTGGGGAACATC
RNA Polymerase II Subunit J (PolJ) Rev	CTCGCTGATGAGGTCTGTGA
Succinate Dehydrogenase Complex Flavoprotein Subunit A (SDHa) For	GCCTGGTCTGTATGCCTGTG
Succinate Dehydrogenase Complex Flavoprotein Subunit A (SDHa) Rev	CCGATTCTTCTCCAGCATTTG
Hydroxymethylbilane Synthase (PBGD) For	GGGAACCAGCTCTCTGAGGA
Hydroxymethylbilane Synthase (PBGD) Rev	GAATTCCTGCAGCTCATCCA

Cell extraction and flow cytometry

Thymus were dissected from mice and put directly in R10 (89.4% 1X RPMI media 1640 (Gibco, 11875-168), 10% fetal bovine serum (Life Science Seradigm, 97068-085), 0.5% gentamycin (Gibco, 15710-072), 0.1% 2-mercaptoethanol (Gibco, 21985-023) until further processing. Once all samples were collected, tissues were squashed between two frosted slides to obtain a single cell suspension. The single cell suspension was then passed through a 100 µm and a 70 µm strainer to ensure the remaining tissue aggregates were left behind and spun at 500 g for 5 min. The cells were further resuspended in 1X BD Pharm Lyse (BD Biosciences, 555899) for 5 min and then washed twice with PBS. Cells were counted and an equal number of cells was placed in each tube for flow cytometry analysis. Samples were first stained with fixable viability stain 510 (BD Biosciences, 564406) according to the manufacturer's protocol. Cells were resuspended in staining buffer (1% bovine serum albumin) and incubated with FcBlock (BD Pharmingen, 553142) for 10 min at 4°C. The following antibodies (BD Biosciences) CD69 (740664 - 1:400), CD44 (563058 - 1:400), CD5 (562739 - 1:100), CD45/B220 (561101 - 1:100), CD4 (561835 - 1:400), TCRβ (560729 - 1:400), CD25 (562695 - 1:400), and CD8a (561095 - 1:100) were added to the suspension and incubated for 30 min in the dark at 4°C. The samples were then washed with staining buffer. Cells were resuspended in 1:1 staining buffer and IC fixation buffer (eBioscience, 00-8222-49). Samples were acquired by the flow cytometry core (BD LSR Fortessa flow cytometer) of the University of Ottawa within 2 days of being stained. Single stain controls were performed with OneComp ebeads (eBioscience, 01-1111-42) as per the manufacturer's protocol and were then used to set the flow cytometer parameter. Fluorescence-minus-one were also performed in parallel and acquired in similar fashion as

the samples to ensure correct identification of populations. P19 thymus acquisition was stopped once 10,000 events were acquired in the DN gate while P9 thymus acquisition was stopped once 3,000 events were acquired in the DN gate to ensure enough events for proper quantification.

Cytokine profiling

Mouse blood was obtained by cardiac puncture from wild type and *Smn*$^{2B/-}$ mice at P19. Blood was left at room temperature for 1-2 hours before centrifugation at 10,000 g for 10 min at 4^{o}C to obtain serum (as per Eve Technologies' instructions). Serum was diluted in a 1:1 ratio with PBS for analysis. Spleens, thymus, and lymph nodes were collected and protein was extracted as described above. All protein lysates were diluted at a concentration of 1 µg/µL in a total of 80 µL for duplicate analysis. Serum and protein lysates were shipped to Eve Technologies for cytokine profiling. We quantified 32 cytokine/chemokine/growth factor biomarkers simultaneously by using a Discovery Assay® called the Mouse Cytokine Array/Chemokine Array 32-Plex (Eve Technologies Corp, Calgary, AB, Canada). The multiplex assay was performed by using the Bio-Plex TM 200 system (Bio-Rad Laboratories, Inc., Hercules, CA, USA), and a Milliplex Mouse Cytokine/Chemokine kit (Millipore, St. Charles, MO, USA) according to their protocol. The 32-plex consisted of eotaxin, G-CSF, GM-CSF, IFNγ, IL-1α, IL-1β, IL-2, IL-3, IL-4, IL-5, IL-6, IL-7, IL-9, IL-10, IL-12 (p40), IL-12 (p70), IL-13, IL-15, IL-17, IP-10, KC, LIF, LIX, MCP-1, M-CSF, MIG, MIP-1α, MIP-1β, MIP-2, RANTES, TNFα, and VEGF. The assay sensitivities of these markers range from 0.1-33.3 pg/mL. Individual analyte values and other assay details are available on Eve Technologies' website or in the

Milliplex protocol. Analytes that were undetectable were defined as 0 pg/mL and labelled as a black box. Extrapolated results were included in the analysis. When analytes were undetectable in all or most animals from both control and SMA mice, analysis were not performed and also represented as a black box in the heat maps (Fig. 3.18 and Fig. 3.19).

Statistics

Data are presented as the mean ± standard error of the mean. A two-tailed Student's *t* test was performed using Microsoft Excel or Graphpad Prism 7 to compare the means of data when only two groups were compared (i.e. wild type vs. $Smn^{2B/-}$). Splenic infarct relative risk was assessed by a Fischer's exact test and confidence interval calculated by Koopman asymptotic score. One-way ANOVA analysis was used to distinguish differences between more than two groups when multiple comparisons were necessary (i.e. wild type vs. $Smn^{2B/+}$ vs. $Smn^{2B/-}$) . The post-test used for the ANOVA was Bonferroni. Significance was set at $P \leq 0.05$ for *, $P \leq 0.01$ for **,$P \leq 0.001$ for *** and $P \leq 0.0001$ for ****.

Study approval

This study was approved by the Animal Care and Veterinary Services (ACVS) of the University of Ottawa as specified by protocol #OHRI-1927 and #OHRI-1948.

Funding

This work was supported by Cure SMA/Families of SMA Canada; Muscular Dystrophy Association (USA) (grant number 294568); Canadian Institutes of Health Research (CIHR) (grant number MOP-130279); and the E-Rare-2 program from the CIHR (grant number ERL-138414).

Acknowledgements

We would like to thank Sabrina Gibeault for assistance with experiments. We also thank Dr. Vera Tang, Emily Chomyshyn, and Emmanuelle Ametepe for their precious assistance with flow cytometry. We would like to thank all members of the Kothary laboratory for helpful discussions. M-O.D was supported by a Frederick Banting and Charles Best CIHR Doctoral Research Award, a Queen Elizabeth II Graduate Scholarship in Science and Technology, and a Canadian Graduate Scholarship (Master's Program - CIHR).

Conflict of Interest statement

All authors have no competing financial interests to declare.

Appendix

Lymph node structure is unaffected

Primary lymphoid organs include the bone marrow and the thymus. These organs are involved in immune cell maturation. Secondary lymphoid organs include the spleen, the lymph nodes (LN) and mucosal associated lymphoid tissues (MALT) (Peyer's patches, adenoids, tonsils and others - reviewed in (257)). These organs act as sentinels against foreign bodies and antigens that could be harmful to our bodies. Our initial investigations in lymphoid organs included limited information about the status of lymph nodes. Interestingly, we had identified some alterations in cytokines profiling, more specifically in VEGF, LIF and TNFα (Figure 3.19). As such, we ought to evaluate its histological structure given the wide array of abnormalities already identified in the spleen and thymus. Preliminary histological analysis of the inguinal and brachial lymph nodes revealed limited changed in histology (Figure 3.22).

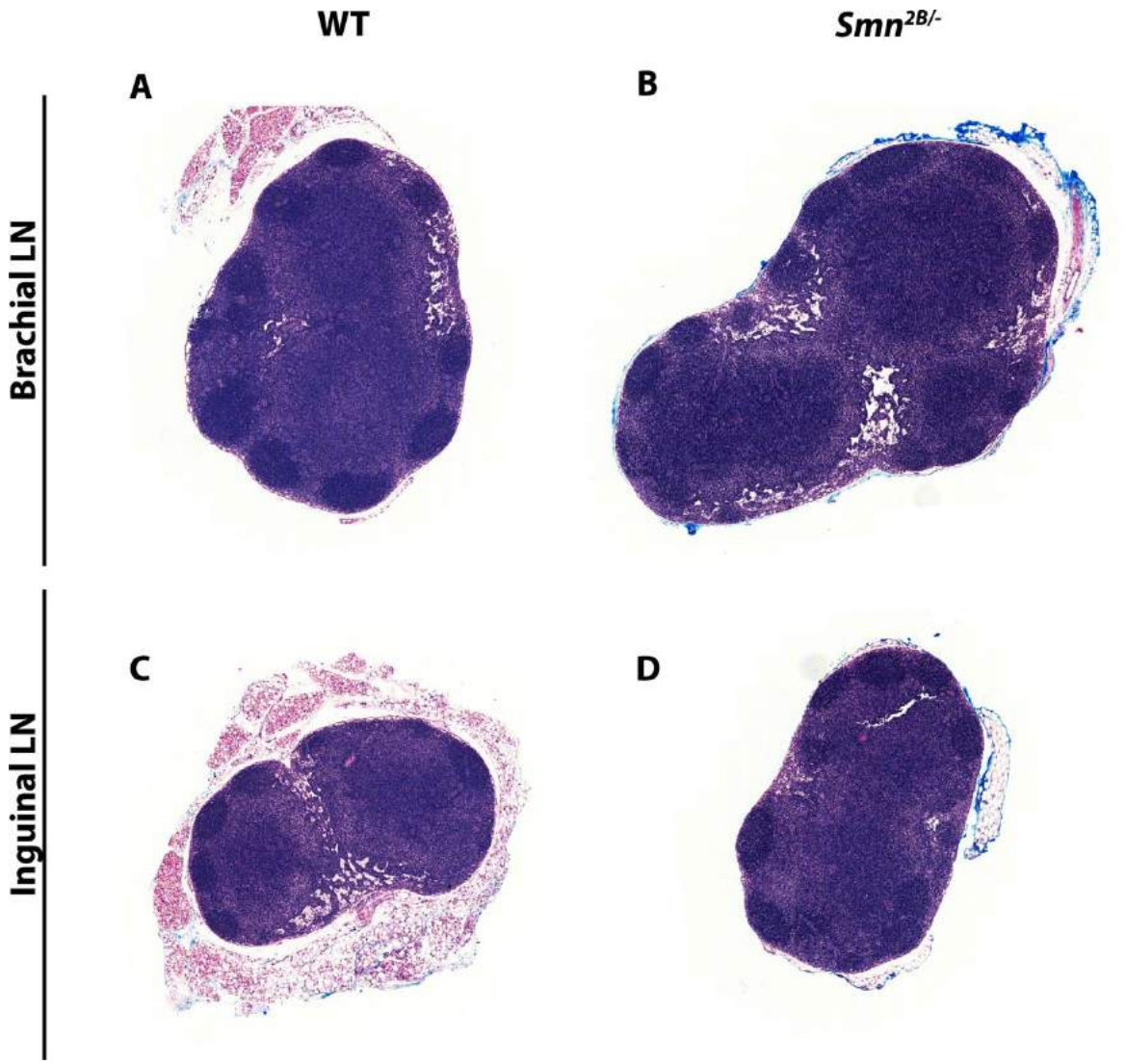

Figure 3.22 No obvious histological changes are observed in different lymph node grouping. Comparable (10X) H&E images of brachial (A-B) and inguinal lymph nodes (C-D) (N value for each experiment is as follows: N = 2-4 for A-D)

Abnormal blood perfusion to the spleen leads to its size reduction

The recent efforts identifying the immune organ defects have offered limited mechanistic insights (258-260). The mechanism leading to the most prominent defect, the small spleens, remained to be determined. Possible explanations include abnormal vasculature, denervation, and cell-intrinsic defects, which have all been previously identified in other non-neuronal organs (83, 121, 255). However, other possibilities also include lack of proliferation or increased apoptosis, which seem unlikely based on current observations (259, 260), and abnormal expression of homing chemokines (219).

We decided to further pursue defective vasculature hypothesis given that the spleen appears as a blood reservoir, possible vasculature problems was pointed out in a concurrent study on immune organs in SMA (261), and that vasculature defects have surfaced in multiple organs in SMA pre-clinical models (124, 254, 255, 261). To get a better appreciation of blood flow to the spleen, we employed an *in vivo* approach by using doppler ultrasonography of the splenic artery in $Smn^{2B/-}$ mice. This is a superior technique to assess aberration in splenic perfusion as it provides a real-time physiological reading of the perfusion of the spleen in comparison to qualitative assessment of blood vessels by histology. We identified that splenic artery blood flow during the systolic phase was significantly reduced in $Smn^{2B/-}$ mice in comparison to control littermates at P19 (Figure 3.23G-M). We next wanted to see whether this reduction in peak blood flow velocity was present at earlier time point, such as P9, where the size difference in the spleen is much less overt. This would represent early pathogenic event, indicating that reduced blood flow may be present earlier than size reduction, hence initiating this phenotype. We were

amazed to see that blood flow was consistently reduced at P9 *Smn*$^{2B/-}$ mice during the systolic phase (Figure 3.23A-F, M). As anesthesia is necessary for this procedure, it is possible that cardiovascular depression be influencing blood flow in *Smn*$^{2B/-}$ mice. Interestingly, these differences could not be attributed to heart rate difference as both groups display similar heart rate despite anesthesia (Figure 3.23N).

The phenotype of Smn$^{2B/-}$ *mice is unchanged by depletion of CD4 positive cells*

Neuroinflammation is a well-established characteristic of neurodegenerative disorders (262). This phenomenon is mainly mediated by astrocytes, microglia, and T-cells (263). Defective immune organs, and more particularly a defective T-cell compartment, could signal a defective inflammatory response in SMA. Of interest, neuroinflammation has already been shown to be an important part of disease pathogenesis in ALS. Given the emerging evidence for common molecular links in disease etiology of ALS and SMA (264-269), the likelihood of neuroinflammation in SMA is high. Indeed, this is supported by astrocytic and microglial activation in SMA (107, 140, 150, 270), and the identification of a pro-inflammatory cytokine profile (e.g. IL-1β and TNF-α) in the spinal cord of *Smn*$^{2B/-}$ mice (Figure 3.19) (271) (also see (272)). On the other hand, it is possible that T-cells and B-cells may provide protection to motor neurons. For example, in ALS, T-cells potentiate the neuroprotection conferred by microglial cells (231, 232).

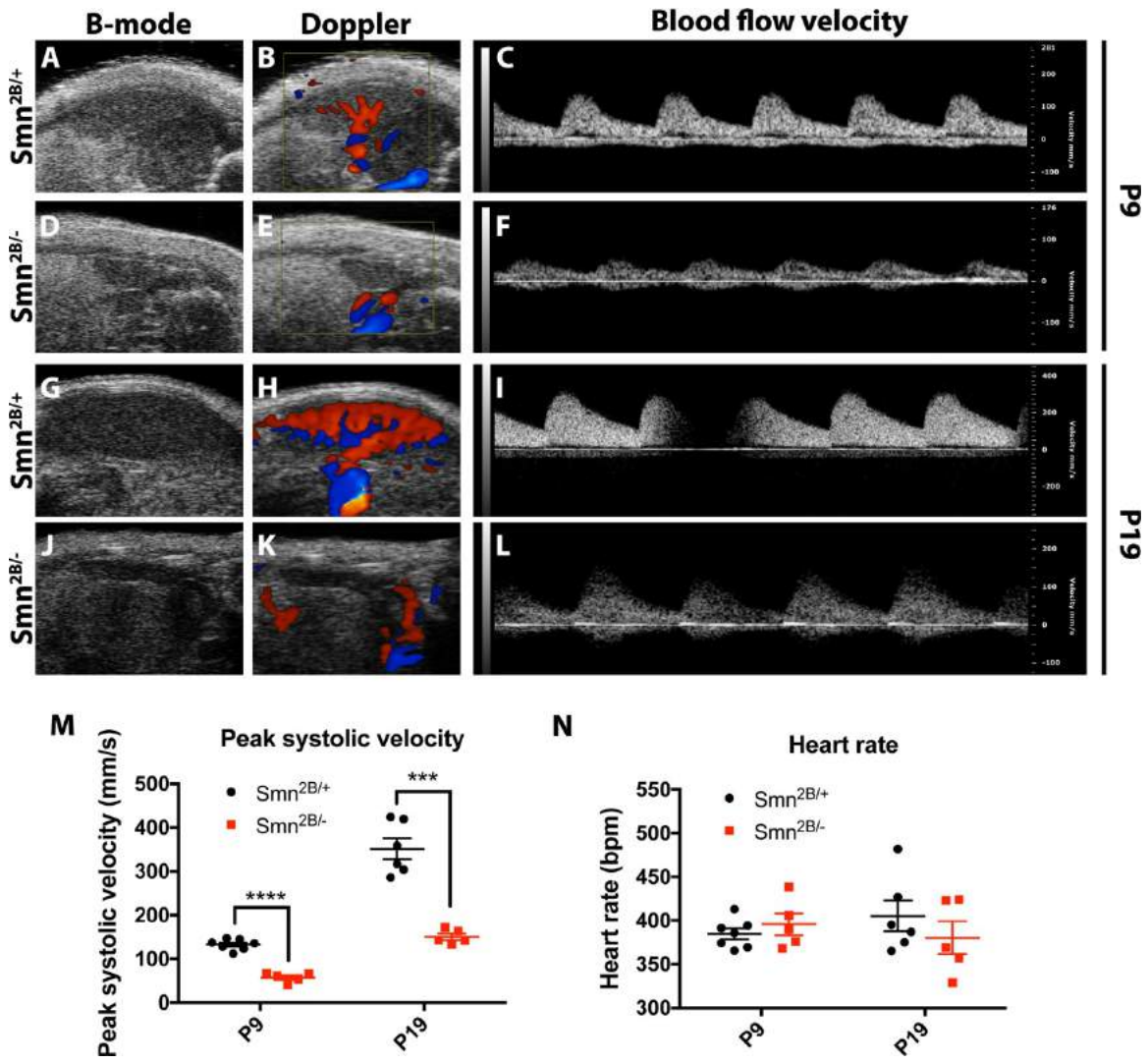

Figure 3.23 Early splenic blood flow deficiency may lead to progressively loss of splenic volume. The spleen of *Smn*$^{2B/+}$ and *Smn*$^{2B/-}$ mice visualized by B-Mode and doppler ultrasonography at P9 (A-B, D-E) and P19 (G-H, J-K). Blood flow velocity highlights reduced systolic velocity in the splenic artery at P9 (C,F) and P19 (I,L). Note the difference in Y-axis graduation between the *Smn*$^{2B/+}$ and *Smn*$^{2B/-}$ mice. Quantification of peak systolic velocity is graphed in (M). (N) Heart rate was unchanged between *Smn*$^{2B/+}$ and *Smn*$^{2B/-}$ mice during these experiments. (The N value is 5-7, $P \leq 0.001$ for *** and $P \leq 0.0001$ for ****).

To get more insight into the role of T-cells, more specifically CD4 T-cells to SMA pathogenesis, breeding of *Smn*$^{2B/2B}$ mice onto the *CD4*$^{-/-}$ (*Cd4*^{tm1Mak}) background were initiated. *CD4*$^{-/-}$ mice are unable to produce any CD4 helper T-cells, which are known to modulate the immune system. Obtaining *Smn*$^{2B/-}$;*CD4*$^{-/-}$ will shed light on the contribution of CD4 T-cells in mediating neuroinflammation or neuroprotection. We expected a worsening of the phenotype, which means that immune cells had a protective effect has been observed in ALS (231, 232). Strikingly, we found that loss of helper T-cells in the *Smn*$^{2B/-}$;*CD4*$^{-/-}$ mice did not significantly impact the survival, weight or motor function of these mice, as indicated by righting reflex, pen test and inverted mesh grip test (Figure 3.24). Interestingly, we identified a longer survival in female than male in both *Smn*$^{2B/-}$ (male 20.5 days VS female 25 days) and *Smn*$^{2B/-}$;*CD4*$^{-/-}$ (male 21 days VS female 25.5 days) mice (data not shown).

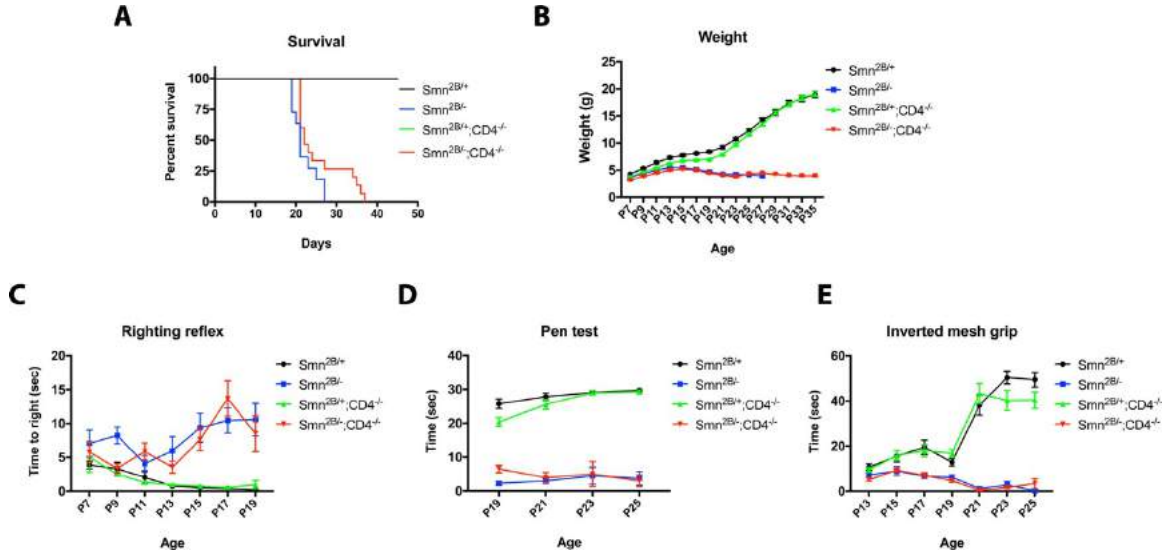

Figure 3.24 Ablation of CD4 T-cells does not impact the *Smn$^{2B/-}$* phenotype. No difference in survival (A), weight (B), righting reflex (C), Pen test (D), or inverted mesh grip (E) could be observed. (N=11-17, with diminishing number of *Smn$^{2B/-}$* mice with time)

Ablation of necroptosis provides some qualitative motor benefit to SMA mice

The defects observed in the spleen and thymus of SMA mice may contribute to neuroinflammation and consequently exacerbate motor neuron death. The receptor interacting protein 1 and 3 kinase (Rip1k, Rip3k) pathway, an important mediator of necroptosis and inflammation, is triggered by TNF-α (273). Interestingly, this pathway appears to play a role in ALS pathology (274). Both genetic knockout and small molecule inhibition of Rip1-Rip3 kinase conferred a protective effect in a mouse model of ALS (274). Furthermore, this pathway has been implicated in various other neurodegenerative disorders (reviewed in (273, 275)). Motor neuron loss has long been recognized as a pathological hallmark of SMA. However, the cell death pathways responsible for this remained unresolved. Most recently, P53 mediated apoptosis is thought to play a role in motor neuron loss in SMA (276-279) but did not confer phenotypical benefits. Given the increased inflammatory profile observed in SMA mice, especially TNF-α, we propose that necroptosis by Rip1k and Rip3k initiates or exacerbates motor neuron death and contributes to SMA pathogenesis.

To do so, Rip3k kinase activity was be disrupted genetically by introducing the caspase 1 and Rip3k double knockout (*Cas1*$^{-/-}$*;Rip3k*$^{-/-}$) onto the *Smn*$^{2B/-}$ mouse background. Homozygous deletion of Rip3k offers a more specific approach to negate necroptosis since Rip1k has additional functions outside of necroptosis. Homozygous deletion of Rip1k is embryonic lethal (280, 281). Production of IL-1β requires caspase 1 activity (282). Thus, homozygous deletion of caspase 1 (*Cas1*$^{-/-}$) offers significant protection against IL-1β mediated inflammation. Hence, the resulting *Smn*$^{2B/-}$*;Cas1*$^{-/-}$

;Rip3k$^{-/-}$ would negate IL-1β mediated inflammation, an initiator of necroptosis, as well as necroptosis pathway through Rip3k ablation. Interestingly, *Smn*$^{2B/-}$*;Cas1*$^{-/-}$*;Rip3k*$^{-/-}$ mice showed an increased survival of 6 days in comparison to *Smn*$^{2B/-}$ mice (27 days VS 21 days, $p > 0.0001$) (Figure 3.25A). No sex difference was observed in the *Smn*$^{2B/-}$*;Cas1*$^{-/-}$*;Rip3k*$^{-/-}$ cohort (male 29 days VS female 27 days). The most interesting finding was the amelioration in mobility of the *Smn*$^{2B/-}$*;Cas1*$^{-/-}$*;Rip3k*$^{-/-}$ mice, a qualitative observation we were unable to quantify with the righting reflex, pen test, or inverted mesh grip (Figure 3.25C-E). A video is provided for a better appreciation of the improvement in mobility of the mice. Altogether, necroptosis likely plays a minor role late in disease pathogenesis.

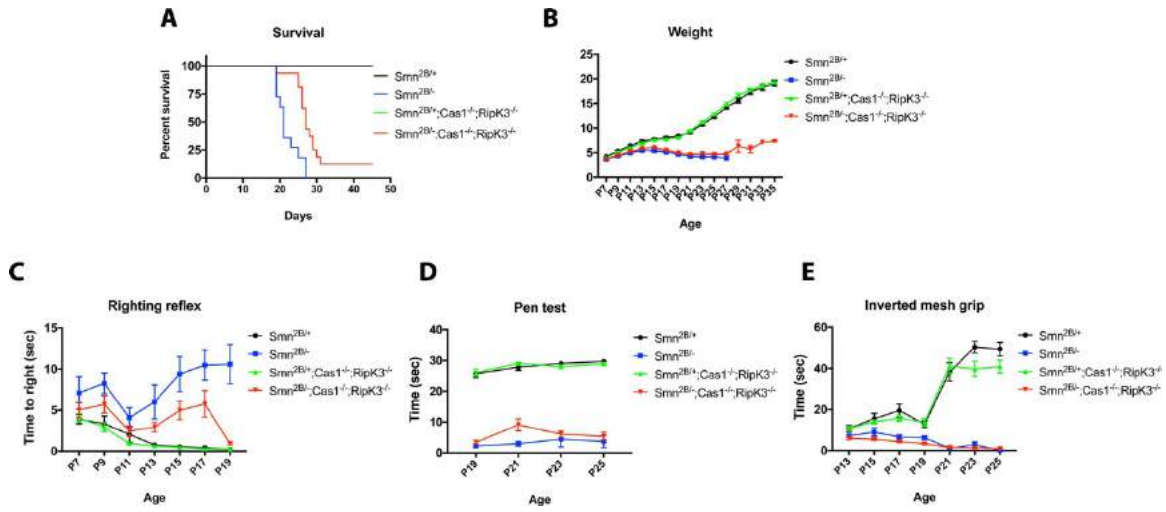

Figure 3.25 Inhibition of necroptosis provide small but significant protection of survival without motor improvement in *Smn$^{2B/-}$;Cas1$^{-/-}$;Rip3k$^{-/-}$* mice. (A) Survival was increased by 6 days in *Smn$^{2B/-}$;Cas1$^{-/-}$;Rip3k$^{-/-}$* mice in comparison to *Smn$^{2B/-}$* mice. Weight of *Smn$^{2B/-}$;Cas1$^{-/-}$;Rip3k$^{-/-}$* mice was comparable to *Smn$^{2B/-}$* mice. No motor improvement could be identified by righting reflex (C), Pen test (D), or inverted mesh grip (E) could be observed. (N=11-18, with diminishing number of *Smn$^{2B/-}$* mice with time)

Appendix methods

Tissue processing and H&E staining

Tissue processing and H&E was performed as previously described in the methods above.

Mouse models generation

The *Smn*$^{2B/-}$*;CD4*$^{-/-}$ mouse model was generated using the breeding scheme as shown in Figure 3.26. *Smn*$^{2B/-}$*;Rag1*$^{-/-}$ were generated in parallel but not experimented upon before the completion of this thesis. *Cd4*^{tm1Mak} were purchased from the Jackson Laboratory. Establishment of the line was established by genotyping as indicated by the Jackson Laboratory protocols (Protocol – Generic Cd4). Mice were kept in stepdown facilities given their potential immune compromise. The *Smn*$^{2B/-}$*;Cas1*$^{-/-}$*;Rip3k*$^{-/-}$ mouse model was generated using the breeding scheme as shown in Figure 3.27. *Cas1*$^{-/-}$*;Rip3k*$^{-/-}$ mouse model were provided by the Sad laboratory at the University of Ottawa. Establishment of the line was confirmed by genotyping. Briefly, Caspase1 alleles was genotyped using the following primers in table 3.2

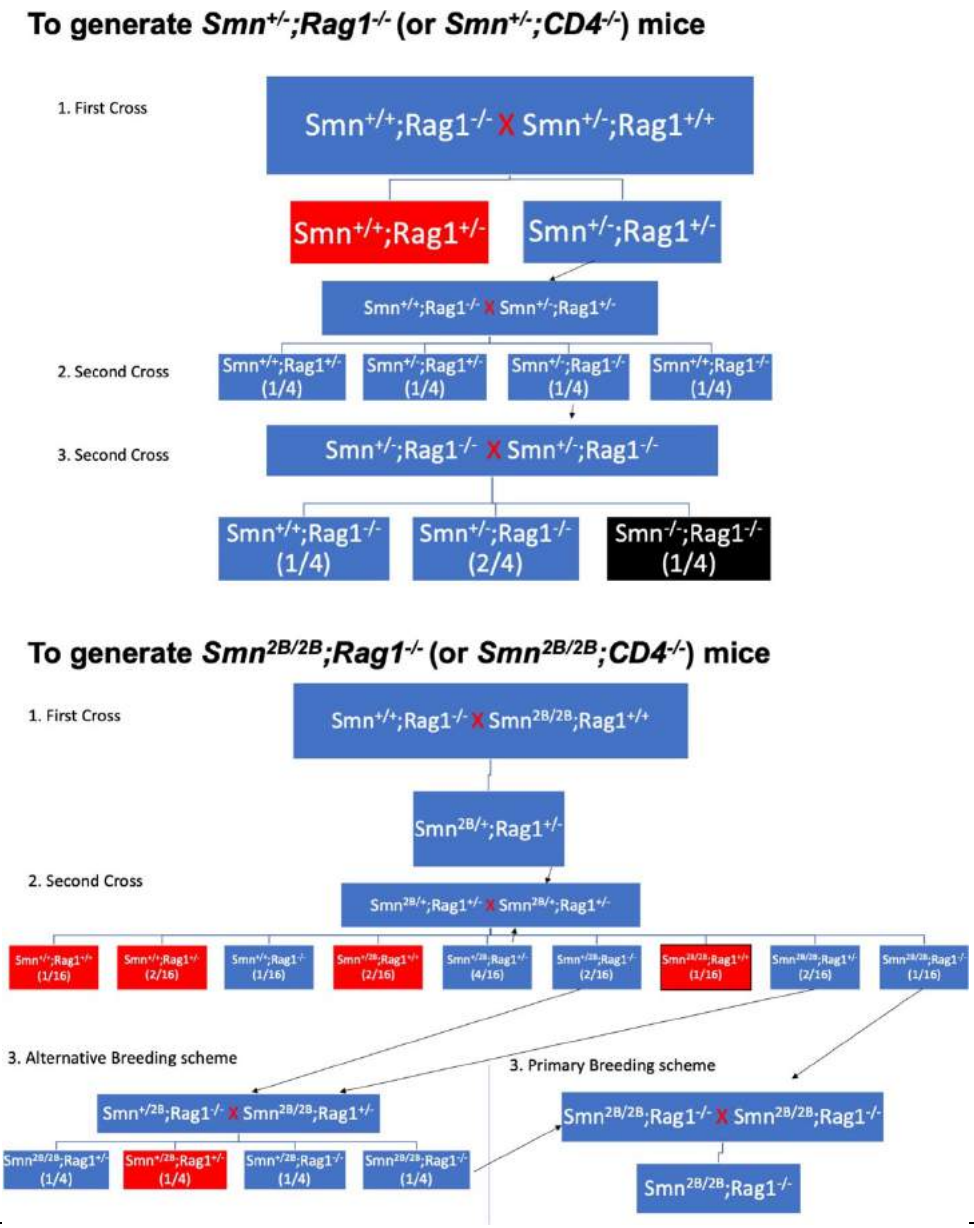

Figure 3.26. Breeding scheme to obtain *Smn$^{2B/-}$;CD4$^{-/-}$* mice. Two separate breeding schemes have been initiated to generate *Smn$^{+/-}$;CD4$^{-/-}$* and *Smn$^{2B/2B}$;CD4$^{-/-}$* mice, respectively from each. These will be crossed to each other to obtain the *Smn$^{2B/-}$;CD4$^{-/-}$* mice for analysis. *Smn$^{2B/-}$;Rag1$^{-/-}$* were also produced but not experiment on in the context of this thesis. Mice in blue boxes will be kept for breeding, in the red boxes will be culled, and in the black boxes are expected to die *in utero.*

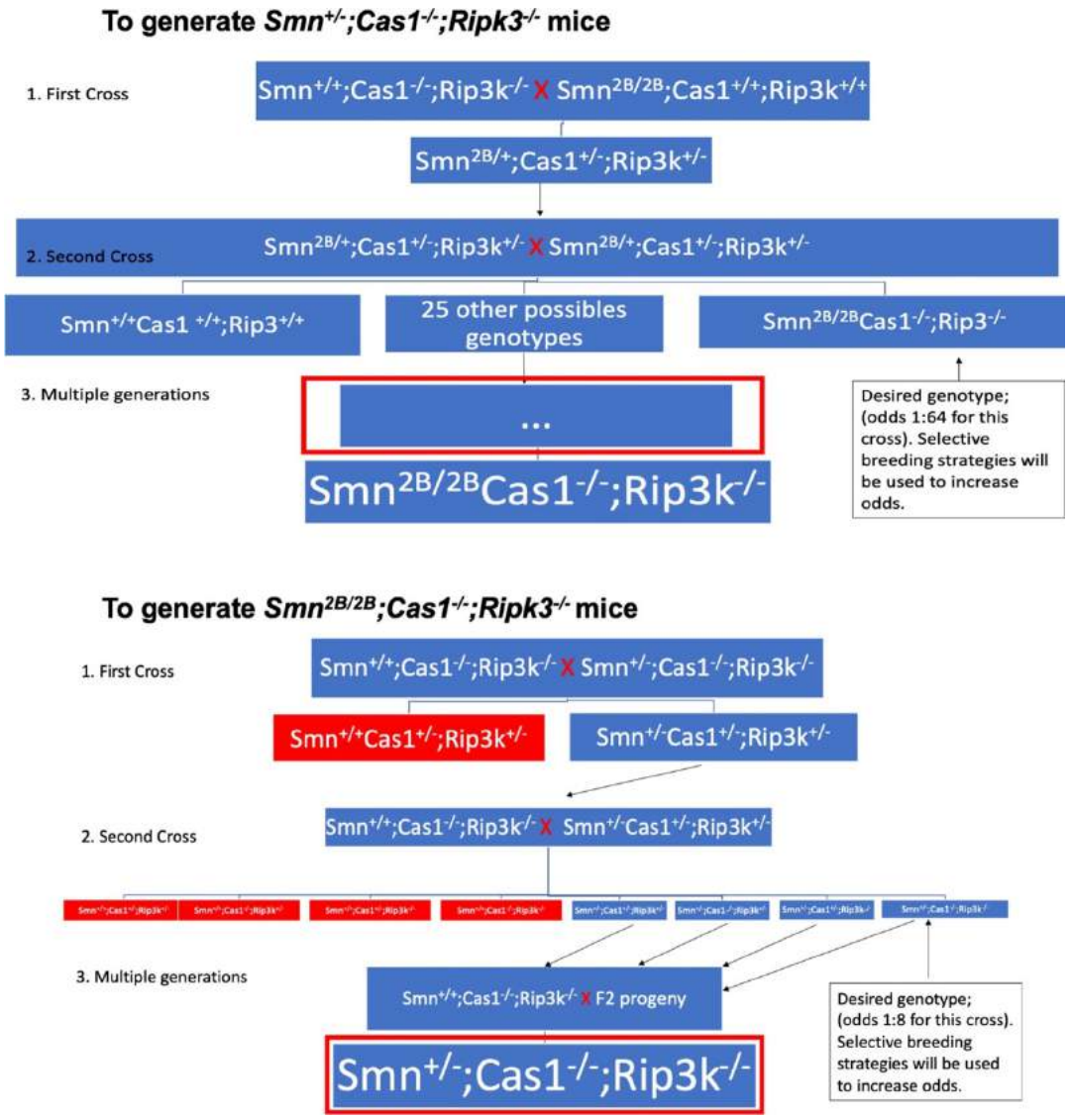

Figure 3.27. Breeding scheme to obtain *Smn$^{2B/-}$;Cas1$^{-/-}$;Rip3k$^{-/-}$* mice. Two separate breeding schemes have been initiated to generate *Smn$^{+/-}$;Cas1$^{-/-}$;Rip3k$^{-/-}$* and *Smn$^{2B/2B}$;Cas1$^{-/-}$;Rip3k$^{-/-}$* mice, respectively from each. These will be crossed to each other to obtain the *Smn$^{2B/-}$;Cas1$^{-/-}$;Rip3k$^{-/-}$* mice for analysis. Mice in blue boxes will be kept for breeding, and in the red boxes will be culled. Box enclosed in a red square indicate our current position in the breeding protocol. As shown, we are very close to *Smn$^{2B/2B}$;Cas1$^{-/-}$;Rip3k$^{-/-}$* mice and already have *Smn$^{+/-}$;Cas1$^{-/-}$;Rip3k$^{-/-}$* mice

Cycling conditions were identical to Cd4 genotyping protocol. This generate WT alleles identified at 500 base pairs (bp) and the KO alleles at 300 bp. The Rip3k allele was genotyped using the primers in Table 3.2. Cycling conditions were as described in table 3.3. This yield the WT allele at 1000 bp and the KO allele at 1200 bp.

Table 3.2 Primers used for the establishment of *Smn$^{2B/-}$;Cas1$^{-/-}$;Rip3k$^{-/-}$* mice.

Primer name	Sequence	Reaction
Cas1 (Wt fwd)	GAGACATATAAGGGAGAAGGG	Reaction A
Cas 1 (Wt rev)	ATGGCACACCACAGATATCGG	Reaction A
Cas 1 (Mutant fwd)	TGCTAAAGCGCATGCTCCAGACTG	Reaction A
Rip3k (Wt fwd)	GGAGCCATTCTCCATGAATC	Reaction B
Rip3k (Wt rev)	AATCGTTCCTGGATGGTGAG	Reaction B
Rip3k (KO fwd)	GATCCTGATCCTGACCCTGA	Reaction C
Rip3k (KO rev)	ATCGACAAGACCGGCTTCCATCCGA	Reaction C

Table 3.3 Cycling conditions for Rip3k genotyping

	T (ºC)	Duration (hh:mm:ss)
1	98	**00:05:00**
2	98	**00:00:05**
3	65	**00:00:05**
4	72	**00:00:25**
5	**Go to 2 – Repeat x34**	
6	72	**00:01:00**
7	4	**Hold**

Behavioural testing

All behavioural testing was performed by one single examiner with assistance of a second examiner for time recording. Each mouse was tattooed between P3-P5 to allow longitudinal examination of motor function. Blinding was not possible given the obvious emergence of the SMA phenotype. Tests were administered in the following order: (1) Righting reflex (2) Pen test (3) Inverted mesh/wire grip. All tests were performed on the same day and testing occurred every two days. Each test was repeated 3 times to ensure reliable measures. Group of 3 mice were taken at the time, allowing for a period of rest between before having the test repeated. Righting reflex followed a similar protocol as previously described in Treat-NMD neuromuscular network (SOP MD_M.2.2.002). The pen test followed a similar protocol as previously described in Treat-NMD neuromuscular network (SOP SMA_M.2.1.001). A maximum of 30 seconds on the pen was defined as a perfect score. The inverted mesh/wire followed a slightly modified protocol than previously described in Treat-NMD neuromuscular network (SOP SMA_M.2.1.002). Briefly, a mesh grip (hole of 1 mm^2) is used from P13 to P19. At P21, the mesh grip is changed to a wire cage top to provide more space for the growing mice to hold on to. Termination of this test was set at 60 seconds.

Ultrasonography

Mice were shaved and Nair was used to ensure complete hair removal, allowing for adequate ultrasonography quality. Mice were then anesthetized using 1-2% continuous isoflurane and placed on warming movable station where each limb were taped to the station to allow heart rate monitoring. For P9 mice, the isoflurane pipe was extended and

taped to the head of the mouse to ensure proper anesthetic delivery given their small size. Ultrasonography was performed using a MS400 or MS550 transducer and the VEVO 2100 (FujiFilm VisualSonics, Toronto, Canada). The spleen was identified under B-mode. Doppler was used to identify splenic artery. Peak flow velocity was sampled as recommended by FujiFilm VisualSonics consultant. In difficult identification of splenic anatomy and vascularity, mice were repositioned in a right lateral decubitus. At least 3 measures of systolic peak flow velocity were measured and averaged over three consecutive measurements. Heart rate measurement was obtained through the distance between each systolic velocity peak.

Chapter 4: Abnormal fatty acid metabolism is a core component of spinal muscular atrophy

Title: Abnormal fatty acid metabolism is a core component of spinal muscular atrophy

One Sentence Summary: Altered fatty acid metabolism in spinal muscular atrophy

Authors: Marc-Olivier Deguise[1,2,3], Ariane Beauvais[1], Giovanni Baranello[4], Chantal Pileggi[5], Chiara Mastella[6], Alexandra Tierney[1], Lucia Chehade[1,2,3], Alessandro Leone[7], Ramona De Amicis[7], Alberto Battezzati[7], Yves De Repentigny[1], Jean Michaud[8], Christopher Dunham[9], Jodi Warman Chardon[2,3,10,11,12], Hugh J McMillan[13], Maica Llavero-Hurtado[14,15], Douglas Lamont[16], Abdelmadjid Atrih[16], Yu-Ting Huang[14,17], Natalie L. Courtney[14,17,18], Alannah J. Mole[14,17,18], Sabrina Kubinski[19], Peter Claus[19], Lyndsay M. Murray[14,17,18], Thomas M. Wishart[14,15], Melissa Bowerman[20] Thomas H. Gillingwater[14,17], Mary-Ellen Harper[5], Simona Bertoli[7], Simon H. Parson[14,21] and Rashmi Kothary[1,2,3,12,*]

Affiliations:

[1]Regenerative Medicine Program, Ottawa Hospital Research Institute, Ottawa, Ontario, Canada

[2]Department of Cellular and Molecular Medicine, University of Ottawa, Ottawa, Ontario, Canada

[3]Centre for Neuromuscular Disease, University of Ottawa, Ottawa, Ontario, Canada K1H 8M5

[4]UO Neurologia dello Sviluppo, Fondazione IRCCS Istituto Neurologico Carlo Besta, Milan, Italy, and The Dubowitz Neuromuscular Centre, University College London Great Ormond Street Institute of Child Health & Great Ormond Street Hospital, London, UK

[5]Department of Biochemistry, Microbiology and Immunology, Ottawa Institute of Systems Biology, University of Ottawa, Ottawa, Ontario, Canada

[6]SAPRE-UONPIA, Fondazione IRCCS Cà' Granda Ospedale Maggiore Policlinico, Milan, Italy

[7]International Center for the Assessment of Nutritional Status (ICANS), Department of Food, Environmental and Nutritional Sciences (DeFENS), University of Milan, Milan, Italy

[8]Dept. of Pathology, Faculty of Medicine, University of Ottawa, On, Canada

[9]Division of Anatomic Pathology, Children's and Women's Health Centre of B.C., British Columbia, Canada

[10]Neuroscience Program, Ottawa Hospital Research Institute, Ottawa, Ontario, Canada

[11]Department of Pediatrics, Children's Hospital of Eastern Ontario, Ottawa, Ontario, Canada

[12]Department of Medicine, University of Ottawa, Ottawa, Ontario, Canada

[13]Children's Hospital of Eastern Ontario Research Institute, University of Ottawa, Ottawa, Ontario, Canada

[14]Euan MacDonald Centre for Motor Neurone Disease Research, University of Edinburgh, Edinburgh, UK

[15]The Roslin Institute, Royal (Dick) School of Veterinary Studies, College of Medicine and Veterinary Medicine, University of Edinburgh, Edinburgh, UK

[16]FingerPrints Proteomics Facility, University of Dundee, Dundee, UK

[17]College of Medicine & Veterinary Medicine, University of Edinburgh, Edinburgh, UK

[18]Centre for Discovery Brain Science, University of Edinburgh, Edinburgh, UK

[19]Institute of Neuroanatomy and Cell Biology, Hannover Medical School, Hannover, Germany and; Center of Systems Neuroscience, Hannover, Germany

[20]School of Medicine, Keele University, Staffordshire, UK and; Institute for Science and Technology in Medicine, Stoke-on-Trent, UK and; Wolfson Centre for Inherited Neuromuscular Disease, RJAH Orthopaedic Hospital, Oswestry, UK

[21]Institute of Medical Sciences, University of Aberdeen, Aberdeen, UK

[*]Correspondence to: Rashmi Kothary, Ottawa Hospital Research Institute, 501 Smyth Road, Ottawa, Ontario, Canada K1H 8L6, Tel: (613) 737-8707, Fax: (613) 737-8803, Email: rkothary@ohri.ca

This chapter was subsequently separated in three manuscripts near completion of the thesis:

1. Marc-Olivier Deguise & *al.* (2019) Abnormal fatty acid metabolism is a core component of spinal muscular atrophy. *Ann Clin Transl Neurol (IF: 4.656)*. DOI : 10.1002/acn3.50855
2. Marc-Olivier Deguise & *al.* (2019) Low fat diets increase survival of a mouse model of spinal muscular atrophy. *Ann Clin Transl Neurol (IF: 4.656)*. DOI : 10.1002/acn3.50920
3. Marc-Olivier Deguise & *al.* (20XX) Spinal muscular atrophy: providing a novel framework to elucidate NAFLD molecular pathogenesis (Not yet submitted).

Author contribution

MOD designed study, performed experiments, main contributor for Figure 4.1 (except E-G), Figure 4.2, Figure 4.3 (except B), Figure 4.4 (except C,D,), 4.5, 4.6, 4.7 (except D-G, J-K, N-O), Figure 4.8, Figure 4.9 (except for I-K), 4.11, 4.12, 4.15 (except D-G), 4.16, 4.18, 4.20. Analyzed data and created all figures and tables. Wrote the manuscript. AB performed and provided support for experiments. GB recruited patients and performed neurological evaluation within Table 4.1 and Table 4.2. Provided a critical review of manuscript. CP provided technical support for mitochondrial experimentation and analysis in Figure 4.15-4.16. CM enrolled patients (Table 4.1 – 4.2). AT performed and provided support for experiments in Figure 4.11, Figure 4.15A, Figure 4.17 and 4.18, and contributed to manuscript preparation. LC performed and provided support for experiments in Figure 4.11, Figure 4.15C and T, and Figure 4.18, and contributed to manuscript preparation. RDA, AL, Alberto B collected patient nutritional data, performed data analysis and contributed to data interpretation (Table 4.1 – 4.2). YDR Performed and provided support for experiments. JM, CD retrieval of pathological specimens and analysis summarized in Table 4.4. JWC, HJM provided patients' biochemical data in Table 4.1-4.3. Provided a critical review of manuscript. MLH, DL, AA analyzed proteomic data. YTH provided liver samples from Taiwanese mouse model of SMA. NLC, AJM dissection of tissues for Figure 4.1E-F; Figure 4.7 and Figure 4.13. SK performed experiments for Figure 4.4. PC supervisor of Sabrina Kubinski. Read and edited the manuscript. LMM Provision of tissues for Figure 4.1E-F; Figure 4.7 and Figure 4.13. provided a critical review of manuscript. TMW Designed and analyzed data for the proteomic study. MB performed experiments for Figure 4.4, provided tissues 4.10. Provided supervision for Sabrina

Kubinski. Provided intellectual input into the project and a critical review of manuscript. THG designed and analyzed data from the proteomic study. Provided a critical review of manuscript. MEH designed experiments in Figure 4.15-4.16. SB collected patient nutritional data and provided biochemical analysis in Table 4.1-4.2. Provided a critical review of manuscript. SHP designed study, provided data for figure 4.1E-G, 4.7D-G, J-K, N, O, Fig 4.13-14 and associated method as well as a critical review of manuscript. RK designed study and prepared manuscript.

Abstract

Spinal muscular atrophy (SMA) is an inherited neuromuscular disorder leading to paralysis and subsequent death. It is caused by mutation or deletion of the *survival motor neuron 1* (*SMN1*) gene. SMA has traditionally been considered a motor neuron disease. However, recent studies have identified important extra-neuronal defects affecting a variety of organs. Here, we identify an increased susceptibility to developing dyslipidemia in a cohort of 72 SMA pediatric patients, together with an increased incidence of liver steatosis in pathological samples from SMA patients. Moreover, fatty acid metabolic abnormalities were a common feature across several mouse models, resulting in a non-alcoholic fatty liver disease (NAFLD) phenotype. Specifically, we observed elevated hepatic triglyceride storage associated with dyslipidemia in the $Smn^{2B/-}$ SMA mouse model, where significant liver damage leads to hepatocyte death without fibrosis. Liver function was impaired in $Smn^{2B/-}$ mice, leading to low protein output, and alterations in complement, coagulation, iron homeostasis, and IGF-1 metabolism. The NAFLD phenotype resulted from low muscle use caused by denervation and fatty substrate overload subsequent to hyperglucagonemia. Hepatic mitochondrial function was enhanced by a compensatory mechanism, rather than defective, as shown by increased β-oxidation and reactive oxygen species production. Diet modulation was sufficient to increase survival in SMA mice but did not alter hepatic triglyceride content, damage or function. This work highlights metabolic abnormalities as a key feature of SMA, suggesting close monitoring is required in human patients, as such defects are likely to increase metabolic distress and cardiovascular risk. This is particularly pertinent for longer-lived SMA patients, such as those receiving clinically approved CNS-restricted therapies (e.g. Spinraza), thereby

highlighting the importance of nutritional care management in patients. In the current era of therapeutic development in SMA, this study emphasizes the contribution of non-neuronal organs and the need for a systemic therapeutic approach to ensure maximal benefits for all SMA patients throughout their life.

Introduction

Spinal muscular atrophy (SMA) is an autosomal recessive disorder characterized primarily by motor neuron death, subsequently leading to loss of voluntary movement and skeletal muscle atrophy. The incidence of SMA is around 1 in 11,000 live births, and most patients rapidly succumb to their symptoms (2, 164, 283). More than half of patients with SMA have a severe, infant-onset form of the disease with a median life expectancy of 12 months without supportive treatment (283). SMA is caused by a mutation or deletion in the ubiquitously expressed *Survival motor neuron 1* (*SMN1*) gene, which produces a protein (SMN) involved in a number of key cellular pathways, including RNA metabolism and splicing (1, 17, 19, 22, 284).

SMA has traditionally been considered a motor neuron disease, however, this view has evolved over recent years as multiple groups have identified defects in multiple non-neuronal cell types (83, 108, 110, 122-124, 128, 138, 142, 147, 148, 150, 169, 208, 210, 211, 214, 254, 255, 258, 259, 285, 286). Taken together with motor neuron defects, these extra-neuronal components likely contribute to the clinical picture of SMA, especially in its most severe forms (reviewed in (110, 206)), and may be particularly relevant for SMA patients where restoration of SMN protein, largely in the nervous system, has been achieved through therapeutic intervention (e.g. Spinraza; (287)).

Metabolic defects in SMA have been reported previously. Pancreatic defects were observed in mouse models of SMA and in SMA patients (210, 211, 288). These alterations appear to be the cause of abnormal glucose homeostasis (211, 288). More recent work has

revealed defects in amino acid metabolism in SMA (289), and diurnal levels of branched-chain amino acids were depleted in the serum of Taiwanese SMA mice, likely linked to KLF15 activation in skeletal muscle (289). Lipid metabolism and fatty acid oxidation defects have also been reported in early studies of patients with SMA (49, 50), where increased esterified carnitine, and reduced β-oxidation capacity are seen (49). Further studies in a larger cohort identified an abnormal plasma ratio of dodecanoic (C12) to tetradecanoic (C14) acid in severe SMA patients, which was not present in a denervated control patient group (50), while upon fasting, some patients develop dicarboxylic aciduria (50). There are also reports of microvesicular steatosis in patients with SMA (49, 51, 127). There is then an urgent need for further investigation of fatty acid metabolism impairment in SMA, and whether intrinsic changes in the liver are responsible for these abnormalities.

The liver is a multifunctional organ involved in many important physiological processes. It is the metabolic factory of the body, which regulates glucose, lipid, and amino acid homeostasis (290). It is responsible for the production of 85-90% of circulating proteins, which act in a wide variety of pathways, including complement, hemostasis, iron regulation, drug metabolism (291) and hormonal cycles (290). Historically there has been only cursory examination of liver function in SMA. Embryonic lethality and iron overload are the main features of liver restricted *Smn* conditional knockout in mice (292). More recently, increased erythropoiesis, megakaryocyte and platelet production, together with mild iron storage abnormalities, were identified in the severe "Taiwanese" mouse model of SMA (128).

Here, we show that SMA patients are more susceptible to dyslipidemia in comparison to the normal population, with a subset of patients harboring significant fatty acid metabolic impairment. Lipid metabolism defects were present in the liver of four mouse models of SMA (Table 1.1 for mouse model characteristics). In a comprehensive analysis of the *Smn*$^{2B/-}$ model, which shows the longest lifespan, we show that the mice develop non-alcoholic fatty liver disease, and more specifically steatohepatitis, without fibrosis. Ultimately, this leads to significant functional impairment in key molecular pathways, including: general protein production, complement protein production, coagulation protein expression, insulin-like growth factor 1 (IGF-1) pathway regulation and iron homeostasis. The emergence of the NAFLD phenotype is likely multifactorial, involving the pancreas-liver axis, intrinsic hepatocyte defects and reduced muscle use because of denervation. Low fat diets were sufficient to enhance survival in mice, without any change in hepatic triglyceride content. Altogether, this work highlights the critical need for investigation of lipid metabolism and the liver in SMA, where extra-neuronal symptoms are currently not addressed by the CNS-restricted treatment with the FDA-approved treatment Spinraza.

Results

SMA patients are at an increased risk of dyslipidemia and fatty liver

We performed lipid profiling on 72 pediatric SMA patients (14 Type I, 52 Type II, 6 Type III). Demographics of the cohort can be found in Table 4.1. We focused on total cholesterol (TC), low density lipoprotein (LDL), high density lipoprotein (HDL), non-HDL and triglycerides (TG) to assess potential abnormalities in fatty acid metabolism in a minimally invasive manner. Interestingly, we found that just over a third (37.5%) of SMA patients, most commonly type I and II, had at least one positive readout out of the five indicative tests for laboratory-defined dyslipidemia (Table 4.2), in comparison to less than a quarter (20-24%) of the general population in published data sets (293). Furthermore, close to 20% and 13% of SMA patients had more than 2 or 3 positive readouts out of the 5 tests of laboratory-defined dyslipidemia, respectively (Table 4.2). Most notably, the prevalence of abnormally increased LDL measurement was doubled in comparison to the general pediatric population (293-295). If we lowered the cut-off to also include the patients with borderline values, up to 61% of SMA patients would have at least one indicative lipid result, and 40% would have 3 or more (Table 4.2). Lipid profiles in the 6 adult SMA patients (Type II/III) were more complex to analyze given the small number of patients and common onset of dyslipidemia with age in the normal population (Table 4.3).

Table 4.1. Pediatric and adult cohort demographic

Pediatric cohort	Nb	Percentage	Median age	Last meal time
Male	39	54,17	3,7	5
Female	33	45,83	4	5
Type I	14	19,44	3,1	5
Male	5	6,94	2	5
Female	9	12,5	3,2	5
Type II	52	72,22	3,8	5
Male	31	43,05	3,7	5
Female	21	29,17	4,2	5
Type III	6	8,33	6,4	5
Male	3	4,17	6,2	5
Female	3	4,17	6,6	5
Adult cohort (Type II/III)	**Nb**	**Percentage**	**Median age**	**Last meal time**
Male	3	50	47	2
Female	3	50	35	5

Table 4.2. SMA patients are more susceptible to dyslipidemia than the normal population

	Criteria	*All SMA patients*	*Type I*	*Type II*	*Type III*	*Normal population**
Abnormal	*TC > 200 mg/dl*	10/72 (13.89%)	1/14 (7.14%)	9/52 (17.31%)	0/6 (0%)	7.7-10.7% (293-295)
	LDL > 130 mg/dl	9/72 (12.5%)	1/14 (7.14%)	7/52 (13.46%)	1/6 (16.67%)	3.2-7.2% (293-295)
	HDL < 40 mg/dl	12/72 (16.67%)	1/14 (7.14%)	10/52 (19.23%)	1/6 (16.67%)	4.1-19.3% (293, 295-297)
	TG > 100 mg/dl[∂]	15/72 (20.83%)	5/14 (35.71%)	7/52 (13.46%)	3/6 (50%)	13.2-22.1% (293, 295, 297)
	Non HDL-cholesterol > 145 mg/dl	10/72 (13.89%)	1/14 (7.14%)	8/52 (15.38%)	1/6 (16.67%)	8.4% (296)
	1/5 abnormal dyslipidemia reading	27/72 (37.5%)	6/14 (42.85%)	18/52 (34.62%)	3/6 (50%)	20.2-22.9% (293, 296)
	2/5 < abnormal dyslipidemia reading	14/72 (19.44%)	2/14 (14.29%)	11/52 (21.15%)	1/6 (16.67%)	5.37%[&] (293)
	3/5 < abnormal dyslipidemia reading	10/72 (13.89%)	1/14 (7.14%)	8/52 (15.38%)	1/6 (16.67%)	-
	HbA1C < 5	30/53 (56.60%)	5/8 (62.5%)	23/41 (56.09%)	2/4 (50%)	
Borderline	*TC > 170 mg/dl*	30/72 (41.67%)	5/14 (35.71%)	23/52 (44.23%)	2/6 (33.33%)	-
	LDL > 110mg/dl	21/72 (29.17%)	2/14 (14.29%)	18/52 (34.62%)	1/6 (16.67%)	-
	HDL < 45 mg/dl	20/72 (27.78%)	5/14 (35.71%)	13/52 (25%)	2/6 (33.33%)	-
	TG > 75 mg/dl[#]	23/72 (31.94%)	7/14 (50%)	13/52 (25%)	3/6 (50%)	-
	Non HDL-cholesterol > 120 mg/dl	32/72 (44.44%)	6/14 (42.86%)	23/52 (44.23%)	3/6 (50%)	-
	1/5 < borderline dyslipidemia reading	44/72 (61.1%)	11/14 (78.57%)	30/52 (57.69%)	3/6 (50%)	-
	2/5 < borderline dyslipidemia reading	35/72 (48.61%)	6/14 (42.86%)	26/52 (50%)	3/6 (50%)	-
	3/5 < borderline dyslipidemia reading	29/72 (40.28%)	6/14 (42.86%)	20/52 (38.46%)	3/6 (50%)	-

* Note that these values were taken from multiple studies and criteria may have varied and not be identical to the present study.

[&]Calculated from results in the particular study – see reference.

[∂]High is defined as >100 for 0-9 years and >130 for 10-19 years of age

[#] Borderline is defined as >75 for 0-9 years and >90 for 10-19 years of age

Table 4.3. Adult SMA patient lipid profiles

	Criteria	*All SMA patients*
Abnormal	*TC > 240 mg/dl*	0/6 (0%)
	LDL > 160 mg/dl	0/6 (0%)
	HDL < 40 mg/dl	3/6 (50%)
	TG > 200 mg/dl	2/6 (33.33%)
	Non HDL-cholesterol > 190 mg/dl	0/6 (0%)
	1/5 < abnormal reading	4/6 (66.66%)
	2/5 < abnormal reading	1/6 (16.67%)
	3/5 < abnormal reading	0/6 (0%)
	HbA1C < 5	1/6 (16.66%)

We have performed a pathological assessment of the liver in SMA children to see whether SMA patients were more likely to have liver steatosis given the significant chance of developing dyslipidemia in our pediatric cohort. Notably, 3/8 (37.5%) of SMA liver necropsies revealed steatosis, reminiscent of the proportion of SMA patients showing dyslipidemia (37.5% as well) (Table 4.4). This is in marked contrast to reported prevalence figures of NALFD in the pediatric population 2-19 years of age, estimated to be between 2% and 13% (298, 299). If we limit the age range to 2-4 years, which is more in line with our SMA necropsy cohort, then liver steatosis incidence is only 0.7% in the normal pediatric population as reported in the current literature (298).

We next assessed whether any associated glucose mishandling defects may be present, as we had previously identified pancreatic defects (210, 211). We chose to use HbA_{1C} which represents glycated hemoglobin, and provides a measure of the mean glucose level over the previous 3 months (300). We obtained HbA_{1C} data for 53 of the 72 patients in our cohort. Interestingly, HbA_{1C} trended lower in most SMA patients, with 30 out of 53 having an abnormally low readout (HbA_{1C} < 5%, normal 5%-6.5%). In fact, most SMA patients had an HbA_{1C} around 5 as the calculated median was 4.94% and calculated mean 4.93% in our cohort (Table 4.2). Overall, a large subset of SMA patients show clinical test results consistent with considerable metabolic abnormalities.

Table 4.4. Presence of steatosis in SMA liver necropsies

Case	Sex	Age	Type	Cause Death	Steatosis*
1	F	14 mo	I	Bronchopneumonia	-/**
2	F	7 mo	I	Bronchopneumonia	-
3	M	8 mo	I	Aspiration pneumonia	+++
4	M	< 1 mo	I	Aspiration pneumonia	-
5	F	9 mo	I	Respiratory insufficiency	+/++
6	F	14 mo	I	Bronchopneumonia	-
7	M	12 mo	I	Respiratory insufficiency + HIE + Chronic pneumonitis	+/++
8	F	13 y	II	Undetermined	-

Abnormal fatty acid metabolism in SMA mouse models

To investigate whether fatty acid metabolism defects identified above may be related to SMN depletion, we performed pathological, histological and biochemical assessment of livers of the *Smn*$^{2B/-}$ mouse model of severe SMA mice at pre-symptomatic age (postnatal day 4 (P4)) and at symptomatic age (P17-19). The livers from P17-19 *Smn*$^{2B/-}$ mice were paler and displayed microvesicular steatosis (Fig 4.1A-B, E-G). Fatty acid profiling showed that the level of triglycerides, the main storage form of fatty acids, was 25-fold higher in livers of P19 *Smn*$^{2B/-}$ mice compared to controls (Fig 4.1H). Lipids are formed of a polar head and hydrophobic side chains, the latter coming in varying lengths and conformations, which modulate lipid function (301, 302). Significant chain length alterations, especially of long chain fatty acids, were noted in P19 *Smn*$^{2B/-}$ mice compared to controls (Fig 4.1I-J). Lipid levels (Fig 4.1K-P) and profiles (Fig 4.2F-J) for every lipid class (phospholipid, free fatty acids, diglycerides, cholesteryl esters, unesterified cholesterol, and total cholesterol) in livers of P19 *Smn*$^{2B/-}$ mice showed alterations, indicating a global misregulation in fatty acid metabolism. By comparison, histology (Fig 4.1C-D), lipid levels (Fig 4.1K-P) and profiles (Fig 4.2A-E) were unchanged in P4 *Smn*$^{2B/-}$ livers.

A similar analysis was performed in 3 additional mouse models of SMA (Table 1.1) to determine if this was a widespread phenomenon associated with depletion of SMN protein. Fat accumulation was confirmed by lipid quantification in livers from symptomatic P9 *SmnΔ7* mice (*Smn*$^{-/-}$;*SMN2*$^{+/+}$;*SmnΔ7*$^{+/+}$) (Fig 4.3). Conversely, more severe mouse models of SMA, such as the "Taiwanese" mice and the *Smn*$^{-/-}$;*SMN2* mice, showed reduced

lipid accumulation in the liver compared to control littermates (Fig 4.3A-B). The absence of lipid accumulation in mouse models of very severe SMA phenotypes is likely due to the reduced life span of these animals preventing the opportunity for these pathologies to develop (Fig 4.3D and Table 1.1). Indeed, a fatty acid pathway-focused polymerase chain reaction (PCR) array in liver of symptomatic *Smn*$^{2B/-}$ and "Taiwanese" mice, revealed several overlapping alterations (Fig 4.4). Significantly, lipid metabolism defects are present across multiple mouse models of SMA. The severity and stage of disease progression influence the extent of lipid accumulation in the liver and the pathological presentation.

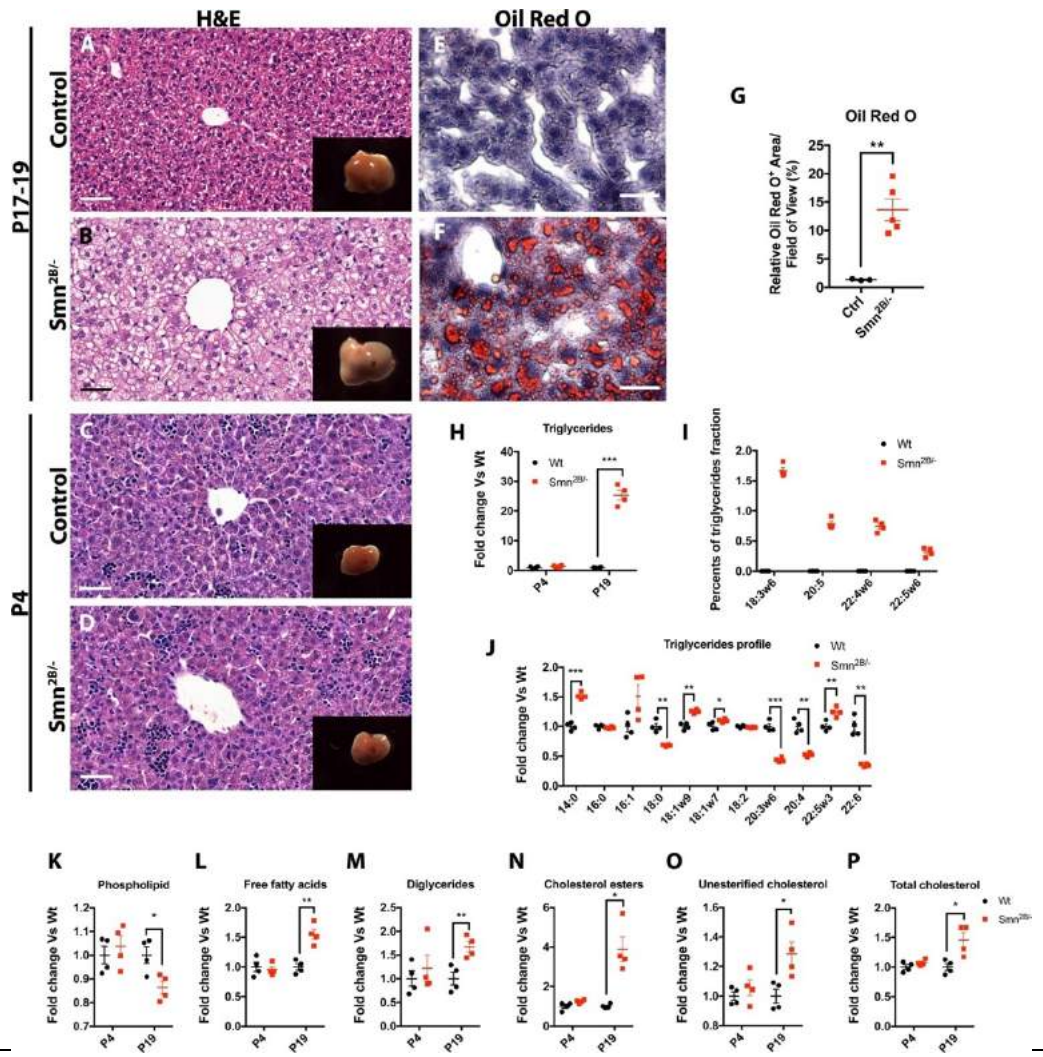

Figure 4.1. *Smn*$^{2B/-}$ mice have fat accumulation in the liver. Gross morphology (0.75X) and histology (H&E - 40X, Oil Red O - 400X) of *Smn*$^{2B/-}$ livers showing fatty inclusions at P17-19 (A-B,E-G) but not P4 (C-D). Lipid profiling identified elevation of triglycerides at P19 in *Smn*$^{2B/-}$ livers (H), with altered chain length (I-J). Other lipid classes, such as phospholipid, free fatty acids, diglycerides, cholesterol esters, unesterified cholesterol and total cholesterol, were also misregulated in P19 *Smn*$^{2B/-}$ livers (K-P). P4 lipid levels were unchanged from control (H, K-P). Scale bar: (A-D) 50 µm, (E-F) 10 µm. (N value for each experiment is as follows: N = 5-6 for A-D, 3-5 for E-G, 4 for H-P, $P \leq 0.05$ for *, $P \leq 0.01$ for **, $P \leq 0.001$ for *** and $P \leq 0.0001$ for ****).

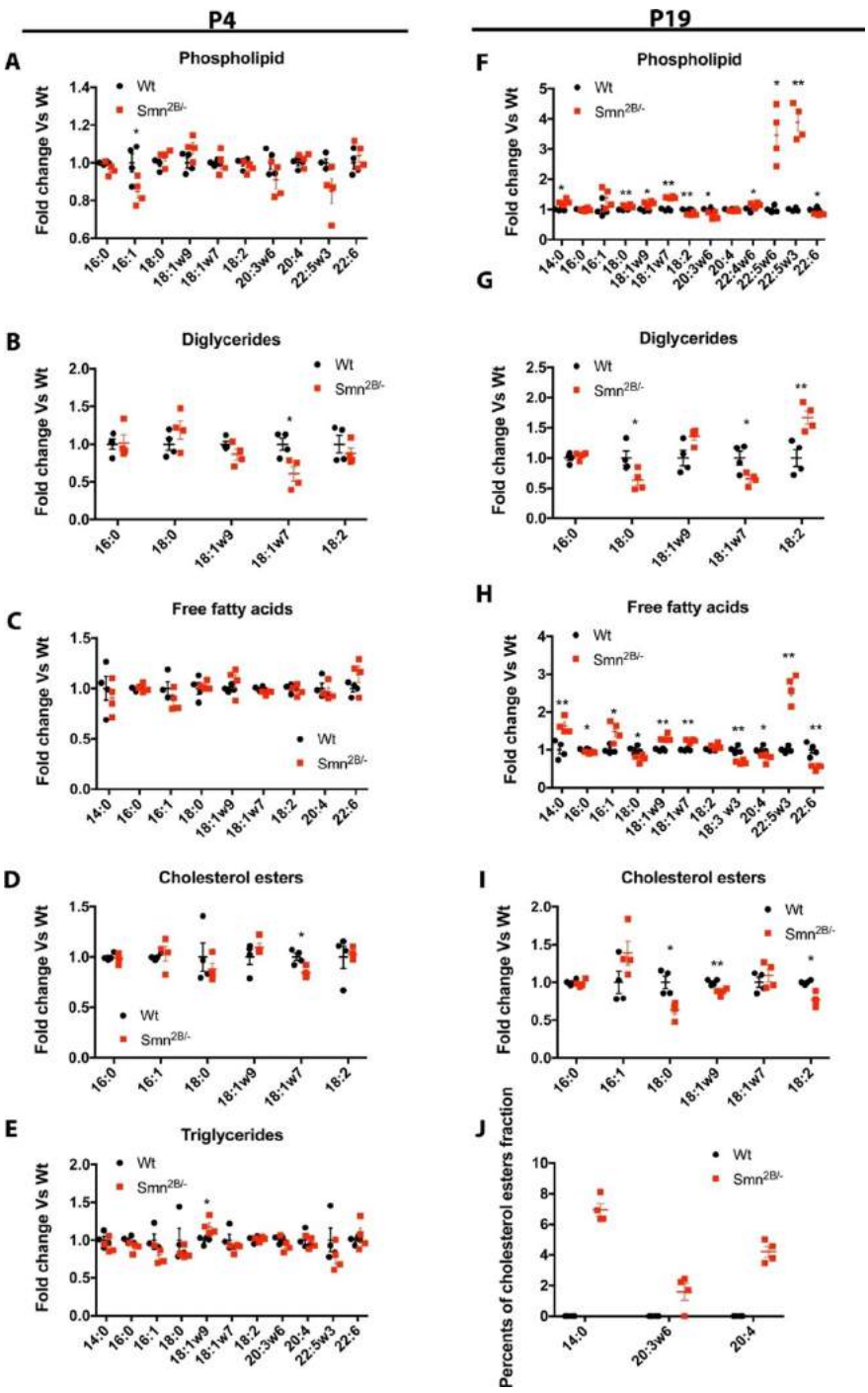

Figure 4.2. Abnormal lipid chain length profiles of various lipid fractions in livers from P19 *Smn$^{2B/-}$* mice. Chain length profile of phospholipids (A), diglycerides (B), free fatty acids (C), cholesterol esters (D), and triglycerides (E) showed no real change in P4 *Smn$^{2B/-}$* livers. Chain length profile of phospholipids (F), diglycerides (G), free fatty acids (H), and cholesterol esters (I) all showed significant alterations in P19 *Smn$^{2B/-}$* livers. (J) Some cholesterol esters were over-represented in P19 *Smn$^{2B/-}$* livers. Only chain length where all samples levels could be measured are represented within the graphs. (N=4, $P \leq 0.05$ for *, $P \leq 0.01$ for **).

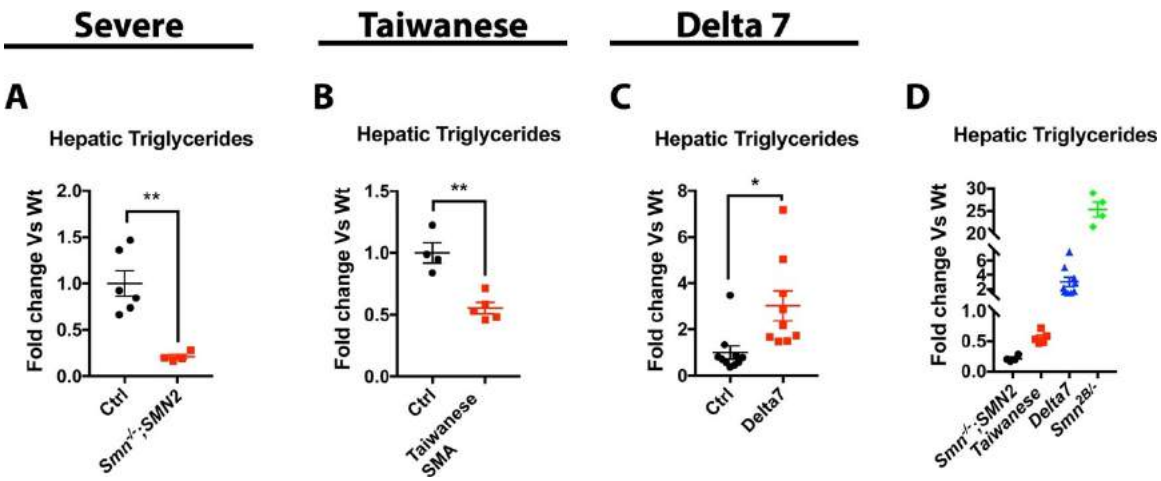

Figure 4.3. Hepatic triglyceride misregulation is a common feature in different SMA models at symptomatic age but dependent on severity. Quantification of hepatic triglycerides showed a 5 fold reduction in P5 *Smn*$^{-/-}$*;SMN2* mice (A), a 2 fold reduction in P9 Taiwanese mice (B), and a 3 fold increase in P10 *SmnΔ7* mice (C) in comparison to control littermates. Analysis of hepatic triglyceride levels for each SMA mouse model in A-C involved a comparison to their own control (N value for each experiment is as follows: N = 4-6 for A-B, 9-10 for C, 4-9 for D, $P \leq 0.05$ for *, $P \leq 0.01$ for **).

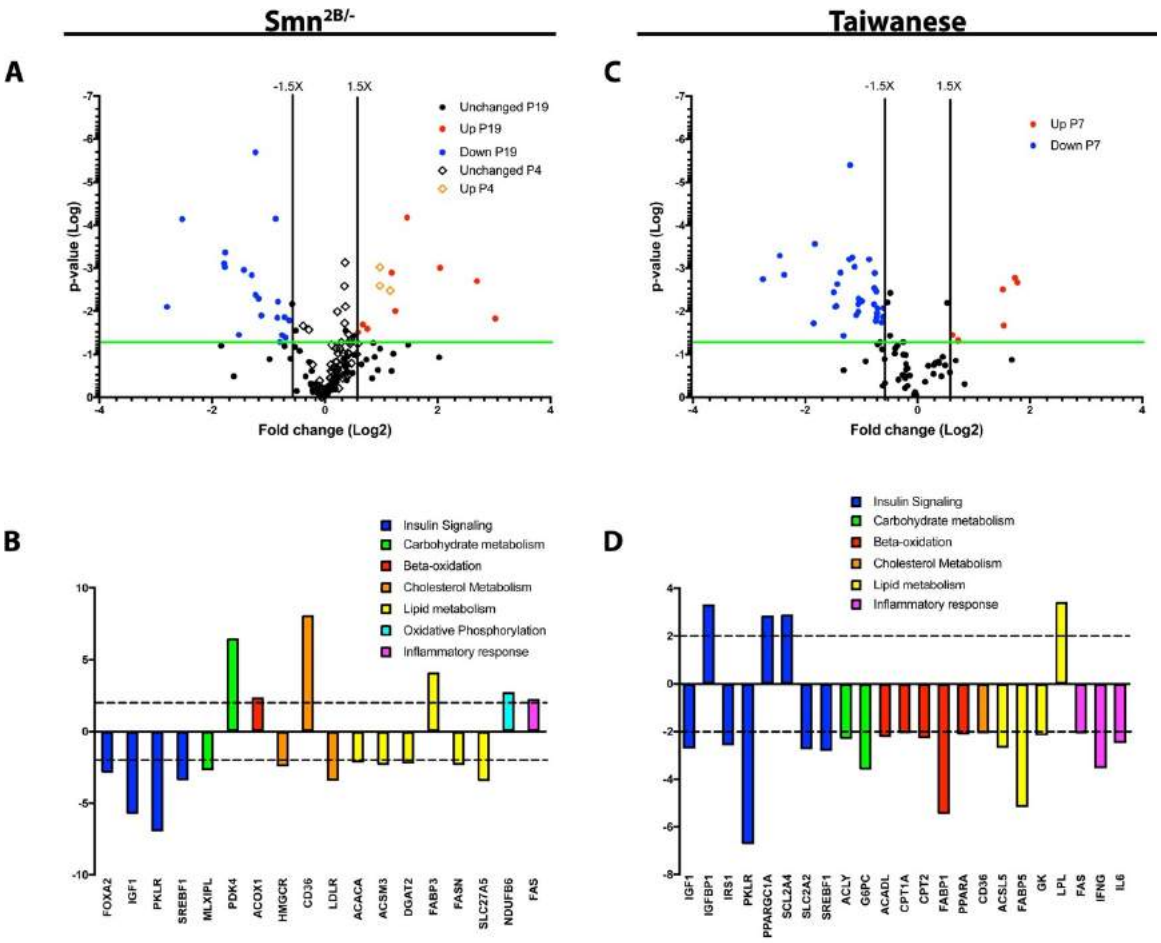

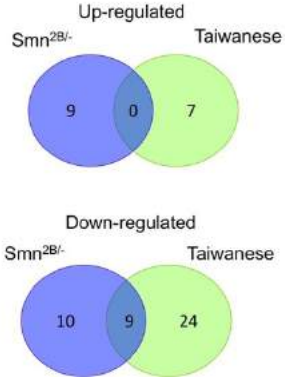

F

Genes	Smn$^{2B/-}$	Taiwanese
Acly	-1,6179	-2,3229
Dgat2	-2,2524	-1,6761
Igf1	-5,7681	-2,725
Irs1	-1,777	-2,5857
Ldlr	-3,4221	-1,9828
Pklr	-6,9536	-6,7341
Ppar-alpha	-1,7928	-2,1338
Slc2a2	-1,6872	-2,7515
Srebf1	-3,4058	-2,8123

Figure 4.4. Commonalities identified in fatty acid metabolism genes between Taiwanese and *Smn*$^{2B/-}$ mice. Volcano plot presentation of all changes (1.5X, $p < 0.05$) in a focused fatty acid metabolism PCR array in *Smn*$^{2B/-}$ mice (A) and *Taiwanese* mice (C) identify general downregulation. Changes more than two-fold are represented for *Smn*$^{2B/-}$ (B) and *Taiwanese* (D). Analysis of commonalities between *Smn*$^{2B/-}$ and *Taiwanese* are represented by Venn diagrams, which identify 9 genes with similar changes (E), listed in (F). (N=4, for *Smn*$^{2B/-}$ mice, and N=3 for *Taiwanese* mice).

Abnormal fatty acid metabolism in other tissues of SMA model mice

Given the wide range of tissues and organs involved in fatty acid metabolism, we next assessed whether fatty acid metabolism abnormalities were present in other tissues in the *Smn*$^{2B/-}$ mouse. We first focused on circulating lipoproteins, because of their role in transporting lipids as well as the increased dyslipidemia in our pediatric SMA cohort. Analysis of plasma lipoproteins from P19 *Smn*$^{2B/-}$ mice revealed a significant increase in total cholesterol, very low density lipoprotein (VLDL - derived from triglycerides) and low density lipoprotein, while high density lipoprotein levels were reduced (Fig 4.5A-D). Consequently, the ratios of TC/HDL and LDL/HDL, both measures of increased cardiovascular risk (303), were significantly elevated (Fig 4.5E-F). These findings align well with our clinical findings in SMA patients. We then determined if the altered lipoprotein profiles in liver and plasma translated to an increased delivery of lipids to motor neurons and skeletal muscle, two primary targets in SMA pathogenesis. No changes were observed in the spinal cord and skeletal muscle (*tibialis anterior*) of P19 *Smn*$^{2B/-}$ mice (Fig

4.5G-H). However, it should be noted that some abnormalities in lipid chain length distribution were present, especially in phospholipid chain length (Fig 4.6A,F). Given that we had previously identified fatty infiltrates in the skeletal muscle of *Smn*$^{2B/-}$ mice (162), we investigated whether lipid metabolism pathways are altered. A focused fatty acid PCR array showed that a number of genes were misregulated in muscles of these mice (Fig 4.5I). These data suggest that fatty acid metabolism is dysregulated in different tissues in SMA mice.

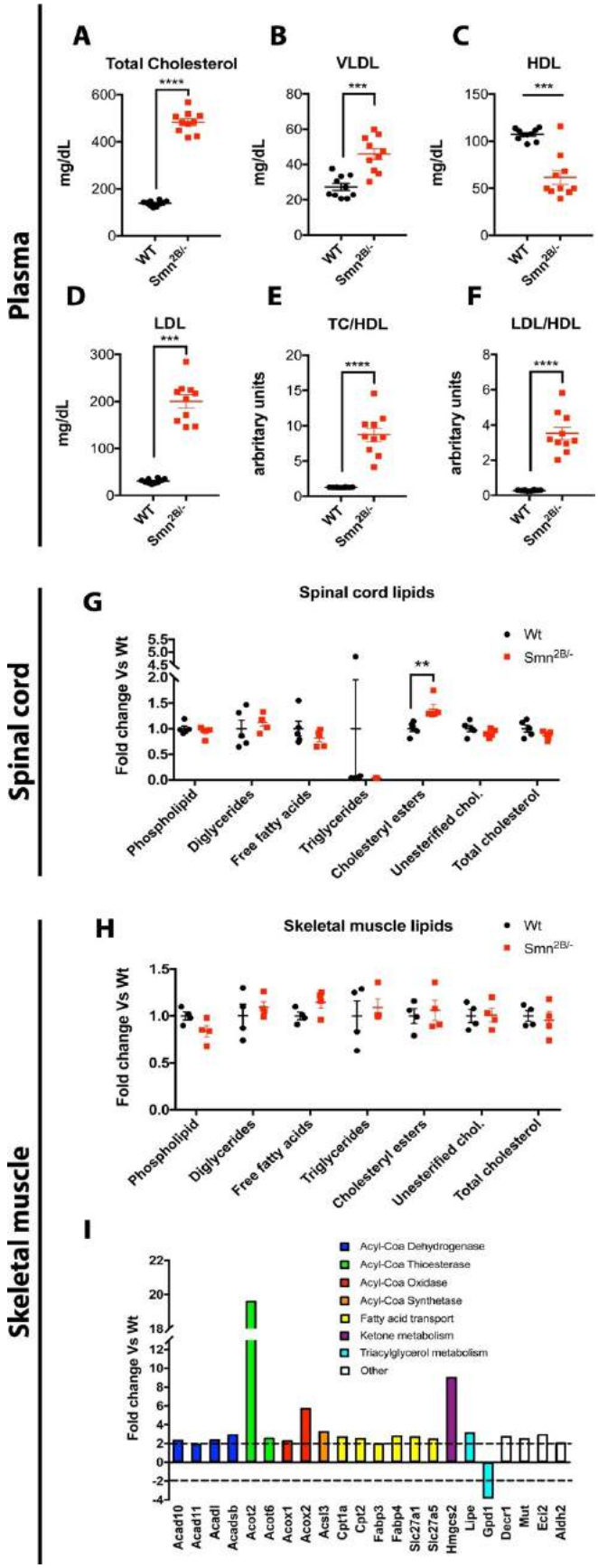

Figure 4.5. *Smn*$^{2B/-}$ mice display dyslipidemia and fatty acid dysfunction in skeletal muscle, but not to the spinal cord. (A-D) Significant up-regulation of total cholesterol, VLDL and LDL in the plasma of *Smn*$^{2B/-}$ animals, while HDL levels were significantly lower. (E,F) Parameters for cardiovascular risks such as TC/HDL and LDL/HDL were significantly increased for *Smn*$^{2B/-}$ mice. (G,H) Every lipid class in the P19 *Smn*$^{2B/-}$ skeletal muscle or spinal cord were at similar levels to WT. (I) Many genes involved in fatty acid metabolism were altered in P19 *Smn*$^{2B/-}$ skeletal muscle in a focused fatty acid PCR array. (N value for each experiment is as follows: N = 10 for A-F, 5 for G, 4 for H-I, $P \leq 0.05$ for *, $P \leq 0.01$ for **, $P \leq 0.001$ for *** and $P \leq 0.0001$ for ****).

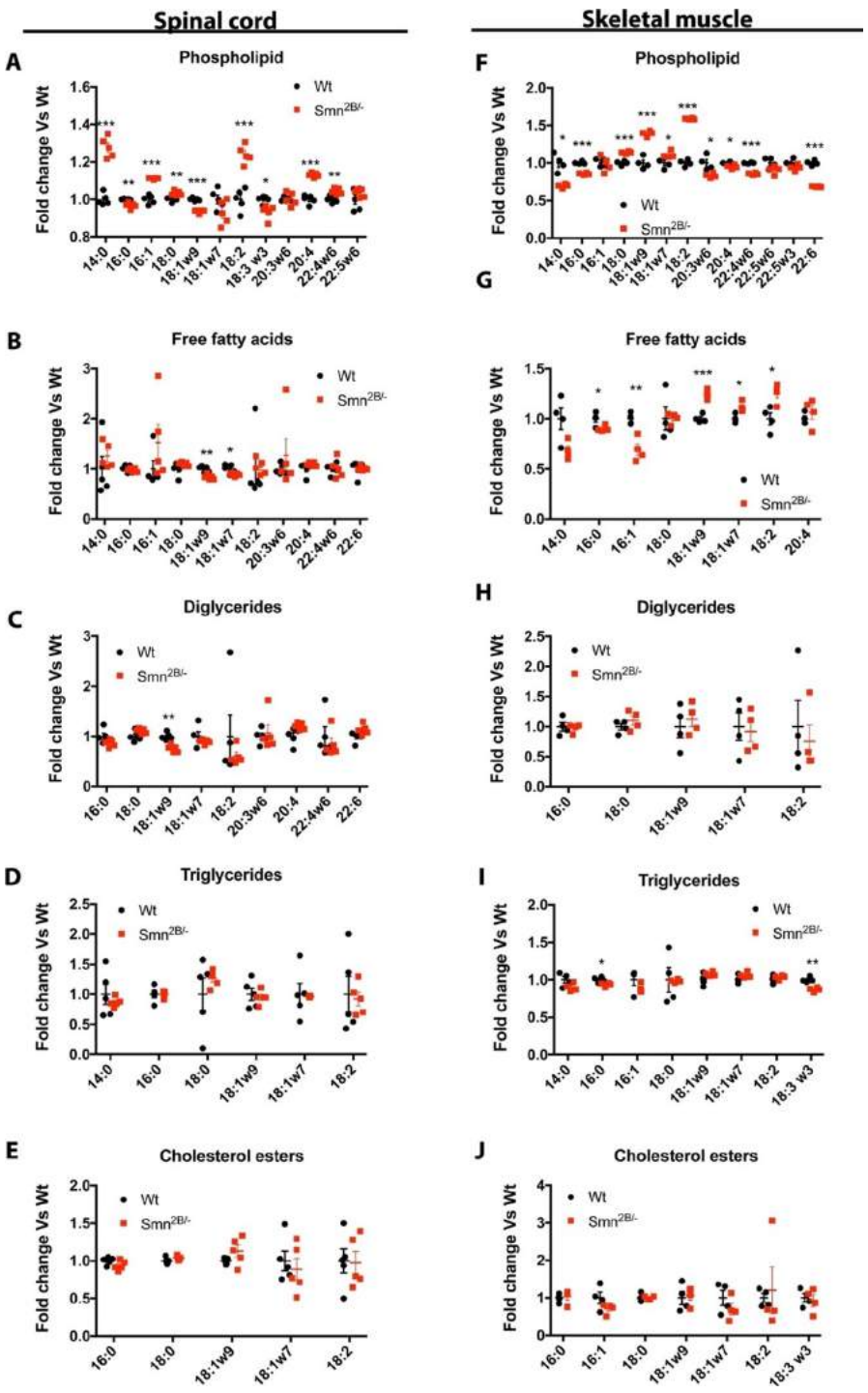

Figure 4.6 Some abnormalities in lipid chain length profiles of various lipid fractions were identified in P19 *Smn$^{2B/-}$* spinal cord and skeletal muscle. Chain length profile of phospholipids (A), free fatty acids (B), diglycerides (C), triglycerides (D) and cholesterol

esters (E) showed little changes in P19 *Smn*$^{2B/-}$ spinal cord except for phospholipids. Chain length profile of phospholipid (F), free fatty acids (G), diglycerides (H), triglycerides (I), and cholesterol esters (J) showed very little change in P19 *Smn*$^{2B/-}$ tibialis anterior muscle except for phospholipids and free fatty acids. Only chain length where all samples levels could be measured are represented within the graphs (N= 4-5, $P \leq 0.05$ for *, $P \leq 0.01$ for **, $P \leq 0.001$ for ***).

Smn$^{2B/-}$ mice develop non-alcoholic fatty liver disease

The fatty acid metabolic changes observed in *Smn$^{2B/-}$* mice closely resemble non-alcoholic fatty liver disease. NAFLD is heterogeneous in its clinical presentation, ranging from least severe steatosis to most severe fibrosis, and can lead to hepatocellular carcinoma (304). Thus, we next determined the severity of the metabolic defects identified in these mice on this NAFLD spectrum. Plasma levels of serum transaminases alanine aminotransferase (ALT) and aspartate aminotransferase (AST), markers of liver damage, were mildly elevated in P19 *Smn$^{2B/-}$* mice (Fig 4.7A-C). However, plasma alkaline phosphatase (ALP) remained normal, but hepatic ALP staining using an enzymatic in situ assay (Fig 4.7D-G) and *Alp* mRNA levels (data not shown) were enhanced in livers from symptomatic *Smn$^{2B/-}$* mice. It has previously been shown that muscular dystrophy patients can exhibit elevated serum transaminase levels, making skeletal muscle a potential source (305). However, muscle from *Smn$^{2B/-}$* mice did not take up Evan's blue dye (83), eliminating the possibility of skeletal muscle degeneration as a source of transaminase in this context. Altogether, our data is therefore indicative of liver damage. ER stress pathways have recently been implicated in NAFLD (306, 307). We observed no signs of endoplasmic reticulum (ER) stress, as the levels of activating transcription factor 4 (*ATF4*), DNA damage inducible transcript 3 (*CHOP*), Heat shock protein 90 beta family member 1 (*GRP94*), and Heat shock protein family A (Hsp70) member 5 (*Bip*) transcripts remained unchanged (data not shown).

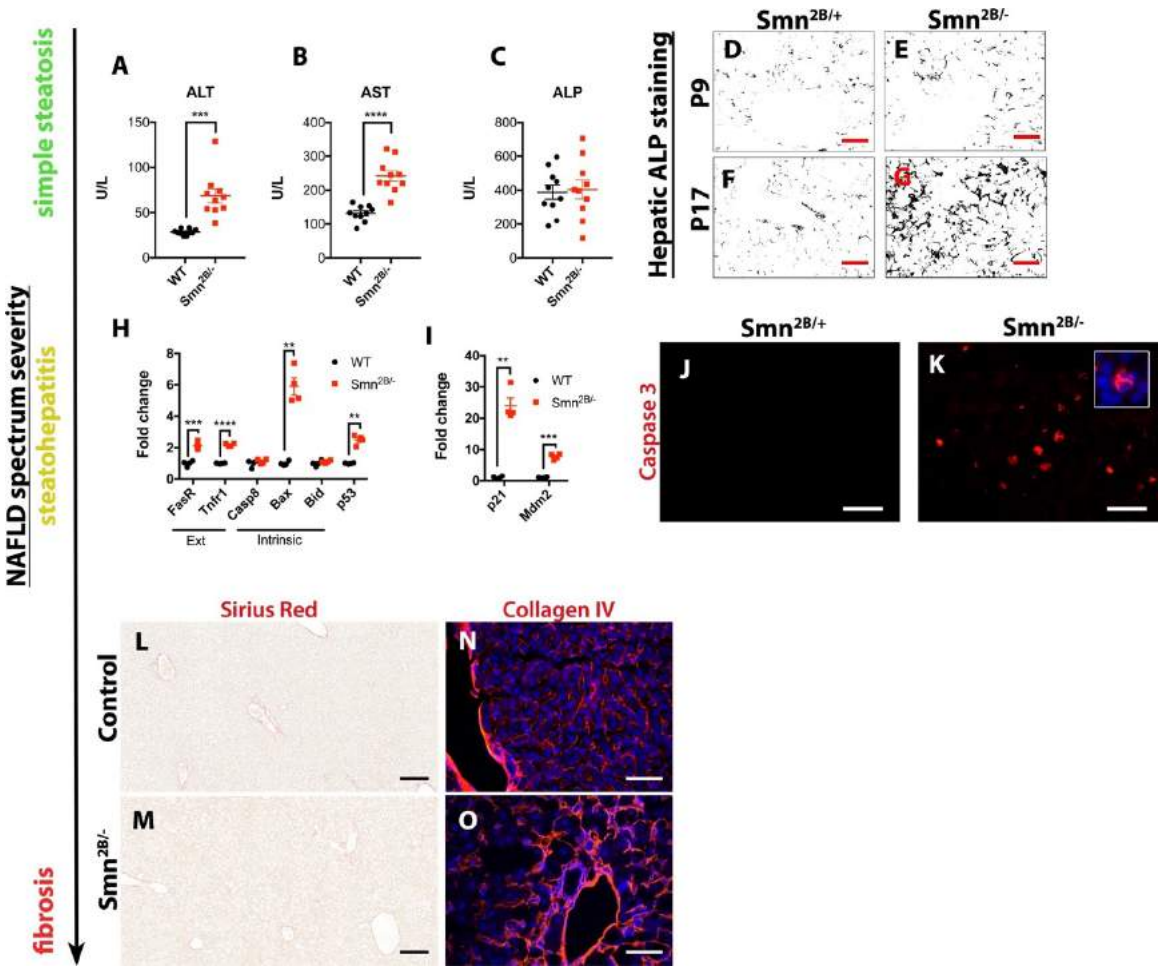

Figure 4.7. Symptomatic *Smn*$^{2B/-}$ mice suffer from significant liver damage without fibrosis. (A-C) Elevation ALT and AST, but not ALP in the plasma of *Smn*$^{2B/-}$ mice at P19. (D-G) Enhanced ALP staining (200X) in P17, but not P9, *Smn*$^{2B/-}$ livers. (H) FasR, TNFR1, Bax, p53, as well as p53 transcriptional targets (I) p21 and Mdm2 transcripts were significantly increased. (J,K) Increased caspase 3 punctae in P17 *Smn*$^{2B/-}$ livers (100X). (L-O) Representative 20X and 200X images of Sirius red and collagen IV staining show no significant hepatic fibrosis in P17-19 *Smn*$^{2B/-}$ mice. QPCR data were normalized with SDHA and PolJ (H-I). Scale bar represents (D-G, J-K, L-O) 100 µm. (N value for each experiment is as follows: N = 10 for A-C, 5 for D-G, 4 for H-I, 3 for J-K, 5 for L-M, 3 for N-O, $P \leq 0.05$ for *, $P \leq 0.01$ for **, $P \leq 0.001$ for *** and $P \leq 0.0001$ for ****).

Nonetheless, an apoptotic process was active as indicated by increased transcript levels for multiple cell death genes such as Fas receptor (*FasR*), TNF receptor superfamily member 1A (*TNFR1*), BCL2 associated X protein (*Bax*), and tumor protein p53 (*p53*) (Fig 4.7H), together with increased caspase 3 staining in livers of P17-19 $Smn^{2B/-}$ mice (Fig 4.7J-K). The hepatic apoptosis appears to be P53-dependent, as expression of classical targets of P53 (308), cyclin dependent kinase inhibitor 1A (*p21*) and *Mdm2,* were strongly upregulated (Fig 4.7I). Finally, liver sections from P17-19 $Smn^{2B/-}$ mice did not display any signs of fibrosis (Fig 4.7L-O). This analysis shows that livers of $Smn^{2B/-}$ mice have steatohepatitis and hepatic cell death, but in the absence of significant fibrosis.

NAFLD in $Smn^{2B/-}$ mice leads to dysfunction in multiple physiological processes

We next sought to identify whether liver damage in SMA translated into functional sequelae. The liver is responsible for the production of a vast array of plasma proteins. We first analyzed plasma levels of total protein and albumin, important clinical readouts of hepatic function. Total protein and albumin were reduced in the plasma of P19 $Smn^{2B/-}$ mice (Fig 4.8A-B). Immune dysregulation has previously been identified in SMA model mice (258-260), and we identified a significant reduction in expression of many complement genes, part of the innate immunity pathway (Fig 4.8C). Abnormal blood clots have been previously reported in SMA (124, 128), and here we found altered transcript levels of genes involved in hemostasis (Fig 4.8D).

Liver is also a key source of growth factors, including insulin growth factor 1 (IGF1), known to contribute to bone length and mass (309). We identified an important reduction in *Igf1* and insulin like growth factor binding protein acid labile subunit (*igfals*) transcript levels but an upregulation of insulin like growth factor 1 receptor (*IGF1R*) and insulin like growth factor binding protein 1 (*IGFbp1*) transcript levels (Fig 4.8E). In addition, a remarkable reduction of IGF1 protein was observed in the plasma of $Smn^{2B/-}$ mice at P19 and P11, but not at P4 (Fig 4.8F). This data corroborates our PCR array findings, where *Igf1* mRNA levels were diminished in both $Smn^{2B/-}$ and the "Taiwanese" SMA mice, and is consistent with several previous reports (112, 310, 311). This change in the regulation of the IGF1 pathway could have a major impact on the health of motor neurons and other organs in addition to overall body size, which is a significant feature of all mouse models of SMA.

The liver is also a key site for iron storage in relation to its early hematopoietic function, and a conditional knockout of Smn in the liver leads to embryonic lethality and iron overload while the "Taiwanese" SMA mice showed transient iron accumulation (128, 292). We identified many misregulated transcripts for genes involved in iron metabolism, including Hepcidin antimicrobial peptide (*Hamp* or *hepcidin*), a gene producing hepcidin protein that acts as a master regulator of iron levels (312) (Fig 4.8G). Despite alterations in these transcripts, plasma iron levels trended lower in $Smn^{2B/-}$ animals, but did not reach significance (Fig 4.8H). Iron overload or deposition was not observed in livers from P19 $Smn^{2B/-}$ mice as determined by Prussian blue staining (Fig 4.8I-J). Finally, we have observed high levels of total bilirubin in the plasma, suggesting reduced efficacy of the

hepatocytes to process this waste product (Fig 4.8K). As such, it is likely that iron dysregulation in our model results from slow heme processing. Together, these findings demonstrate major impairments in many functions of the liver, resulting in significant impacts on overall health.

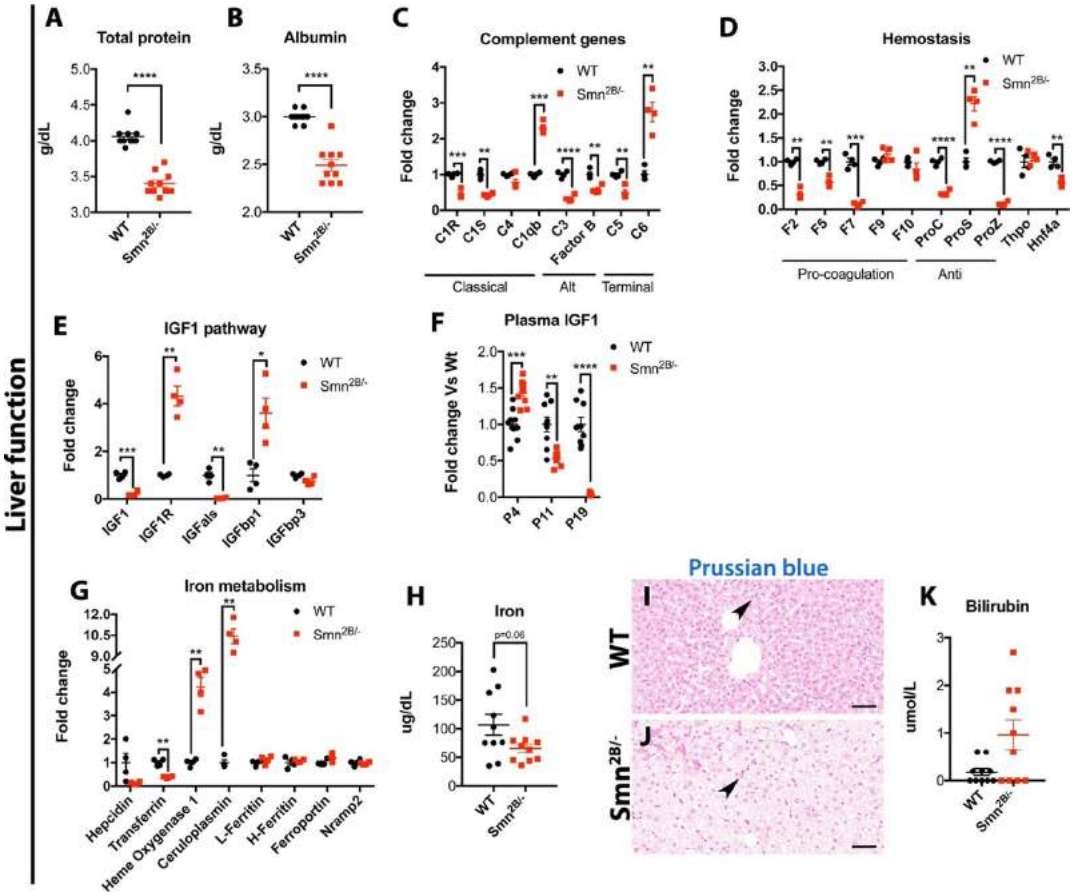

Figure 4.8 Liver functional deficits in multiple pathways in symptomatic *Smn$^{2B/-}$* mice. (A,B) Low levels of total protein and albumin in plasma from P19 *Smn$^{2B/-}$* mice. (C-E) Major alterations in levels of transcripts for complement, hemostasis and IGF1 pathway components in livers from P19 *Smn$^{2B/-}$* mice. (F) Progressive depletion of IGF-1 hormone in the plasma from *Smn$^{2B/-}$* mice. Iron metabolism genes are misregulated (G), and iron levels are reduced in plasma (H) but unchanged in liver (Prussian blue staining, 40X) (I,J). (K) A trend towards higher total bilirubin protein in the plasma in *Smn$^{2B/-}$* mice. QPCR data were normalized with SDHA and PolJ (C,D, E). Scale bar represent 50 µm (I,J). (N value for each experiment is as follows: N = 8-10 for A-B, F, H, and K, 4 for C-E and G, 5 for I-J, $P \leq 0.05$ for *, $P \leq 0.01$ for **, $P \leq 0.001$ for *** and $P \leq 0.0001$ for ****).

Identification of molecular mechanisms underpinning NAFLD

Denervation

To better understand the mechanisms underlying the NAFLD observed in $Smn^{2B/-}$ mice, we next examined the progression of fat accumulation in the liver. Interestingly, the liver appeared relatively normal at P9, but became progressively fatty as soon as P10 with a spike by P13-14 (Fig 4.9). This raised the possibility that muscle denervation, which occurs around this time in $Smn^{2B/-}$ mice, could be sufficient to induce liver steatosis. However, $SOD1^{G93A}$ mice, a well-established model of amyotrophic lateral sclerosis (ALS) that shows denervation comparable to that in the SMA model mice, displayed normal liver histology, and unaltered triglyceride and cholesteryl ester levels at symptomatic age (20 weeks) (Fig 4.10A-D). Denervation is therefore not sufficient for fat accumulation in the liver, but may contribute to a lower metabolic demand by skeletal muscle.

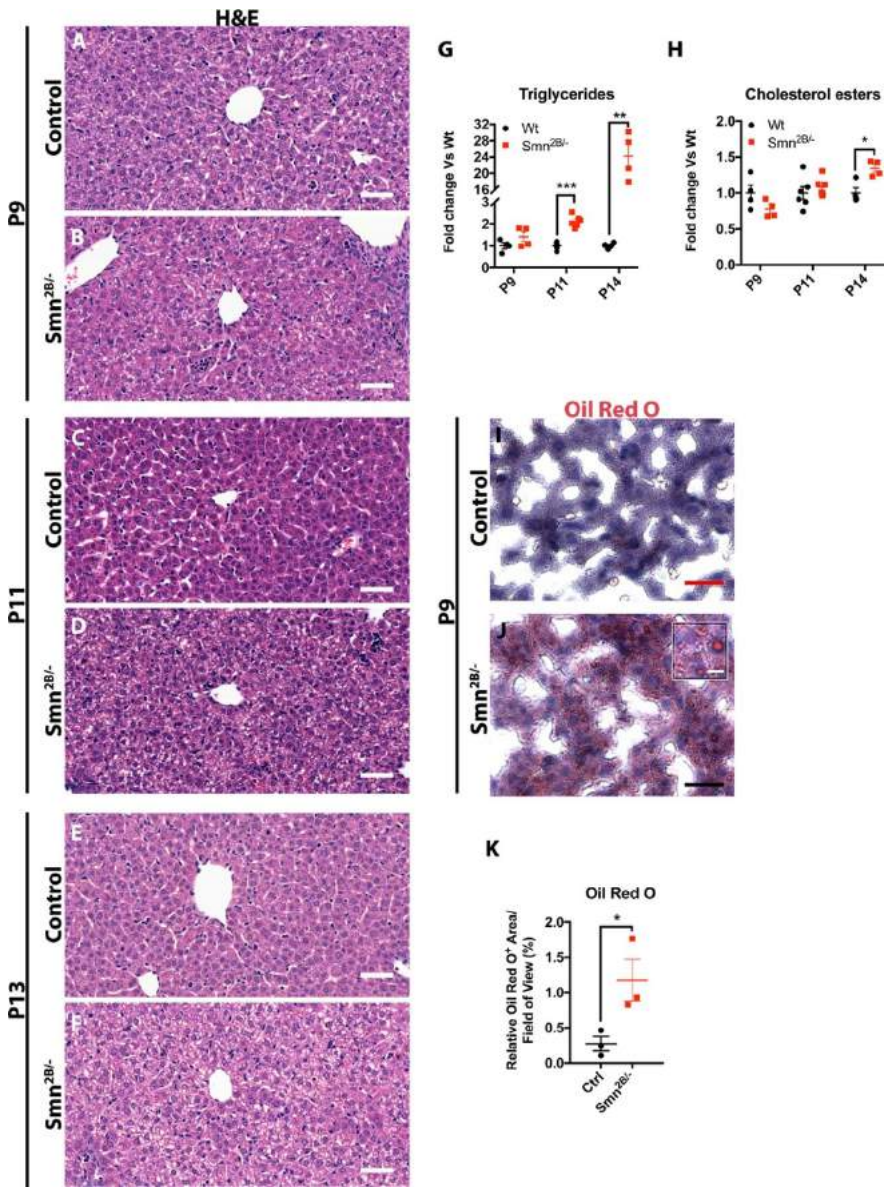

Figure 4.9. Fat accumulation is first observed between P9 and P11 in *Smn*$^{2B/-}$ mouse model. Temporal progression of H&E staining (40X) of livers from *Smn*$^{2B/-}$ mice identifies fat accumulation between P9 and P11 (A-F). Triglycerides and cholesterol esters quantification confirmed histological findings (G,H). Oil Red O staining (400X) additionally showed increased fat at P9 (I-K) Scale bar represent 50 µm in A-F, 50 µm in I-J (10 µm in the inset). (N value for each experiment is as follows: N = 5-7 for A-F, 4-6 for G-H, 3 for I-K, $P \leq 0.05$ for *, $P \leq 0.01$ for **, $P \leq 0.001$ for ***).

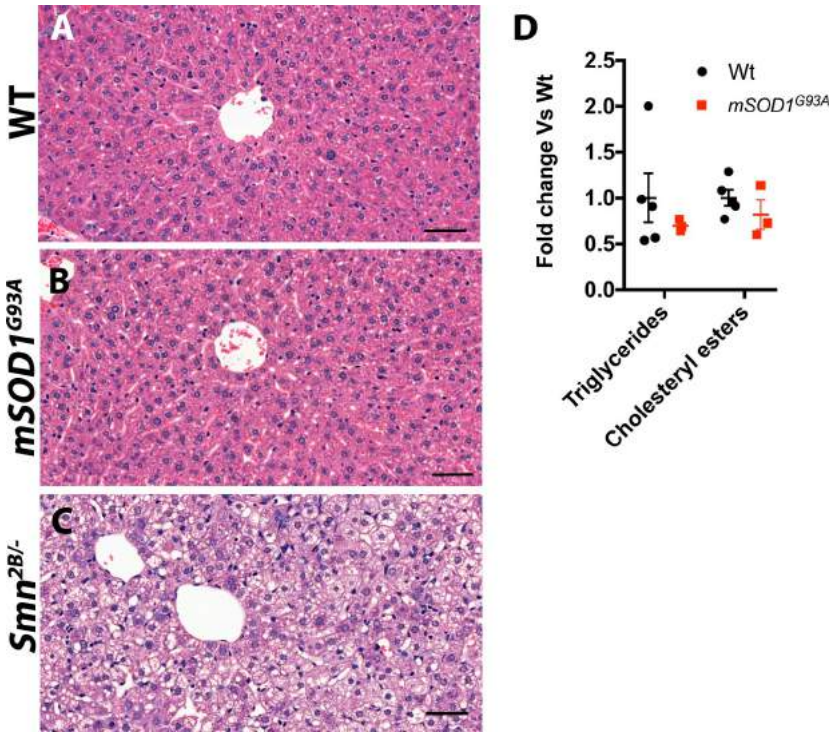

Figure 4.10. Denervation is not sufficient to trigger a hepatic steatosis. (A-C) H&E staining (40X) of livers of 20-week-old *SOD1*^{G93A} mutant mice, a model of ALS, did not show hepatic fat accumulation in comparison to livers from *Smn*$^{2B/-}$ mice, even though denervation is well-established at this time point. (D) Triglycerides and cholesteryl esters quantification showed no difference between mutant *SOD1*^{G93A} and WT controls. Scale bar: (A-C) 50 μm. (N value for each experiment is as follows: N = 3-5).

Pancreas-liver axis

The close functional relationship between the pancreas and the liver could contribute to the NAFLD in *Smn*$^{2B/-}$ mice. We noted a progressive elevation of plasma glucagon levels, which was first evident at P11 in *Smn*$^{2B/-}$ mice (Fig 4.11A). This increase in glucagon likely results from the increase in alpha-cell number in *Smn*$^{2B/-}$ pancreas (211). Similarly, there is a robust increase in the levels of GLP-1, another byproduct of proglucagon, produced in the gastrointestinal tract (Fig 4.11B). Other metabolic gastrointestinal (ghrelin, GIP, PYY), pancreatic (PP, amylin, insulin, C-peptide) and adipocytic (leptin, resistin, adiponectin) hormones did not show a consistent pattern of misregulation (Fig 4.12). Glucagon signaling mediates some of its effects through the phosphorylation of Creb, which leads to expression of the gluconeogenic program (313, 314). We observed increased phospho-Creb levels in livers of P19 *Smn*$^{2B/-}$ mice (Fig 4.11C). Enhanced glucagon levels/signaling lead to glycogenolysis and gluconeogenesis in the liver, and lipolysis in the white adipose tissue (WAT) to increase energetic substrate availability in the blood stream (315). Pathological glucagon signaling could lead to energy substrate overload in the blood, and subsequent stimulation of the liver to restore homeostasis via uptake of these substrates, including lipids. We observed hepatic glycogen depletion (Fig 4.11D-E), a trend towards a reduced adipocyte size and a significant increase in non-esterified fatty acids (NEFA), a direct product of lipolysis, in the blood at P19 (Fig 4.11J,K,P,R). These findings are consistent with enhanced glucagon signaling. To determine if this mechanism is driving fat accumulation in the liver, we performed similar analysis in P11 and P13 *Smn*$^{2B/-}$ mice when steatosis is first seen. No clear trend could be identified in glycogen storage (Fig 4.11F-I) and adipocyte size was largely unchanged at

P11 and P13 (Fig 4.11L-O,P). This is perhaps not surprising, as significant glycogen breakdown or lipolysis is needed to occur to identify changes in these measures. In an attempt to capture any earlier changes, we next investigated levels of blood glucose and NEFA, which are direct products of glycogen breakdown or lipolysis respectively. Strikingly, we observed low blood glucose at all time points examined (Fig 4.11Q), which could be a driver of the hyperglucagonemia and pancreatic defects in the *Smn*$^{2B/-}$ mice. Interestingly, this data is consistent with the low glycated hemoglobin HbA_{1C} levels identified in our pediatric SMA patient cohort. Additionally, elevated NEFA was readily observable at P11 and worsened over time in comparison to control (Fig 4.11R). Triglyceride levels followed a similar progression, albeit in a delayed fashion (Fig 4.11S). Altogether, these findings point to a fatty substrate overload in the blood as a consequence of glucagon pathway activation.

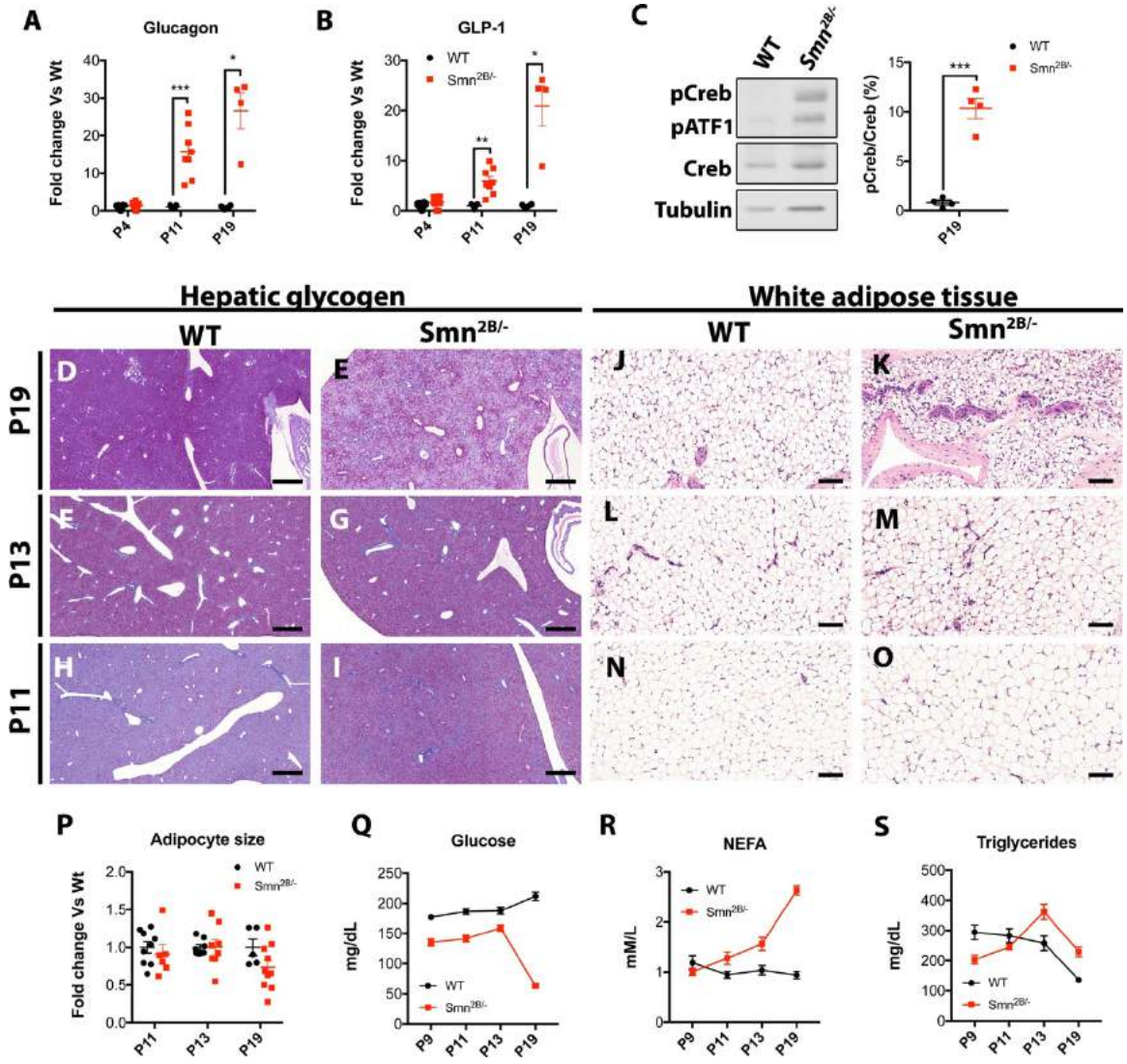

Figure 4.11 Hyperglucagonemia leads to increased substrate release in the plasma of *Smn$^{2B/-}$* mice. (A) Progressive elevation of plasma glucagon occurs in *Smn$^{2B/-}$* mice with a ~15-fold increase by P11. (B) Plasma GLP-1, a product of the cleavage of proglucagon, is altered in a similar fashion. (C) Western blot analysis shows a 10-fold increase in phospho-Creb, a downstream molecular event of glucagon activation, in P19 *Smn$^{2B/-}$* livers in comparison to WT. (D-I) PAS stained liver sections (5X) at P19, P13 and P11 reveal glycogen depletion in P19 *Smn$^{2B/-}$* mice (D,E), but not at P13 (F,G) and P11 (H,I). (J-O) H&E sections (20X) of subcutaneous fat adipose tissue show reduction in adipocyte size

at P19 *Smn*$^{2B/-}$ mice (J,K,P) but not at P13 (L,M,P) and P11 (N-P). (Q) Plasma glucose was lower throughout P9 to P13 in *Smn*$^{2B/-}$ mice in comparison to wild type mice. (R) Plasma NEFA progressively increase from P9 to P19, concordant with increased lipolysis of white adipose tissue. (S) Plasma triglyceride quantification showed a similar trend as NEFA, albeit in a delayed fashion. Scale bar represents 500 μm in D-I and 100 μm in J-O. (N value for each experiment is as follows: N = 8-10 for P4, P11 and 4-6 at P19 in A, 4 in C, 5 for D-I, 5-10 for J-P, 10 in Q-S, $P \leq 0.001$ for *** and $P \leq 0.0001$ for ****).

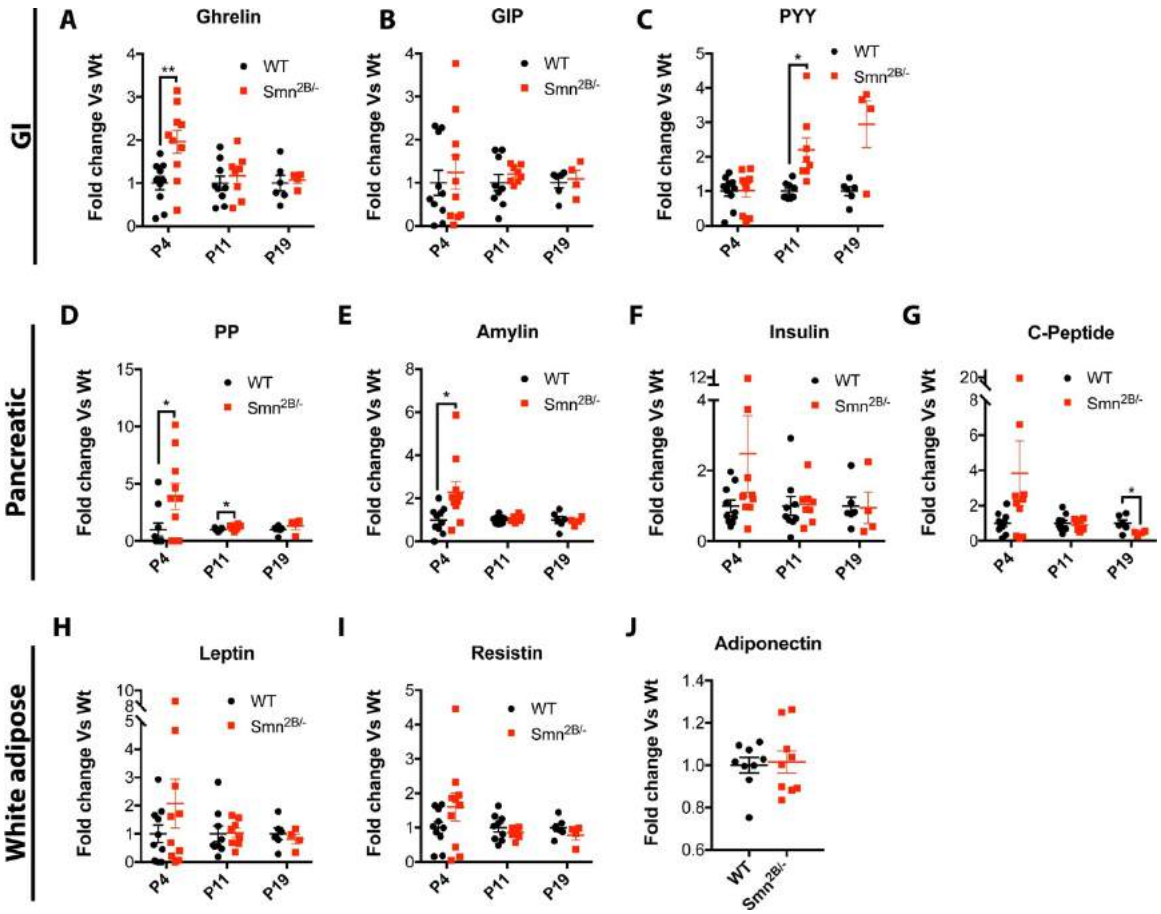

Figure 4.12. Major metabolic hormone levels are largely unchanged in the plasma of Smn$^{2B/-}$ mice. (A-C) PYY is the only significantly changed hormone originating from the gastrointestinal system while ghrelin and GIP were largely unchanged. (D-G) Minor differences are present in pancreatic hormones. (H-J) No changes were observed in hormones released from adipocytes such as leptin, resistin, and adiponectin. (N value for each experiment is as follows: N = 8-10 for P4, P11 and 4-6 at P19 in A-I, 9 for J, $P \leq 0.05$ for *, $P \leq 0.01$ for **).

Liver-intrinsic defects

To identify alterations in specific molecular pathways that could render SMA liver more susceptible to NAFLD, we undertook Tandem Mass Tagging (TMT) proteomic analysis of livers from pre-symptomatic P0 and P2 *Smn*$^{2B/-}$ mice compared to wild type, specifically to look for molecular changes present in advance of the appearance of overt pathology. We initially identified 7229 unique peptide sequences in samples examined. To refine this complex data set into more readily accessible groupings, we broke the data down into biologically relevant subgroups based on the timing of altered protein abundance detection. This produced four subgroups, A, B, C and D, where proteins in subgroup A (14% of the total IDs) represent those whose expression is already significantly altered at P0, but revert to wild type basal levels at P2. Subgroup D (not altered at either P0 or P2) contained 65% of IDs (Fig 4.13A). We concluded that the proteins in these subgroups (A and D) were therefore unlikely to be important for the NAFLD phenotype. Conversely, proteins in subgroup B (unchanged at P0, but significantly changed at P2) included 11% of total proteins, while subgroup C (altered at both P0 and P2) including 10% of total proteins were of more interest. Analysis of subgroup B using BioLayout *Express*^{3D} and DAVID (tools for visualizing and identifying biological networks) identified the mitochondrion cluster (increased protein expression) and the lipid metabolism cluster (decreased protein expression) (Fig 4.13B). A similar analysis of subgroup C identified clusters again associated with mitochondria (proteins significantly upregulated at both P0 and P2), extracellular signaling (proteins significantly decreased at both P0 and P2), and extracellular matrix proteins (significantly decreased at P0, however significantly increased at P2) (Fig 4.13C).

We decided to focus on perturbations identified in mitochondria and lipid metabolism clusters in the pre-symptomatic *Smn*$^{2B/-}$ livers. To further refine potential pathways involved, we used ingenuity pathway analysis (IPA) software on proteins within subgroups B (Fig 4.14) and C (Fig 4.13D). Of interest, the results from subgroup C revealed alterations in pathways related to "oxidative phosphorylation" (p = 6.35x10^{-3}) and "mitochondrial dysfunction" (p = 1.11x10^{-2}) (Fig 4.13D). Furthermore, IPA analysis identified "metabolism" (p = 3.53x10^{-12}) and "homeostasis of lipids" (p = 1.68x10^{-9}) as some of the top functional subgroupings perturbed in *Smn*$^{2B/-}$ liver at P0 (Fig 4.13E). Thus, our screen points towards mitochondrial dysfunction, a critical player in fatty acid clearance through β-oxidation, as a driver of lipid dysregulation in SMA.

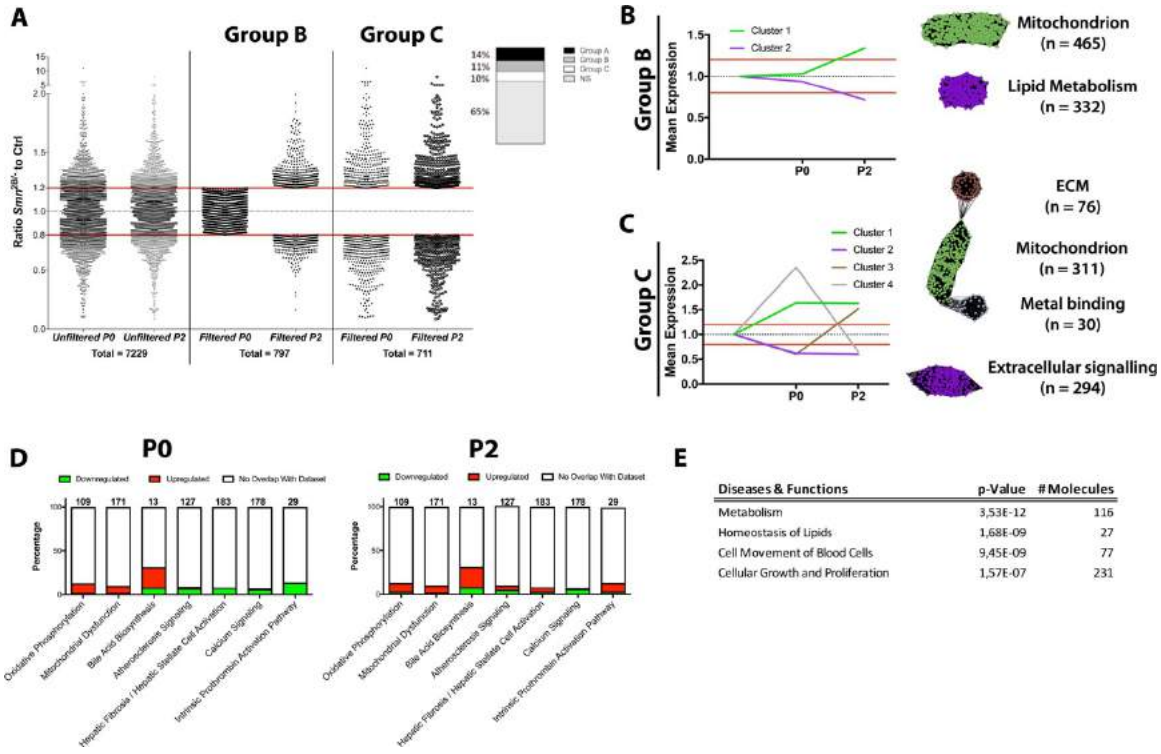

Figure 4.13. Proteomic analysis of P0 and P2 *Smn*$^{2B/-}$ livers identifies mitochondrial and lipid metabolism as prominent perturbations. (A) Scatterplots showing protein expression ratios of *Smn*$^{2B/-}$ to P0 wild type liver. A 20% threshold altered expression was applied. Left column of paired scatterplots shows *Smn*$^{2B/-}$ to wild type ratios for 7229 proteins at birth (P0) and P2. Group B identified by filtering for proteins altered only at P2 in *Smn*$^{2B/-}$ livers (P0 = ns ($0.8 \leq x \leq 1.2$) and P2 = $p \leq 0.05$ ($x < 0.8$ or $x > 1.2$)). Group C filters for proteins altered at P0 and at P2 in *Smn*$^{2B/-}$ (P0 and P2 = $p \leq 0.05$ ($x < 0.8$ or $x > 1.2$). Group B and Group C graphical representation of *Smn*$^{2B/-}$ to wild type ratio proteins at P0 and P2, left graph prior to clustering, right graphic post application of the Markov Clustering Algorithm (MCL) clustering algorithm (inflation value 2.2) analyzing coordinately expressed proteins. These are represented as mean ratio-change per cluster. In cluster visualization the proteins are spheres with correlation between them of $r \geq 0.9$

indicated by black lines. Each identified cluster has a functional annotation with n number stating how many proteins are present within the cluster. (D) IPA top canonical pathways highlighting the main disrupted cascades in Group C data set at P0 (left) P2 (right). Stacked bar chart displays the percentage of proteins that were upregulated (red), downregulated (green), and proteins that did not overlap with our data set (white) in each canonical pathway. The numerical value at the top of each bar represents the total number of proteins in the canonical pathway. (E) Top diseases and functions linked to our Group C data set identified by IPA functional analysis (see methods for comprehensive description of analysis).

A

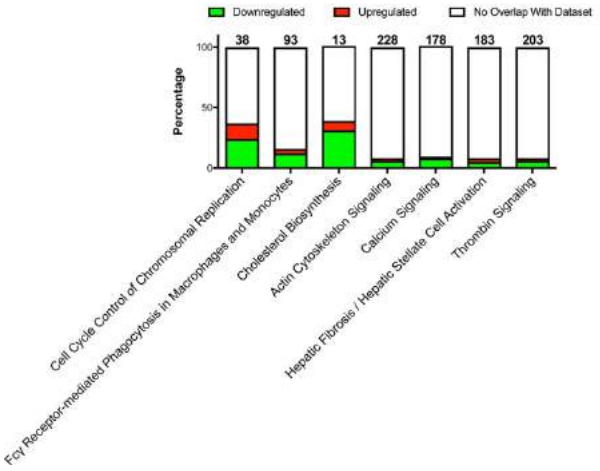

B

Diseases & Functions	p-Value	# Molecules
Metabolism	4,13E-10	49
DNA Replication, Recombination, and Repair	4,41E-10	36
Cell Death	4,7E-10	254
Cellular Growth and Proliferation	3,17E-08	135

Figure 4.14. IPA analysis of group B identify metabolism but also cell cycle pathways. (A) IPA top canonical pathways highlighting the main disrupted cascades in Group B data set. Stacked bar chart displays the percentage of proteins that were upregulated (red), downregulated (green), and proteins that did not overlap with our data set (white) in each canonical pathway. The numerical value at the top of each bar represents the total number of proteins in the canonical pathway. (B) Top diseases and functions linked to our Group D data set identified by IPA functional analysis.

Assessment of mitochondrial function in livers of $Smn^{2B/-}$ mice

Given the proteomic data findings, we decided to further investigate mitochondrial function. Oxidative phosphorylation complex protein levels are largely unchanged at P9. However, the levels of SDHB (complex II), MTCO1 (complex IV) and ATP5A (complex V) in mitochondria from livers of P19 $Smn^{2B/-}$ mice were reduced (Fig 4.15A,B), highlighting a potential depletion of these complexes and in mitochondrion number, which was confirmed by a reduction in citrate synthase activity (Fig 4.15C) (316). Ultrastructural screening of mitochondria revealed no significant alterations (Fig 4.15D-G), suggesting that the mitochondria that remained were of normal structure. Surprisingly, high-resolution respirometry of isolated mitochondria from P19-21 $Smn^{2B/-}$ mice identified increased leak and ADP phosphorylation capacities when fueled by pyruvate, malate, and succinate (Fig 4.15H-L), or palmitoyl carnitine (Fig 4.16). Interestingly, $Smn^{2B/-}$ mitochondria function similarly to control at P9, a time point where hepatic fat accumulation is not readily observed. There was also an increase in reactive oxygen species (ROS) production in the isolated mitochondria from livers of P19-21 $Smn^{2B/-}$ mice in comparison to $Smn^{2B/+}$ mice, but not at P9 (Fig 4.15M-Q). It is possible that this increased capacity for respiration in isolated mitochondria is a compensatory mechanism to restore metabolic homeostasis. In addition, the enhanced ROS production could be responsible in part for liver damage and the hepatocyte death identified (Fig 4.7J-K). The increased capacity for fatty acid-supported respiration was consistent with the elevated levels of microsomal oxidation enzyme CYP4A (Fig 4.15R,S), known to be active upon β-oxidation overload (304, 317, 318). Interestingly, this system leads to production of dicarboxylic acids (317) and SMA patients have previously been identified with dicarboxylic aciduria (49-51). CPT1, a

protein responsible for shuttling long chain fatty acid into the mitochondria for β-oxidation, can be inhibited by malonyl-CoA, a product of *de novo* lipogenesis (318, 319). This would lead to further fatty acid overspill in the microsomal oxidation pathway. In fact, we found CPT1 was significantly inhibited in comparison to both wild type and $Smn^{2B/+}$ mice at P19 (Fig 4.15T). Overall, results show that mitochondrial respiratory functions are normal or increased, when oxidative processes are supported directly by substrates for Complexes I and II. Given that CPT1 activity was decreased, it is possible that there is impaired formation of acyl carnitine species or inhibition of CPT1 activity, and thus reduced uptake of long chain fatty acids for mitochondrial oxidation *in vivo,* further exacerbating hepatic steatosis.

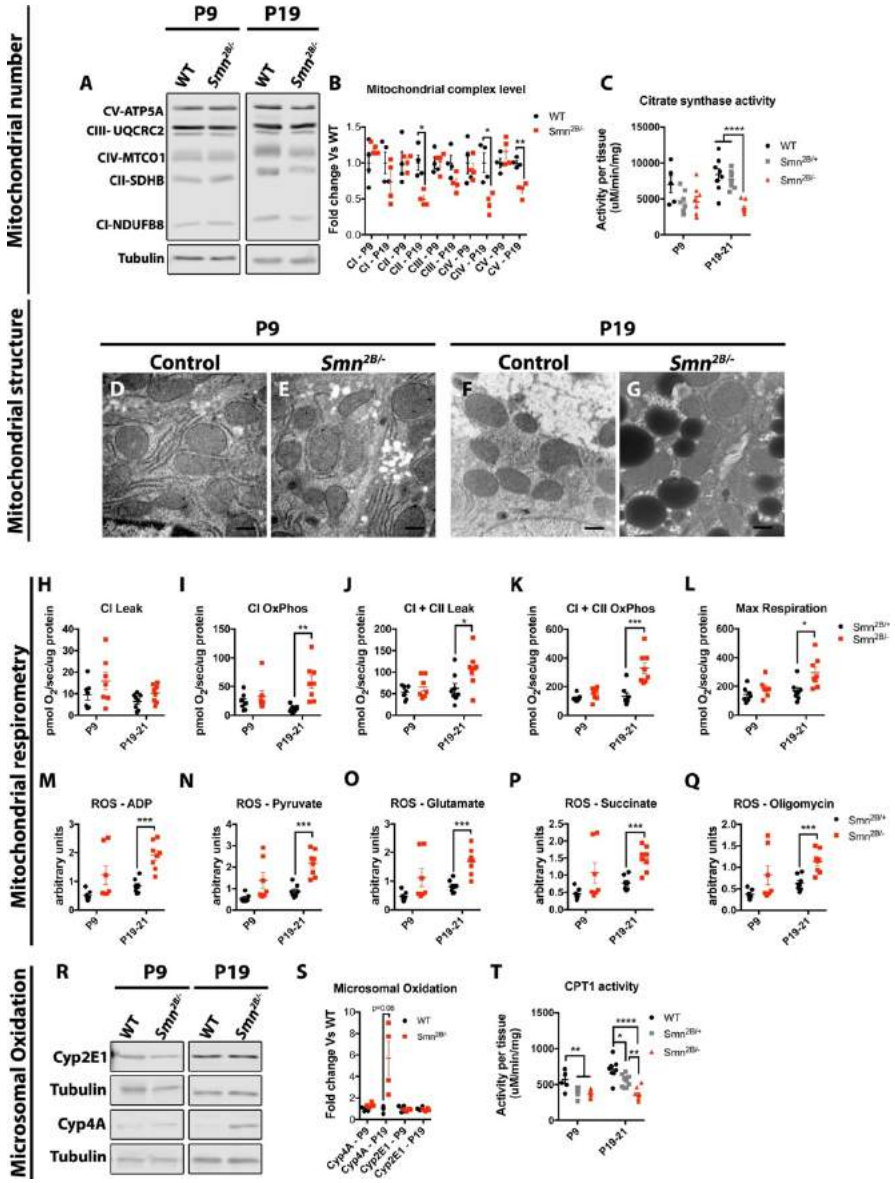

Figure 4.15. *Smn*$^{2B/-}$ liver mitochondria function is not compromised. (A,B) Western blot analysis of component oxidative phosphorylation chains shows no significant change prior to hepatic fat accumulation at P9 but shows significant down-regulation of CII, CIV and CV at P19. (C) Lower citrate synthase activity in livers of P19-21 *Smn*$^{2B/-}$ mice, suggests lower mitochondria number. (D-G) Mitochondrial structure appears relatively spared at both P9 and P19 in *Smn*$^{2B/-}$ livers. (H-L) High resolution respirometry of *Smn*$^{2B/-}$ hepatic mitochondria shows increased leak and higher respiration capacity at P19 but not

at P9 in comparison to *Smn*$^{2B/+}$ hepatic mitochondria, suggesting intact mitochondrial function. (M-Q) Hepatic *Smn*$^{2B/-}$ mitochondria had an increase in ROS production at most levels of the oxidative respiration chain in comparison to *Smn*$^{2B/+}$ mitochondria. (R,S) Increased expression of CYP4A is evident in P19 *Smn*$^{2B/-}$ livers. (T) Reduced CPT1 activity is evident in livers of *Smn*$^{2B/-}$ mice compared to WT and *Smn*$^{2B/+}$. (N value for each experiment is as follows: N = 3-4 for A-B, & R-S, 1 for D-G, 6-9 for C, H-Q & T, unpaired two-sided student's t-test for all except C & T one-way ANOVA with Tukey's correction, $P \leq 0.05$ for *, $P \leq 0.01$ for **, $P \leq 0.001$ for *** and $P \leq 0.0001$ for ****)

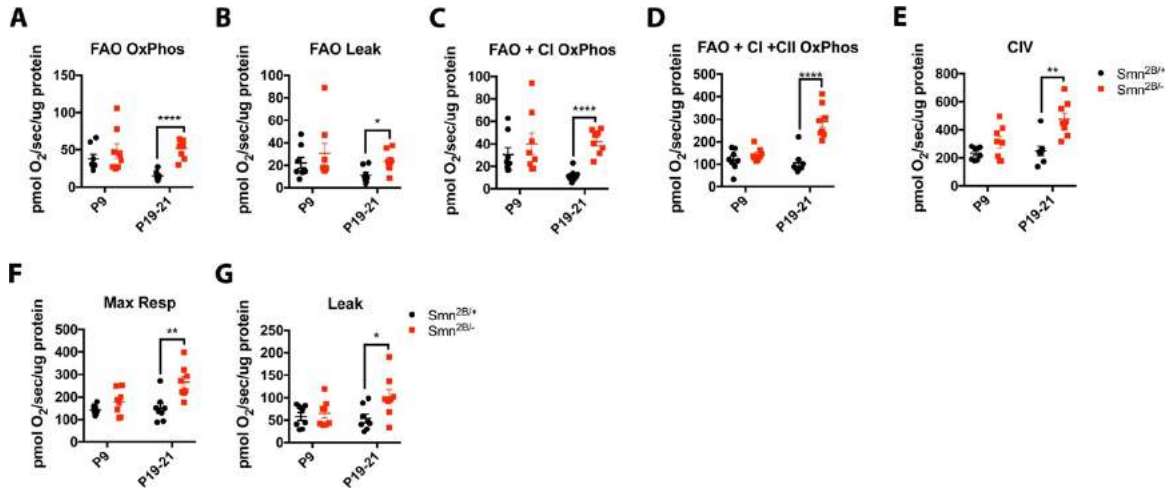

Figure 4.16. *Smn*$^{2B/-}$ liver mitochondria function is not compromised even in the presence of fatty acids. High resolution respirometry of *Smn*$^{2B/-}$ hepatic mitochondria shows increased leak and higher respiration capacity at P19 but not at P9 in comparison to *Smn*$^{2B/+}$ hepatic mitochondria, suggesting intact mitochondrial function in the presence of fatty acids.

Low fat diet leads to an increase in survival without a correction of hepatic triglyceride level or liver function

Dietary intake can play an important part in NAFLD progression (304, 320). As such, we next examined whether modulating the diet of *Smn*$^{2B/-}$ mice affected survival and metabolic phenotypes. We tested 3 different diets: high fat diet (HFD), low fat diet (LFD) and high sucrose diet (HSD) (details and composition in Fig 4.17). Given the short lifespan of *Smn*$^{2B/-}$ mice, we administered the diets to the dams until the pups could freely feed on their own. It has previously been shown that milk of rat dams fed high fat diet had higher fat content than those on normal chow by 21 days post-partum, while their offspring showed increased weights, change in body composition and metabolic abnormalities (321). Surprisingly, the introduction of LFD (median lifespan of 38 days - male 37 days, female 41 days $p = 0.9937$) and HSD (median lifespan of 39 days - male 35 days, female 39 days $p = 0.22$) significantly doubled life expectancy in comparison to *Smn*$^{2B/-}$ mice on normal chow (median lifespan of 21 days - male 21 days, female 26.5 days $p = 0.0171$) (Fig 4.18A). HFD (median lifespan of 22 days - male 21 days, female 27 days $p = 0.700$) did not lead to any improvement. Whilst not always reaching statistical significance, it was intriguing to observe that female *Smn*$^{2B/-}$ mice tended to live longer than male *Smn*$^{2B/-}$ mice in all different diet groups. Interestingly, the weight of the mice was only marginally changed regardless of diet (Fig 4.18B). Furthermore, the enhanced survival of the mice on LFD and HSD was not related to changes in hepatic SMN protein levels, fat content (as measured by hepatic triglyceride levels and plin2 mRNA levels (322)) or serum glucagon levels, all of which remained constant (Fig 4.18C-F). However, we did observe a reduction of GLP-1 in the HSD group (Fig 4.18G). We next speculated that LFD and HSD may simply restore

appropriate proportions of energy substrate for usage, by reducing circulating fat and increasing glucose. Indeed, we noted a modest increase in plasma glucose levels in *Smn*$^{2B/-}$ mice on the HSD regimen (Fig 4.18H). More importantly, levels of circulating ketone bodies were reduced in both LFD and HSD cohorts, implying reduced β-oxidation and a lower reliance on fatty acids as an energy source (Fig 4.18I). NEFA were not reduced significantly in the LFD or HSD *Smn*$^{2B/-}$ cohort in comparison to normal chow (NC) *Smn*$^{2B/-}$ mice (Fig 4.18J), likely pointing towards white adipose tissue abnormalities not modifiable by diet change. Interestingly, liver damage was diminished in *Smn*$^{2B/-}$ fed LFD and HSD diets in comparison to NC *Smn*$^{2B/-}$ mice, as assessed by ALT levels (Fig 4.18K). However, the reduced damage did not improve hepatic function as total protein production (Fig 4.18L) and *Igf1* mRNA production (data not shown) were unchanged amongst the different *Smn*$^{2B/-}$ diet cohorts. Altogether, diet modulation can significantly improve lifespan of *Smn*$^{2B/-}$ mice, likely by altering mitochondrial bioenergetic substrate utilization, without influence on hepatic fat accumulation.

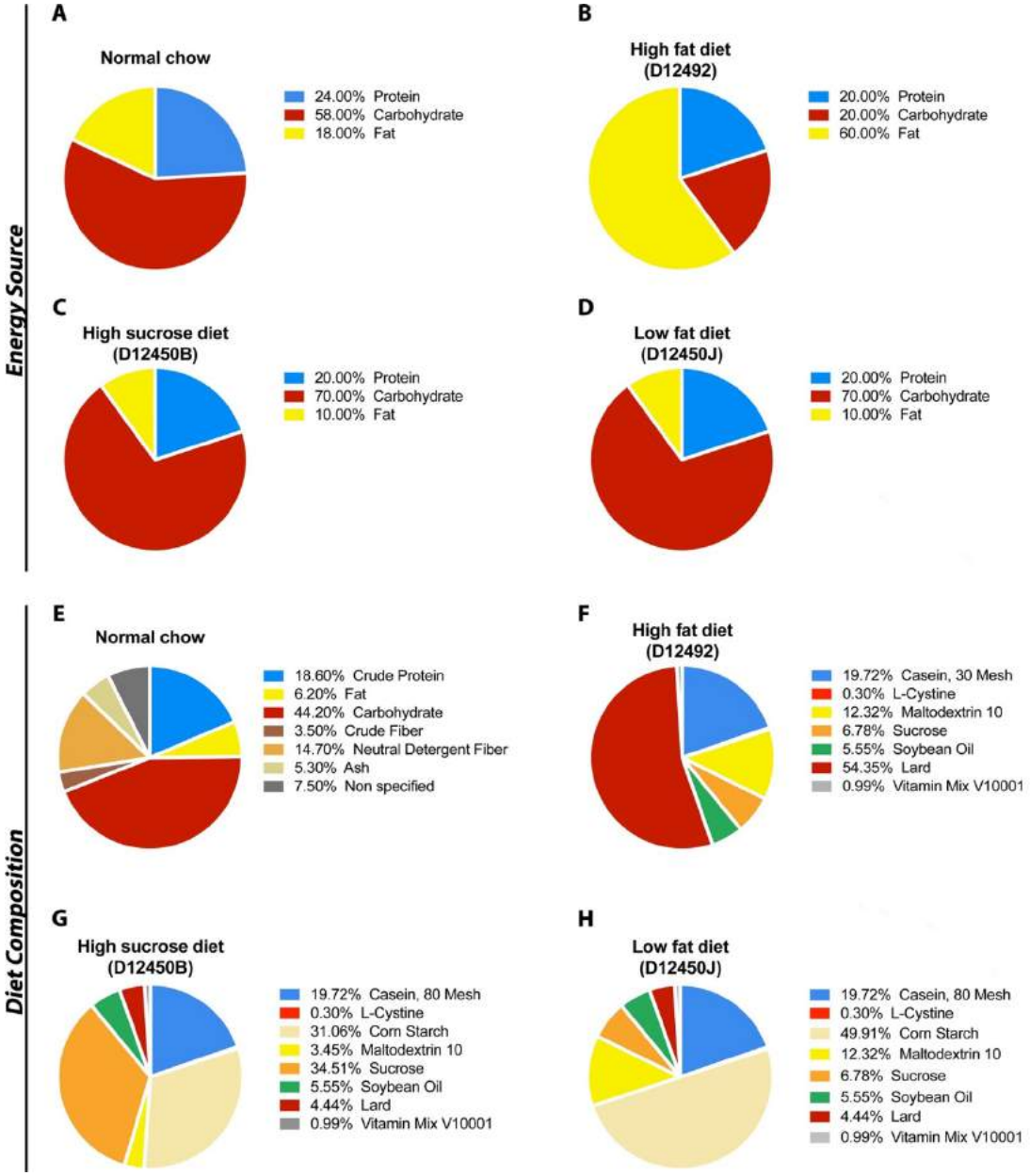

Figure 4.17. Composition of diets used in this study. Energy sources for normal chow (A), high fat diet - Research Diets D12492 (B), high sucrose diet - Research Diets D12450B (C), and low fat diet - Research Diets D12450J (D), are presented. The diet content is shown for normal chow (E), high fat diet - Research Diets D12492 (F), high sucrose diet - Research Diets D12450B (G), and low fat diet - Research Diets D12450J (H).

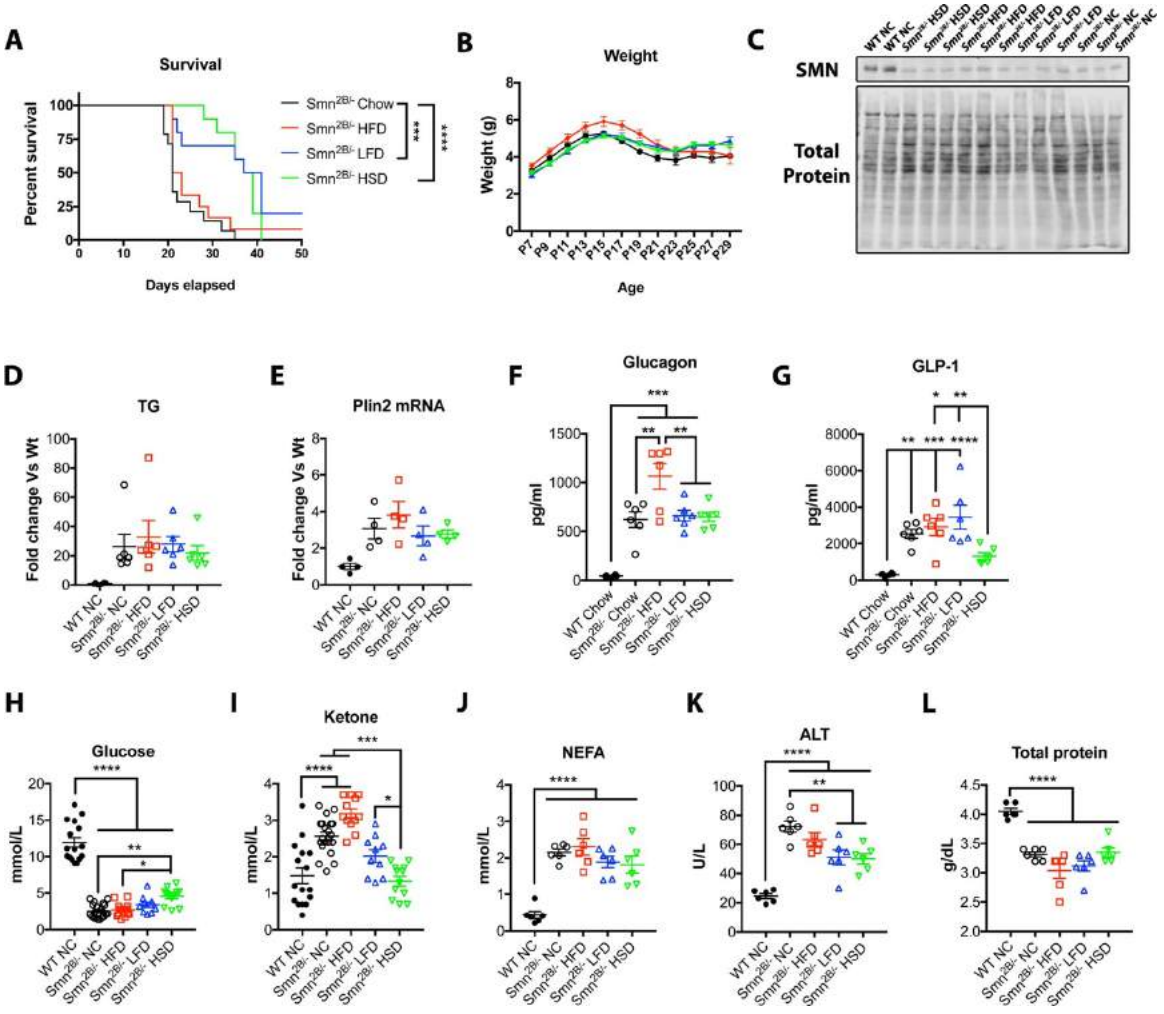

Figure 4.18. Low fat diets enhance survival by switching cell metabolism away from fat as an energy source. (A) LFD and HSD lead to a median survival of 38 and 39 days for *Smn*$^{2B/-}$ mice in comparison to 21 and 22 days when fed NC and HFD, respectively. (B-E) Weight, hepatic SMN, hepatic triglycerides and plin2 mRNA levels were unchanged by the introduction of different diets in *Smn*$^{2B/-}$ mice. (F) Glucagon was further elevated by HFD diet in *Smn*$^{2B/-}$ mice while no change was observed by the introduction of other diets. (G) GLP-1 was considerably diminished upon administration of HSD but not with other diets. (H) Glucose was mostly unchanged by diet modulation, albeit slightly elevated in HSD group. (I) Levels of ketone bodies were enhanced further by introduction of HFD,

significantly diminished by LFD diet, while back to normal with the HSD diet in *Smn*$^{2B/-}$ mice. (J) NEFA were unchanged upon diet modulation, albeit slightly reduced in the HSD cohort. (K) Significant reduction in plasma ALT levels was observed in LFD and HSD cohort, supporting reduced hepatocyte damage. (L) Liver function, as shown by total protein output, was not restored in LFD and HSD cohorts**.** QPCR data were normalized with HPRT1 and Ywhaz in (E) (N value for each experiment is as follows: N = 10-19 for A-B, 3-6 for C-G & J-M, 10-20 for H-I, one-way ANOVA with Tukey's correction, $P \leq 0.05$ for *, $P \leq 0.01$ for **, $P \leq 0.001$ for *** and $P \leq 0.0001$ for ****)

Discussion

Even though metabolic abnormalities, such as impaired glucose homeostasis (210, 211, 288) and amino acid metabolism dysregulation (289) in SMA have emerged recently, systematic research on fatty acid metabolism has remained unexplored. We have shown that patients with SMA are more prone to develop dyslipidemia as well as liver steatosis than the general pediatric population (293-298), with a large subset showing abnormalities when screened with a common lipid and cholesterol panel and SMA liver necropsies. In pre-clinical models, fatty acid abnormalities were identified in 4 commonly used SMA mouse models. With a focus on the $Smn^{2B/-}$ mice, we observe the development of a NAFLD phenotype. This eventually leads to major hepatotoxicity and functional impairment that will impact on multiple organ systems. The NAFLD phenotype likely arises from aberrant glucose levels, leading to altered signaling between liver and pancreas combined with low muscle activity post-denervation. Interestingly, dietary modulation positively impacted lifespan in the $Smn^{2B/-}$ model.

In this study, we provide strong evidence for the susceptibility to dyslipidemia and low glycated hemoglobin levels in large cohort of SMA patients. To our knowledge, this is the first time that such abnormalities are reported. Current statistics on dyslipidemia in one laboratory-defined measure in otherwise healthy children is estimated to be roughly 20% (293, 296). Our studies showed that 37% of SMA patients have dyslipidemia. More strikingly 14% of patients had more than 3 laboratory-defined measures of dyslipidemia, for which prevalence data is sparse in the normal pediatric population. In the same vein, on pathological examination of SMA liver necropsies, we found that a similar proportion

(37.5%) displayed liver steatosis. This is strikingly higher than the prevalence of liver steatosis in 2-4 years old normal children, where fatty liver was found in 0.7% of cases (298). The proportion of fatty liver in our SMA samples was closer to fatty liver prevalence reported in older obese pediatric population, where prevalence can range from 28-77% of the cases (299). Additionally, low HbA_{1C} has been associated with increased all-cause mortality (323-325) and liver disease (326). Given the significant size of our cohort, we feel confident that early screening for metabolic defects will ensure proper clinical metabolic management of SMA patients.

To obtain better insight into the potential mechanisms leading to fatty acid defects in SMA patients, we primarily focused on the longer surviving *Smn*$^{2B/-}$ model mice, which developed an NAFLD phenotype. We conclude from our systematic analysis that NAFLD development in *Smn*$^{2B/-}$ mice is likely multifactorial. A summary of our findings and the proposed mechanism underpinning the defects is illustrated in Figure 4.19. With our current body of evidence, we propose that the initial event leading to fatty acid dysregulation in the liver likely stems from abnormal glucose homeostasis. Hyperglucagonemia is induced early in *Smn*$^{2B/-}$ mice in response to low blood glucose in the bloodstream. Surprisingly, glucose levels in the *Smn*$^{2B/-}$ mice are reduced as early as P9. The glucose level remains low but is sustained, likely due to gluconeogenesis. Eventually, gluconeogenesis fails due to depleted glycogen storage in P19 *Smn*$^{2B/-}$ mice, leading to a sudden drop in glucose level in the blood. Simultaneously, lipolysis of white adipose tissue, a by-product of glucagon signaling, is induced to ensure availability of energy substrate, represented by a progressive increase in NEFA from P9 to P19 in *Smn*$^{2B/-}$

mice. This leads to increased fatty substrates in the bloodstream, which precede or coincide with muscle denervation. Skeletal muscle, a major consumer of energy substrates when innervated and fully functional, will have a diminished requirement for energy as denervation renders it non-functional in SMA. As such, this leads to overload of fatty energy substrates in the circulation. Eventually, the liver will take up the lipid substrates for storage in an attempt to restore homeostasis, which in turn leads to liver steatosis. Pathological fat storage could spill over to the muscle compartment once the liver has reached saturation, which is consistent with our previous description of lipid droplets on ultrastructural analysis of skeletal muscle of *Smn*$^{2B/-}$ mice (162).

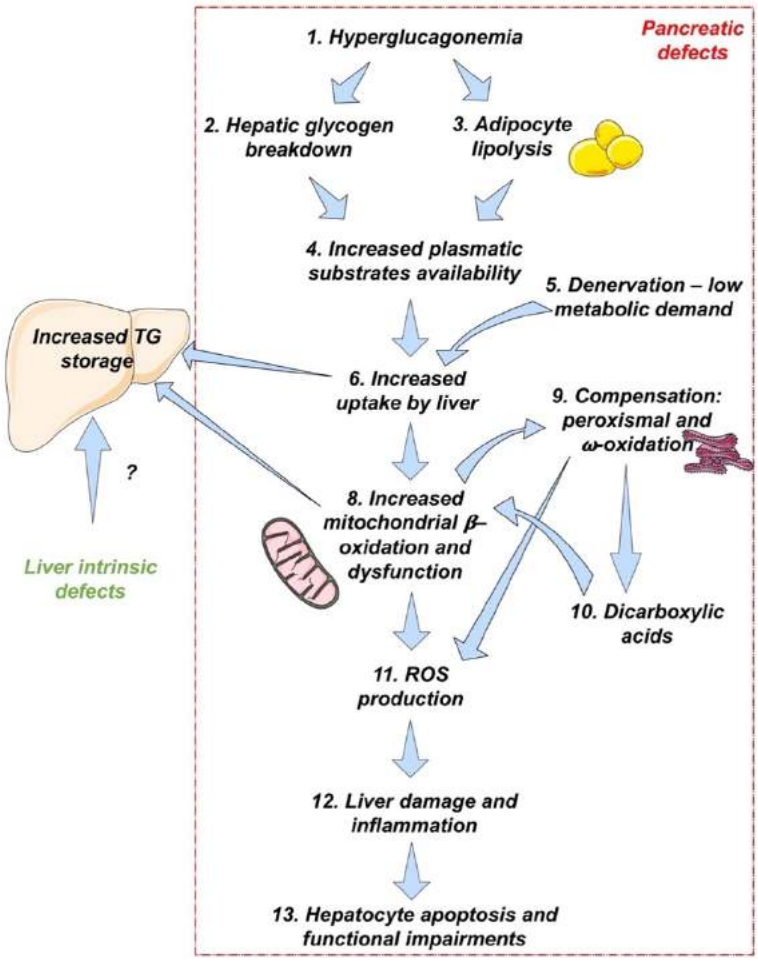

Figure 4.19. Schematic summarizing the findings of the present study. Undefined glucose abnormalities lead to hyperglucagonemia leading to hepatic glycogen breakdown and adipocyte lipolysis. This results in increased plasma energy substrate availability prior or concomitantly to muscle denervation, the major user of energy in the blood. This leads to overload of fatty substrates in the blood, which the liver takes up to restore homeostasis, leading to steatosis. To compensate and dispose the unnecessary lipids, mitochondrial oxidation is increased to burn the lipids, which eventually becomes overloaded and requires alternative peroxisomal and microsomal oxidation pathway. Such a compensation leads to increased ROS production, liver damage, hepatocyte apoptosis and eventually functional impairment.

Strikingly, we found that the rate of triglyceride accumulation in the liver increases very rapidly with progression of disease in the mouse, which could reflect the overall denervation status of the animal. However, denervation alone, in the *SOD1*^{G93A} mouse model of ALS, was not sufficient for the development of liver steatosis. Previous literature in ALS described lipid redistribution rather than accumulation in *SOD1*^{G93A} mice, consistent with our findings (327). This would suggest that a pathological event in SMA, perhaps the hyperactivation of glucagon, is required for the development of NAFLD. The events subsequent to liver steatosis in *Smn*$^{2B/-}$ mice reflects compensatory mechanisms and eventual failure of the hepatocytes. For example, mitochondrial oxidative phosphorylation and leak is enhanced, likely to remove excess fat from the liver. In fact, fatty acid overload enhances secondary pathways of β-oxidation in the peroxisome and microsomal oxidation through cytochrome CYP4A in the endoplasmic reticulum (304). This leads to increased ROS production, and mitochondrial damage and depletion. Interestingly, microsomal oxidation is responsible for dicarboxylic acid production, and dicarboxylic aciduria appears to be a common finding in SMA patients (49-51). Hepatocyte damage then ensues, which compromises liver function.

To further understand the mechanism behind NAFLD, we have performed a proteomic analysis of livers from early neonatal *Smn*$^{2B/-}$ mice. Strikingly, we identified alterations in two important clusters, namely mitochondria and lipid metabolism at and close to birth, and well before any overt pathology develops. SMN depletion may confer susceptibility to liver steatosis, either through deficient fatty acid processing or a reduced mitochondrial oxidative phosphorylation capacity. Interestingly, “mitochondrial pathway

components" are often represented in "omic" data of SMN depleted tissue, including motor neurons (276) diaphragmatic NMJs (328), spinal cord synaptosome fractions (329), hippocampal synapses (330), isolated motor neurons (331), induced pluripotent stem cell motor neurons (332), or directly related to motor neuron vulnerability (333). We assessed whether the main disrupted pathway in the mitochondrial cluster, namely "oxidative phosphorylation", had any functional consequences. Interestingly, we did not observe any deficit in the oxidative capacity of isolated mitochondria from livers of *Smn*$^{2B/-}$ mice. On the contrary, it appears that the mitochondria may even have enhanced capacity, perhaps reflective of a compensatory reaction. It is important to note that abnormal mitochondrial findings have previously been reported in cell culture, SMA models, and patients with SMA (333-338). More specifically, Smn-depleted NSC34 cells had lower levels of ATP, oxidative phosphorylation activation by cytochrome C oxidase and consequent increased free radical production (334). Another report found lower basal and maximal mitochondrial respiration, increased oxidative stress, abnormal mitochondrial transport and structure in primary isolated motor neurons from SMA mice (331). More recently, low ATP levels were identified in spinal cords of SMA mice while reduction of basal respiration and ATP linked respiration were decreased in a *Smn* morphant zebrafish embryo (333). Furthermore, SMA patient muscle biopsies or permeabilized fibers showed decreased complex activity (335-337) and low mitochondrial content (335, 336, 338), with some debate as to whether it is a cause or consequence of the pathogenesis in the muscle. No reports have investigated mitochondrial function in the liver up to now. Given the wide array of findings in the SMA field, it is likely that mitochondrial phenotype in the context of SMA is cell-specific.

To alleviate the NAFLD phenotype, we placed *Smn*$^{2B/-}$ mice and their parents on different diets. Of interest, the median lifespan of the *Smn*$^{2B/-}$ mice was doubled by simple introduction of a new diet. Perhaps not surprising, the two diets with lowest amount of fat, namely LFD and HSD, had the greatest impact. The use of "Research diets" minimized the effect of other substances while maximizing the differences in fat intake or sucrose, in contrast to previous studies comparing two chow diets in an SMA context (339) (Fig 4.17), especially fat content (HFD 60 kcal% VS NC 18 kcal% VS HSD and LFD 10 kcal%). Perhaps one limitation of our study was that the feeding was given to the dams until the pups could freely feed on their own. Hence, it is unknown whether the full extent of the nutritional content of each diet was carried in the milk of the dams. Nonetheless, it was interesting to see that hepatic TG levels, glucagon levels as well as function (total protein and IGF1) of the liver was unchanged by diet modulation, and therefore likely not contributing to the survival benefit. As such, it appears that diet modulation simply decreases fatty substrate availability coming directly from dietary intake, diminishing the load on fatty acid oxidation, as shown by normalization of ketone bodies. This suggests that supplementation of non-fatty substrates for energy use is a key beneficial determinant of survival. Interestingly, it has been speculated that a high-carbohydrate/low-fat diet would benefit SMA patients, as it would provide energy substrates that do not depend on fatty acid oxidation (49). Additionally, hypoglycemia has been reported in SMA, leading the authors to suggest frequent meals consisting of carbohydrates and proteins (134, 340). A LFD/high carbohydrate diet with riboflavin, coenzyme Q10, and L-carnitine supplementation was tested in 13 SMA patients in the 1990's (341). While the authors claimed beneficial outcome in the majority of SMA patients, there was some controversy

about the classification scheme used in the study, which may have made interpretation of the results difficult (49). As such, it remains unknown whether LFD/HSD could provide significant clinical improvement in SMA patients. Currently, a popular diet with the SMA patient community is the amino acid diet. This diet offers high protein, low fat, and high glucose. Indeed, such diets may help to normalize metabolic homeostasis and perhaps lead to a reduction in comorbidities. Regardless, our findings strongly suggest that clinical nutritional guidelines need to be established to provide better care for SMA patients.

Altogether, our clinical studies in SMA patients as well as preclinical mouse studies, provide strong evidence of defects in fatty acid metabolism. The greater predisposition to develop dyslipidemia in SMA patients as well as the identification of a NAFLD in the $Smn^{2B/-}$ mice emphasize the possibility that defects in metabolism can lead to added comorbidities, especially in the new therapeutic era of SMA, where lifespan is extended. Indeed, this work further highlights the importance of establishing currently lacking nutritional guidelines, performing early screening for metabolic defects in treated SMA patients, as well as developing systemic therapeutic strategies that incorporate non-neuronal organs to ensure overall optimal management of SMA.

Materials and Methods

Mouse Models

The *Smn*$^{-/-}$*;SMN2* (Jackson Laboratory), *Smn*$^{-/-}$*;SMN2*$^{+/+}$*;SMNΔ7* and *Smn*$^{2B/-}$ (wild type BL/6J background) (157) mouse lines were housed at the University of Ottawa Animal Facility and cared for according to the Canadian Council on Animal Care. Experimentation and breeding were performed under protocol OHRI-1948 and OHRI-1927. *Smn*$^{+/-}$ mice were crossed to *Smn*$^{2B/2B}$ mice to obtain *Smn*$^{2B/+}$ and *Smn*$^{2B/-}$ animals. C57BL/6J wild type mice were bred separately. The Taiwanese *Smn*$^{-/-}$*;SMN2* (FVB/N background, FVB.Cg-Smn1^{tm1Hung}Tg(SMN2)2Hung/J from Jackson Laboratory #005058) and *SOD1*^{G93A} mice (B6.Cg-Tg(SOD1*G93A)1Gur/J from Jackson Laboratory #004435) were housed at the Biomedical Sciences Unit, University of Oxford or within Biological Research Resources at the University of Edinburgh. All experiments using mice in the UK were performed in accordance with the licensing procedures authorized by the UK Home Office (Animal Scientific Procedures Act 1986). All tissues were collected while mice were fed *ad libitum*. Sex difference analysis was performed in the diet modulation experiments set.

Patient data

Infant and young SMA patients were recruited from two clinical referral centers for SMA in Italy (UO Neurologia dello Sviluppo, Fondazione IRCCS Instituto Neurologico Carlo Besta, Milan, Italy and SAPRE-UONPIA, Fondazione IRCCS Ca' Granda Ospedale Maggiore Policlinico, Milan, Italy). The study protocol was approved by institution ethics review boards (University of Milan #7/16 and Carlo Besta Neurological Institute

Foundation #37/2016). Adult SMA patients were recruited at the Ottawa Hospital under the Care 4 Rare protocol (Protocol #20150232-O1H), and necropsies were obtained at BC Children's Hospital (Protocol #H18-00038). All patients have genetically confirmed diagnosis of SMA (except necropsies – see below) and they were explained benefits and risks of the study, and consented to the study. This study used cut-off values proposed by the National Cholesterol Education Program (NCEP) (342, 343). Adult dyslipidemia cut-off values were extracted from the third report of the National Cholesterol Education Program (NCEP) expert panel on Detection, Evaluation and Treatment of High Blood Cholesterol in Adults (Adult Treatment Panel III) and The National Lipid Association recommendations for patient-centered management of dyslipidemia: Part 1 - executive summary.

Liver pathology of human necropsies

Ten cases of human SMA were retrieved from the pathology files of the British Columbia's Children Hospital and the Children's Hospital of Eastern Ontario. After review, two cases were not retained: one had associated features of olivo-ponto-cerebellar atrophy; the other because of negative familial genetic studies performed 16 years later and because of the presence of non-motor changes at histology, in the spinal cord. The autopsies were performed between 1977 and 1996. The pathology reports were available. The neuropathological findings of the eight retained cases were reviewed and the diagnosis of SMA was confirmed. Slides from the liver were available in all cases. The selected clinical and histological findings of the eight retained cases of SMA type I or II are

summarized in Table 4.4. Seven cases were of SMA type I: four females and three males, aged from less than a month to 3 years. One SMA type II case was a female aged 13 years.

Gross morphology, tissue processing and staining of animal tissues

A 0.75X picture of the liver was taken with a Leica M80 dissection microscope mounted with a camera (Leica IC80 HD). Livers, WAT and TA muscles were fixed in formalin (1:10 dilution buffered, from Protocol, cat #245-684) for 24-48 h or 72 h (WAT) at 4ºC and then transferred in 70% ethanol at 4ºC until processing. All samples were processed at the University of Ottawa (Department of Pathology and Laboratory Medicine) and embedded in wax using a LOGOS microwave hybrid tissue processor. Paraffin block tissues were cut with a microtome at 3-4 μm thickness. Hematoxylin & eosin (H&E) staining was performed using a Leica autostainer XL Leica CV. Periodic acid-Schiff (PAS), Prussian blue, oil red O and Sirius red staining were performed using standard methods. Tissue sections for immunofluorescence staining were sectioned (5 μm) on cryostat for frozen sections (Leica, CM3050 S) or microtome for wax-embedded sections (Leica, RM2125 RTS). Liver sections were stained for caspase 3 (Abcam Ab13847 1:100) and collagen IV (Millipore AB756P 1:100). Antigen retrieval was performed to visualize Casp3. Briefly, air dried sections were quickly washed in PBS, then submerged into pre-warmed Antigen Retrieval Buffer and placed into water bath set at 90°C for 40 min (Caspase 3). Once the time was up, the sections were removed from the bath but left submerged in the buffer allowing them to cool down but not dry out. After approximately 30 min, the slides were quickly washed in PBS and subjected to the traditional IHC staining protocol. Acquisition of signal was either obtained by slide scanning with a MIRAX MIDI digital slide scanner (Zeiss) and images acquired using 3DHISTECH Panoramic Viewer

1.15.4/CaseViewer 2.1 or directly captured using a Nikon eclipse e400 microscope (x10, x20 or x40 objective) and its images captured using QICAM Fast 1394 camera and Improvision Velocity 4 image capture software.

Total Protein Assay

Frozen liver samples were homogenized in 100 µl of RIPA buffer containing 1% of Halt Protease Inhibitor cocktail. The protein concentration of individual liver samples was determined by BCA assay.

Total ALP in situ *assay*

Liver sections on slides were washed in PBS twice for 5 min each, followed by three washes in NTMT (100 mM NaCl, 100 mM Tris-HCl pH 9.5, 50 mM MgCl2, and 1% Tween-20) for 10 min each. After incubation in color reaction solution (NTB, BCIP, and NTMT buffer), sections were washed in NTMT twice for 10 min each, followed by two washes in PBS for 10 min each. Sections were post-fixed in 4%PFA for 30 min, washed in PBS twice for 10 min each, and slides mounted in 90% glycerol.

Gene expression studies

RNA from liver, spinal cord, and tibialis anterior muscle were extracted using Qiagen RNeasy Mini kit and reverse transcribed using RT^2 first strand kit according to manufacturer's protocol. Qiagen microarray fatty acid metabolism (PAMM-007Z) and fatty liver (PAMM-157Z) were used and were analyzed using RT^2 Profiler PCR Array Data

Analysis (http://saweb2.sabiosciences.com/pcr/arrayanalysis.php). Automatic selection from Housekeeping group panel was used as a method of normalization. Individual QPCR was performed in triplicate for each sample. A complete list of primers is available in the supplementary material (Table 4.5). A standard curve was performed for each primer set to ensure their efficiencies. Each QPCR reaction contained equal amount of cDNA, Evagreen SyBR (Biorad), RNase/DNase-free water and appropriate primers (100-200 nM or according to PrimePCR protocol) in a final volume of 25 µl or 20 µl (for primePCR primers). To confirm amplicon specificity, a melting curve analysis was performed. Two negative controls were included in every QPCR plate and consisted of water in lieu of cDNA. QPCR results were quantified using $2^{-\Delta\Delta Ct}$ method. Results were normalized with 2 genes (mentioned in each figure legend containing QPCR data) identified as appropriate stable internal reference given M value below 0.5 and coefficient of variance below 0.25.

Table 4.5. Primers used in this study

Gene name	Short form	Forward	Reverse	Prime PCR
TNF Receptor Superfamily Member 6	FasR	TGTGAACATGGAACCCTTGA	TTCAGGGTCATCCTGTCTCC	
TNF Receptor Superfamily Member 1A	TNFR1	CCGGGAGAAGAGGGATAGCTT	TCGGACAGTCACTCACCAAGT	
Caspase 8	Casp8	GGCCTCCATCTATGACCTGA	TGTGGTTCTGTTGCTCGAAG	
BCL2 Associated X, Apoptosis Regulator	Bax	TGCAGAGGATGATTGCTGAC	GATCAGCTCGGGCACTTTAG	
BH3 interacting domain death agonist	Bid			qMmuCID0022679
Tumor Protein P53	p53	GCTTCTCCGAAGACTGGATG	CTTCACTTGGGCCTTCAAAA	
Cyclin-dependent kinase inhibitor 1A (P21)	p21			qMmuCED0046265
Transformed mouse 3T3 cell double minute 2	Mdm2			qMmuCID0025320
Complement C1r	C1R	AACCATATTACAAGATGCTGACCA	CCTTGGGCTGTGCAGGTA	
Complement C1s	C1S	GGTGGATACTTCTGCTCCTGTC	AGGGCAGTGAACACATCTCC	
Complement C1q B chain	C1qb	CGTCGGCCCTAAGGGTACT	GGGGCTGTTGATGGTCCTC	
Complement C3	C3	CCAGCTCCCCATTAGCTCTG	GCACTTGCCTCTTTAGGAAGTC	
Complement C4	C4	TCTCACAAACCCCTCGACAT	AGCATCCTGGAACACCTGAA	
Complement C5	C5	AGGGTACTTTGCCTGCTGAA	TGTGAAGGTGCTCTTGGATG	
Complement C6	C6			qMmuCID0025195
Complement Factor B	Factor B	GAGCGCAACTCCAGTGCTT	GAGGGACATAGGTACTCCAGG	
Coagulation Factor II, Thrombin	F2			qMmuCED0046327
Coagulation Factor V	F5	CATGGAAACCTTACCGACAGAAA	CATGTGCCCCTTGGTATTGC	
Coagulation Factor VII	F7	CGTCTGCTTCTGCCTCTTAGA	ATTTGCACAGATCAGCTGCTCAT	
Coagulation Factor IX	F9	GCAAAACCGGGTCAAATCC	ACCTCCACAGAATGCCTCAATT	
Coagulation Factor X	F10			qMmuCED0048020
Protein C, Inactivator Of Coagulation Factors Va And VIIIa	ProC			

Protein S	ProS			qMmuCED0045958
Protein Z, Vitamin K Dependent Plasma Glycoprotein	ProZ			
Thrombopoietin	Thpo			qMmuCED0037967
Hepatocyte Nuclear Factor 4 Alpha	Hnf4a	AGAGGTTCTGTCCCAGCAGATC	CGTCTGTGATGTTGGCAATC	
Insulin-like growth factor 1	IGF1			qMmuCID0005726
Insulin-like growth factor I receptor	IGF1R			qMmuCID0005315
Insulin-like growth factor binding protein, acid labile subunit	IGFals			qMmuCID0008201
Insulin-like growth factor binding protein 1	IGFbp1			qMmuCID0027402
Insulin-like growth factor binding protein 3	IGFbp3			qMmuCID0005232
Hepcidin	Hamp	CCTATCTCCATCAACAGATG	AACAGATACCACACTGGGAA	
Transferrin	TF	CCATCCCATCACAACAAGGTATC	GCTAGTGTCCGATGCCTTCAC	
Heme Oxygenase	Hmox1	GCCACCAAGGAGGTACACAT	GCTTGTTGCGCTCTATCTCC	
Ceruloplasmin	Cp	TCTACCAAGGAGTAGCCAGGA	ATCTTCCCTCTCATCCGTGC	
Ferritin light chain	L-Ferritin	CGTCTCCTCGAGTTTCAGAAC	CTCCTGGGTTTTACCCCATTC	
Ferritin heavy chain	H-Ferritin	CCATCAACCGCCAGATCAAC	GCCACATCATCTCGGTCAAA	
Solute Carrier Family 40 Member 1	Ferroportin	GCTGCTAGAATCGGTCTTTGGT	CAGCAACTGTGTCACCGTCAA	
Solute carrier family 11 (proton-coupled divalent metal ion transporters), member 2	Nramp2			qMmuCID0016356
tyrosine 3-monooxygenase/ tryptophan 5-monooxygenase activation protein, zeta polypeptide	Ywhaz	AAGACAGCACGCTAATAATGC	TTGGAAGGCCGGTTAATTTTC	
succinate dehydrogenase	Sdha	GCCTGGTCTGTATGCCTGTG	CCGATTCTTCTCCAGCATTTG	

complex, subunit A, flavoprotein				
polymerase (RNA) II (DNA directed) polypeptide J	Polr2j	ACCACACTCTGGGGAACATC	CTCGCTGATGAGGTCTGTGA	
hypoxanthine guanine phosphoribosyl transferase	Hprt1	CCCAGCGTCGTGATTAGTGATG	TTCAGTCCTGTCCATAATCAGTC	

Immunoblotting

Total protein lysate was collected by homogenization of flash frozen liver and tibialis anterior muscles in RIPA lysis buffer (Cell Signaling). Protein concentrations were determined using the Bradford assay (Bio-Rad). Protein extracts were subjected to sodium dodecyl sulfate polyacrylamide gel electrophoresis and examined by immunoblot, as previously described (205) with modified blocking conditions where Odyssey blocking buffer (Li-Cor 927-40000) replaced 5% milk. Revert Total protein stain (Li-Cor 926-11010) was used as per the manufacturer's protocol. Primary antibodies used were as follows: Anti-Smn (BD Transduction, 610647 - 1:15000), pCreb (Ser133) (Cell Signalling 9198, 1:1000), Creb (Cell Signalling 9104, 1:1000), MitoOxphos (Abcam, ab110413 - 1:250), alpha-tubulin (Abcam, ab4074 - 1:2500-5000 and Calbiochem, CP06 1:10000), Cyp4A (Abcam, ab3573 - 1:1000), Cyp2E1 (Abcam, ab28146 - 1:2500), Secondary antibodies used were IRDye (Li-Cor) 680 or 800 (Li-Cor - 1:10000 to 1:20000). Signals were detected with Odyssey CLx (Li-Cor). Results were normalized to total protein or tubulin. Full western blots can be visualized in Fig. 4.20.

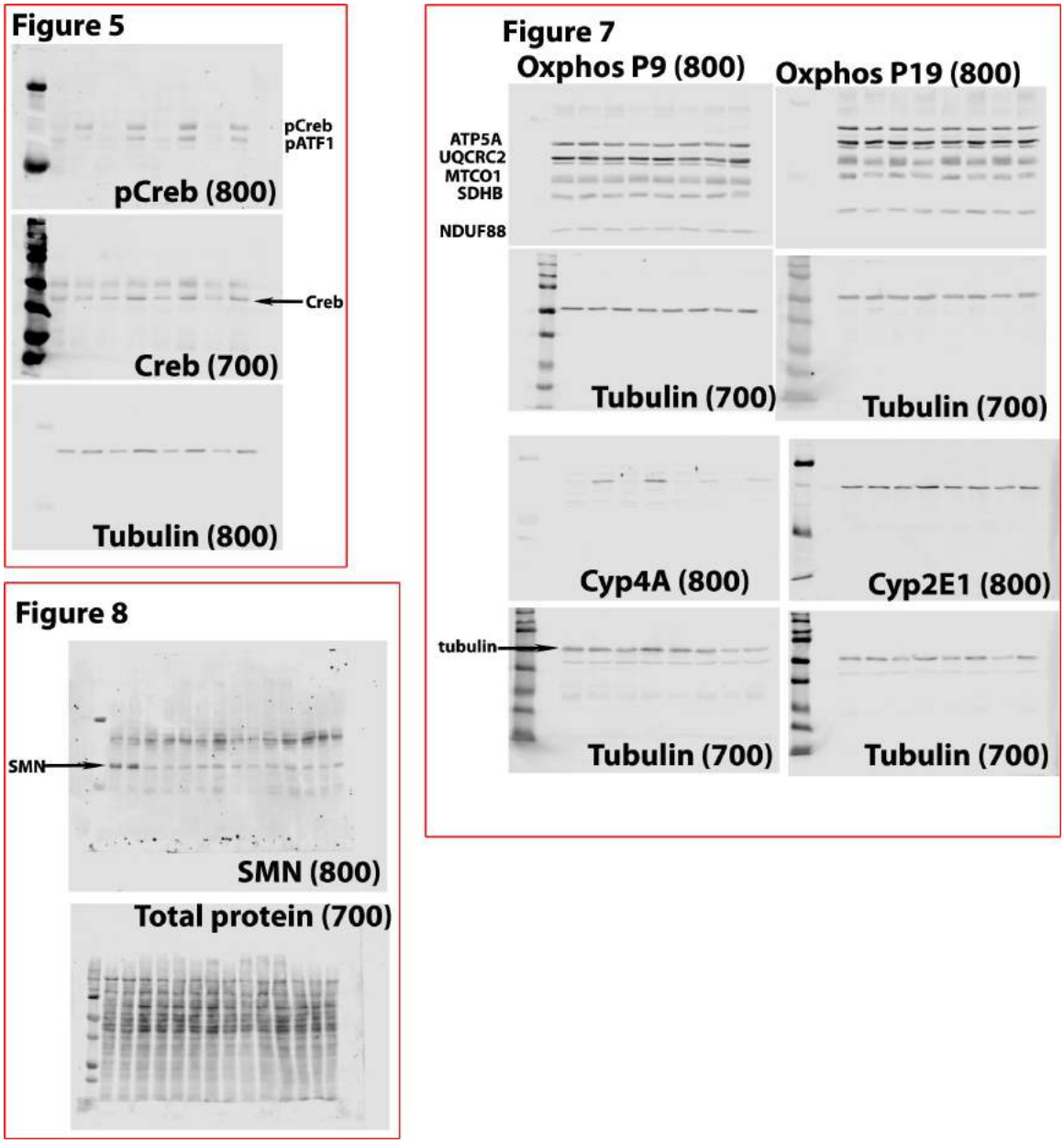

Figure 4.20. Non-cropped raw western blot data. Raw western blots presented per figure. Protein probed by antibody as well as channel used for identification via Odyssey acquisition system are written on each image. The numbers identify either the 700 or 800 nm wavelength fluorescence.

Transmission Electron Microscopy

Electron microscopy was performed as previously described in (162) .

High-resolution respirometry

Livers were excised from P9 and P19-21 *Smn*$^{2B/+}$ and *Smn*$^{2B/-}$ mice. Mitochondria were isolated using a slightly modified version from (344). Briefly, livers were washed in IB_C buffer and then minced and resuspended into 3 (P19) or 2 ml (P9) of IB_C buffer. Liver pieces were then transferred to a glass-Teflon homogenizer for homogenization using electric rotator. The homogenates were then spun at 800g for 10 min at 4ºC, supernatant was transferred to a new tube and spun again 8600g 10 mins at 4ºC, where pellet was resuspended in half initial volume of IB_C buffer. This process was repeated once. Mitochondria were indirectly quantified by Bradford assay. 700 ug (P19-21) and 500 ug (P9) of mitochondria were then introduced in the high-resolution respirometer (O2K; Oroboros, Austria) for respirometry measurements. The list and order of substrates and compounds introduced in the chamber for each protocol can be found in Table 4.6 and 4.7. The substrates and compounds were added to the chamber after mitochondria reached steady state. Quantification was performed using the Oroboros software.

Table 4.6. Oxygraph protocol in the absence of fatty acids

Substrate	Volume	Concentration of Stock	Concentration of substrate in the chamber
Amplex ultra red	2 uL	10 mM	50 uM
Horseradish peroxidase	10 uL	10 mM	10 U/mL
H2O2	5 ul	40 uM	0.1 uM titrations X3
800 mM Malate	5 uL	800 mM	2 mM
Pyruvate	10 uL	2 M	5 mM
ADP/Mg2+	20 uL, 20 uL	500 mM	5 mM
Glutamate	10 uL	2 M	10 mM
Succinate	20 uL	1 M	10 mM
500 mM ADP/Mg	20 uL, 20 uL	500 mM	5 mM
Oligomycin	1 ul	5 mM	2.5 μM
FCCP	0.5 uL titrations until max respiration	1 mM	0.25 uM titration
Antimycin A	1 uL	5 mM	2.5 uM
Ascorbate + TMPD	5 uL, 5 uL	800 mM Asc, 200 mM TMPD	2 mM Asc, 0.5 mM TMPD
Sodium Azide	50 uL	4 M	100 mM

Table 4.7. Oxygraph protocol in the presence of fatty acids

Substrate	Volume	Concentration of Stock	Concentration of substrate in the chamber
800 mM Malate	5 uL	800 mM	2 mM
Oct Car	4 uL	100 mM	0.2 mM
ADP/Mg2+	20 uL, 20 uL	500 mM	5 mM
Pyruvate	10 uL	2 M	5 mM
Glutamate	10 uL	2 M	10 mM
Succinate	20 uL	1 M	10 mM
500 mM ADP/Mg	20 uL, 20 uL	500 mM	5 mM
Oligomycin	1 ul	5 mM	2.5 uM
FCCP	0.5 uL titrations until max respiration	1 mM	0.25uM titration
Antimycin A	1 uL	5 mM	2.5 uM
Ascorbate + TMPD	5 uL, 5 uL	800 mM Asc, 200 mM TMPD	2 mM Asc, 0.5 mM TMPD
Sodium Azide	50 uL	4 M	100 mM

CPT1 enzymatic assay

For CPT1 enzymatic assay, liver was homogenized in ice-cold Tris-EDTA buffer (25 mM Tris-HCl pH7.8, 1 mM EDTA, 2 mM $MgCl_2$, 50 mM KCl, 0.50% TritonX-100). Homogenates were centrifuged at 14,000 × g for 10 min at 4ºC. CPT1 activity was determined by measuring absorbance at 412 nm in 50 mM Tris-HCl pH8.0 with 0.2 mM DTNB in a buffer containing 150 mM KCl, 0.1 mM palmitoyl-CoA and 0.25 mM l-carnitine.

Diet modulation

Dams and partner were provided normal chow, HFD (Research diets – D12492), LFD (Research diets – D12450J), HSD (Research diets – D12450B) 2 weeks after putting the breeding pair together. Diet composition is illustrated in Fig 4.17. It was previously shown to be sufficient to induce composition change in milk and in the body composition of the pups (321). Food was put at the bottom of the cage and changed every two days as recommended by Research diets. Following weaning, mice were provided with the diets their parents were on until endpoint. At least 3 males and females were found in each group to account for sex differences.

Lipid quantification

Tissues were extracted and flash frozen. When required, tissues were pooled to obtain 100 mg. Tissue lipid analysis for quantification and profiles were performed at the Vanderbilt Mouse Metabolic Phenotyping Center. Lipids were extracted using the method

of Folch-Lees (345). The extracts were filtered, and lipids recovered in the chloroform phase. Individual lipid classes were separated by thin layer chromatography using Silica Gel 60 A plates developed in petroleum ether, ethyl ether, acetic acid (80:20:1) and visualized by rhodamine 6G. Phospholipids, diglycerides, triglycerides and cholesteryl esters were scraped from the plates and methylated using BF3/methanol as described in (346). The methylated fatty acids were extracted and analyzed by gas chromatography. Gas chromatographic analyses were performed on an Agilent 7890A gas chromatograph equipped with flame ionization detectors, a capillary column (SP2380, 0.25 mm x 30 m, 0.25 μm film, Supelco, Bellefonte, PA). Helium was used as a carrier gas. The oven temperature was programmed from 160ºC to 230ºC at 4ºC/min. Fatty acid methyl esters were identified by comparing the retention times to those of known standards. Inclusion of lipid standards with odd chain fatty acids permitted quantification of the amount of lipid in the sample. Dipentadecanoyl phosphatidylcholine (C15:0), diheptadecanoin (C17:0), trieicosenoin (C20:1), and cholesteryl eicosenoate (C20:1) were used as standards. Cholesterol and unesterified cholesterol quantification protocol was adapted from (347). Briefly, for cholesterol, internal standard (5-a-cholestane) was added to a portion of the lipid extract and then saponified at 80ºC in 1 N KOH in 90% methanol for 1 h. The nonsaponifiable sterol was extracted into hexane, concentrated under nitrogen, and then solubilized in carbon disulfide to inject into the gas chromatograph. For unesterified cholesterol, internal standard is added to a portion of the lipid extract, concentrated under nitrogen and then solubilized in carbon disulfide to inject into the gas chromatograph. The Agilent 7890A gas chromatograph was equipped with an HP-50+ column (0.53 mm i.d x 30 m, Agilent) and a flame ionization detector. The oven temperature was 260ºC and

nitrogen was used as the carrier gas. Data shown includes chain length for which data was available (i.e. within the dynamic quantification range) for all animals in each analysis, with the exception of Fig. 4.1I and Fig. 4.2J where only SMA samples had lipids identifiable.

Blood chemistry

Blood was collected following decapitation of the mice and collection of the blood via capillary using Microcuvette CB 300 K2E coated with K2 EDTA (16.444.100). All the blood collected in this study was sampled randomly (i.e. no fasting period) between 9 and 11 am to limit the effect of the circadian rhythm. Mice were subsequently dissected as soon as possible to limit the effect of fasting. Samples were then spun at 2000 g for 5 min at room temperature to extract plasma. Samples were pooled when large assay volume were required. Analysis of albumin, total protein, ALP, ALT, AST, bilirubin, iron, total cholesterol, HDL, LDL, triglycerides, NEFA (P19 only), and glucose were performed at the National Mouse Metabolic Phenotyping Center (MMPC) at the University of Massachusetts Medical School using a Cobas Clinical Chemistry Analyzer (Roche Diagnostics, Indianapolis, IN, USA) while plasma non-esterified fatty acid (NEFA) levels were measured photometrically using a kit (Zenbio, Durham, NC), according to the manufacturer's protocol. Analysis of glucose, triglycerides and NEFA (P9-P13) was performed at Comparative Clinical Pathology Services, LLC., Columbia, Missouri, using commercially available assays on a Beckman-Coulter AU680 Automated Clinical Chemistry analyzer (Beckman-Coulter, Inc., Brea, CA). Triglyceride and glucose assays were obtained from Beckman-Coulter and the assay for non-essential Fatty Acids from

Randox Laboratories (Randox Laboratories, Ltd., Kearneysville, West Virginia). For the analysis of random ketone and glucose over the lifespan of the *Smn*$^{2B/-}$ mice, we used the Freestyle Precision Neo Blood Glucose and Ketone monitor system and its associated glucose and ketone strips. In this study, we also used Luminex xMAP technology for multiplexed quantification of cytokines, chemokines, and growth factors. The multiplexing analysis was performed using the Luminex™ 100 system (Luminex, Austin, TX, USA) by Eve Technologies Corp. (Calgary, Alberta). Eleven markers were simultaneously measured in the samples using a MILLIPLEX Mouse Cytokine/Chemokine 11-plex kit (Millipore, St. Charles, MO, USA) according to the manufacturer's protocol. The 11-plex consisted of Amylin (active), C-Peptide 2, GIP (total), GLP-1 (active), ghrelin (active), glucagon, insulin, leptin, PP, PYY and Resistin. The assay sensitivities of these markers range from 1-23 pg/mL for the 11-plex. Individual analyte values are available in the MILLIPLEX protocol. IGF-1 was measured in the samples using a R&D Systems Mouse 1-Plex Luminex Assay (R&D Systems, Minneapolis, MN, USA) according to the manufacturer's protocol. The assay sensitivity of this marker is 3.46 pg/mL. Adiponectin was measured in the samples using MILLIPLEX Mouse Cytokine/Chemokine 1-plex kit (Millipore, St. Charles, MO, USA) according to the manufacturer's protocol. The assay sensitivity of this marker is 3 pg/mL. For experiments using Luminex system, if analytes were too low to be identified and outside of the dynamic range, it was deemed to be zero and reflected as such on dot plot graphs.

Proteomic analysis

Tandem mass tagging and fractionation of extracted samples was performed by the FingerPrints Proteomics facilities at the University of Dundee, to the following protocol: Protein samples were thawed, trypsinised and desalted at room temperature. 100µg of desalted tryptic peptides per sample were dissolved in 100µl of 100mM tetraethylammonium bromide (TEAB). The 10 different tandem mass tag (TMT) labels comprising the TMT10plex™ kit (Thermo Fisher Scientific) were dissolved in 41µL anhydrous acetonitrile. Each dissolved label was added to a different sample. Samples were labelled as follows: **Sample B** – Tag 127N Liver from WT at P0; **Sample D** – Tag 128N Liver from *Smn*$^{2B/-}$ mice at P0; **Sample G** – Tag 129C Liver from WT at P2; **Sample I** – Tag 130C Liver from *Smn*$^{2B/-}$ mice at P2 (this was part of a wider proteomic screen, hence the discontinuous lettering). The sample-label mixture was incubated for 1 hour at room temperature. Labelling reaction was stopped by adding 8µl of 5% hydroxylamine per sample. Following labelling with TMT, samples were mixed, desalted, and dried in a speed-vac at 30°C. Samples were re-dissolved in 200µl ammonium formate (NH_4HCO_2) (10mM, pH 10) and peptides were fractionated using an Ultimate 3000 RP-High pH High Performance Liquid Chromatography column (Thermo-Scientific) containing an XBridge C18 column (XBridge peptide BEH, 130Å, 3.5 µm, 2.1 X 150 mm) (Waters, Ireland) with an XBridge guard column (XBridge, C18, 3.5 µm, 2.1X10mm) (Waters, Ireland). Buffers A and B used for fractionation consist, respectively, of (A) 10mM ammonium formate in milliQ water and (B) 10mM ammonium formate with 90% acetonitrile. Before use, both buffers were adjusted to pH10 with ammonia. Fractions were collected using a WPS-3000FC auto-sampler (Thermo-Scientific) at 1 minute intervals. Column and guard column

were equilibrated with 2% Buffer B for twenty minutes at a constant flow rate of 0.2ml/min. 175µl per sample was loaded onto the column at a rate of 0.2ml/min, and the separation gradient was started 1 minute after sample was loaded onto the column. Peptides were eluted from the column with a gradient of 2% Buffer B to 5% Buffer B in 6 minutes, and then from 5% Buffer B to 60% Buffer B in 50 minutes. Column was washed for 16 minutes in 100% Buffer B and equilibrated at 2% Buffer B for 20 minutes as mentioned previously. The fraction collection started 1 minute after injection and stopped after 80 minutes (total 80 fractions, 200µl each). The total number of fractions concatenated was set to 15 and the content of the fractions was dried and suspended in 50µl of 1% formic acid prior to analysis with liquid chromatography-mass spectrometry (LC-MS).

LC-MS/MS Analysis

Liquid chromatography- tandem mass spectrometry was performed by FingerPrints Proteomics Facilities at the University of Dundee, to the following protocol:

Analysis of peptide readout was performed on a Q Exactive™ HF Hybrid Quadrupole-Orbitrap™ Mass Spectrometer (Thermo Scientific) coupled with a Dionex Ultimate 3000 RS (Thermo Scientific). LC buffers were made up to the following: Buffer A (2% acetonitrile and 0.1% formic acid in Milli-Q water (v/v)) and Buffer B (80% acetonitrile and 0.08% formic acid in Milli-Q water (v/v). Aliquots of 15µl per sample were loaded at a rate of 5µL/minute onto a trap column (100 µm × 2 cm, PepMap nanoViper C18 column, 5 µm, 100 Å, Thermo Scientific) which was equilibrated with 98% Buffer A. The trap column was washed for 6 minutes at the same flow rate and then the trap column was switched in-line with a resolving C18 column (Thermo Scientific) (75 µm × 50 cm,

PepMap RSLC C18 column, 2 µm, 100 Å). Peptides were eluted from the column at a constant flow rate of 300 nl/min with a linear gradient from 95% Buffer A to 40% Buffer B in 122 min, and then to 98% Buffer B by 132 min. The resolving column was then washed with 95% Buffer B for 15 min and re-equilibrated in 98% Buffer A for 32 min. Q Exactive™ HF was used in data dependent mode. A scan cycle was comprised of a MS1 scan (m/z range from 335-1800, with a maximum ion injection time of 50 ms, a resolution of 120 000 and automatic gain control (AGC) value of $3x10^6$) followed by 15 sequential-dependent MS2 scans (with an isolation window set to 0.4 Da, resolution at 60000, maximum ion injection time at 200 ms and AGC 1x105. To ensure mass accuracy, the mass spectrometer was calibrated on the first day that the runs were performed.

Database search and protein identifications

Raw MS data from the 15 fractions were searched against mouse (*Mus musculus*) protein sequences from UniProtKB/Swiss-Prot (Version 20160629) using the MASCOT search engine (Matrix Science, Version 2.4) through Proteome Discoverer™ software (Version 1.4.1.14, Thermo Fisher). Parameters for database search were as follows: MS1 Tolerance: 10ppm; MS2 Tolerance: 0.06da; fixed modification: Carbamidomethyl (C) Variable Modification: Oxidation (M), Dioxidation (M), Acetyl (N-term), Gln->pyro-Glu (N-term Q), TMT 10(N-term and K); maximum missed cleavage: 2; and target false discovery rate (FDR) 0.01. All identifications were quantified as relative ratios of expression compared to relevant controls through Proteome Discoverer™ software (Thermo Fisher, Version detailed above). Relative ratios along with UnitProtKB/Swiss-

Prot identifications were exported into Microsoft Excel as a raw data file for further in-silico analysis.

In-Silico Analysis

Mass spec data (from above) was manually subdivided into four distinct groups - Group A (changed at P1 but not at P3), B (changed at P1 and P3), C (not changed at P1, but changed at P3) and NS, depending on the protein expression changes at P1 and P3 with level of significance identified as expression change increased or decreased by 20%. This procedure allows proteins most likely to be involved in the development of pathology, namely those altered at P1 and P3 or P4 only (Groups B and C) to be identified. These subgroups were then uploaded into the BioLayout *Express*3D for expression profile clustering, DAVID functional annotation for enrichment analysis or Ingenuity Pathway analysis (IPA) for hierarchical cascade mapping and upstream regulator prediction. See below.

BioLayoutExpress3D

BioLayout*Express*3D (348) is a tool for visualization and clustering data. Routinely, proteomic data sets are uploaded to BioLayout *Express*3D, a Pearson's correlation coefficient (*r*-value) is used to measure similarity between protein expression profiles and a threshold for the Pearson's correlation coefficient is set. The data set is then visualized as nodes (proteins) that are connected to each other in a network based on their expression levels (edges). This data set can further be subdivided into discreet "clusters"

based on a Markov Clustering Algorithm (MCL), thus segregating data in an unbiased manner (as previously described (as previously described (349-351)).

DAVID

The Database for Annotation, Visualization and Integrated Discovery (DAVID) provides a widely accepted set of functional annotation tools to interrogate the molecular composition of data sets relative to known findings in the current literature (352, 353). The functional clustering tool divides a list of proteins into functional protein groups, each with a different Enrichment Score (ES), thus assigning a significance value. Analysis where appropriate was carried out as previously described (349, 351).

Statistical analyses

Data are presented as the mean ± standard error of the mean. A Student's *t* test was performed using Microsoft Excel or Graphpad Prism 7 to compare the means of data when only two groups were compared (i.e. wild type vs. $Smn^{2B/-}$). One-way ANOVA analysis was used to distinguish differences between more than two groups when multiple comparisons were necessary (i.e. wild type vs. $Smn^{2B/+}$ vs. $Smn^{2B/-}$). The post-test used for the ANOVA was Tukey. Survival curves were compared using a Mantel-Cox test. Significance was set at $P \leq 0.05$ for *, $P \leq 0.01$ for **, $P \leq 0.001$ for *** and $P \leq 0.0001$ for ****.

Funding

RK was supported by Cure SMA/Families of SMA Canada; Muscular Dystrophy Association (USA) (grant number 575466); Canadian Institutes of Health Research (CIHR) (grant number PJT-156379); and the E-Rare-2 program from the CIHR (grant number ERL-138414). MEH was funded by CIHR (grant number FDN 143278). The Italian group (GB, CM, RDA, AB, AL) was funded by the Italian Association of SMA Families (Famiglie SMA, 2015-2016 contribution) and by Fondazione Telethon (Application GUP15014, 2015, Italy). LM is supported by grants from Cure SMA (grant number MU1415); Fight SMA; Muscular Dystrophy Association (grant number 417757); Tenovus Scotland (E15/4); and Newlife foundation for disabled children (SG/14-15/08). THG was supported by UK SMA Research Consortium and SMA Europe. SHP was supported by Tenovus (Scotland) and The Euan Macdonald Centre for Research into Motor Neurone Diseases. TMW was supported by BBSRC ISP. MB was supported by UK SMA Research Consortium and SMA Angels Charity. MLH was supported by the Darwin Trust. The Vanderbilt Mouse Metabolic Phenotyping Center was supported by NIH grant DK59637. The University of Massachusetts Medical School National Mouse Metabolic Phenotyping Center (MMPC) is supported by NIH grant (2U2C-DK093000). MOD was supported by Frederick Banting and Charles Best CIHR Doctoral Research Award.

Acknowledgements

We would like to thank Dr. Jocelyn Coté and his student Andréanne Didillon for providing *Smn*$^{-/-}$*;SMN2;SMNΔ7* mice to the Kothary laboratory. We would like to extend

our gratitude to Eva Szunyogova, Sabrina Gibeault, My Tran Trung, and Rebecca Yaworski for assistance with experiments.

Conflict of interest

Marc-Olivier Deguise received honoraria and travel accommodations by Biogen for the SMA Summit 2018 held in Montreal, Canada.

Chapter 5: Myopathic phenotype precedes neuronal phenotype in a new mild mouse model of spinal muscular atrophy

Myopathic phenotype precedes neuronal phenotype in a new mild mouse model of spinal muscular atrophy

Marc-Olivier Deguise[1,2,3], Alexandra Tierney[1], Lucia Chehade[1,2,3], Ariane Beauvais[1], Mohamed Thabet[2], Brittany Paul[1,3], Yves De Repentigny[1], Sabrina Gibeault[1], Jean-Marc Renaud[2,3], and Rashmi Kothary[1,2,3,4,#]

[1]Regenerative Medicine Program, Ottawa Hospital Research Institute, Ottawa, Ontario, Canada K1H 8L6

[2]Department of Cellular and Molecular Medicine, University of Ottawa, Ottawa, Ontario, Canada K1H 8M5

[3]Centre for Neuromuscular Disease, University of Ottawa, Ottawa, Ontario, Canada K1H 8M5

[4]Department of Biochemistry, Microbiology, and Immunology, Faculty of Medicine, and Department of Medicine, University of Ottawa, Ottawa, Ontario, Canada K1H 8M5

#Correspondence to: Rashmi Kothary; Ottawa Hospital Research Institute; 501 Smyth Road, Ottawa, Ontario, Canada K1H 8L6; Tel: (613) 737-8707; Fax: (613) 737-8803; Email: rkothary@ohri.ca

Manuscript to be submitted

Marc-Olivier Deguise & *al.* (20XX) Myopathic phenotype precedes neuronal phenotype in a new mild mouse model of spinal muscular atrophy. To be submitted to *Ebiomedicine (I.F: 6.680)*.

Contribution

Marc-Olivier Deguise: Generated the mouse model, designed study, produced and analyzed data for all figures, and wrote the manuscript

Alexandra Tierney: Contributed to parts of Table 5.1 and Fig 5.3, 5.4.

Lucia Chehade: Contributed to parts of Fig 5.3, 5.4.

Ariane Beauvais: Assistance with experiments

Brittany Paul: Contributed to parts of Fig 5.3, 5.4.

Yves De Repentigny: Provided electron microscopy and assistance with dissections

Sabrina Gibeault: Maintenance of mouse models and genotyping

Mohamed Thabet: Assistance with electrophysiology experiments

Jean-Marc Renaud: Designed electrophysiological experiments and provided assistance with experiments

Rashmi Kothary: Designed study and wrote manuscript

Abstract

Background

Mouse models of mild spinal muscular atrophy (SMA) have been extremely challenging to generate. This paucity of model systems has limited our understanding of pathophysiological events in milder forms of the disease and of the effect of SMN depletion during aging.

Methods

The mild mouse model of SMA, termed *Smn*$^{2B/-}$;*SMN2*$^{+/-}$, was generated by crossing *Smn*$^{-/-}$;*SMN2* and *Smn*$^{2B/2B}$ mice . This new model was characterized using behavioral testing, histology, western blot, muscle-nerve electrophysiology as well as ultrasonography to study classical SMA features and extra-neuronal involvement.

Findings

The *Smn*$^{2B/-}$;*SMN2*$^{+/-}$ mice have normal survival, but have an early myopathic phenotype, a sustained motor weakness, a late motor neuron loss and skeletal muscle atrophy. They show electrophysiological evidence of denervation and neuronal/NMJ transmission defects that are more prominent in male mice. Intrinsic contractile and relaxation muscle defects were also identified. There was an absence of extra-neuronal pathologies.

Interpretation

The *Smn*$^{2B/-}$;*SMN2*$^{+/-}$ mouse provides a mild model of SMA, displaying hallmark features of motor neuron loss, denervation and muscle atrophy. Its use will allow for the understanding of the most susceptible pathogenic molecular changes in motor neurons and muscles, investigation of the effects of SMN depletion in aging, sex differences and most importantly will provide guidance for the currently aging SMA patients treated with the recently approved genetic therapies.

Funding

This work was supported by Cure SMA/Families of SMA Canada (grant number KOT-1819); Muscular Dystrophy Association (USA) (grant number 575466); and Canadian Institutes of Health Research (CIHR) (grant number PJT-156379).

Keywords: Aging, SMN, Type IV, electrophysiology, myopathy

Research in Context

Evidence before this study

Reproducing the heterogeneity of spinal muscular atrophy (SMA) in mouse models has proven difficult. In pre-clinical models, SMN depletion causes an SMA phenotype in a very narrow range of SMN level, leading to an all-or-nothing phenomenon. As such, the mice are either very sick and severe, or almost unaffected. Current mild mouse models of SMA show limited or discordant features of SMA and do not permit aging studies. This has limited our understanding of pathophysiological events in milder states of the disease and the effect of SMN depletion during aging.

Added value of this study

This study established a new preclinical model of mild SMA. The levels of SMN introduced from one *SMN2* allele on the $Smn^{2B/-}$ background is sufficient for recovery of normal lifespan but still allowing development of motor weakness, motor neuron loss, and denervation of skeletal muscle. This model also reveals new insights into sex differences, with a stronger male susceptibility. Of further interest, it also shows the emergence of a myopathic phenotype that precedes the neuronal loss.

Implications of all the available evidence

The use of this model will allow for the understanding of the most susceptible pathogenic molecular changes in motor neurons and muscles, investigation of the effects of SMN depletion in aging, sex differences and most importantly will provide guidance for the currently aging SMA patient population treated with anti-sense oligonucleotides or gene therapy.

Introduction

Spinal muscular atrophy (SMA) is an autosomal inherited neurological disorder largely affecting alpha motor neurons, leading to paralysis and skeletal muscle atrophy. The genetic basis of SMA involves a deletion or mutation of the *survival motor neuron 1* (*SMN1*) gene (1), which leads to drastically reduced levels of SMN protein. The low level of SMN protein in SMA patients comes from a nearly identical copy of the *SMN1* gene, called *SMN2*. Indeed, copy number of *SMN2* is the most prominent genetic modifier of SMA severity, making clinical presentation and severity widely varied. At one end of the spectrum, type I SMA patients account for more than 50% of the incidence of SMA (283). These patients generally have only 2 copies of *SMN2* and do not reach major motor milestones such as sitting, standing and walking(4, 9). At the other end of the spectrum, type IV SMA patients account for a very small percentage of the SMA population. Most of these patients harbor four to five copies of *SMN2* and start to show symptoms at 21 years of age or older. Type IV SMA patients have minor functional deficits and generally a normal life expectancy(4). For this reason, the screening and identification of these patients, as well as epidemiological data from this group has been limited (283).

In the last two years, we have witnessed the emergence of the first therapy for SMA, called Spinraza, which improves symptoms and motor function in patients but cannot be considered a cure(113). More recently, Zolgensma, the AAV9-SMN based therapy, also received FDA approval and will become available in the near future (354). It is expected that these therapeutics will increase lifespan and subsequently shift the severe infantile SMA population to a milder SMA adult population. It is unknown whether such lifespan extension will reveal new, previously unknown, comorbidities that could arise with age in this new population.

Reproducing the heterogeneity of SMA in mouse models has proven difficult (152). The copy number of human *SMN2* in a mouse model does not result in similar severity as in human patients (152). For example, four copies of the *SMN2* gene leads to important motor deficits in humans (type III SMA) while very few defects are observed in the equivalent mouse model (152). Interestingly, it appears that the threshold at which SMN depletion causes a SMA phenotype in mice is very narrow, with an almost all-or-nothing phenomenon, where mice are either very sick, or almost unaffected (152). The most widely used pre-clinical models for SMA, such as the *Smn*$^{-/-}$*;SMN2,* the *Smn*$^{-/-}$*;SMN2;SMN*$^{\Delta 7/\Delta 7}$ and the *Taiwanese* mice (two copies of SMN2) are very short-lived, with a lifespan of less than 14 days (153-155). They are considered as good models of type I SMA. The *Smn*$^{2B/-}$ mouse model results in an average lifespan of 25 days, however it is still considered to represent severe SMA (156, 157). Even though milder models have been generated (152, 158-161, 355-357), their use has been limited, since many showed only a few of the hallmark SMA features (see Table 5.1). Therefore, the less severe end of the clinical spectrum in SMA (type II to IV) has never been extensively studied in preclinical models. At the moment, results obtained from severe models are the only information we have, with little information about molecular and pathological events in milder forms of SMA. There exists a clear need for a mouse model to study milder forms of SMA, which will allow for better characterization of molecular changes within motor neurons, and to determine whether these differ in any way to those identified in severe SMA pathogenesis

Table 5.1 Review of mild mouse models of SMA

Mouse model	Follow-up time	Lifespan	Neuronal pathology	NMJ pathology	Muscle size	Motor function	Extra-neuronal findings	Tail length	Ref.
SMN^{RT}	100 d	34 d	↓ proprioceptive synapses #MN: same	↑ immaturity ↓ innervation	↓	↓	IVS ↓ ↑ heart fibrosis	N/A	(356)
Burgheron	6 m	~3 m	↓ In CMAP/SMUP no axonal loss #MN: N/A	↓ size ↑ immaturity	=	N/A	Heart defects	Full loss	(357)
Taiwanese (4 copies)	15 m	~12 m	↓ CMAP #MN: ↓	N/A	↓	↓	N/A	Shorter tails	(358)
Smn1$^{C/C}$	60 w	>12 m	↓ synaptic efficacy no axonal loss #MN: N/A	Slightly abnormal	N/A	Normal	↓ HR ↓ BMD	necrosis	(161)
SmnC>T/C>T	800 d	Normal	Similar #MN: same	No abnormalities identified	↑	↓	N/A	N/A	(355)
A2G Smn$^{-/-}$;SMN2	N/A	227 d	↓ CMAP amplitude #MN: ↓	↑ sprouting	↓	N/A	N/A	N/A	(158)
A111G Smn$^{-/-}$;SMN2	1.5 y	Normal	No axonal loss #MN: N/A	N/A	↑	N/A	N/A	N/A	(160)
Smn$^{+/-}$	1 y	N/A	Degenerating axons CMAP normal #MN: ↓	↑ sprouting Mild denervation	N/A	Normal	N/A	N/A	(359, 360)

Abbreviations : d – days, m – Months, y – years, N/A – Not available, CMAP – compound motor action potential, SMUP – single motor unit potentials, MN – motor neurons, NMJ – Neuromuscular junction, IVS – interventricular septum, HR – heart rate, BMD – bone mineral density

Here, we have generated a *Smn*$^{2B/-}$;*SMN2*$^{+/-}$ mice, a new model for mild SMA. This mouse harbors one copy of the human *SMN2* gene on the *Smn*$^{2B/-}$ background and presents with nearly normal lifespan but with subtle SMA features appearing in adulthood. The *Smn*$^{2B/-}$;*SMN2*$^{+/-}$ mice are mildly weaker on motor tests and start losing weight at around 9 months of age, show evidence of progressive electrophysiological neuronal/NMJ transmission defects, and a myopathic pathology that appears earlier than the neuropathy. Overall, this is the first mouse model that reproduces most of the SMA classical features, while offering additional insight into sex differences. This model will also offer valuable information concerning SMN depletion in aging.

Materials and Methods

Study design

Upon generation of the mouse model, three pre-specified objectives were: (1) Identify whether *Smn*$^{2B/-}$;*SMN2*$^{+/-}$ mice display motor weakness, (2) Assess for hallmark neuronal and muscular features of SMA in the mouse model, (3) Assess extra-neuronal involvement in the mild model. All objectives were pursued in a simultaneous manner. Behavioral data in the adult phase, echoMRI and lipid quantification were outsourced, and, thus, analyses were performed in a blinded fashion. Quantification of SC and muscle histology were also performed in a blinded fashion. Sample size calculations were not performed. N number are described in each figure legend. Statistical approach is as described below and in figure captions.

Mouse Model Generation

Smn$^{2B/-}$;*SMN2*$^{+/-}$ and *Smn*$^{2B/+}$;*SMN2*$^{+/-}$ mice were generated by crossing an *Smn*$^{2B/2B}$ (FVB background) (157) with a *Smn*$^{+/-}$;*SMN2* (FVB background - Jackson Laboratory(153)). *Smn*$^{+/-}$;*SMN2*$^{+/+}$ mice were crossed to *Smn*$^{2B/2B}$;*SMN2*$^{-/-}$ mice to obtain *Smn*$^{2B/-}$;*SMN2*$^{+/-}$ animals. The following primers were used for genotyping: Common forward primer (5' GGG TTG ATC TAG GGA CTT TGA G 3'), reverse wild type primer (5' GGG AGT TGT GGC ATT CTT CT 3'), reverse SMA primer (5' GCT GAT TTG TGT AGT CGG TTT ATG 3'). Young WT mice were 12-16 weeks old B6.SJL-*Ptprca Pepcb*/BoyJ mice which harbour the differential *Ptprca* pan leukocyte marker commonly known as CD45.1, useful for discrimination of host vs. donor in transplantation experiments. These mice are otherwise WT mice. All mice were housed at the

University of Ottawa Animal Facility and cared for according to the Canadian Council on Animal Care. Experimentation and breeding were performed under protocol OHRI-1948 and OHRI-1927.

In vivo *measurement and behavioral testing*

Tail length was taken with a ruler by stretching the tail to its full length. The same group of mice were subjected to an array of behavioral tests throughout development (as described below). All behavioral testing was performed by one single examiner per time point with the assistance of a second examiner for time recording. Each mouse was tattooed between P3-P5 to allow longitudinal examination of motor function. Tests were administered in the following order: (1) righting reflex, (2) pen test, and (3) inverted mesh/wire grip. All tests were performed on the same day and testing occurred every two days. The righting reflex was performed from P12 to P18, the pen test from P18 to P24 and inverted mesh grip from P12 to P30. Each test was repeated 3 times to ensure reliable measures. Group of 3 mice were taken at a time, allowing for a period of rest before having the test repeated. Righting reflex followed a similar protocol as previously described in Treat-NMD neuromuscular network (SOP MD_M.2.2.002). The pen test followed a similar protocol as previously described in Treat-NMD neuromuscular network (SOP SMA_M.2.1.001). A maximum of 30 seconds on the pen was defined as a perfect score. The inverted mesh/wire followed a slightly modified protocol than previously described in Treat-NMD neuromuscular network (SOP SMA_M.2.1.002). Briefly, a mesh grip (hole of 1 mm^2) is used from P13 to P19. At P21, the mesh grip was changed to a wire cage top to provide more space for the growing mice to hold on to. Termination of this test was set at 60 sec. The rotarod and grip strength were performed by the behavioral core of the University of Ottawa every two months. One test per day was performed and the assays were separated by at least one day of rest. Forepaw grip strength was measured

using a Chatillon grip meter (Columbus Instruments, Columbus, OH, USA). Rotarod performance (IITC Life Sciences, Woodland Hills, CA, USA) was done on two consecutive days, with each day consisting of 4 trials of 1-45 rpm accelerating over 60 sec with an inter-trial interval of 10 min. The same cohort of mice was assessed by EchoMRI (EchoMRI LLC, Houston, TX, USA). Mice that develop circling over their lifetime were removed from analysis of weight, grip strength, rotarod, and echoMRI after the onset of circling. All testing by the behavioral core was performed in a blinded fashion.

Gross morphology of organs

The mouse measurements for normalization were done prior to dissection using a ruler for the length of the mouse and a scale for its weight. Organs were weighed with a scale. Tissues were then fixed in 10% formalin for 24-48 h and transferred to 70% ethanol for long-term storage.

Tissue processing and staining

Spleens, tibialis anterior skeletal muscle and livers were fixed in formalin (1:10 dilution buffered, from Protocol, cat #245-684) for 48 h while spinal cords were fixed for (96 h) at 4ºC and then transferred in 70% ethanol at 4ºC until processing. All samples were processed at the University of Ottawa (Department of Pathology and Laboratory Medicine) and embedded in wax using a LOGOS microwave hybrid tissue processor. Paraffin block tissues were cut with a microtome at 3-4 µm of thickness and stained for H&E using a Leica autostainer XL Leica CV5030. Spinal cord were stained with cresyl violet to label motor neurons. Stained samples were scanned with a MIRAX MIDI digital slide scanner (Zeiss). Images were acquired using

3DHISTECH Pannoramic Viewer 1.15.4 at different magnifications. Quantification of motor neuron number and size was performed on a total of 5 sections separated by 8 sections each. Three criteria were used for motor neuron identification and ensuring appropriate counts: location in the ventral horn, presence of nucleolus, and cells were at least 200 um^2 in size. For the quantification of the TA muscle, pictures were taken to ensure complete coverage of the TA muscles. 100-150 fibers were counted in each picture for a minimum of 200-600 fibers at 6 and 12 months. At 18 months, the size of the muscle for some SMA mice would only allow for 100 fibers to be counted.

Lipid quantification

Tissue lipid analysis for quantification and profiles were performed at the Vanderbilt Mouse Metabolic Phenotyping Center in a blinded fashion. Lipids were extracted and analyzed as described (345, 346, 361).

Electrophysiology

A nerve-soleus muscle preparation was used for this study as previously reported (362). Briefly, mice were anaesthetized with a single intraperitoneal injection of 2.2 mg ketamine/0.4 mg xylazine/0.22 mg acepromazine per 10 g of animal body weight and sacrificed by cervical dislocation. The soleus and its associated nerve were then dissected in continuously oxygenated physiological control solution (118.5 mM NaCl, 4.7 mM KCl, 1.3 mM CaCl2, 3.1 mM MgCl2, 25 mM NaHCO3, 2 mM NaH2PO4, 5.5 mM d-glucose and continuously bubbled with 95% O_2:5% CO_2 to maintain pH at 7.4). The muscle nerve preparation was then transferred and positioned into a 2 ml plexiglass chamber where it was fixed to the stationary hook and a force transducer (model

402A; Aurora Scientific Canada). Experimental temperature was kept at 37°C and physiological control solution (described above) continuously ran through the chamber at 15 ml/min. Data were digitized at a sampling rate of 5 kHz using a KCP13104 data acquisition system (Keithley Instruments Inc, U.S.A.) Muscle length giving maximal force was identified and muscle was allowed to stabilize for 30 min. Following this, the nerve was stimulated via a suction electrode containing platinum wires connected to a Grass S88 stimulator and Grass SIU5 isolation unit (Grass Technologies, U.S.A). Twitch contractions were elicited with a single stimulation or tetanic contractions were elicited with a 400 ms train of 0.3 ms, 1 V (supramaximal voltage) pulses at 10 to 180 Hz. Stimulations were performed every 5 min. Maximal force (180 Hz stimulation) was first measured followed by a force-frequency curve. Muscles were then exposed to 30 μM tubocurarine hydrochloride pentahydrate (Sigma 93750, Oakville, ON, Canada) to completely blocked neural transmission at the neuromuscular junction. This was confirmed when no force was generated by the muscle when the nerve was stimulated. Muscles were then directly stimulated by two platinum wire located on the opposite side of the muscle also connected to a Grass S88 stimulator and Grass SIU5 isolation unit (Grass Technologies, U.S.A.). Twitch and tetanic contractions were again elicited, except that the stimulation voltage was increased to 10V. The following parameters were later analyzed as follows: Twitch and tetanic force was calculated as the difference between the resting baseline force and force generated upon stimulation and normalized to N/cm^2 using muscles length and weight; half-rise time was calculated as the time interval from the first stimulation to the time force had reached 50% of the contraction amplitude; twitch half-relaxation time was calculated as the time interval between the time force reached a peak and force had decayed by 50% while for a tetanic contraction half-relaxation time was calculated as the time interval between the last stimulation and the time force had decayed by 50%;

width represented the time interval between half-rise and half-relaxation time; maximum rate of force development and relaxation was obtained by first applying a linear regression analysis to every 10 data points to calculate the rate of force change over time and then finding the maximum and minimum peak during the contracting and relaxation phase, respectively.

Ultrasonography

Mice were shaved and Neer was used to ensure complete hair removal, allowing for adequate ultrasonographic quality. Mice were then anesthetized using continuous 3% isoflurane inhalation and placed on warming movable station where each limb were taped to the station to allow heart rate monitoring. A rectal probe was inserted for temperature monitoring and temperature was maintained between 36˚C and 38.5˚C. Ultrasonography was performed using a MS400 or MS550 transducer and the VEVO 2100 (FujiFilm VisualSonics, Toronto, Canada). M-mode acquisition was obtained ensuring the visualization of the papillary muscles for consistency of depth the slice. Quantification was performed by left ventricular trace to provide heart rate, stroke volume, cardiac output, ejection fraction and fractional shortening. For the splenic artery measurement, the position of the mice remained the same or repositioned in a right lateral decubitus in difficult identification of splenic anatomy and vascularity. As such, heart rate and temperature were not actively monitored. The spleen was identified under B-mode imaging, and doppler was used to identify the splenic artery. Peak flow velocity and heart rate was sampled and quantified as recommended by FujiFilm VisualSonics consultant.

Statistical analyses

Data are presented as the mean ± standard error of the mean. A Student's *t* test was performed using Microsoft Excel or Graphpad Prism 7 to compare the means of data when only two groups were compared (i.e. $Smn^{2B/+};SMN2^{+/-}$ and $Smn^{2B/-};SMN2^{+/-}$ mice). One-way ANOVA analysis was used to distinguish differences between more than two groups when multiple comparisons were necessary (i.e. young wild type vs. $Smn^{2B/+};SMN2^{+/-}$ and $Smn^{2B/-};SMN2^{+/-}$ mice). The post-test used for the ANOVA was Tukey. Significance was set at $P \leq 0.05$ for *, $P \leq 0.01$ for **, $P \leq 0.001$ for *** and $P \leq 0.0001$ for ****.

Data availability

All data will be made available upon contacting the corresponding author.

Results

The $Smn^{2B/-};SMN2^{+/-}$ mice have a normal life span, reduced tail length and progressive muscle weakness with age

Mild mouse models of SMA have been extremely challenging to generate (152, 158-161, 355-357). We have recently produced congenic $Smn^{2B/2B}$ mice on both the FVB and C57BL6 genetic backgrounds (157). This allowed pairing of the $Smn^{2B/2B}$ (FVB) with the $Smn^{+/-};SMN2$ (FVB), giving a progeny of $Smn^{2B/+};SMN2^{+/-}$ and $Smn^{2B/-};SMN2^{+/-}$ mice on a congenic FVB background. We have previously shown that $Smn^{2B/-};SMN2^{+/-}$ mice (FVB) display about 10% more SMN protein that the standard $Smn^{2B/-}$ mice (C57Bl6) (25% VS 15% of SMN protein) (258). We initially characterized $Smn^{2B/-};SMN2^{+/-}$ mice for survival, weight and motor behavior. $Smn^{2B/-};SMN2^{+/-}$ mice had a lifespan and morphology quite similar to the control $Smn^{2B/+};SMN2^{+/-}$ mice (Fig 5.1 A-E). For monitoring weight, we separated the data based on sex of the mice, as male adult mice are generally bigger than their female counterparts. We observed a slowing down of weight gain in $Smn^{2B/-};SMN2^{+/-}$ mice beginning at 6 months of age (Fig 5.1F), which became statistically significant at 12 months of age and 15 months of age for female and male mice, respectively. A subsequent weight stabilization occurred, a phenomenon that we did not observe in control mice. We also noticed a considerable reduction of tail length, a feature present in many other mouse models of SMA (112, 159, 356, 357). Reduced tail length was observed as soon as 3 weeks of age (more pronounced in male) and was constant over time, regardless of sex (Fig 5.1G).

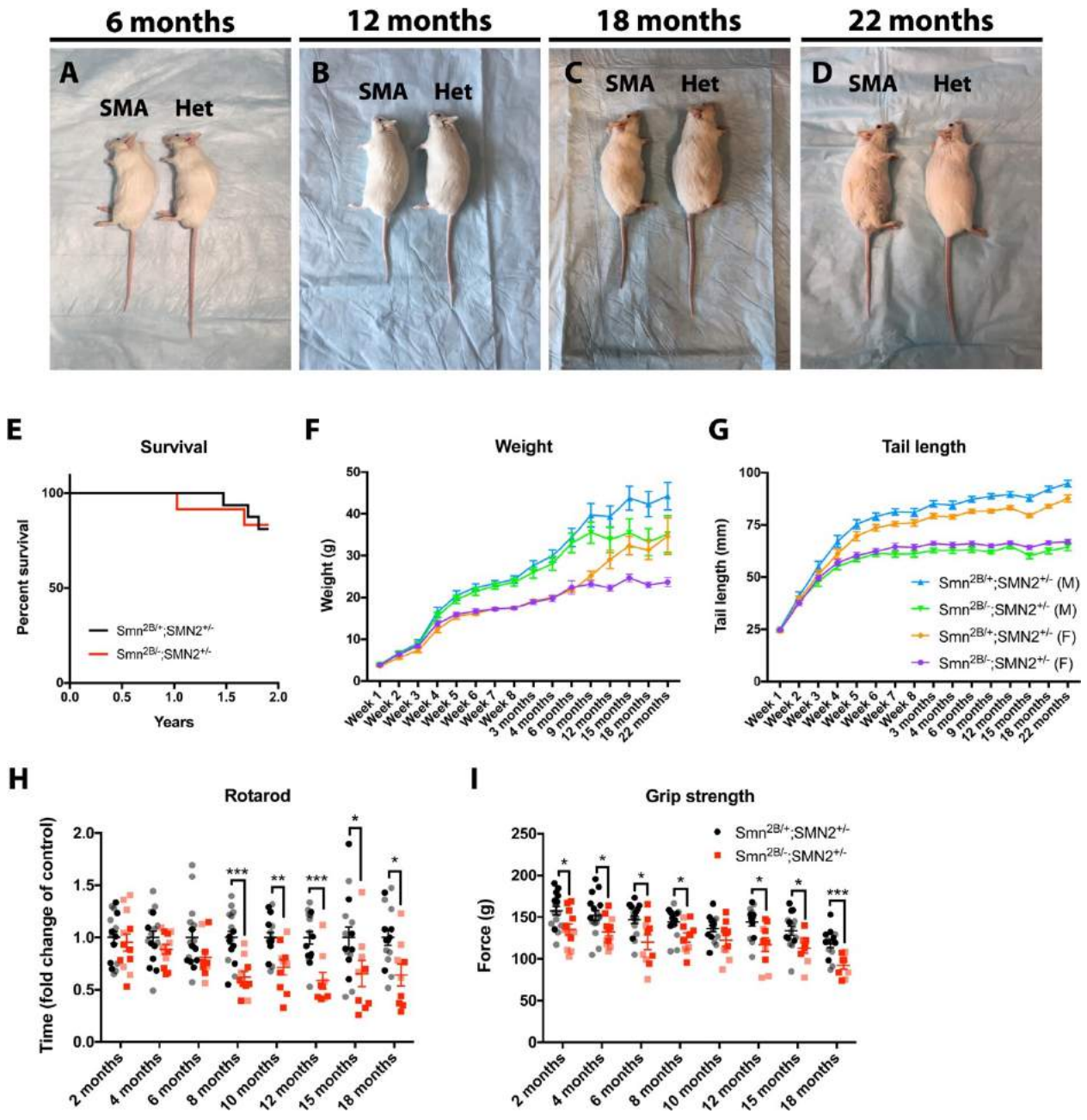

Figure 5.1 *Smn$^{2B/-}$;SMN2$^{+/-}$* live a normal life but have reduced weight gain, and display motor impairment. (A-D) Representative images of *Smn$^{2B/-}$;SMN2$^{+/-}$* and *Smn$^{2B/+}$;SMN2$^{+/-}$* mice aged between 6 months and 22 months. (E) Survival was unchanged between *Smn$^{2B/-}$;SMN2$^{+/-}$* and *Smn$^{2B/+}$;SMN2$^{+/-}$* mice. (F) Reduced weight gain was obvious by 12 and 15 months for female and male *Smn$^{2B/-}$;SMN2$^{+/-}$* mice. (G) *Smn$^{2B/-}$;SMN2$^{+/-}$* mice showed reduced tail length at 3 weeks of

age. (H) Impairment on rotarod test were identified by 8 months of age and was sustained in *Smn*$^{2B/-}$*;SMN2*$^{+/-}$ mice. (I) Reduction of grip strength was nearly constantly seen over time in *Smn*$^{2B/-}$*;SMN2*$^{+/-}$ mice. (*Smn*$^{2B/+}$*;SMN2*$^{+/-}$ mice - Het and *Smn*$^{2B/-}$*;SMN2*$^{+/-}$ - SMA. The n value for each experiment is as follows (E) 12-16, (F-G) 4-9, (H-I) 9-16, dark colour represent male while light colour represent female data points, average ± SEM displayed, unpaired student t-test, $P \leq 0.05$ for *, $P \leq 0.01$ for ** and $P \leq 0.001$ for ***).

We next investigated whether motor functions were affected in *Smn*$^{2B/-}$*;SMN2*$^{+/-}$ mice. We did not see any difference between *Smn*$^{2B/-}$*;SMN2*$^{+/-}$ mice and control *Smn*$^{2B/+}$*;SMN2*$^{+/-}$ mice in righting reflex, pen test or mesh grip during early life (Fig 5.2A-C). We next moved to adult appropriate motor function tests such as grip strength and rotarod. Motor impairment was readily identified in rotarod test at 8 months while grip strength measurements revealed diminished force as early as 2 months of age in *Smn*$^{2B/-}$*;SMN2*$^{+/-}$ mice (Fig 5.1H-I). Interestingly, the deficits were more sustained in male versus female mice (Fig 5.2D-G). It is important to keep in mind that the shorter tail length may act as a confounding factor in the rotarod test. However, the tails of *Smn*$^{2B/-}$*;SMN2*$^{+/-}$ mice, albeit shorter, remained constant over time while their performance worsened on the rotarod test. In addition, it was shown that performance is not impaired by tail cutting in a previous study (159). A video of showing the overall mobility and motor impairment of the *Smn*$^{2B/-}$*;SMN2*$^{+/-}$ mice can be found under this link. Therefore, we conclude that motor weakness is present during adulthood in our new mild mouse model, reminiscent of what is observed in type IV SMA patients. Altogether, these features are very consistent with delayed onset of SMA pathology, similar to less severe type III and IV SMA patients.

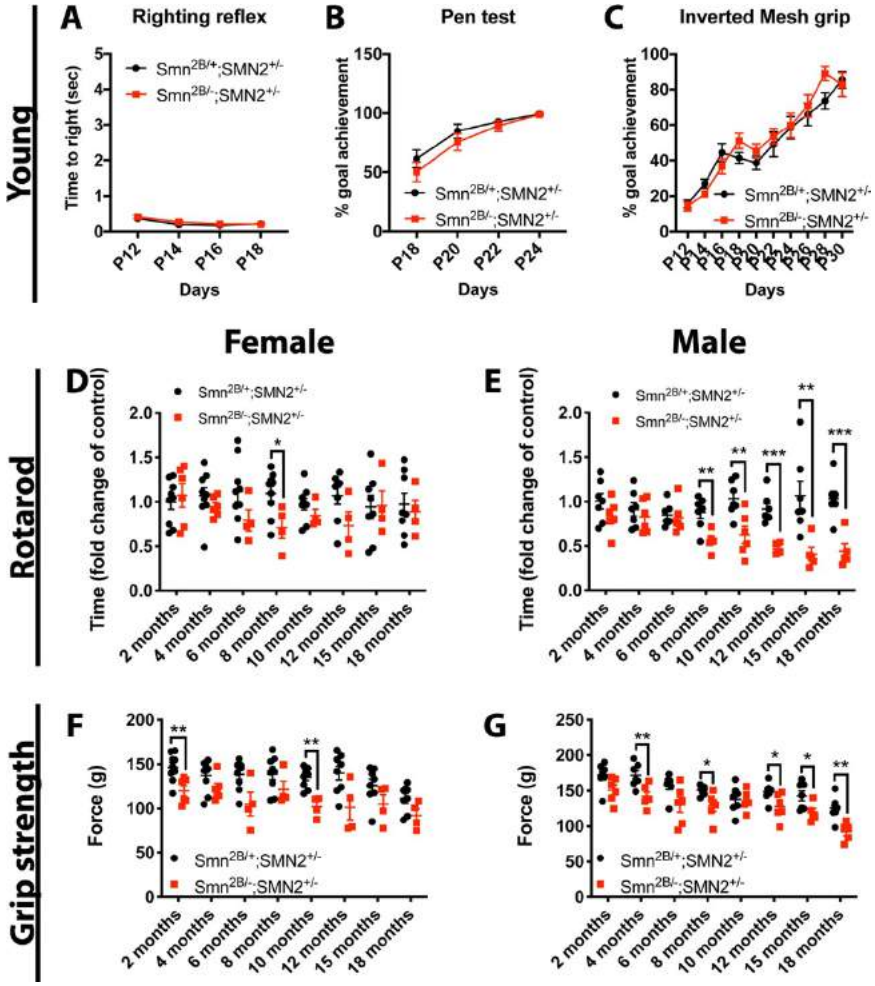

Figure 5.2. No change in motor function early, but segregation of male and female *Smn$^{2B/+}$;SMN2$^{+/-}$* and *Smn$^{2B/-}$;SMN2$^{+/-}$* mice shows more evident deficit in male *Smn$^{2B/-}$;SMN2$^{+/-}$* mice during aging. (A-C) No change in righting reflex, pen test, and inverted mesh grip in *Smn$^{2B/-}$;SMN2$^{+/-}$* at a young age. Rotarod result in females (D) and males (E) reveal progressive deficiencies in male *Smn$^{2B/-}$;SMN2$^{+/-}$* mice while female *Smn$^{2B/-}$;SMN2$^{+/-}$* mice remain relatively stable compared to control counterparts. Grip strength results in females (F) and males (G) offers similar findings, albeit with a slight force reduction noted in female *Smn$^{2B/-}$;SMN2$^{+/-}$* mice. (The n value is *Smn$^{2B/+}$;SMN2$^{+/-}$* female (8-9), *Smn$^{2B/-}$;SMN2$^{+/-}$* female (4-6), *Smn$^{2B/+}$;SMN2$^{+/-}$* male (7), *Smn$^{2B/-}$;SMN2$^{+/-}$* male (5-6), average ± SEM displayed, unpaired student t-test, $P \leq 0.05$ for *, $P \leq 0.01$ for ** and $P \leq 0.001$ for ***).

The $Smn^{2B/-};SMN2^{+/-}$ mice have a myopathy that precedes neuropathy

Next, we investigated motor neuron number and muscle pathology, two characteristic hallmarks of SMA. In the lumbar region of the spinal cord, we did not detect any differences in motor neuron number or size between $Smn^{2B/+};SMN2^{+/-}$ and $Smn^{2B/-};SMN2^{+/-}$ mice at 6 or 12 months of age (Fig 5.3). However, by the age of 18 months, $Smn^{2B/-};SMN2^{+/-}$ mice displayed a significant reduction in motor neuron cell body counts and size (Fig 5.3E-H). We next assessed whether any neurogenic atrophy is present in tibialis anterior muscle of $Smn^{2B/-};SMN2^{+/-}$ mice. We observed a reduced mean fiber size at 6 and 12 months that eventually normalized at 18 months in $Smn^{2B/-};SMN2^{+/-}$ mice (Fig 5.4). This normalization may be due to re-innervation or hypertrophic fibers (163, 336) commonly seen in SMA muscles. Alternatively, it might be due to atrophy secondary to aging muscles in control $Smn^{2B/+};SMN2$ mice since their mean fiber size was reduced in comparison to 12 months, while the mean fiber size of $Smn^{2B/-};SMN2^{+/-}$ mice remained relatively constant across all time points (Fig 5.4P). Of particular interest, there was a steep reduction in the size of the TA muscle in $Smn^{2B/-};SMN2^{+/-}$ mice at 18 months (Fig 5.4M). This was accompanied by a marked drop in fiber number at 18 months (Fig 5.4N). Central nucleation also progressively increased in the muscle over the lifetime of the mice (Fig 5.4O), suggesting pathological satellite cell activation or muscle immaturity, a feature previously identified in other mouse models of SMA (168). These results show an early myopathy, with late onset motor neuron loss.

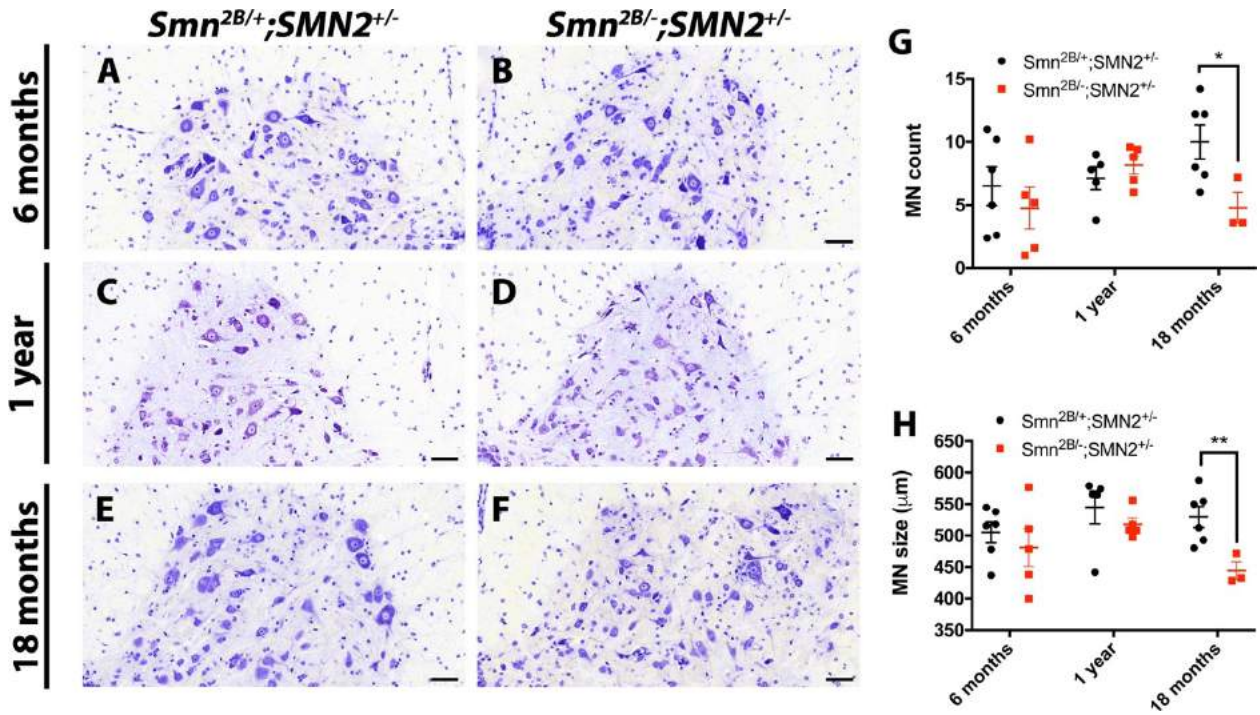

Figure 5.3 *Smn$^{2B/-}$;SMN2$^{+/-}$* mice display motor neuron loss late in adulthood. Representative 30X images (A-F) and quantification (G-H) of the motor neuron number and size in spinal cord sections (cresyl violet) from *Smn$^{2B/+}$;SMN2$^{+/-}$* and *Smn$^{2B/-}$;SMN2$^{+/-}$* mice at 6, 12 and 18 months. Scale bars represent 50 μm. (The n value is 3-6, average ± SEM displayed, unpaired student t-test, $P \leq 0.05$ for * and $P \leq 0.01$ for **).

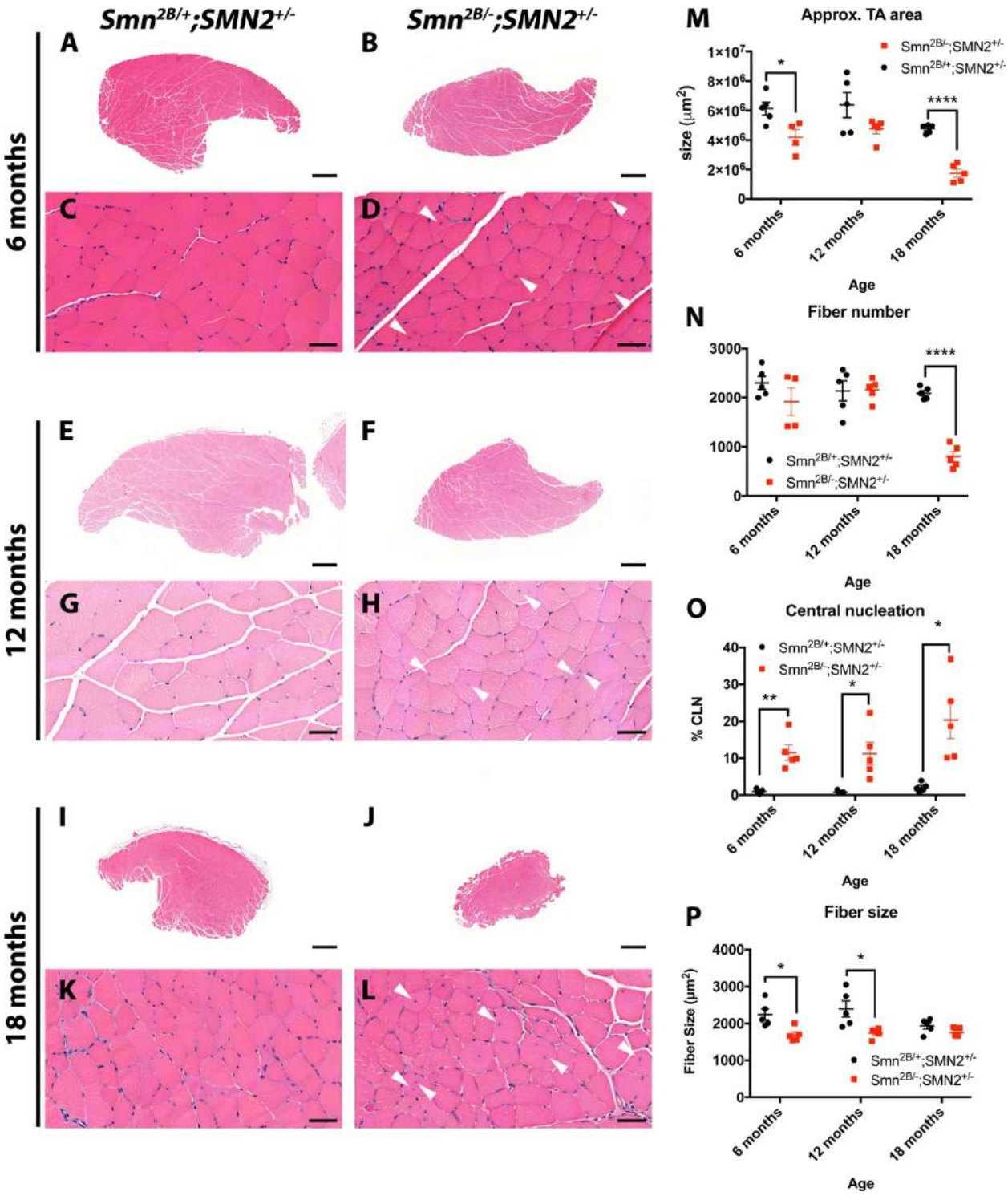

Figure 5.4 *Smn$^{2B/-}$;SMN2$^{+/-}$* mice develop an early myopathic phenotype. Representative H&E images of the *tibialis anterior* muscle (3.5X and 40X) of *Smn$^{2B/+}$;SMN2$^{+/-}$* and *Smn$^{2B/-}$;SMN2$^{+/-}$* mice at 6 (A-D), 12 (E-H) and 18 months (I-L). TA size (M) and fiber number (N) was most

significantly reduced at 18 months in *Smn$^{2B/-}$;SMN2$^{+/-}$* mice. (O) Central nucleation was constantly and progressively increased from 6 months to 18 months. (P) Fiber size were initially reduced at 6 and 12 months but normalized by 18 months of age. Scale bars represent 500 µm in A,B,E,F,I,J and 50 µm in C,D,G,H,K,L (The n value is 4-5, average ± SEM displayed, unpaired student t-test, $P \leq 0.05$ for *, $P \leq 0.01$ for **, and $P \leq 0.0001$ for ****).

Neurological and myopathic electrophysiological impairment in Smn$^{2B/-}$;SMN2$^{+/-}$ mice

To better understand the neurological and muscular abnormalities in *Smn$^{2B/-}$;SMN2$^{+/-}$* mice, we performed a set of electrophysiological assessments on *ex-vivo* nerve-muscle preparations (Fig 5.5). By comparing the force obtained by stimulating first the nerve of the soleus muscle and then the muscle directly (in the presence of tubocurarine to block the neural stimulation at the neuromuscular junction), one can identify deficiencies in NMJ transmission. As aging can lead to denervation, young 3-4 months old wild type mice were included as a positive control to show expected values without denervation. Intriguingly, nerve stimulation only generated about 80% of the force generated by direct muscle stimulation in nerve-muscle preparations from *Smn$^{2B/-}$;SMN2$^{+/-}$* mice (Fig 5.5A). This is because *Smn$^{2B/-}$;SMN2$^{+/-}$ soleus generated less tetanic force than Smn$^{2B/+}$;SMN2$^{+/-}$ only when stimulated through the nerve* (Fig. 5.6A-D), suggesting disrupted transmission at the level of the nerve or NMJ. Furthermore, male mice (filled in dots) were considerably more affected than female mice (empty dots) (Fig 5.5A, Fig 5.6A-D). Time to reach peak force was also shorter followed by a small force decrease, mostly in male mice, suggesting that the axons and/or NMJs are unable to maintain neural signaling during a tetanus stimulus (Fig

5.5B, Fig 5.6E, F). This is better depicted by a representative waveform curve from *Smn$^{2B/-}$;SMN2$^{+/-}$* mice, which shows a reduced force generation, early force peak and eventual inability to sustain force production when the nerve is stimulated (Fig 5.5C). Other alterations were also readily observed in the muscle component, but this time in both male and female *Smn$^{2B/-}$;SMN2$^{+/-}$* mice. The force-frequency curve of *Smn$^{2B/+}$;SMN2$^{+/-}$* and *Smn$^{2B/-}$;SMN2$^{+/-}$* muscles was shifted to lower stimulation frequency in comparison to muscles from young wild type mice (Fig 5.5D). This feature was worse in the *Smn$^{2B/-}$;SMN2$^{+/-}$* mice. Such shift can be due to changes in fiber type composition toward slower fibers or slower relaxation. Prolonged half relaxation time was indeed observed while maximum rate of relaxation became slower after a tetanic stimulation of either the muscle or the nerve (Fig 5.5E,F); an effect also observed with twitch contraction (Fig. 5.5K, L). Interestingly, while age appears to have an effect on these defects (young wild type vs. *Smn$^{2B/+}$;SMN2$^{+/-}$*), it is considerably worse with further SMN depletion as in the *Smn$^{2B/-}$;SMN2$^{+/-}$* mice. Other defects included longer twitch half-rise time and time to peak, defects that were exacerbated by SMN depletion (Fig 5.5H,I). Similar relaxation abnormalities as tetanus stimulation were also observed, as exemplified by the slower half relaxation time and maximum relaxation rate, resulting in a wider contraction period (width), which were once again worse in the *Smn$^{2B/-}$;SMN2$^{+/-}$* mice, in comparison to *Smn$^{2B/+}$;SMN2$^{+/-}$* mice (Fig 5.5J-L). In the twitch stimulation, the defects appeared more prominent in the male mice (Fig 5.7) and were independent of nerve or muscle stimulation. Overall, these findings confirm a pathologic neuronal/NMJ component and intrinsic muscle defects, especially evident in the relaxation phase of muscle contraction.

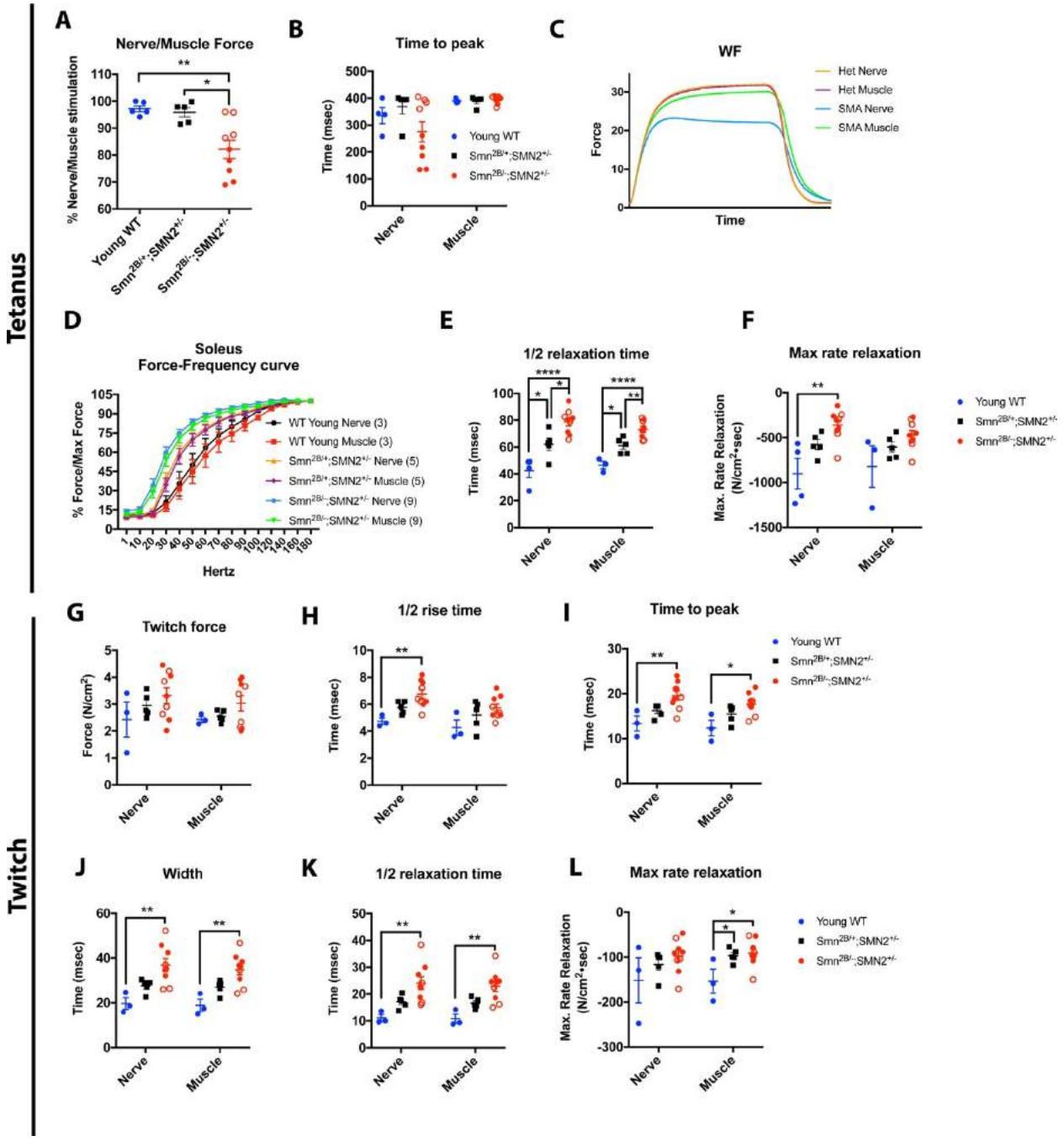

Figure 5.5 Impaired neuromuscular transmission and intrinsic muscle relaxation defects at 18 months in *Smn$^{2B/-}$;SMN2$^{+/-}$* mice. (A) Tetanic forces via neural stimulation are expressed as a percent of the tetanic force when solei were directly stimulated. *Smn$^{2B/-}$;SMN2$^{+/-}$* soleus generated less tetanic force when stimulated via the nerve than directly in male *Smn$^{2B/-}$;SMN2$^{+/-}$* mice (full circle), while female *Smn$^{2B/-}$;SMN2$^{+/-}$* mice (hollow circle) were much less affected. This indicates

a failure of nerve or NMJ to match the maximum force that can be produced. (B) Peak force occurred sooner in male *Smn*$^{2B/-}$;*SMN2*$^{+/-}$ mice (full circle) at 18 months, while female *Smn*$^{2B/-}$;*SMN2*$^{+/-}$ mice (hollow circle) were much less affected, indicating incapacity to sustain neural input by the nerve. (C) Representative waveform of the tetanic force produced by nerve or muscle stimulation in *Smn*$^{2B/-}$;*SMN2*$^{+/-}$ mice (only male depicted). (D) Force frequency curve of *Smn*$^{2B/-}$;*SMN2*$^{+/-}$ mice was shifted lower stimulation frequencies possibly linked to slower relaxation. (E-F) Half relaxation time was longer and max rate of relaxation slower in *Smn*$^{2B/-}$;*SMN2*$^{+/-}$ mice, independent of their sex. Twitch contractions were marked by relatively unchanged force (G), prolonged half rise time (H), time to peak (I), width (J), half relaxation time (K) and maximum rate of relaxation, independent of their sex. (The n value for each experiment were young WT (3-5), *Smn*$^{2B/+}$;*SMN2*$^{+/-}$ mice (5), *Smn*$^{2B/-}$;*SMN2*$^{+/-}$ mice (9, 5 males, 4 females), average ± SEM displayed, one-way ANOVA with tukey post-hoc test, $P \leq 0.05$ for *, $P \leq 0.01$ for **, and $P \leq 0.0001$ for ****).

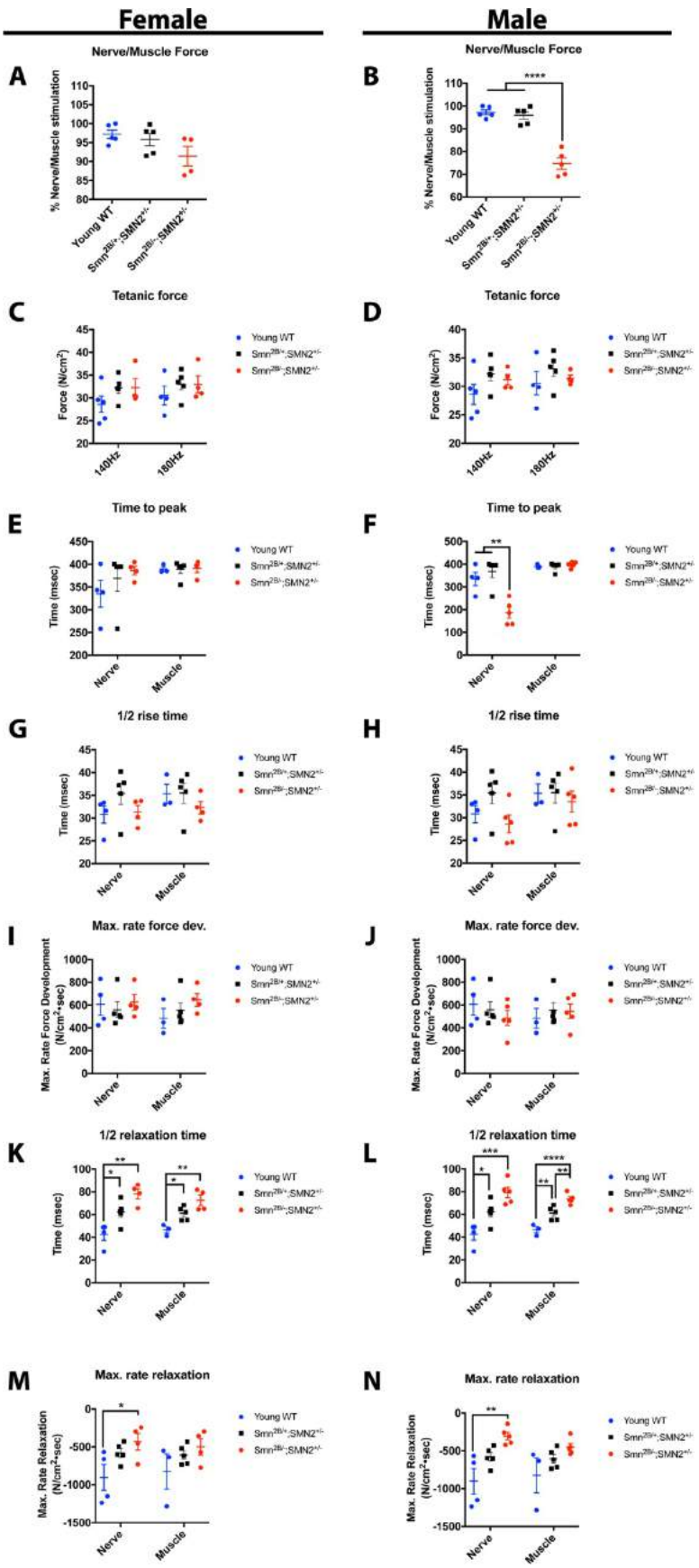

Figure 5.6 Deficiencies in nerve dependent force production and time to reach peak force only in male *Smn$^{2B/-}$;SMN2$^{+/-}$* mice upon tetanus stimulation. Separation of female and male data for the percentage of nerve generated force on maximal muscle generated force (A-B), tetanic force (C-D) time to peak (E-F) half rise time (G-H), maximal rate force development (I-J), half relaxation time (K-L), maximal rate of relaxation (M-N) during tetanic stimulation. Difference in sex is more predominant in nerve generated force development and time to peak. Note that only *Smn$^{2B/-}$;SMN2$^{+/-}$* mice are separated by sex. Young WT and *Smn$^{2B/+}$;SMN2$^{+/-}$* mice were not separated by sex. The young WT and *Smn$^{2B/+}$;SMN2$^{+/-}$*

mice cohort are the same for either male and female comparison. (The n value for each experiment were young WT (3-5), *Smn*$^{2B/+}$;*SMN2*$^{+/-}$ mice (5), *Smn*$^{2B/-}$;*SMN2*$^{+/-}$ mice (5 males, 4 females), average ± SEM displayed, one-way ANOVA with tukey post-hoc test, $P \leq 0.05$ for *, $P \leq 0.01$ for **, $P \leq 0.001$ for *** and $P \leq 0.0001$ for ****).

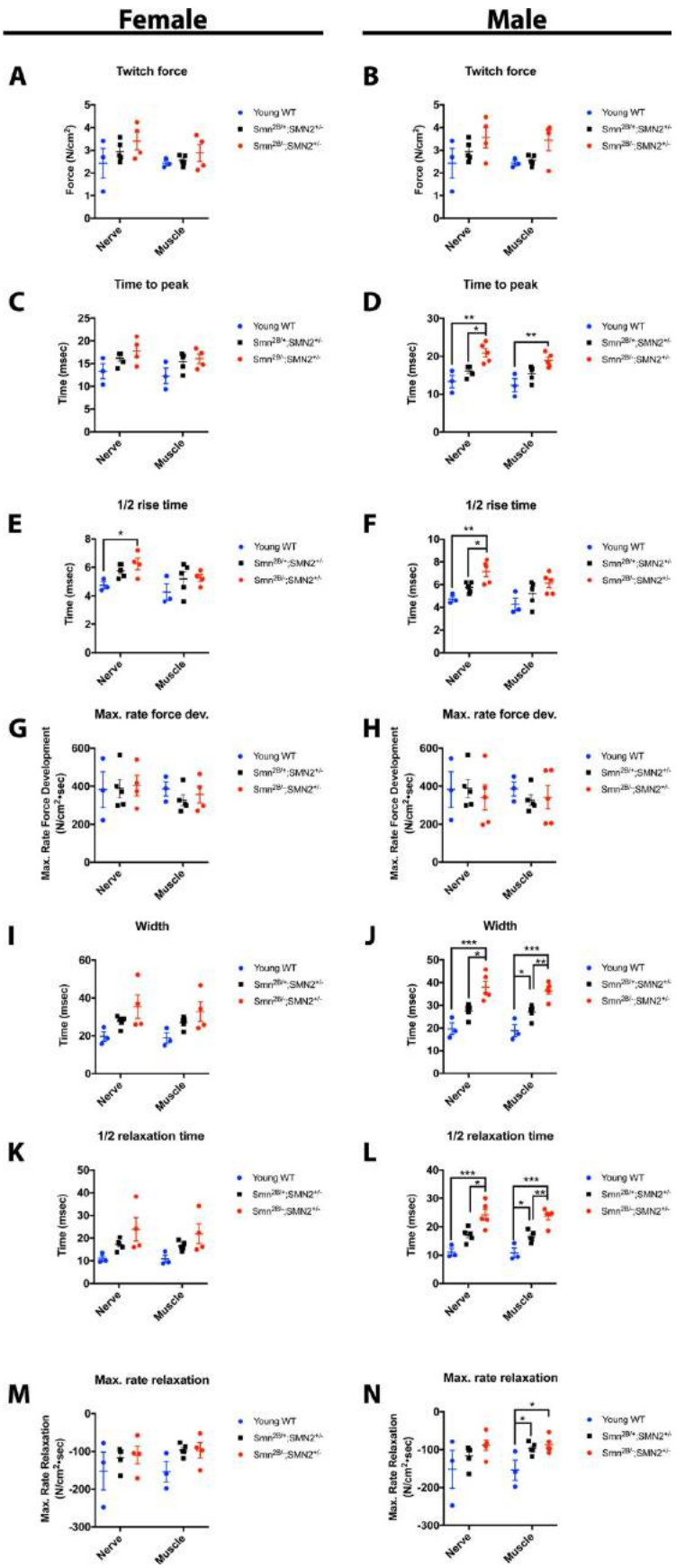

Figure 5.7 Many contraction and relaxation dynamic measures are more prominent in male *Smn$^{2B/-}$;SMN2$^{+/-}$* mice upon twitch stimulation. Results of female and male twitch force (A-B), time to peak (C-D) half rise time (E-F), maximal rate force development (G-H), width (I-J), half relaxation time (K-L). Maximal rate of relaxation (M-N) during twitch stimulation. Difference in sex is more predominant in time to peak, half rise time, width, half relaxation time, maximal rate of relaxation. There is a trend toward alteration in female *Smn$^{2B/-}$;SMN2$^{+/-}$* mice for these measures. Note that only *Smn$^{2B/-}$;SMN2$^{+/-}$* mice are separated by sex. Young WT and *Smn$^{2B/+}$;SMN2$^{+/-}$* mice were not separated by sex. The young WT and *Smn$^{2B/+}$;SMN2$^{+/-}$* mice group are the same for either male and female

comparison(The n value for each experiment were young WT (3), *Smn*$^{2B/+}$;*SMN2*$^{+/-}$ mice (5), *Smn*$^{2B/-}$;*SMN2*$^{+/-}$ mice (5 males, 4 females), average ± SEM displayed, one-way ANOVA with tukey post-hoc test, $P \leq 0.05$ for *, $P \leq 0.01$ for **, and $P \leq 0.001$ for ***).

The Smn$^{2B/-}$;SMN2$^{+/-}$ mouse model does not display extra-neuronal pathology over time

Extra-neuronal pathology has been described over the past few years in mouse models of SMA. We took advantage of the *Smn*$^{2B/-}$;*SMN2*$^{+/-}$ mice to see whether SMN may be required for cellular maintenance of other organ systems during aging. We first analyzed gross organ size of the heart, spleen, liver, and kidney at 6, 12, 18 and 22 months. No clear and sustained difference was readily apparent over the course of the lifespan (Fig 5.8).

We next investigated whether lymphoid organ abnormalities may be present in *Smn*$^{2B/-}$;*SMN2*$^{+/-}$ mice. Three laboratories independently identified small and disorganized spleen in multiple severe mouse models of SMA (150, 258-260). Of note, we did not observe any changes in histology (Fig 5.9A-F). We believe that poor perfusion is the reason for the small spleen size in *Smn*$^{2B/-}$ mice (Fig 3.23). Interestingly, splenic artery peak systolic velocity and the heart rate remained normal in *Smn*$^{2B/-}$;*SMN2*$^{+/-}$ mice (Fig 5.9G-H), thus possibly explaining the normal appearing spleens. More recently, fatty acid metabolism defects were described, where SMA patients were more susceptible to dyslipidemia and fatty liver (361) in accordance with initial reports (49-51, 127). In the *Smn*$^{2B/-}$ mouse models, it led to non-alcoholic fatty liver disease and subsequent functional deficit (361). *Smn*$^{2B/-}$;*SMN2*$^{+/-}$ liver were unchanged from control and showed no difference in triglycerides and cholesterol esters from 6 to 18 months of age (Fig 5.10

A-H). Lean mass was increased while fat mass was decreased at 18 months in the *Smn*$^{2B/-}$;*SMN2*$^{+/-}$ mice (Fig 5.10 I-J).

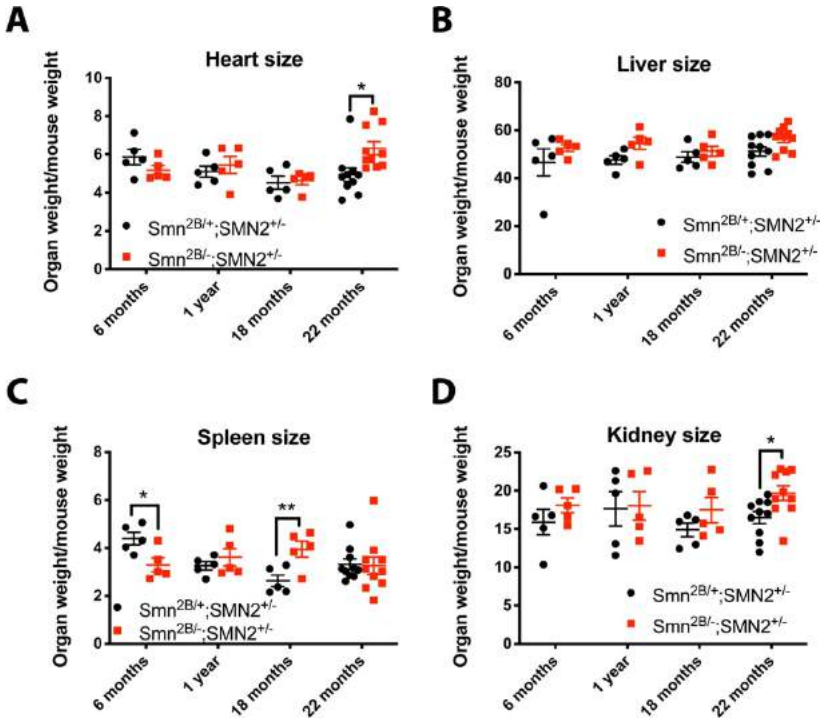

Figure 5.8 No gross abnormalities in extra-neuronal organs in the *Smn$^{2B/-}$;SMN2$^{+/-}$* mice. Gross morphological assessment of heart (A), liver (B), spleen (C), and kidney (D) shows minimal changes in organ size apart from the increased size of heart and kidneys in 22 months *Smn$^{2B/-}$;SMN2$^{+/-}$* mice. (The n value for *Smn$^{2B/+}$;SMN2$^{+/-}$* and *Smn$^{2B/-}$;SMN2$^{+/-}$* (5-10), average ± SEM displayed, unpaired student t-test, $P \leq 0.05$ for * and $P \leq 0.01$ for **).

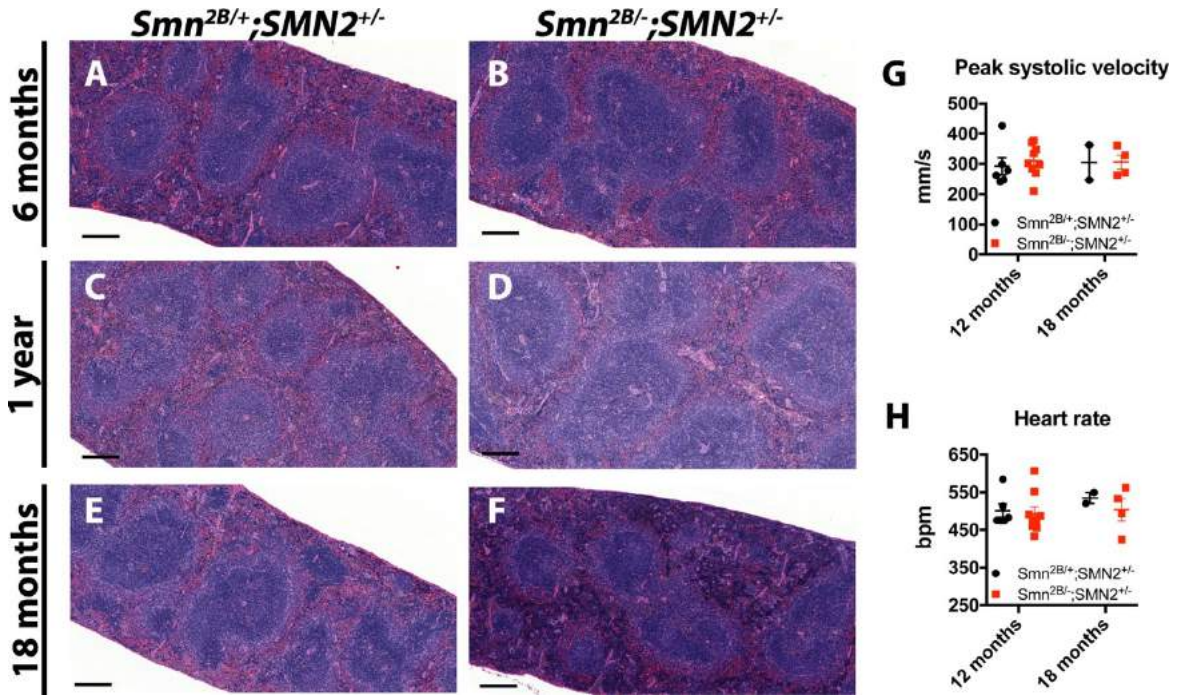

Figure 5.9 Spleen architecture is normal in *Smn$^{2B/-}$;SMN2$^{+/-}$* mice. Representative 10X images of H&E staining in spleens of *Smn$^{2B/+}$;SMN2$^{+/-}$* and *Smn$^{2B/-}$;SMN2$^{+/-}$* mice at 6 (A-B), 12 (C-D) and 18 months (E-F). (G) Peak systolic flow velocity was essentially unchanged at 12 and 18 months from *Smn$^{2B/-}$;SMN2$^{+/-}$* mice compared to *Smn$^{2B/+}$;SMN2$^{+/-}$* mice as assessed by ultrasonography. (H) Heart rate between *Smn$^{2B/+}$;SMN2$^{+/-}$* and *Smn$^{2B/-}$;SMN2$^{+/-}$* mice was similar for the peak systolic velocity assessment. Scale bars represent 200 µm. (n = 5 for A-F, 6-9 for 12 months and 2-4 for 18 months in G-H, average ± SEM displayed, unpaired student t-test).

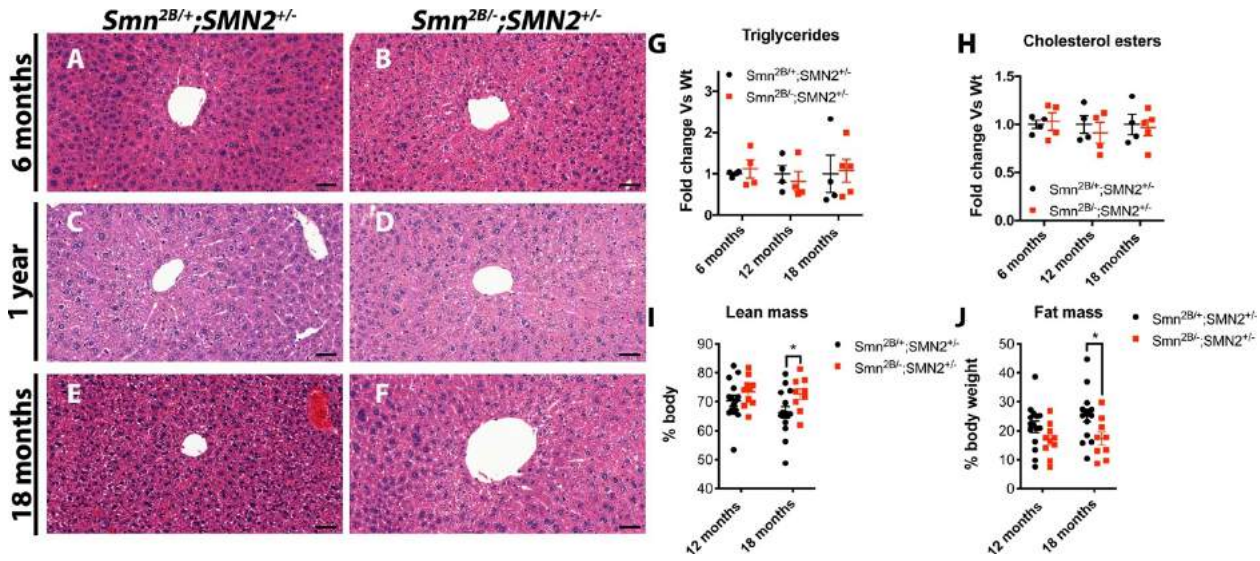

Figure 5.10 *Smn$^{2B/-}$;SMN2$^{+/-}$* mice do not develop fatty liver or body composition disturbance.

Representative 30X images of H&E stained liver of *Smn$^{2B/+}$;SMN2$^{+/-}$* and *Smn$^{2B/-}$;SMN2$^{+/-}$* mice at 6 (A-B), 12 (C-D) and 18 months (E-F). (G-H) Levels of triglycerides and cholesteryl esters were unchanged in *Smn$^{2B/-}$;SMN2$^{+/-}$* mice over their lifetime. (I-J) Body composition analysis identified a slightly higher lean mass and lower fat mass in 18 months *Smn$^{2B/-}$;SMN2$^{+/-}$* mice compared to *Smn$^{2B/+}$;SMN2$^{+/-}$* mice. Scale bars represent 50 µm. (The n value is 5 A-F, 4-5 G-H, 9-15, I-J, average ± SEM displayed, unpaired student t-test, $P \leq 0.05$ for *).

Over the past 10 years, a resurgence of case studies have highlighted potential heart defects in severe SMA patients (114). Similarly, multiple studies of the heart in preclinical models demonstrated bradycardia, reduced function, innervation and vascularization (120-123). We investigated whether cardiac defects were present in 12 and 18 month old *Smn*$^{2B/-}$;*SMN2*$^{+/-}$ mice using cardiac echography. We found no change in heart rate, stroke volume, cardiac output, ejection fraction and fractional shortening (Fig 5.11 A-E). As such, it appears that the tail length reduction is not dependent on poor cardiac function but rather subsequent to vasculature issues or dysfunctional neovascularization.

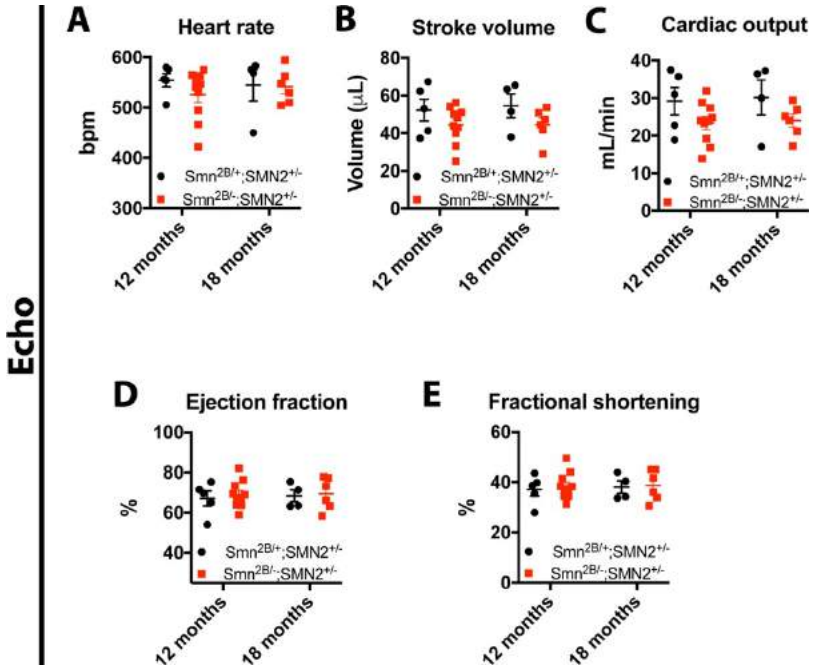

Figure 5.11 Cardiac function is normal in *Smn$^{2B/-}$;SMN2$^{+/-}$* mice. No obvious change was observed in heart rate (A), stroke volume (B), cardiac output (C), ejection fraction (D), and fractional shortening (E) at 12 and 18 months in *Smn$^{2B/-}$;SMN2$^{+/-}$* mice in comparison to *Smn$^{2B/+}$;SMN2$^{+/-}$* mice. (n=5-10 for A-E, average ± SEM displayed, unpaired student t-test).

Discussion

Mild mouse models of SMA have been extremely difficult to generate (152). As such, pre-clinical modeling of the milder phenotypic spectrum of the disease, such as type III-IV SMA patients, and understanding SMN-dependent molecular changes during aging have remained challenging. To fill this gap, we have generated the *Smn$^{2B/-}$;SMN2$^{+/-}$* mouse model, by introducing one allele of *SMN2* to the *Smn$^{2B/-}$* mice.

In comparison to other mild mouse models (Table 5.1), the *Smn$^{2B/-}$;SMN2$^{+/-}$* mice display the hallmark features that are commonly reported in SMA. These include early and sustained motor weakness, eventual motor neuron loss, electrophysiological signs of denervation, and muscle atrophy. Other mild mouse models of SMA either show limited features of SMA (A111G *Smn$^{-/-}$ SMN2* (160), *Smn$^{C>T/C>T}$* (355), *Smn$^{C/C}$* (161), have shown smaller myofibers without any overt motor neuron loss (356, 357) or motor neuron loss without motor function impairment (359, 360). Yet, the few models that showed promise (SMN^{RT} (356), A2G *Smn$^{-/-}$SMN2* (158), the Taiwanese mice (four copies of SMN2)(159), could not be used for aging studies. One study made use of antisense oligonucleotides to further reduce SMN levels in the Taiwanese model (four copies of SMN2) to study SMN function in adulthood (311). However, this system is unlike the usual SMA pathology given a further reduction in SMN protein in adulthood. As such, the *Smn$^{2B/-}$;SMN2$^{+/-}$* mouse represents the first mild model of SMA for studies in adulthood and aging. In this respect, the *Smn$^{2B/-}$;SMN2$^{+/-}$* mice provide many benefits. They allow study of the earliest and perhaps most susceptible molecular changes that occurs with SMN depletion. They will also permit long experimental paradigms such as muscle regeneration after cardiotoxin treatment, diet modulation, and exercise.

Our characterization of the *Smn*$^{2B/-}$;*SMN2*$^{+/-}$ mice revealed some surprising information. First, the electrophysiological data showed selective preferential transmission/denervation defects in the male mice, with the female mice showing almost no deficiencies in these measurements. In male *Smn*$^{2B/-}$;*SMN2*$^{+/-}$ mice, neuronal stimulation could only reach about 80% of the tetanic force generated by stimulating the muscle directly, implying that 20% of the fibers do not get recruited by neurons. The inability to sustain tetanic contraction in male vs. female *Smn*$^{2B/+}$;*SMN2*$^{+/-}$ mice, as shown by the time to peak force was striking. This feature is not reproduced by muscle stimulation, thereby eliminating a possible muscle etiology and confirming that the localization of the defect lies at the axon or the NMJ. It should be noted that the electrophysiological experimental paradigm used in this study does not allow us to distinguish between a conduction block within the nerve or a deficient process at the NMJ in the inability to sustain tetanic contraction. Nevertheless, the reason for the sex difference in our study remains unclear. It is not the first time that sex differences are brought up in the context of SMA. The preferential severity to the male population is in line with the majority of clinical reports discussing sex differences, particularly in milder types of SMA (363-366). Some studies highlight a lower incidence of disease onset after female puberty and subsequently a predominance of males in the mild SMA types (364, 367), (368). Furthermore, females appear over-represented in the asymptomatic biallelic *SMN1* deletion carrier population (365, 366, 369-373). This may be related to genetic modifiers, such as plastin 3, that appear to be female sex dependent (374, 375). The exact mechanism for this sex difference remains unclear, but it strongly highlights the importance of considering sex in pre-clinical and clinical experimental framework.

Another interesting but unexpected feature of the *Smn*$^{2B/-}$;*SMN2*$^{+/-}$ mice was the emergence of a myopathic phenotype prior to any obvious neuropathy. This is first evidenced by the sustained increase in the proportion of centrally located nuclei in skeletal muscle. In our experimental scheme, it is possible that the increased central nucleation in the muscle of *Smn*$^{2B/-}$;*SMN2*$^{+/-}$ mice is a sign of constant satellite cell activation or regeneration, highlighting a possible compensatory mechanism or abnormal satellite cell functioning. If so, upon extended period of compensation, a consequent satellite cell pool depletion could explain the drastic loss of muscle fibers we observed at 18 months of age. Interestingly, we have previously identified increased central nucleation in *Smn*$^{2B/-}$ and *Smn*$^{-/-}$;*SMN2*$^{+/-}$ mice despite the absence of degenerating fibers (168), both representing severe models of SMA. Furthermore, the appearance of a myopathy was also described in mice where inducible SMN depletion was performed in adulthood (376). However, the studies reported for this latter model extended only until 9 months of age, giving limited information about aged SMN-depleted muscle and motor neurons (376). Future thorough assessment of muscle regeneration during aging in a mild SMA mice will be required to understand SMN involvement, if any, in satellite cell biology. Furthermore, the electrophysiological data we present also revealed some relaxation defects in both the tetanus and twitch stimulation (half relaxation time, maximum rate of relaxation, width) despite receiving stimulation through the nerve or the muscle. It also showed some contraction defects in twitch stimulation. Interestingly, the SMN depletion appears to exacerbate the usual process of aging, as the *Smn*$^{2B/+}$;*SMN2*$^{+/-}$ showed similar deficiency in comparison to young wild type mice, albeit not as severe as *Smn*$^{2B/-}$;*SMN2*$^{+/-}$ mice. In contrast to the defect in NMJ/neuronal transmission, the muscle defects appear to be similar amongst male and female *Smn*$^{2B/-}$;*SMN2*$^{+/-}$ mice. Of importance, the overall capacity to generate force was not affected when normalized on muscle weight, meaning the muscle

intrinsic weakness is unlikely to contribute to the motor impairment seen in this mild model. This is in contrast with more severe SMA models (108). Altogether, these results further stress probable SMN-dependent muscle intrinsic defects and the *Smn*$^{2B/-}$;*SMN2*$^{+/-}$ mice offer a new framework to easily identify defects prior and independent to neuronal disturbances.

While direct comparison to human SMA is difficult, the *Smn*$^{2B/-}$;*SMN2*$^{+/-}$ mice more closely represents the mild type III or type IV SMA patients. Literature on type IV SMA patients is extremely sparse and date prior to genetic studies (377). Their symptomatology is usually extremely slow (i.e. over 20 years course), marked by gradual fasciculations and mild progressive weakness which may eventually lead to the patient becoming wheelchair bound or requiring assistance with walking(377). In the new era of SMA treatment, it remains unclear whether persistent interventions will be required and long-term complete reversal of symptoms will be attained. Therefore, it is likely that type I SMA patients will transition into a less severe type III-IV once treated, giving them a longer or normal lifespan. There is a paucity of studies investigating the support and medical needs of type IV SMA patients (and soon the treated patients) as they age. Ideally, one would want to limit comorbidities that may arise naturally or upon challenges. In recent years, the SMA field has witnessed a surge in the identification of extra-neuronal defects, mostly in pre-clinical models and less often in humans (reviewed in (110)). With some reassurance, according to the model studied here, the spleen, the liver and heart remain unaffected.

Altogether, the *Smn*$^{2B/-}$;*SMN2*$^{+/-}$ mouse model provides the first adequate model of mild SMA. It will allow investigation of the most susceptible defects that arise with SMN-depletion,

particularly in aging. Furthermore, this model will confer anticipatory guidance of treated SMA patients that are likely to age far beyond SMA natural history.

Acknowledgements

We would like to thank My Tran Trung for assistance with experiments. We would like to thank all members of the Kothary laboratory for helpful discussions.

Funding Sources

This work was supported by Cure SMA/Families of SMA Canada; Muscular Dystrophy Association (USA) (grant number 294568); and Canadian Institutes of Health Research (CIHR) (grant number MOP-130279). M-O.D was supported by a Frederick Banting and Charles Best CIHR Doctoral Research Award.

Conflict of interest

Marc-Olivier Deguise received honoraria and travel accommodations by Biogen for the SMA Summit 2018 held in Montreal, Canada. Rashmi Kothary and the Ottawa Hospital Research Institute have a licensing agreement with Biogen for the *Smn*$^{2B/-}$ mouse model. All other authors have no competing interests to declare

Chapter 6: Discussion

Contribution

This section comprises some parts directly taken from the following manuscripts:

Marc-Olivier Deguise and Rashmi Kothary (2017) New insights into SMA pathogenesis: Immune dysfunction and neuroinflammation. *Annals of Clinical and Translational Neurology (IF: 4.656).* Doi:10.1002/acn3.423

My Contribution: ~85% (Wrote the majority of the manuscript)

Authors contributions: RK wrote manuscript and critically reviewed it.

Marc-Olivier Deguise & Rashmi Kothary (2019) Chapter 2: Spinal muscular atrophy. Chromatin signalling and Neurological disorders. Edited by Olivier Binda, Elsevier

My contribution: 85% (Wrote the majority of the manuscript)

Authors contributions: RK wrote manuscript and critically reviewed it.

The current status of muscle involvement in SMA and therapies

Deciphering the molecular etiologies of atrophy pathways in SMA

The contribution of muscle in SMA pathogenesis has long been debated. Initially considered a prime suspect in the disease (54, 55), it eventually lost considerable ground to the motor neurons, for which the evidence for clear pathophysiological defects was not questionable. It was once even suggested that the muscle had no impact on disease development (378). Indeed, this shift in perspective delayed our true understanding of SMN depletion in muscle and how it can affect the SMA symptoms.

Our laboratory had initially identified myogenic impairment, which suggested muscle intrinsic defects (88, 168). This finding was reproduced at numerous occasions in other model systems (59, 169, 209) but also in SMA patient biopsies and cells (336, 379). While the complete molecular mechanism underpinning these defects has yet to be elucidated, therapies aimed at muscle pathology and growth could offer improvement, especially in combination with SMN-dependent therapies. Initial therapies to stimulate muscle growth have focused on IGF-1 and its related pathways (100-102, 105). They have yielded limited improvement in pre-clinical models (100-102, 105). Atrophy, although considered one of the main features of SMA, has surprisingly not been studied to any extent by scientists. Yet, atrophy could offer an easily targetable avenue for therapeutic development to improve muscle function that could be translatable to other diseases. In the first part of this thesis, we showed that atrophy in SMA is mediated through the FoxO transcription factor family, capable of inducing both the proteasomal and autophagosomal

pathways. To modulate this pathway, we used TSA, a HDAC inhibitor (HDACi) that induces transcriptome wide changes. The complete reversal of atrophy pathways upon TSA treatment both in skeletal muscle and the heart was striking. This study complemented other positive pre-clinical studies identifying advantageous effects of HDACi (121, 169, 175, 176, 200, 253, 380-383). A recent review highlighted the successes and failures of HDACi in the context of SMA (384). Indeed, clinical trials with valproic acid (VPA) and sodium phenylbutyrate (4-phenylbutyric acid, 4-PBA) yielded mixed results (385-395) (See Table 6.1). Since the results of the clinical trials, the excitement for HDACi as a therapy for SMA progressively faded in the shadow of new and more effective SMN inducing therapies such as Spinraza and ZolgenSMA. Even though HDACi may not represent a suitable and translational therapeutic option, they could still serve as a proxy to identify pathogenic events or protective pathways in the context of SMA.

More importantly, our work highlighted that molecular pathologies may be dependent on the severity of the SMA phenotype, but also the survival time. These factors are raising additional consideration when designing studies, such as inclusion of pre-clinical models of various severities. Indeed, subsequent studies within this thesis provided additional evidence of overlapping and divergent findings that can occur between different pre-clinical models (such as in immune organ defects in Chapter 3 and fatty liver infiltrations in Chapter 4). The identification of a common pathway amid the phenotypic diversity will likely pinpoint the earliest molecular changes that are directly dependent on SMN-depletion.

Table 6.1. Overview of HDACi clinical trials

Compound	*Experimental setting*	*Observations*	*FL-SMN transcript*	*SMN protein*	*Ref.*
Sodium phenyl-butyrate (4-PBA)	Human (Type II)	modest ↑ in motor function	N.A.	N.A.	(386)
	Human (Type II-III)	↑ SMN transcription and slight improvement on motor function	↑ 1-2.4-fold[1]	N.A.	(385)
Valproic acid (VPA)	Human (Type I-III)	↑ SMN transcription (↑ in 7 of 20 SMA patients)	↑ 1-3.4-fold in carriers[1]	↑ 1-13.7-fold in carriers[1]	(387)
	Human (Type II-III)	some motor improvement in some patients	N.A.	N.A.	(388)
	Human (Type I-III)	some toxicity, better motor function in type II, ↑ bone density	N.C.	N.A.	(391)
	Human (Type II-III)	↑ SMN proteins in some patients	N.A.	↑ 1.2-2.9-fold	(389)
	Human (Type II-III)	N.C. in motor function, electrophysiological studies, bone density, and QOL	N.C.	N.A.	(390)
	Human (Type III)	no or very modest change in motor function, electrophysiological studies and QOL	N.C.	N.A.	(392)
	Human (Type II-III)	some motor benefits in type II	N.A.	N.A.	(393)
	Human (adult SMA patients)	N.C. in motor function or electrophysiological studies	N.C.	N.C.	(394)
	Human (adult SMA patients)	↑ H4 acetylation without ↑ SMN expression	N.C.	N.C.	(395)

Abbreviations: Ref. – references, ↑ - increase, N.A. – not assessed, N.C. – no change, QOL – quality of life

[1] 1-fold denotes no change

Additional findings of muscle intrinsic defects

Over the last few years, very little research has attempted to further our understanding of muscle intrinsic defects (379). Serendipitously, we have reaffirmed the presence of muscle intrinsic defects with the production of the *Smn*$^{2B/-}$*;SMN2*$^{+/-}$ mice (Chapter 5). The explicit and progressive appearance of centrally located nuclei over the course of their lifespan is in keeping with more severe models like the *Smn*$^{-/-}$*;SMN2* and the *Smn*$^{2B/-}$ models (168). We had previously hypothesized that they were consequent to satellite cell dysfunction (168), which could be linked to impaired myogenesis. Nevertheless, studies of satellite cell function have been complicated by the extremely short lifespan of the SMA mouse models available at the time. The *Smn*$^{2B/-}$*;SMN2*$^{+/-}$ model offers great potential, allowing for cardiotoxin challenge, which may give us functional insight into satellite cell function during aging. Of note, central nucleation has been featured in limited reports (396-399) involving SMA patients and will warrant further research. Centronuclear myopathy is a neuromuscular disease that displays central nucleation as its main features. It can be caused by mutations in various genes such as myotubularin 1 (*MTM1*), dynamin 2 (*DNM2*), bridging integrator 1 (*BIN1*), ryanodine receptor 1 (*RYR1*) and titin (*TTN*) and the underlying pathological phenomenon remains unclear but span across alterations in calcium (400-402), satellite cells (403), in the cytoskeleton (404) or at the neuromuscular junctions (405, 406). SMN depletion could lead to splicing alterations in those candidate genes, increasing the propensity of centrally located nuclei. Indeed, a link between SMN depletion and myotubularin expression has previously been suggested (396).

Not limited to satellite cell defects, *Smn*$^{-/-}$;*SMN2*$^{+/-}$ mice also showed electrophysiological evidence of relaxation and contraction dynamic impairment. Limited electrophysiological studies had been performed, likely given the complexity of completing these experiments with extremely small muscles, such as in severe models of SMA mice. A previous study in our laboratory had identified muscle intrinsic weakness in severe SMA models, subsequent to maturation lag of ion channels (108). Better understanding excitation contraction coupling and relaxation could offer therapeutic target to optimize strength. The most advanced therapy (Reldesemtiv or CK-2127107 by Cytokinetics/Astellas) currently in clinical trial (ClinicalTrials.gov, NCT02644668) to improve muscle functions in SMA does so by increasing the sensitivity of the sarcomere to calcium (407, 408). This allows for increased force production at lower frequencies due to low neural output (407). It is considered a fast skeletal muscle troponin activator (FSTA). Results from this clinical trial have only been released at SMA conferences or on the website of Cytokinetics. Most recently, the company provided preclinical data showing additive therapeutic effect on muscle force by reldesemtiv when combined with SMN-dependent therapies such as nusinersen. However, the weakness was still not completely relieved (see website). Clinical trial data showed increased performance in the 6 minutes walk test, improved endurance, and respiratory function but did not show differences in the Hammersmith functional motor scale – expanded (HFMSE) in SMA patients (see website). Other muscle-enhancing drugs are in the research pipeline including SRK-015, an anti-proMyostatin monoclonal antibody, by Scholar Rock (ClinicalTrials.gov, NCT03921528) and BIIB110, a Type-II-B activin receptor antagonist, by Biogen. These are in an early phase with limited available data. It will be interesting to see their efficacy as pre-clinical

evidence of modulating these pathways were unsuccessful (100-102, 105), likely due to low myostatin activity in neuromuscular disorders in general (104).

The current status of the immune system in spinal muscular atrophy

Lymphoid organ defects are a consistent feature in different SMA mouse models

Most recently, there has been many concurrent advancements in understanding the pathology of immune organs in SMA. Indeed, our group along with two others has independently published a whole array of abnormalities in immune organs, such as the spleen and thymus, in different SMA mouse models (Fig 6.1) (258-260). The strikingly small spleens was observed in four SMA mouse models of different severity (258-260). Similarly, the spleen architecture was disrupted in 3 out of 4 SMA mouse models. SMA type 1 patient necropsies showed an array of splenic abnormalities such as accessory spleens, congested red pulp and increased numbers of precursors but no change in size were reported (259).

The reasons behind the small spleen sizes in the SMA mouse models could be multifactorial. Possible etiologies include abnormal vasculature, denervation, cell-intrinsic defects, proliferative/apoptotic abnormalities, and abnormal expression of homing chemokines (219) (Figure 6.2). Proliferation of cells in the spleen appeared abnormal only at late stages in the Taiwanese SMA model mice, while it remained unchanged in the *SmnΔ*7 mice (259, 260). Investigation of cell death revealed very little change in the Taiwanese model (259). Vasculature abnormalities were reported in other organs and could

have been the initial trigger (123, 255). Immunostaining of blood vessel markers revealed very little change in the spleens of Taiwanese and *SmnΔ*7 mice (259, 260). While other factors can't be eliminated, inability to maintain appropriate perfusion appears most likely. Indeed, we have observed a significant decrease of peak systolic flow in the splenic artery at both P9 and P19 in $Smn^{2B/-}$ mice. Consequently, much like a balloon, the spleen does not fill with appropriate blood volume, assuming a smaller shape. Additionally, the $Smn^{2B/-}$ spleens displayed increased necrosis on gross morphological observation, which may suggest abnormal blood flow (258). In a similar manner, smooth muscle cell clumping observed in these spleens may be due to abnormal vasculature (258). As a proof of concept, re-introducing one copy of SMN2 on the $Smn^{2B/-}$ background (the $Smn^{2B/-};SMN2^{+/-}$mice) resulted in normal spleen size and peak systolic blood flow velocity that was sustained throughout their lifetime. As such, this may explain the discrepancy between pre-clinical data and human patient data, given that humans do not harbor a small spleen nor show overt vascular abnormalities. Vascular abnormalities have been reported in one case series of two patients with SMA but are considered a rare event in SMA symptomatology (237).

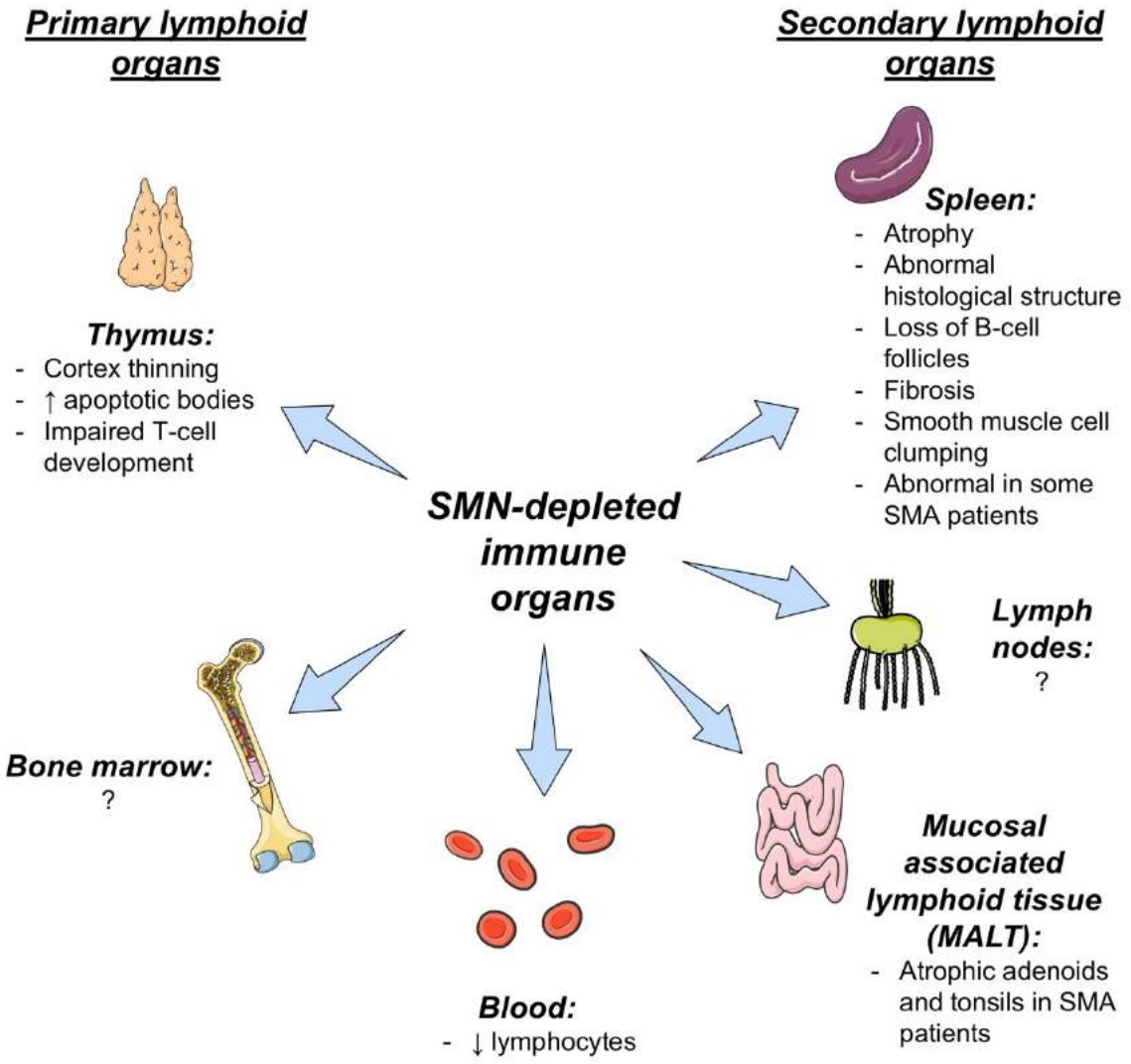

Figure 6.1 A summary of immune organ defects described from studies on SMA model mice. Spleens have the most drastic changes, although cortex thinning has also been described in the thymus. Very limited information is available on the status of the bone marrow, lymph nodes and MALTs in SMA. The schematic art pieces used in this figure were provided by Servier Medical art. Servier Medical Art by Servier is licensed under a Creative Commons Attribution 3.0 Unported License.

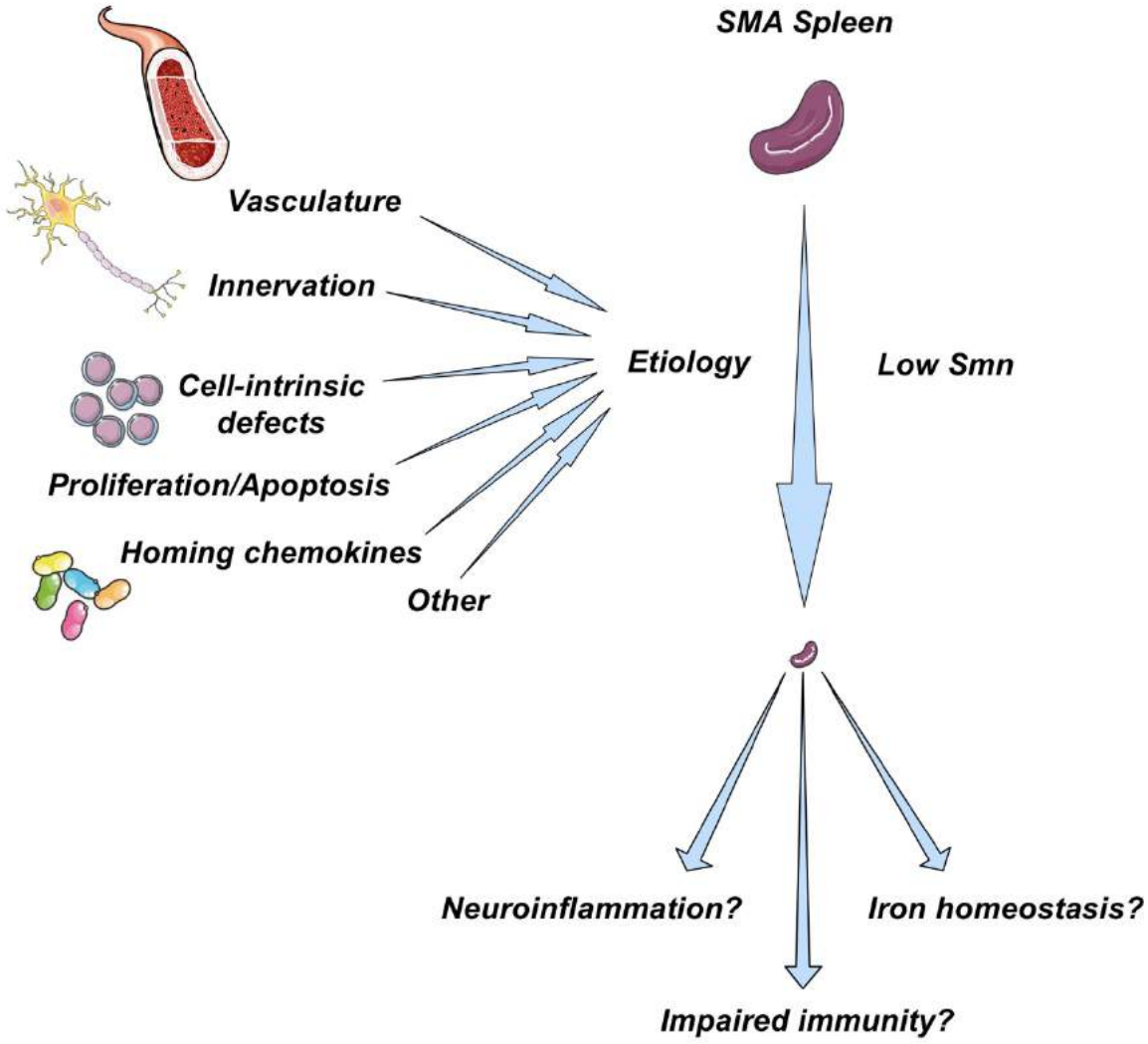

Figure 6.2 Possible mechanisms leading to small spleens in SMA mice and its consequences. Vasculature, innervation, cell-intrinsic defects, proliferation/apoptosis and homing chemokines could all lead to small spleen size. The consequences of small spleen size include neuroinflammation, impaired immunity and iron homeostasis defects. The schematic art pieces used in this figure were provided by Servier Medical art. Servier Medical Art by Servier is licensed under a Creative Commons Attribution 3.0 Unported License.

Potential functional consequences of lymphoid organ defects in SMA

Immunity

It is likely that the multiple abnormalities observed in the lymphoid organs of the SMA mice result in impaired immunity. The structure of the spleen is crucial for its function (as previously discussed in Chapter 3) (219). This places the spleen as a major player in the clearance of encapsulated bacteria like *Mycobacterium tuberculosis* and *Streptococcus pneumoniae*, but also of *Staphylococcus aureus*, and potentially of viruses (219, 249, 251, 409, 410). Moreover, asplenic patients are immunodeficient, are recommended to be on a more stringent immunization schedule, and more aggressive clinical management is initiated at an earlier stage when facing fever or infection (411, 412). A very recent report highlights the inflammatory state in *Taiwanese* mice, a higher bacterial burden under uninfected condition as well as faster deterioration and death upon LPS challenge (413).

It is interesting to note that early reports described atrophic Waldeyer's ring and cervical lymph nodes in addition to impaired cell-mediated immunity, as assessed by lymphocyte transformation and skin test, in *clinically* diagnosed SMA patients (52, 53). Accordingly, some SMA patients had non-mucocutaneous candidiasis, which usually only occurs in immunodeficient individuals (414). Moreover, pulmonary infection, especially pneumonia, appears to be a common feature of SMA patients (113, 212, 415-417). Decreased respiratory efficiency and stasis of secretions can increase risk of infections (417, 418). For this reason, a superimposed immunodeficient state has not previously been considered as contributory to the disease etiology but may indeed play a major role in the

presentation of chronic pulmonary infection in SMA patients. Nonetheless, evidence in human SMA patients remains sparse at the moment and more research is warranted on this aspect to better understand whether murine defects are reflective of true human pathology.

Many areas of the immune system remain unexplored in the context of SMA. The bone marrow, MALTs and peripheral blood have yet to be investigated (Fig 6.1). Future endeavors should aim at expanding our knowledge on the role of other organs of the immune system in SMA pathogenesis, and decipher whether SMA mice and patients can correctly mount an immune response to a variety of pathogens that include both bacteria and viruses in the setting of infection or simply vaccination. Of course, retrospective clinical studies should also aim at discovering over-represented pathogens causing infections in the SMA patient population and their likelihood of infections in comparison to healthy individuals to ensure enhanced care is provided if needed.

Iron homeostasis

The spleen is also involved in blood filtration and iron homeostasis (219). Strikingly, macrophages involved in iron recycling are depleted in SMA (260). However, splenic iron metabolism was not investigated in the latter study. Interestingly, impaired liver development, iron overload and embryonic lethality were the main features of *Smn* conditional knockout restricted to the liver (292). Recently, iron homeostasis defects were also observed in the Taiwanese mouse model of SMA (128, 413). We have corroborated these findings in the $Smn^{2B/-}$ mice (361). Whether the spleen is causative of iron

dysregulation, and potential cross-talk between the liver and the spleen exists to regulate the pool of iron remains to be determined.

Neuroinflammation

Neuroinflammation is a well established characteristic of neurodegenerative disorders (228). This process is mainly mediated by astrocytes, microglia and T-cells (263). Defective immune organs, and more particularly a potentially defective T-cell compartment, might signal defective inflammatory response in SMA (Fig 6.3). It is interesting to note that lymphoid organs, and more specifically the spleen, may actively participate in the process of neurodegeneration (419). ALS, an adult onset motor neuron disorder, has received attention from the SMA community for their possible common molecular ties in disease pathogenesis (420). Neuroinflammation research in ALS has gained considerable ground since reports described microglial and astrocytic activation features, as well as presence of lymphocytes in necropsies of ALS patients (421, 422).

In the context of SMA, neuroinflammation has never been thoroughly investigated (Fig 6.3). Microglia and T-cells have been mainly overlooked while some reports have highlighted the contributions of astrocytes to disease pathogenesis. Astrogliosis was observed in necropsies of patients (137-140) and in the *SmnΔ*7 mouse model at both pre-symptomatic and symptomatic stages (142). SMA patient induced pluripotent stem cell-derived astrocytes revealed abnormal calcium regulation, decreased glial cell derived neurotrophic factor (GDNF) production but normal GLT1 expression (142). There is no doubt that astrocyte intrinsic abnormalities contribute to SMA pathogenesis, however their link to neuroinflammation and motor neuron death has not been determined (144). SMN

restoration restricted to the astrocyte compartment significantly increased lifespan and motor behavior, but did not improve motor neuron survival (138). More related to the context of neuroinflammation, proinflammatory cytokines could be elevated in SMA patients and mouse models (138, 258, 413). Microglial activation has been observed in the *SmnΔ7* mouse model but not in the more severe *Smn*$^{-/-}$*;SMN2* mice (107, 139, 140). Most recently, a slightly more extensive description of microglial cells in *Smn*$^{2B/-}$ mice was published (423). *Smn*$^{2B/-}$ mice were shown to have microgliosis at late stage of the disease (P20 and onwards) and show a polarization towards inflammatory M1 microglia (423). The beneficial M2 microglial cells were seen in reduced proportions in comparison to WT mice (423). Normal proportions of M1/M2 microglia could be re-established by the Sig1G agonist PRE-084 (423).

We investigated the potential role of T-cells, more specifically CD4 helper T-cells, by impairing their production through genetic ablation (*Smn*$^{2B/-}$*;CD4*$^{-/-}$). We identified minimal change in lifespan, weight or motor behavior, highlighting that their contribution is likely minimal. Using a similar approach, we attempted to decipher the role of inflammation and necroptosis in SMA pathogenesis. The production of the *Smn*$^{2B/-}$*;Cas1*$^{-/-}$*;Rip3k*$^{-/-}$ would abolish IL-1β mediated inflammation as well as necroptosis through Rip3k ablation (280-282). Interestingly, the triple KO mice showed a modest improvement in survival and a qualitative improvement in motor function. While video evidence demonstrate a clear improvement in mobility of *Smn*$^{2B/-}$*;Cas1*$^{-/-}$*;Rip3k*$^{-/-}$ mice, we have yet to find a behavioral test that will allow us to properly quantify this finding (see Chapter 3). This necroptosis pathway may contribute to late features of the disease in SMA, more

specifically as a consequence to the primary insult and death of motor neurons. This is supported by the observation that *Smn*$^{2B/-}$;*Cas1*$^{-/-}$;*Rip3k*$^{-/-}$ mice essentially exhibit the same features as *Smn*$^{2B/-}$ mice until P19, at which point lifespan extension and improvement in mobility becomes evident. This is also in line with the recent findings of microglial activation in the *Smn*$^{2B/-}$ mice (423).

Despite the paucity of information, it is very likely that neuroinflammation contributes to some extent to SMA disease progression. At the moment, the very few reports on astrocytes are focused on cell-autonomous dysfunction and their relation to motor neurons, while the emphasis on the overall relationship of other glial cells in the potential neuroinflammatory CNS milieu is overlooked (Fig 6.3). Given the importance these cells may have on phenotypic progression and, potentially, in halting/reducing the full extent of therapeutic benefits that chronic SMA patients may experience, more research is warranted to dissect the important players in the context of the nervous system.

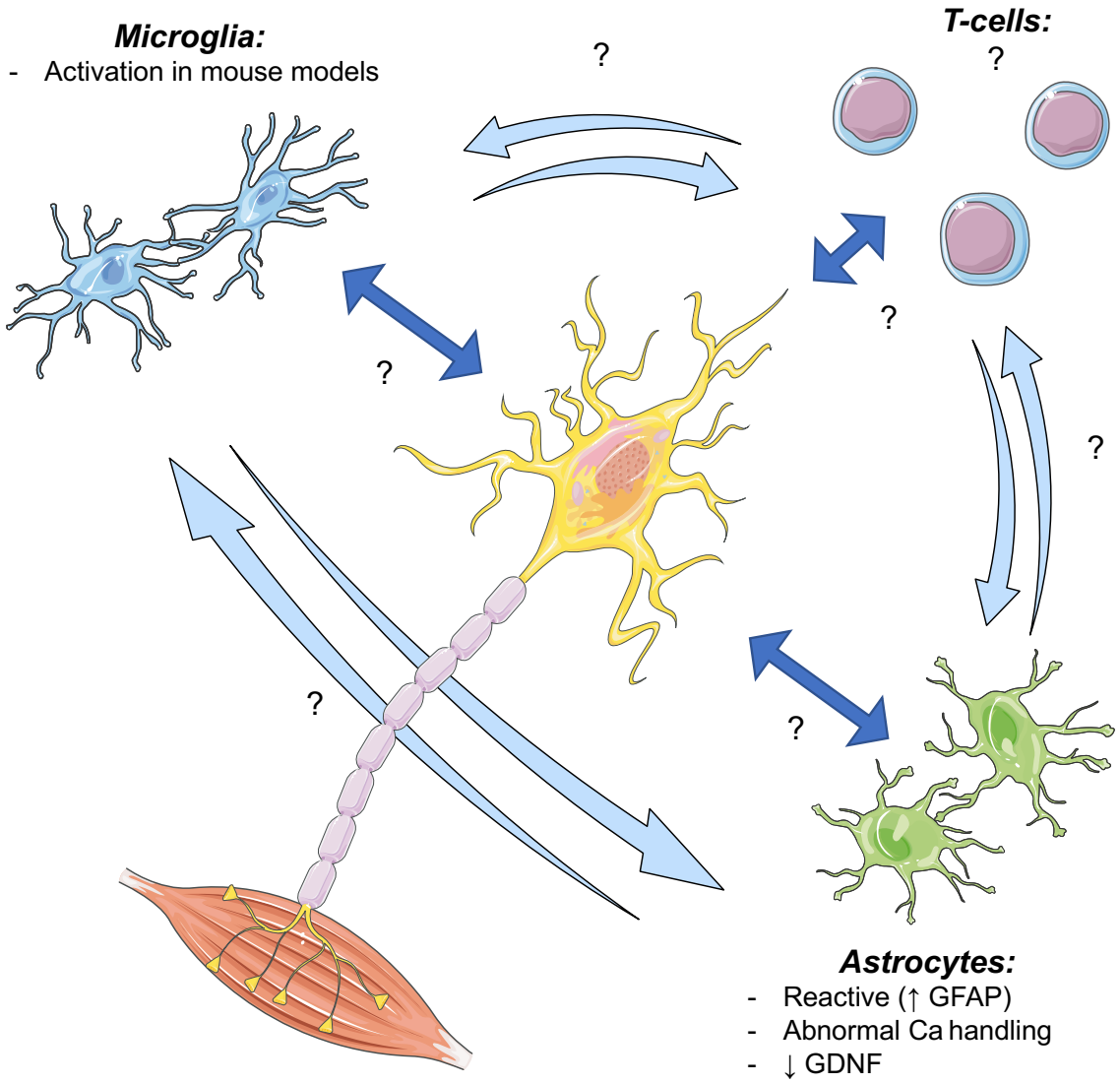

Figure 6.3 Current knowledge of neuroinflammation in SMA and its main contributors. Most of the work so far has focused on astrocytes with very limited information on microglia and T-cells. Their interaction in the CNS milieu has also not been addressed in the SMA context. The schematic art pieces used in this figure were provided by Servier Medical art. Servier Medical Art by Servier is licensed under a Creative Commons Attribution 3.0 Unported License.

Metabolic status in SMA

Increased susceptibility to dyslipidemia, NAFLD and low blood sugar in SMA patients and in pre-clinical models of SMA

Interest in metabolic abnormalities was present long before the genetic basis of SMA was even established (51, 341, 424). Early reports mostly focused on mitochondrial function and fatty acid metabolism disturbances (49-51, 341, 424). Even though the consensus statement for care of SMA patients urged scientists for more research in metabolic aspects and for the establishment of nutritional guides, there has been very little progress in these areas. To address this, we have screened for fatty acid alterations in a large cohort of SMA patients and in pre-clinical models of SMA. Interestingly, we identified increased susceptibility to dyslipidemia, fatty liver disease and hypoglycemia in SMA patients. In addition, these features were completely penetrant in the $Smn^{2B/-}$ mice. Perhaps most interesting was the propensity of SMA patients with more than three laboratory-defined measures of dyslipidemia, which is suspected to be quite low in the absence of familial dyslipidemia in this age group. Furthermore, the prevalence of liver steatosis in our cohort more closely matched the older obese pediatric population, where prevalence can range from 28-77% (299). Fatty liver in 2-4 years old normal children is quasi-nonexistent (0.7%) (298). Despite their muscle atrophy and small stature, a subset of SMA patients had increased fat mass (425-427) in the context of low caloric intake. As such, some SMA patients have also been classified as obese (288, 425). Perhaps, this may also be part or contributing to the fatty acid disturbance observed in SMA patients.

Our study provides an easy widely accessible manner to identify and monitor fatty acid metabolic abnormalities in SMA patients that can be acted upon with current cholesterol-lowering therapy if needed. While necropsies were used for the identification of fatty liver, this can be easily determined through ultrasonography, which consists of a widely used and non-invasive imaging modality (428). In contrast, early metabolic studies on SMA patients focused on urinary organic acids, muscle β-oxidation enzyme function, and plasma acylcarnitine and free fatty acid profiling (49, 51, 126). These tests are rarely used, are not widely available, and their interpretation requires a specialist's advice, hence making them poor choices in the screening and identification of SMA patients with potential metabolic abnormalities. In the future, screening and preventive treatment of dyslipidemia and fatty liver could be particularly important to limit significant co-morbidities, such as cardiovascular and cerebrovascular disease, in the newly aging demographics of treated SMA patients.

Etiology of fatty acid disturbances in SMA

Mechanistically, much of the work remains ahead of us. NAFLD occurs when an imbalance between input of fatty acid into the liver overshadows the mechanisms that get rid of the fatty acids (Fig 6.4). In tandem with the previous SMA literature, we have delineated five different entities that may participate in the development of liver steatosis in SMA, namely denervation, liver intrinsic defects, pancreas-liver axis impairment, mitochondrial dysfunction and muscle intrinsic defects.

As explained above, the contribution of denervation is critical in the evaluation of non-neuronal defects. To overcome the absence of a denervated control group in our clinical screen for dyslipidemia and NAFLD, we turned to pre-clinical mouse models. We found that denervation, such as in the *SOD1*^{G93A} mouse model of ALS, did not lead to development of liver steatosis. Previous literature in ALS described lipid redistribution rather than accumulation in *SOD1*^{G93A} mice, consistent with our findings (327). It should be noted that this model is also associated with increased lipid clearance in the periphery, which could abrogate fatty accumulation brought on by denervation (429).

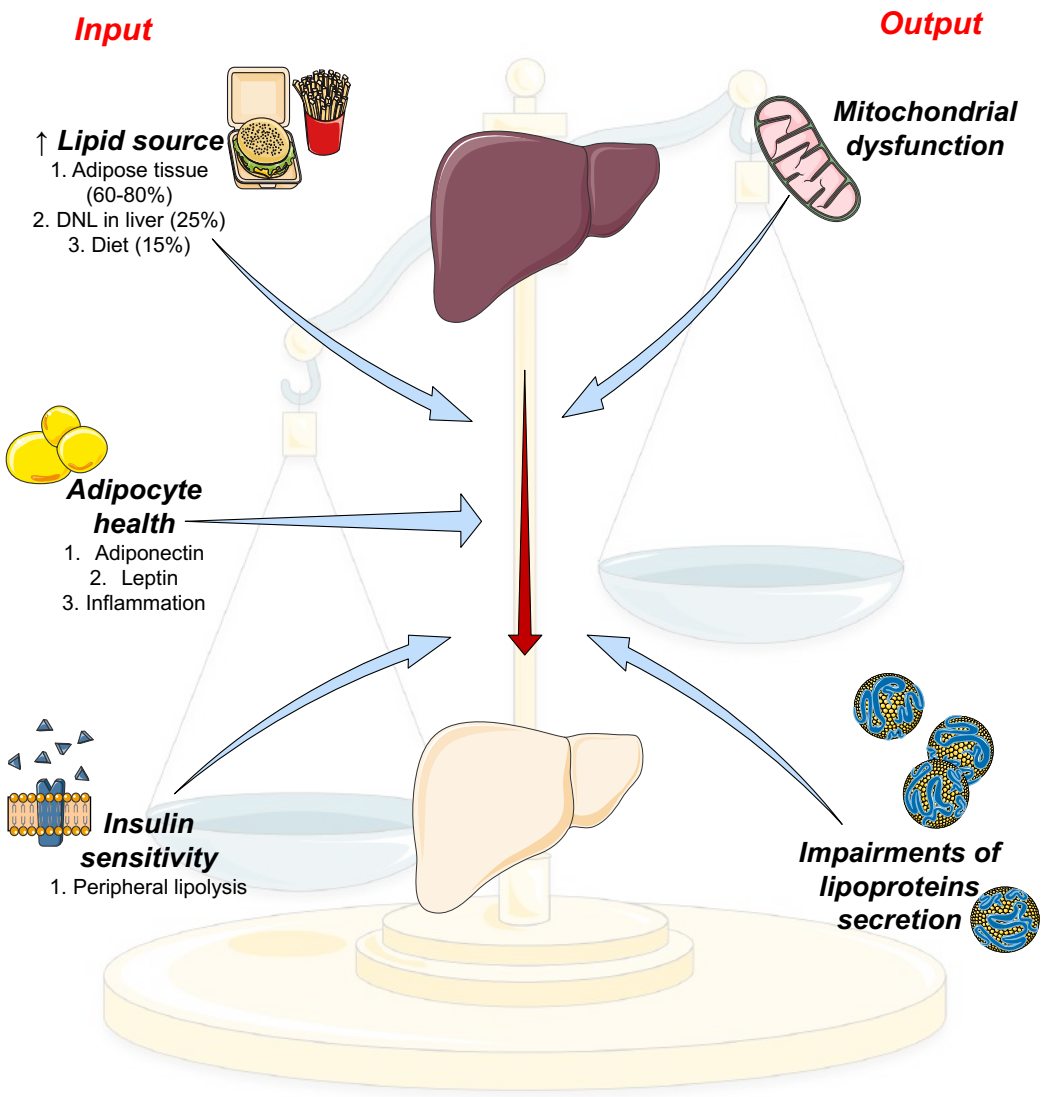

Figure 6.4 NALFD development consist of imbalance between fatty acid input and output. Fatty acid input includes all mechanisms that can lead to accumulation of lipid in the liver, which encompass the lipids from diet, *de novo* lipogenesis, and NEFA from periphery but also factors contributing to accumulation such as adipocyte physiology and insulin sensitivity. Output mechanism include the catabolism of fatty acid through oxidative pathways and export of lipoproteins. The schematic art pieces used in this figure were provided by Servier Medical art. Servier Medical Art by Servier is licensed under a Creative Commons Attribution 3.0 Unported License.

Our first attempt at identifying liver intrinsic defects, through a proteomic screen, pointed towards mitochondrial dysfunction. This appeared to be a good avenue given that mitochondrial dysfunction in SMA has surfaced in multiple reports (276, 328-333). However, our investigation identified supra-functional, rather than dysfunctional, liver mitochondria. This is also in line with early reports on fatty acid defects, which speculated that β-oxidation in muscle and liver is unaffected (49, 50). In fact, enhanced mitochondrial fatty acid oxidation also seemed to be present in SMA patients, as an emergence of case studies highlight ketoacidosis in SMA patients under various conditions (430-433). The onset of peroxisomal and microsomal oxidation in the *Smn*$^{2B/-}$ mice ensues as a result of lipid overload trafficked through the β-oxidation pathway. Induction of peroxisomal and microsomal oxidation was previously suspected, as some of the more severe SMA patients developed dicarboxylic aciduria (49-51). It is possible that fusion/fission or alternative defects are present but yet uncovered. Furthermore, the proteomic screen may have been performed too early to identify important pathogenic events that would trigger liver steatosis (i.e. P0 and P2 rather than P9 and P11). As such, liver intrinsic defects are still not ruled out. Indeed, systemic delivery of AAV9-SMN under the albumin promoter in *Smn*$^{2B/-}$ mice has partially rescued the pale liver phenotype (preliminary observations). Understanding molecular etiologies of liver intrinsic defects will be better performed using *in vitro* models, such as primary hepatocytes at various ages or SMN depleted HepG2 hepatocytes. This will allow thorough investigation of lipid uptake, lipid export and lipogenesis under various conditions.

Previous work from our laboratory had identified significant pancreatic alterations in both SMA mouse models and human patients (210, 211). The glucagon production appears to be consequent to either a lack of negative feedback, a strong initiation stimulus that remains present or simply pathological overactivation. We have identified *Smn*$^{2B/-}$ mice to be hypoglycemic from an early stage of development (361). Hypoglycemia had previously been observed in symptomatic SMA mice (211, 339, 413). Additionally, SMA patients appear relatively prone to low blood glucose, as expressed by glycated hemoglobin, in our cohort and in other case reports (134, 288, 431, 432). Of note, hyperglucagonemia has never been investigated in SMA patients. Glucagon levels were below detection limit in a small cohort of 6 Type II SMA patients (288). Testing glucagon levels would be best suited for the proportion of SMA patients that do develop NAFLD. More data on this would provide us with translational information as to whether or not the interplay between the liver and the pancreas is significant in the development of the NAFLD phenotype. The cause of hypoglycemia in the *Smn*$^{2B/-}$ mice remains unknown. Increased insulin sensitivity is thought to occur in *Smn*$^{2B/-}$ mice (211). In contrast, reports in SMA patients identify hyperinsulinemia and insulin resistance (288, 434). To rule out pancreatic alpha cell contribution to NAFLD, a rescue experiment with AAV9-SMN under the glucagon promoter would be helpful. Indeed, dissecting the involvement of eah metabolic organ (liver, muscle, pancreas, white adipose tissue) may require this approach.

Nutritional guidelines for SMA patients

Consensus on standards of care in SMA (212, 435) repeatedly highlighted the need for more research in SMA metabolism to ensure proactive care when it comes to nutrition

for SMA patients. Despite this, implementation of optimal nutritional guidelines for SMA patients is still lacking. Over the years, many SMA families have adopted the "amino acid diet". This diet was developed purely based on observations and experiences of caregivers. This diet consists of a reduced fat intake consumption and elemental free amino acid formula amongst other components. Many families declare subjective improvement and a positive impact on quality of life as a result of this particular diet. Nevertheless, the benefit of this diet has not been systematically studied scientifically and pre-clinical evidence remains sparse. At the current time, many SMA patients are found to be malnourished and some will be underfed while others overfed (426, 436).

In our study in a mouse model of SMA, it was intriguing that simple modulation of maternal diet, and eventually the offspring diet as they grow older, with low-fat diet or low fat/high sucrose diet led to doubling of the lifespan. This is consistent with some aspects of the "amino acid" diet. Furthermore, this phenomenon occurred independently of SMN levels, hepatic TG, liver damage or function. The exact mechanism for this is yet to be determined. Interestingly, Tein & *al.* (1995) speculated that a high-carbohydrate/low-fat diet would benefit SMA patients, as it would provide energy substrates that do not depend on fatty acid oxidation. Such a diet would keep the level of free fatty acids under control and diminish production of dicarboxylic acid in the circulation; products which are thought to have toxic potential (49). Others have also expressed similar ideas (134). A controversial small study had trialed SMA patients on low fat/high carbohydrate diet and showed positive results (341). The study has not since been reproduced. Diet modulation in pre-clinical models has been previously reported and showed contrasting results (339). It was concluded that higher fat content may confer a protective beneficial aspect (339). However,

the difference in fat content was about 5% and the benefits were marginal with lifespan extension of about 3 days in a severe model (339). Additionally, the diets used in their study consisted of two different chows, with many differences amongst them, and did not control exclusively for the fat content. In our study, the use of "research diets" minimized the effect of other substances while maximizing the differences in fat intake or sucrose, especially fat content (HFD 60% VS NC 18% VS HSD and LFD 10%). Nevertheless, clinical studies involving a large number of SMA patients will be needed to identify the optimal regimen and confirm the utility of the much-appraised amino acid diet.

Functional consequences of a damaged liver

The extent of fatty accumulation in *Smn*$^{2B/-}$ mice is likely to result in functional consequences. The liver is the metabolic factory of the body, producing plasmatic proteins, processing toxins as well as medications, and regulating glucose, lipid, and amino acid homeostasis. Liver defects were not systematically studied in the past, but issues in iron metabolism and hematopoiesis have surfaced (128, 292). Our study showed significant impairments in various pathways. Liver damage has yet to be studied in the human SMA population and may only be present in the subset that carries a significant fatty liver phenotype. Interestingly, many of our findings were reproduced in the "Taiwanese" mouse model where liver damage (by serum AST & ALT), low IGF-1, low serum iron, low albumin production was reported (413). Noteworthy, the "Taiwanese" mouse model did not show fatty acid accumulation in our study but had overlapping molecular changes in "fatty liver" genes with the *Smn*$^{2B/-}$ mice. Decreased levels of IGF1 have been found almost universally in pre-clinical studies (112, 310, 311, 413) and may very well explain features

of SMA mice, including their short stature. Nevertheless, IGF1 levels in a small cohort of SMA patients were not affected (288). Going forward, liver function in SMA will be a particularly important consideration in formulation of new therapeutics for SMA. Indeed, pro-drugs metabolized through the liver may not gain optimal levels while those cleared/processed by the liver might harbor more significant toxic potential.

The $Smn^{2B/-}$ mice as a model for NAFLD

NAFLD disease presents as a spectrum of severity that encompasses simple steatosis, steatohepatitis (also known as NASH) with or without fibrosis, cirrhosis and hepatocellular carcinoma (HCC) (304). Its pathogenesis is complex and involves multiple organ systems. It is currently hypothesized that "multiple hits" are required to develop NASH and more severe phenotypes (304). Multiple mouse models of NAFLD exist and, as in other diseases, they offer great insight into molecular signaling events. However, these models are invariably imperfect in modelling the true phenotype of patients with NAFLD (304, 437-439). In addition, many of them rely on a dietary component and necessitate a long time to develop the desired features. Indeed, these two variables can make the NAFLD models costly to use. The *$Smn^{2B/-}$* mice display many positive features of NALFD. They develop microvesicular steatohepatitis without fibrosis within two weeks of life, with increased serum markers of liver damage and hepatocyte cell death. They also display significant dyslipidemia, peripheral lipolysis, functional hepatic deficits, involvement of alternative oxidative pathway and ROS production. All these features have been observed in NAFLD (304). Nevertheless, the *$Smn^{2B/-}$* mouse as a model for NAFLD also has some drawbacks. They do not develop fibrosis, a component that is seen in NASH

patients (304). Furthermore, microvesicular steatosis is present in all of the mutant mice, whereas it is only present in a minority (10%) of NAFLD patients (440). *Smn*$^{2B/-}$ mice also lose weight, display low blood sugar, normal insulin, leptin and adiponectin levels. In contrast, most NAFLD patients have metabolic syndrome, which includes features of obesity, insulin resistance, hyperglycemia, hyperinsulinemia, low adiponectin and hyperleptinemia (304). Note that it is unclear whether the *Smn*$^{2B/-}$ mice develop insulin resistance as the proper studies have yet to be performed. SMA patients appear prone to insulin resistance (288). In comparison, some popular NAFLD models also show incongruent features. For example, the methionine and choline deficient diet model does not exhibit any of the metabolic features (304, 437, 438, 441). The ob/ob and db/db mice, which display altered leptin signaling, have metabolic features but no inflammation or fibrosis. A second hit, such as HFD or MCD, is needed to develop these features in the *db/db* mouse (442). The HFD diet appears to result in all features of the NAFLD spectrum, however, fibrosis is minimal and can take up to 36-50 weeks to develop (443). Although not perfect, the *Smn*$^{2B/-}$ mice could provide an efficient mouse model of NAFLD with a short turnaround time, which would speed up identification of molecular targets. In addition, it would allow a different outlook on molecular players and organ system involvement. Indeed, they could act as one of the few mouse models for pediatric NAFLD.

Can SMA be considered a multi-organ disorder: Translation to human patients?

Over the course of my training, there was an increased interest in extra-neuronal defects and a consequent emergence of many interesting findings in pre-clinical models (444-449)

(Figure 6.5). These features have extended far beyond the classical realm of SMA pathology that included the motor unit and now encompass defects in testes, GI tract, and immune system among others. Of note, our laboratory has been at the forefront in the identification of many of these disturbances in pre-clinical models (Figure 6.5, highlighted in red are contributions from the work presented in this thesis). In the mice, the accumulation of data is very convincing that SMA should in fact be considered multi-organ disorder. However, very few murine findings have been confirmed or even formally studied in SMA patients (Figure 6.6 - highlighted in red are contributions from the work presented in this thesis). Findings that have similarities from mouse to humans are checked (√) while those that were not found have an X. Normal bullet designed the lack of research to confirm the murine or human defect. Indeed, the translation of these defects is not overly obvious in the human population, which has tempered the excitement in studying extra-neuronal pathology in the context of SMA. For example, dyslipidemia and fatty liver only affect a small subset of the SMA population, attributed to the much greater heterogeneity of the genetic make-up in humans in comparison to laboratory mice. Mice also seem more susceptible to peripheral defects than human patients. This is better exemplified by the notion of heart defects being present mostly in severe SMA patients (114), while observed in many mouse models of SMA (120-123). This could also represent species differences to SMN depletion. Other issues that have stemmed from clinical findings in humans, such as GI tract and bone health, were easily translated to mice.

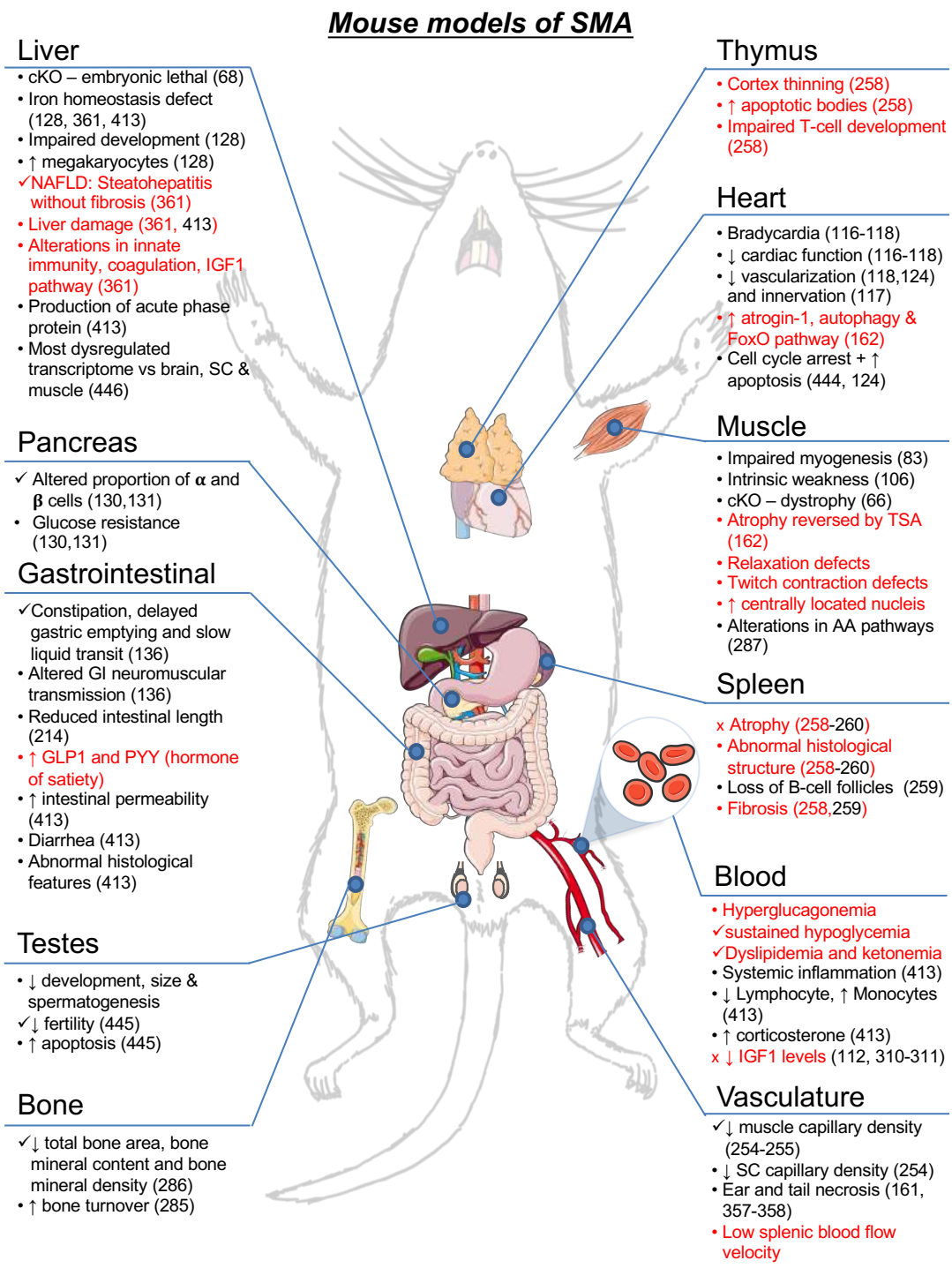

Figure 6.5 Contributions of non-neuronal organs in SMA pathology in mouse models of SMA. This schematic highlights the major findings to date of non-neuronal organs in

mouse models. This figure is by no means inclusive of all findings in the different systems but represent a good overview. Points in red highlight the findings from this thesis. √ designate similarities identified in human patients. X designated that this findings has not been reproduced in human patients. Abbreviations - ASD: atrial septal defect, VSD: ventricular septal defect, cKO: conditional knockout, GI: gastrointestinal, NAFLD: non-alcoholic fatty liver disease, SC: spinal cord, TSA: Trichostatin A, AA: amino acids. The schematic art pieces used in this figure were provided by Servier Medical art. Servier Medical Art by Servier is licensed under a Creative Commons Attribution 3.0 Unported License.

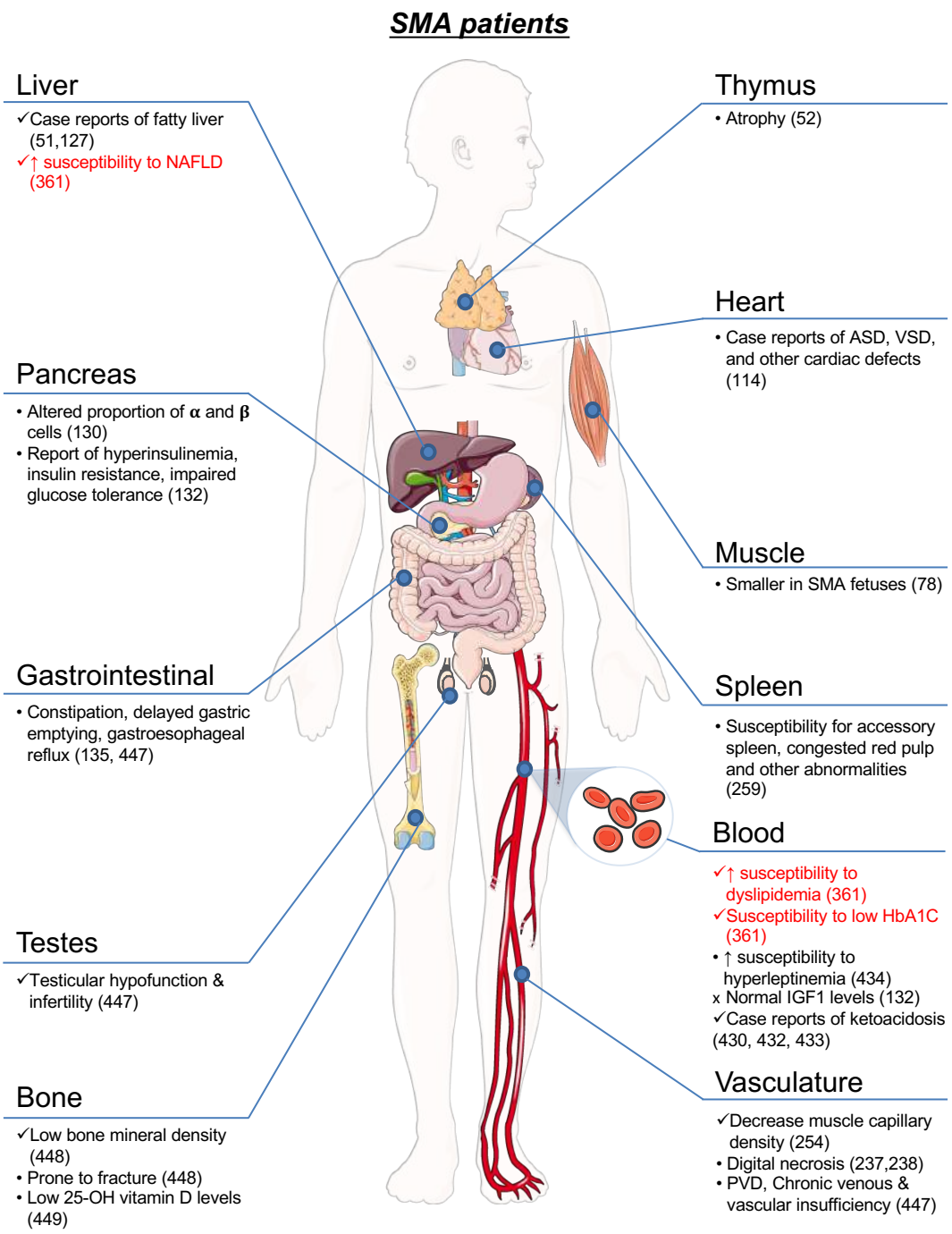

Figure 6.6 Contributions of non-neuronal organs in SMA pathology in SMA patients. This schematic highlights the major findings to date of non-neuronal organs in SMA patients. This figure is by no means inclusive of all findings in the different systems but

represent a good overview. Points in red highlight the findings from this thesis. √ designate similarities identified in mouse models of SMA. X designated that these findings has not been reproduced in human patients in comparison to mouse models of SMA. Abbreviations - ASD: atrial septal defect, VSD: ventricular septal defect, NAFLD: non-alcoholic fatty liver disease, PVD: Peripheral vascular disease . The schematic art pieces used in this figure were provided by Servier Medical art. Servier Medical Art by Servier is licensed under a Creative Commons Attribution 3.0 Unported License.

Understandably, human tissue acquisition is not trivial. Muscle biopsies were once used for the diagnosis of SMA but this has essentially vanished once genetic testing became available. Currently, access to SMA tissues relies on necropsies of SMA patients. In the current therapeutic era, SMA patients are likely to live a normal lifespan and, hopefully, without peripheral sequelae. On the contrary, if extra-neuronal organ involvement were to arise, fundamental pathogenesis in those tissues will be masked by the much necessary therapeutic course that will have improve their motor function, breathing and lifespan. As such, further studies aimed at confirming and identifying important extra-neuronal involvement seen in pre-clinical models of SMA will seemingly become logistically complex, if not unfeasible. Going forward, we shall remain vigilant of the symptomatology that treated SMA patients will present with and keeping in mind these pre-clinical extra-neuronal organ defects, whether they have been confirmed or not. This will allow prompt identification and optimal management. To avoid such situations from arising, focus should be put upon therapeutic strategies delivered systematically rather than intrathecally to prophylactically ensure the maximal benefits.

References

1 Lefebvre, S., Bürglen, L., Reboullet, S., Clermont, O., Burlet, P., Viollet, L., Benichou, B., Cruaud, C., Millasseau, P. and Zeviani, M. (1995) Identification and characterization of a spinal muscular atrophy-determining gene. *Cell*, **80**, 155-165.

2 Sugarman, E.A., Nagan, N., Zhu, H., Akmaev, V.R., Zhou, Z., Rohlfs, E.M., Flynn, K., Hendrickson, B.C., Scholl, T., Sirko-Osadsa, D.A. *et al.* (2012) Pan-ethnic carrier screening and prenatal diagnosis for spinal muscular atrophy: clinical laboratory analysis of >72,400 specimens. *Eur J Hum Genet*, **20**, 27-32.

3 Hendrickson, B.C., Donohoe, C., Akmaev, V.R., Sugarman, E.A., Labrousse, P., Boguslavskiy, L., Flynn, K., Rohlfs, E.M., Walker, A., Allitto, B. *et al.* (2009) Differences in SMN1 allele frequencies among ethnic groups within North America. *J Med Genet*, **46**, 641-644.

4 Oskoui, M., Darras, B. and De Vivo, D. (2017) Sumner, C.J., Paushkin, S. and Ko, C.P. (eds.), In *Spinal Muscular Atrophy: Disease Mechanisms and Therapy*. Elsevier, in press., pp. 3-19.

5 Rochette, C.F., Gilbert, N. and Simard, L.R. (2001) SMN gene duplication and the emergence of the SMN2 gene occurred in distinct hominids: SMN2 is unique to Homo sapiens. *Hum Genet*, **108**, 255-266.

6 Lorson, C.L., Hahnen, E., Androphy, E.J. and Wirth, B. (1999) A single nucleotide in the SMN gene regulates splicing and is responsible for spinal muscular atrophy. *Proceedings of the National Academy of Sciences of the United States of America*, **96**, 6307-6311.

7 Lorson, C.L., Strasswimmer, J., Yao, J.M., Baleja, J.D., Hahnen, E., Wirth, B., Le, T., Burghes, A.H. and Androphy, E.J. (1998) SMN oligomerization defect correlates with spinal muscular atrophy severity. *Nat Genet*, **19**, 63-66.

8 Schrank, B., Götz, R., Gunnersen, J.M., Ure, J.M., Toyka, K.V., Smith, A.G. and Sendtner, M. (1997) Inactivation of the survival motor neuron gene, a candidate gene for human spinal muscular atrophy, leads to massive cell death in early mouse embryos. *Proceedings of the National Academy of Sciences of the United States of America*, **94**, 9920-9925.

9 Feldkotter, M., Schwarzer, V., Wirth, R., Wienker, T.F. and Wirth, B. (2002) Quantitative analyses of SMN1 and SMN2 based on real-time lightCycler PCR: fast and highly reliable carrier testing and prediction of severity of spinal muscular atrophy. *Am J Hum Genet*, **70**, 358-368.

10 Wirth, B., Brichta, L., Schrank, B., Lochmuller, H., Blick, S., Baasner, A. and Heller, R. (2006) Mildly affected patients with spinal muscular atrophy are partially protected by an increased SMN2 copy number. *Hum Genet*, **119**, 422-428.

11 Oskoui, M., Levy, G., Garland, C.J., Gray, J.M., O'Hagen, J., Vivo, D.D.C. and Kaufmann, P. (2007) The changing natural history of spinal muscular atrophy type 1. *Neurology*, **69**, 1931-1936.

12 So, B.R., Zhang, Z. and Dreyfuss, G. (2016) Sumner, C.J., Paushkin, S. and Ko, C.P. (eds.), In *Spinal Muscular Atrophy: Disease Mechanisms and Therapy*. Elsevier, in press., pp. 99-111.

13 Burlet, P., Huber, C., Bertrandy, S., Ludosky, M.A., Zwaenepoel, I., Clermont, O., Roume, J., Delezoide, A.L., Cartaud, J., Munnich, A. *et al.* (1998) The distribution of SMN protein complex in human fetal tissues and its alteration in spinal muscular atrophy. *Human molecular genetics*, **7**, 1927-1933.

14 La Bella, V., Cisterni, C., Salaün, D. and Pettmann, B. (1998) Survival motor neuron (SMN) protein in rat is expressed as different molecular forms and is developmentally regulated. *The European journal of neuroscience*, **10**, 2913-2923.

15 Liu, Q., Fischer, U., Wang, F. and Dreyfuss, G. (1997) The spinal muscular atrophy disease gene product, SMN, and its associated protein SIP1 are in a complex with spliceosomal snRNP proteins. *Cell*, **90**, 1013-1021.

16 Hebert, M.D., Szymczyk, P.W., Shpargel, K.B. and Matera, A.G. (2001) Coilin forms the bridge between Cajal bodies and SMN, the spinal muscular atrophy protein. *Genes Dev*, **15**, 2720-2729.

17 Pellizzoni, L., Kataoka, N., Charroux, B. and Dreyfuss, G. (1998) A novel function for SMN, the spinal muscular atrophy disease gene product, in pre-mRNA splicing. *Cell*, **95**, 615-624.

18 Lotti, F., Imlach, W.L., Saieva, L., Beck, E.S., Hao le, T., Li, D.K., Jiao, W., Mentis, G.Z., Beattie, C.E., McCabe, B.D. *et al.* (2012) An SMN-dependent U12 splicing event essential for motor circuit function. *Cell*, **151**, 440-454.

19 Zhang, Z., Lotti, F., Dittmar, K., Younis, I., Wan, L., Kasim, M. and Dreyfuss, G. (2008) SMN deficiency causes tissue-specific perturbations in the repertoire of snRNAs and widespread defects in splicing. *Cell*, **133**, 585-600.

20 Monani, U.R. (2005) Spinal muscular atrophy: a deficiency in a ubiquitous protein; a motor neuron-specific disease. *Neuron*, **48**, 885-896.

21 Baumer, D., Lee, S., Nicholson, G., Davies, J.L., Parkinson, N.J., Murray, L.M., Gillingwater, T.H., Ansorge, O., Davies, K.E. and Talbot, K. (2009) Alternative splicing events are a late feature of pathology in a mouse model of spinal muscular atrophy. *PLoS Genet*, **5**, e1000773.

22 Tisdale, S. and Pellizzoni, L. (2016) Sumner, C.J., Paushkin, S. and Ko, C.P. (eds.), In *Spinal Muscular Atrophy: Disease Mechanisms and Therapy*. Elsevier, in press., pp. 75-97.

23 Pagliardini, S., Giavazzi, A., Setola, V., Lizier, C., Di Luca, M., DeBiasi, S. and Battaglia, G. (2000) Subcellular localization and axonal transport of the survival motor neuron (SMN) protein in the developing rat spinal cord. *Human molecular genetics*, **9**, 47-56.

24 Fan, L. and Simard, L.R. (2002) Survival motor neuron (SMN) protein: role in neurite outgrowth and neuromuscular maturation during neuronal differentiation and development. *Human molecular genetics*, **11**, 1605-1614.

25 Zhang, H., Xing, L., Rossoll, W., Wichterle, H., Singer, R.H. and Bassell, G.J. (2006) Multiprotein complexes of the survival of motor neuron protein SMN with Gemins traffic to neuronal processes and growth cones of motor neurons. *J Neurosci*, **26**, 8622-8632.

26 Rossoll, W., Kroning, A.K., Ohndorf, U.M., Steegborn, C., Jablonka, S. and Sendtner, M. (2002) Specific interaction of Smn, the spinal muscular atrophy determining gene product, with hnRNP-R and gry-rbp/hnRNP-Q: a role for Smn in RNA processing in motor axons? *Hum Mol Genet*, **11**, 93-105.

27 Fallini, C., Zhang, H., Su, Y., Silani, V., Singer, R.H., Rossoll, W. and Bassell, G.J. (2011) The survival of motor neuron (SMN) protein interacts with the mRNA-binding protein HuD and regulates localization of poly(A) mRNA in primary motor neuron axons. *The Journal of neuroscience : the official journal of the Society for Neuroscience*, **31**, 3914-3925.

28 Tadesse, H., Deschenes-Furry, J., Boisvenue, S. and Cote, J. (2008) KH-type splicing regulatory protein interacts with survival motor neuron protein and is misregulated in spinal muscular atrophy. *Hum Mol Genet*, **17**, 506-524.

29 Piazzon, N., Rage, F., Schlotter, F., Moine, H., Branlant, C. and Massenet, S. (2008) In vitro and in cellulo evidences for association of the survival of motor neuron complex with the fragile X mental retardation protein. *J Biol Chem*, **283**, 5598-5610.

30 Fallini, C., Rouanet, J.P., Donlin-Asp, P.G., Guo, P., Zhang, H., Singer, R.H., Rossoll, W. and Bassell, G.J. (2014) Dynamics of survival of motor neuron (SMN) protein interaction with the mRNA-binding protein IMP1 facilitates its trafficking into motor neuron axons. *Dev Neurobiol*, **74**, 319-332.

31 Rossoll, W., Jablonka, S., Andreassi, C., Kroning, A.K., Karle, K., Monani, U.R. and Sendtner, M. (2003) Smn, the spinal muscular atrophy-determining gene product, modulates axon growth and localization of beta-actin mRNA in growth cones of motoneurons. *J Cell Biol*, **163**, 801-812.

32 Akten, B., Kye, M.J., Hao le, T., Wertz, M.H., Singh, S., Nie, D., Huang, J., Merianda, T.T., Twiss, J.L., Beattie, C.E. *et al.* (2011) Interaction of survival of motor neuron (SMN)

and HuD proteins with mRNA cpg15 rescues motor neuron axonal deficits. *Proc Natl Acad Sci U S A*, **108**, 10337-10342.

33 Rage, F., Boulisfane, N., Rihan, K., Neel, H., Gostan, T., Bertrand, E., Bordonne, R. and Soret, J. (2013) Genome-wide identification of mRNAs associated with the protein SMN whose depletion decreases their axonal localization. *RNA*, **19**, 1755-1766.

34 Cheever, T.R., Olson, E.A. and Ervasti, J.M. (2011) Axonal regeneration and neuronal function are preserved in motor neurons lacking ss-actin in vivo. *PLoS One*, **6**, e17768.

35 Consortium, T.D.-B.F.X. (1994) Fmr1 knockout mice: a model to study fragile X mental retardation. The Dutch-Belgian Fragile X Consortium. *Cell*, **78**, 23-33.

36 Lin, W.J., Zheng, X., Lin, C.C., Tsao, J., Zhu, X., Cody, J.J., Coleman, J.M., Gherzi, R., Luo, M., Townes, T.M. *et al.* (2011) Posttranscriptional control of type I interferon genes by KSRP in the innate immune response against viral infection. *Mol Cell Biol*, **31**, 3196-3207.

37 Hansen, T.V., Hammer, N.A., Nielsen, J., Madsen, M., Dalbaeck, C., Wewer, U.M., Christiansen, J. and Nielsen, F.C. (2004) Dwarfism and impaired gut development in insulin-like growth factor II mRNA-binding protein 1-deficient mice. *Mol Cell Biol*, **24**, 4448-4464.

38 DeBoer, E.M., Azevedo, R., Vega, T.A., Brodkin, J., Akamatsu, W., Okano, H., Wagner, G.C. and Rasin, M.R. (2014) Prenatal deletion of the RNA-binding protein HuD disrupts postnatal cortical circuit maturation and behavior. *J Neurosci*, **34**, 3674-3686.

39 Akamatsu, W., Fujihara, H., Mitsuhashi, T., Yano, M., Shibata, S., Hayakawa, Y., Okano, H.J., Sakakibara, S., Takano, H., Takano, T. *et al.* (2005) The RNA-binding protein HuD regulates neuronal cell identity and maturation. *Proc Natl Acad Sci U S A*, **102**, 4625-4630.

40 Tisdale, S., Lotti, F., Saieva, L., Van Meerbeke, J.P., Crawford, T.O., Sumner, C.J., Mentis, G.Z. and Pellizzoni, L. (2013) SMN is essential for the biogenesis of U7 small nuclear ribonucleoprotein and 3'-end formation of histone mRNAs. *Cell Rep*, **5**, 1187-1195.

41 Marzluff, W.F., Wagner, E.J. and Duronio, R.J. (2008) Metabolism and regulation of canonical histone mRNAs: life without a poly(A) tail. *Nat Rev Genet*, **9**, 843-854.

42 Pillai, R.S., Grimmler, M., Meister, G., Will, C.L., Luhrmann, R., Fischer, U. and Schumperli, D. (2003) Unique Sm core structure of U7 snRNPs: assembly by a specialized SMN complex and the role of a new component, Lsm11, in histone RNA processing. *Genes Dev*, **17**, 2321-2333.

43 Pillai, R.S., Will, C.L., Luhrmann, R., Schumperli, D. and Muller, B. (2001) Purified U7 snRNPs lack the Sm proteins D1 and D2 but contain Lsm10, a new 14 kDa Sm D1-like protein. *EMBO J*, **20**, 5470-5479.

44 Weber, C.M. and Henikoff, S. (2014) Histone variants: dynamic punctuation in transcription. *Genes Dev*, **28**, 672-682.

45 Wagner, E.J. and Marzluff, W.F. (2006) ZFP100, a component of the active U7 snRNP limiting for histone pre-mRNA processing, is required for entry into S phase. *Mol Cell Biol*, **26**, 6702-6712.

46 Ideue, T., Hino, K., Kitao, S., Yokoi, T. and Hirose, T. (2009) Efficient oligonucleotide-mediated degradation of nuclear noncoding RNAs in mammalian cultured cells. *RNA*, **15**, 1578-1587.

47 Grice, S.J. and Liu, J.L. (2011) Survival motor neuron protein regulates stem cell division, proliferation, and differentiation in Drosophila. *PLoS Genet*, **7**, e1002030.

48 Martínez-Hernández, R., Soler-Botija, C., Also, E., Alias, L., Caselles, L., Gich, I., Bernal, S. and Tizzano, E.F. (2009) The developmental pattern of myotubes in spinal muscular atrophy indicates prenatal delay of muscle maturation. *Journal of neuropathology and experimental neurology*, **68**, 474-481.

49 Tein, I., Sloane, A.E., Donner, E.J., Lehotay, D.C., Millington, D.S. and Kelley, R.I. (1995) Fatty acid oxidation abnormalities in childhood-onset spinal muscular atrophy: primary or secondary defect(s)? *Pediatr Neurol*, **12**, 21-30.

50 Crawford, T.O., Sladky, J.T. and Hurko, O. (1999) Abnormal fatty acid metabolism in childhood spinal muscular atrophy. *Abnormal fatty acid metabolism in childhood spinal muscular atrophy*, in press.

51 Kelley, R.I. and Sladky, J.T. (1986) Dicarboxylic aciduria in an infant with spinal muscular atrophy. *Ann Neurol*, **20**, 734-736.

52 Ryniewicz, B. and Pawinska, M. (1978) Preliminary immunological studies in spinal muscular atrophy. *Eur J Pediatr*, **128**, 57-60.

53 Migaj, M., Janowicz, W., Krajewska, G., Bernatowska, E. and Madalinski, K. (1986) Evaluation of cell-mediated and humoral immunity in children suffering from spinal muscular atrophy. *Arch Immunol Ther Exp (Warsz)*, **34**, 561-567.

54 Henderson, C.E., Hauser, S.L., Huchet, M., Dessi, F., Hentati, F., Taguchi, T., Changeux, J.P. and Fardeau, M. (1987) Extracts of muscle biopsies from patients with spinal muscular atrophies inhibit neurite outgrowth from spinal neurons. *Neurology*, **37**, 1361-1364.

55 Braun, S., Croizat, B., Lagrange, M.C., Warter, J.M. and Poindron, P. (1995) Constitutive muscular abnormalities in culture in spinal muscular atrophy. *Lancet*, **345**, 694-695.

56 Guettier-Sigrist, S., Coupin, G., Braun, S., Warter, J.M. and Poindron, P. (1998) Muscle could be the therapeutic target in SMA treatment. *Journal of neuroscience research*, **53**, 663-669.

57 Kariya, S., Park, G.H., Maeno-Hikichi, Y., Leykekhman, O., Lutz, C., Arkovitz, M.S., Landmesser, L.T. and Monani, U.R. (2008) Reduced SMN protein impairs maturation of the neuromuscular junctions in mouse models of spinal muscular atrophy. *Human molecular genetics*, **17**, 2552-2569.

58 Murray, L.M., Comley, L.H., Thomson, D., Parkinson, N., Talbot, K. and Gillingwater, T.H. (2008) Selective vulnerability of motor neurons and dissociation of pre- and post-synaptic pathology at the neuromuscular junction in mouse models of spinal muscular atrophy. *Human molecular genetics*, **17**, 949-962.

59 Kong, L., Wang, X., Choe, D.W., Polley, M., Burnett, B.G., Bosch-Marce, M., Griffin, J.W., Rich, M.M. and Sumner, C.J. (2009) Impaired synaptic vesicle release and immaturity of neuromuscular junctions in spinal muscular atrophy mice. *J Neurosci*, **29**, 842-851.

60 Singhal, N. and Martin, P.T. (2011) Role of extracellular matrix proteins and their receptors in the development of the vertebrate neuromuscular junction. *Dev Neurobiol*, **71**, 982-1005.

61 Arnold, A.S., Gueye, M., Guettier-Sigrist, S., Courdier-Fruh, I., Coupin, G., Poindron, P. and Gies, J.P. (2004) Reduced expression of nicotinic AChRs in myotubes from spinal muscular atrophy I patients. *Laboratory investigation; a journal of technical methods and pathology*, **84**, 1271-1278.

62 Martinez, T.L., Kong, L., Wang, X., Osborne, M.A., Crowder, M.E., Van Meerbeke, J.P., Xu, X., Davis, C., Wooley, J., Goldhamer, D.J. *et al.* (2012) Survival motor neuron protein in motor neurons determines synaptic integrity in spinal muscular atrophy. *The Journal of neuroscience : the official journal of the Society for Neuroscience*, **32**, 8703-8715.

63 Shafey, D., Boyer, J.G., Bhanot, K. and Kothary, R. (2010) Identification of novel interacting protein partners of SMN using tandem affinity purification. *Journal of proteome research*, **9**, 1659-1669.

64 Rajendra, T.K., Gonsalvez, G.B., Walker, M.P., Shpargel, K.B., Salz, H.K. and Matera, A.G. (2007) A Drosophila melanogaster model of spinal muscular atrophy reveals a function for SMN in striated muscle. *The Journal of cell biology*, **176**, 831-841.

65 Walker, M.P., Rajendra, T.K., Saieva, L., Fuentes, J.L., Pellizzoni, L. and Matera, A.G. (2008) SMN complex localizes to the sarcomeric Z-disc and is a proteolytic target of calpain. *Human molecular genetics*, **17**, 3399-3410.

66 Cifuentes-Diaz, C., Frugier, T., Tiziano, F.D., Lacene, E., Roblot, N., Joshi, V., Moreau, M.H. and Melki, J. (2001) Deletion of murine SMN exon 7 directed to skeletal muscle leads to severe muscular dystrophy. *The Journal of cell biology*, **152**, 1107-1114.

67 Le, T.T., Pham, L.T., Butchbach, M.E., Zhang, H.L., Monani, U.R., Coovert, D.D., Gavrilina, T.O., Xing, L., Bassell, G.J. and Burghes, A.H. (2005) SMNDelta7, the major product of the centromeric survival motor neuron (SMN2) gene, extends survival in mice with spinal muscular atrophy and associates with full-length SMN. *Human molecular genetics*, **14**, 845-857.

68 Vitte, J.M., Davoult, B., Roblot, N., Mayer, M., Joshi, V., Courageot, S., Tronche, F., Vadrot, J., Moreau, M.H., Kemeny, F. *et al.* (2004) Deletion of murine Smn exon 7 directed to liver leads to severe defect of liver development associated with iron overload. *The American journal of pathology*, **165**, 1731-1741.

69 Gavrilina, T.O., McGovern, V.L., Workman, E., Crawford, T.O., Gogliotti, R.G., DiDonato, C.J., Monani, U.R., Morris, G.E. and Burghes, A.H. (2008) Neuronal SMN expression corrects spinal muscular atrophy in severe SMA mice while muscle-specific SMN expression has no phenotypic effect. *Human molecular genetics*, **17**, 1063-1075.

70 Nicole, S., Desforges, B., Millet, G., Lesbordes, J., Cifuentes-Diaz, C., Vertes, D., Cao, M.L., De Backer, F., Languille, L., Roblot, N. *et al.* (2003) Intact satellite cells lead to remarkable protection against Smn gene defect in differentiated skeletal muscle. *The Journal of cell biology*, **161**, 571-582.

71 Martinez, T.L., Kong, L., Wang, X., Osborne, M.A., Crowder, M.E., Van Meerbeke, J.P., Xu, X., Davis, C., Wooley, J., Goldhamer, D.J. *et al.* (2012) Survival motor neuron

protein in motor neurons determines synaptic integrity in spinal muscular atrophy. *The Journal of neuroscience : the official journal of the Society for Neuroscience*, **32**, 8703-8715.

72 Iyer, C.C., McGovern, V.L., Murray, J.D., Gombash, S.E., Zaworski, P.G., Foust, K.D., Janssen, P.M. and Burghes, A.H. (2015) Low levels of Survival Motor Neuron protein are sufficient for normal muscle function in the SMNDelta7 mouse model of SMA. *Human molecular genetics*, **24**, 6160-6173.

73 Hua, Y., Sahashi, K., Rigo, F., Hung, G., Horev, G., Bennett, C.F. and Krainer, A.R. (2011) Peripheral SMN restoration is essential for long-term rescue of a severe spinal muscular atrophy mouse model. *Nature*, **478**, 123-126.

74 Battaglia, G., Princivalle, A., Forti, F., Lizier, C. and Zeviani, M. (1997) Expression of the SMN gene, the spinal muscular atrophy determining gene, in the mammalian central nervous system. *Human molecular genetics*, **6**, 1961-1971.

75 Burlet, P., Huber, C., Bertrandy, S., Ludosky, M.A., Zwaenepoel, I., Clermont, O., Roume, J., Delezoide, A.L., Cartaud, J., Munnich, A. *et al.* (1998) The distribution of SMN protein complex in human fetal tissues and its alteration in spinal muscular atrophy. *Human molecular genetics*, **7**, 1927-1933.

76 La Bella, V., Cisterni, C., Salaun, D. and Pettmann, B. (1998) Survival motor neuron (SMN) protein in rat is expressed as different molecular forms and is developmentally regulated. *The European journal of neuroscience*, **10**, 2913-2923.

77 Gabanella, F., Carissimi, C., Usiello, A. and Pellizzoni, L. (2005) The activity of the spinal muscular atrophy protein is regulated during development and cellular differentiation. *Human molecular genetics*, **14**, 3629-3642.

78 Martinez-Hernandez, R., Bernal, S., Also-Rallo, E., Alias, L., Barcelo, M.J., Hereu, M., Esquerda, J.E. and Tizzano, E.F. (2013) Synaptic defects in type I spinal muscular atrophy in human development. *The Journal of pathology*, **229**, 49-61.

79 Hosoyama, T., McGivern, J.V., Van Dyke, J.M., Ebert, A.D. and Suzuki, M. (2014) Derivation of myogenic progenitors directly from human pluripotent stem cells using a sphere-based culture. *Stem cells translational medicine*, **3**, 564-574.

80 Lee, Y.I., Mikesh, M., Smith, I., Rimer, M. and Thompson, W. (2011) Muscles in a mouse model of spinal muscular atrophy show profound defects in neuromuscular development even in the absence of failure in neuromuscular transmission or loss of motor neurons. *Developmental biology*, **356**, 432-444.

81 Dachs, E., Hereu, M., Piedrafita, L., Casanovas, A., Caldero, J. and Esquerda, J.E. (2011) Defective neuromuscular junction organization and postnatal myogenesis in mice with severe spinal muscular atrophy. *Journal of neuropathology and experimental neurology*, **70**, 444-461.

82 Hayhurst, M., Wagner, A.K., Cerletti, M., Wagers, A.J. and Rubin, L.L. (2012) A cell-autonomous defect in skeletal muscle satellite cells expressing low levels of survival of motor neuron protein. *Developmental biology*, **368**, 323-334.

83 Boyer, J.G., Deguise, M.O., Murray, L.M., Yazdani, A., De Repentigny, Y., Boudreau-Lariviere, C. and Kothary, R. (2014) Myogenic program dysregulation is contributory to disease pathogenesis in spinal muscular atrophy. *Hum Mol Genet*, **23**, 4249-4259.

84 Bricceno, K.V., Martinez, T., Leikina, E., Duguez, S., Partridge, T.A., Chernomordik, L.V., Fischbeck, K.H., Sumner, C.J. and Burnett, B.G. (2014) Survival motor neuron protein deficiency impairs myotube formation by altering myogenic gene expression and focal adhesion dynamics. *Human molecular genetics*, **23**, 4745-4757.

85 Bentzinger, C.F., Wang, Y.X. and Rudnicki, M.A. (2012) Building muscle: molecular regulation of myogenesis. *Cold Spring Harbor perspectives in biology*, **4**.

86 Frontera, W.R. and Ochala, J. (2015) Skeletal muscle: a brief review of structure and function. *Calcified tissue international*, **96**, 183-195.

87 Guettier-Sigrist, S., Coupin, G., Braun, S., Rogovitz, D., Courdier, I., Warter, J.M. and Poindron, P. (2001) On the possible role of muscle in the pathogenesis of spinal muscular atrophy. *Fundamental & clinical pharmacology*, **15**, 31-40.

88 Shafey, D., Cote, P.D. and Kothary, R. (2005) Hypomorphic Smn knockdown C2C12 myoblasts reveal intrinsic defects in myoblast fusion and myotube morphology. *Experimental cell research*, **311**, 49-61.

89 Cifuentes-Diaz, C., Frugier, T. and Melki, J. (2002) Spinal muscular atrophy. *Seminars in pediatric neurology*, **9**, 145-150.

90 Schiaffino, S. and Mammucari, C. (2011) Regulation of skeletal muscle growth by the IGF1-Akt/PKB pathway: insights from genetic models. *Skeletal muscle*, **1**, 4.

91 Bricceno, K.V., Sampognaro, P.J., Van Meerbeke, J.P., Sumner, C.J., Fischbeck, K.H. and Burnett, B.G. (2012) Histone deacetylase inhibition suppresses myogenin-dependent atrogene activation in spinal muscular atrophy mice. *Human molecular genetics*, **21**, 4448-4459.

92 Iyer, C.C., McGovern, V.L., Wise, D.O., Glass, D.J. and Burghes, A.H. (2014) Deletion of atrophy enhancing genes fails to ameliorate the phenotype in a mouse model of spinal muscular atrophy. *Neuromuscular disorders : NMD*, **24**, 436-444.

93 Coleman, M.E., DeMayo, F., Yin, K.C., Lee, H.M., Geske, R., Montgomery, C. and Schwartz, R.J. (1995) Myogenic vector expression of insulin-like growth factor I stimulates muscle cell differentiation and myofiber hypertrophy in transgenic mice. *The Journal of biological chemistry*, **270**, 12109-12116.

94 Lee, S.J. and McPherron, A.C. (2001) Regulation of myostatin activity and muscle growth. *Proceedings of the National Academy of Sciences of the United States of America*, **98**, 9306-9311.

95 Musaro, A., McCullagh, K., Paul, A., Houghton, L., Dobrowolny, G., Molinaro, M., Barton, E.R., Sweeney, H.L. and Rosenthal, N. (2001) Localized Igf-1 transgene expression sustains hypertrophy and regeneration in senescent skeletal muscle. *Nature genetics*, **27**, 195-200.

96 Grobet, L., Pirottin, D., Farnir, F., Poncelet, D., Royo, L.J., Brouwers, B., Christians, E., Desmecht, D., Coignoul, F., Kahn, R. *et al.* (2003) Modulating skeletal muscle mass by postnatal, muscle-specific inactivation of the myostatin gene. *Genesis*, **35**, 227-238.

97 Barton, E.R., Morris, L., Musaro, A., Rosenthal, N. and Sweeney, H.L. (2002) Muscle-specific expression of insulin-like growth factor I counters muscle decline in mdx mice. *The Journal of cell biology*, **157**, 137-148.

98 Dobrowolny, G., Giacinti, C., Pelosi, L., Nicoletti, C., Winn, N., Barberi, L., Molinaro, M., Rosenthal, N. and Musaro, A. (2005) Muscle expression of a local Igf-1 isoform protects motor neurons in an ALS mouse model. *The Journal of cell biology*, **168**, 193-199.

99 Guiraud, S., Aartsma-Rus, A., Vieira, N.M., Davies, K.E., van Ommen, G.J. and Kunkel, L.M. (2015) The Pathogenesis and Therapy of Muscular Dystrophies. *Annual review of genomics and human genetics*, in press.

100 Rose, F.F., Jr., Mattis, V.B., Rindt, H. and Lorson, C.L. (2009) Delivery of recombinant follistatin lessens disease severity in a mouse model of spinal muscular atrophy. *Human molecular genetics*, **18**, 997-1005.

101 Rindt, H., Buckley, D.M., Vale, S.M., Krogman, M., Rose, F.F., Jr., Garcia, M.L. and Lorson, C.L. (2012) Transgenic inactivation of murine myostatin does not decrease the severity of disease in a model of Spinal Muscular Atrophy. *Neuromuscular disorders : NMD*, **22**, 277-285.

102 Sumner, C.J., Wee, C.D., Warsing, L.C., Choe, D.W., Ng, A.S., Lutz, C. and Wagner, K.R. (2009) Inhibition of myostatin does not ameliorate disease features of severe spinal muscular atrophy mice. *Human molecular genetics*, **18**, 3145-3152.

103 Rindt, H., Buckley, D.M., Vale, S.M., Krogman, M., Rose, F.F., Jr., Garcia, M.L. and Lorson, C.L. (2011) Transgenic inactivation of murine myostatin does not decrease the

severity of disease in a model of Spinal Muscular Atrophy. *Neuromuscular disorders : NMD*, in press.

104 Mariot, V., Joubert, R., Hourde, C., Feasson, L., Hanna, M., Muntoni, F., Maisonobe, T., Servais, L., Bogni, C., Le Panse, R. *et al.* (2017) Downregulation of myostatin pathway in neuromuscular diseases may explain challenges of anti-myostatin therapeutic approaches. *Nat Commun*, **8**, 1859.

105 Bosch-Marce, M., Wee, C.D., Martinez, T.L., Lipkes, C.E., Choe, D.W., Kong, L., Van Meerbeke, J.P., Musaro, A. and Sumner, C.J. (2011) Increased IGF-1 in muscle modulates the phenotype of severe SMA mice. *Hum Mol Genet*, **20**, 1844-1853.

106 Boyer, J.G., Murray, L.M., Scott, K., De Repentigny, Y., Renaud, J.M. and Kothary, R. (2013) Early onset muscle weakness and disruption of muscle proteins in mouse models of spinal muscular atrophy. *Skeletal muscle*, **3**, 24.

107 Ling, K.K., Lin, M.Y., Zingg, B., Feng, Z. and Ko, C.P. (2010) Synaptic defects in the spinal and neuromuscular circuitry in a mouse model of spinal muscular atrophy. *PLoS One*, **5**, e15457.

108 Boyer, J.G., Murray, L.M., Scott, K., De Repentigny, Y., Renaud, J.-M.M. and Kothary, R. (2013) Early onset muscle weakness and disruption of muscle proteins in mouse models of spinal muscular atrophy. *Skeletal muscle*, **3**, 24.

109 Shababi, M., Lorson, C.L. and Rudnik-Schöneborn, S.S. (2014) Spinal muscular atrophy: a motor neuron disorder or a multi-organ disease? *Journal of anatomy*, **224**, 15-28.

110 Deguise, M.O., Patitucci, T.N., Ebert, A.D., Lorson, C. and Kothary, R. (2017) Sumner, C.J., Paushkin, S. and Ko, C.P. (eds.), In *Spinal Muscular Atrophy: Disease Mechanisms and Therapy*. Academic Press, London, in press., pp. 167-190.

111 Hua, Y., Liu, Y.H., Sahashi, K. and Rigo, F. (2015) Motor neuron cell-nonautonomous rescue of spinal muscular atrophy phenotypes in mild and severe transgenic mouse models. *Genes & …*, in press.

112 Hua, Y., Sahashi, K., Rigo, F., Hung, G., Horev, G., Bennett, C.F. and Krainer, A.R. (2011) Peripheral SMN restoration is essential for long-term rescue of a severe spinal muscular atrophy mouse model. *Nature*, **478**, 123-126.

113 Finkel, R.S., Chiriboga, C.A., Vajsar, J., Day, J.W., Montes, J., De Vivo, D.C., Yamashita, M., Rigo, F., Hung, G., Schneider, E. *et al.* (2016) Treatment of infantile-onset spinal muscular atrophy with nusinersen: a phase 2, open-label, dose-escalation study. *Lancet*, **388**, 3017-3026.

114 Rudnik-Schöneborn, S., Heller, R., Berg, C., Betzler, C., Grimm, T., Eggermann, T., Eggermann, K., Wirth, R., Wirth, B. and Zerres, K. (2008) Congenital heart disease is a feature of severe infantile spinal muscular atrophy. *Congenital heart disease is a feature of severe infantile spinal muscular atrophy.*, **45**.

115 Menke, L.A., Poll-The, B.T. and Clur, S.A. (2008) Congenital heart defects in spinal muscular atrophy type I: a clinical report of two siblings and a review of the literature. *Congenital heart defects in spinal muscular atrophy type I: a clinical report of two siblings and a review of the literature*, in press.

116 Bevan, A.K., Hutchinson, K.R., Foust, K.D., Braun, L., McGovern, V.L., Schmelzer, L., Ward, J.G., Petruska, J.C., Lucchesi, P.A., Burghes, A.H. *et al.* (2010) Early heart failure in the SMNDelta7 model of spinal muscular atrophy and correction by postnatal scAAV9-SMN delivery. *Human molecular genetics*, **19**, 3895-3905.

117 Heier, C.R., Satta, R., Lutz, C. and DiDonato, C.J. (2010) Arrhythmia and cardiac defects are a feature of spinal muscular atrophy model mice. *Human molecular genetics*, **19**, 3906-3918.

118 Shababi, M., Habibi, J., Ma, L., Glascock, J.J., Sowers, J.R. and Lorson, C.L. (2012) Partial restoration of cardio-vascular defects in a rescued severe model of spinal muscular atrophy. *Journal of molecular and cellular cardiology*, **52**, 1074-1082.

119 Shababi, M., Habibi, J., Yang, H.T., Vale, S.M., Sewell, W.A. and Lorson, C.L. (2010) Cardiac defects contribute to the pathology of spinal muscular atrophy models. *Human molecular genetics*, **19**, 4059-4071.

120 Bevan, A.K., Hutchinson, K.R., Foust, K.D., Braun, L., McGovern, V.L., Schmelzer, L., Ward, J.G., Petruska, J.C., Lucchesi, P.A., Burghes, A.H. *et al.* (2010) Early heart failure in the SMNDelta7 model of spinal muscular atrophy and correction by postnatal scAAV9-SMN delivery. *Human molecular genetics*, **19**, 3895-3905.

121 Heier, C.R., Satta, R., Lutz, C. and DiDonato, C.J. (2010) Arrhythmia and cardiac defects are a feature of spinal muscular atrophy model mice. *Human molecular genetics*, **19**, 3906-3918.

122 Shababi, M., Habibi, J., Ma, L., Glascock, J.J., Sowers, J.R. and Lorson, C.L. (2012) Partial restoration of cardio-vascular defects in a rescued severe model of spinal muscular atrophy. *Journal of molecular and cellular cardiology*, **52**, 1074-1082.

123 Shababi, M., Habibi, J., Yang, H.T., Vale, S.M., Sewell, W.A. and Lorson, C.L. (2010) Cardiac defects contribute to the pathology of spinal muscular atrophy models. *Human molecular genetics*, **19**, 4059-4071.

124 Maxwell, G.K., Szunyogova, E., Shorrock, H.K., Gillingwater, T.H. and Parson, S.H. (2018) Developmental and degenerative cardiac defects in the Taiwanese mouse model of severe spinal muscular atrophy. *J Anat*, **232**, 965-978.

125 Shababi, M., Lorson, C.L. and Rudnik-Schoneborn, S.S. (2014) Spinal muscular atrophy: a motor neuron disorder or a multi-organ disease? *Journal of anatomy*, **224**, 15-28.

126 Crawford, T.O., Sladky, J.T., Hurko, O., Besner-Johnston, A. and Kelley, R.I. (1999) Abnormal fatty acid metabolism in childhood spinal muscular atrophy. *Annals of neurology*, **45**, 337-343.

127 Zolkipli, Z., Sherlock, M., Biggar, W.D., Taylor, G., Hutchison, J.S., Peliowski, A., Alman, B.A., Ling, S.C. and Tein, I. (2012) Abnormal fatty acid metabolism in spinal muscular atrophy may predispose to perioperative risks. *Eur J Paediatr Neurol*, **16**, 549-553.

128 Szunyogova, E., Zhou, H., Maxwell, G.K., Powis, R.A., Francesco, M., Gillingwater, T.H. and Parson, S.H. (2016) Survival Motor Neuron (SMN) protein is required for normal mouse liver development. *Sci Rep*, **6**, 34635.

129 Sahashi, K., Ling, K.K., Hua, Y., Wilkinson, J.E., Nomakuchi, T., Rigo, F., Hung, G., Xu, D., Jiang, Y.P., Lin, R.Z. *et al.* (2013) Pathological impact of SMN2 mis-splicing in adult SMA mice. *EMBO molecular medicine*, **5**, 1586-1601.

130 Bowerman, M., Swoboda, K.J., Michalski, J.P., Wang, G.S., Reeks, C., Beauvais, A., Murphy, K., Woulfe, J., Screaton, R.A., Scott, F.W. *et al.* (2012) Glucose metabolism and pancreatic defects in spinal muscular atrophy. *Annals of neurology*, **72**, 256-268.

131 Bowerman, M., Michalski, J.P., Beauvais, A., Murray, L.M., DeRepentigny, Y. and Kothary, R. (2014) Defects in pancreatic development and glucose metabolism in SMN-depleted mice independent of canonical spinal muscular atrophy neuromuscular pathology. *Human molecular genetics*, **23**, 3432-3444.

132 Davis, R.H., Miller, E.A., Zhang, R.Z. and Swoboda, K.J. (2015) Responses to Fasting and Glucose Loading in a Cohort of Well Children with Spinal Muscular Atrophy Type II. *The Journal of pediatrics*, in press.

133 Butchbach, M.E., Rose, F.F., Jr., Rhoades, S., Marston, J., McCrone, J.T., Sinnott, R. and Lorson, C.L. (2010) Effect of diet on the survival and phenotype of a mouse model for spinal muscular atrophy. *Biochemical and biophysical research communications*, **391**, 835-840.

134 Bruce, A.K., Jacobsen, E., Dossing, H. and Kondrup, J. (1995) Hypoglycaemia in spinal muscular atrophy. *Lancet*, **346**, 609-610.

135 Wang, C.H., Finkel, R.S., Bertini, E.S., Schroth, M., Simonds, A., Wong, B., Aloysius, A., Morrison, L., Main, M., Crawford, T.O. *et al.* (2007) Consensus statement for standard of care in spinal muscular atrophy. *Journal of child neurology*, **22**, 1027-1049.

136 Gombash, S.E., Cowley, C.J., Fitzgerald, J.A., Iyer, C.C., Fried, D., McGovern, V.L., Williams, K.C., Burghes, A.H., Christofi, F.L., Gulbransen, B.D. *et al.* (2015) SMN deficiency disrupts gastrointestinal and enteric nervous system function in mice. *Human molecular genetics*, **24**, 3847-3860.

137 Kuru, S., Sakai, M., Konagaya, M., Yoshida, M., Hashizume, Y. and Saito, K. (2009) An autopsy case of spinal muscular atrophy type III (Kugelberg-Welander disease). *Neuropathology*, **29**, 63-67.

138 Rindt, H., Feng, Z., Mazzasette, C., Glascock, J.J., Valdivia, D., Pyles, N., Crawford, T.O., Swoboda, K.J., Patitucci, T.N., Ebert, A.D. *et al.* (2015) Astrocytes influence the severity of spinal muscular atrophy. *Human molecular genetics*, **24**, 4094-4102.

139 Dachs, E., Hereu, M., Piedrafita, L., Casanovas, A., Calderó, J. and Esquerda, J.E. (2011) Defective neuromuscular junction organization and postnatal myogenesis in mice with severe spinal muscular atrophy. *Journal of neuropathology and experimental neurology*, **70**, 444-461.

140 Tarabal, O., Caraballo-Miralles, V., Cardona-Rossinyol, A., Correa, F.J., Olmos, G., Llado, J., Esquerda, J.E. and Caldero, J. (2014) Mechanisms involved in spinal cord central synapse loss in a mouse model of spinal muscular atrophy. *J Neuropathol Exp Neurol*, **73**, 519-535.

141 Kumagai, T. and Hashizume, Y. (1982) Morphological and morphometric studies on the spinal cord lesion in Werdnig-Hoffmann disease. *Brain Dev*, **4**, 87-96.

142 McGivern, J.V., Patitucci, T.N., Nord, J.A., Barabas, M.-E.A.E., Stucky, C.L. and Ebert, A.D. (2013) Spinal muscular atrophy astrocytes exhibit abnormal calcium regulation and reduced growth factor production. *Glia*, **61**, 1418-1428.

143 Cervero, C., Montull, N., Tarabal, O., Piedrafita, L., Esquerda, J.E. and Caldero, J. (2016) Chronic Treatment with the AMPK Agonist AICAR Prevents Skeletal Muscle Pathology but Fails to Improve Clinical Outcome in a Mouse Model of Severe Spinal Muscular Atrophy. *Neurotherapeutics*, **13**, 198-216.

144 Zhou, C., Feng, Z. and Ko, C.-P.P. (2016) Defects in Motoneuron-Astrocyte Interactions in Spinal Muscular Atrophy. *The Journal of neuroscience : the official journal of the Society for Neuroscience*, **36**, 2543-2553.

145 Sison, S.L., Patitucci, T.N., Seminary, E.R., Villalon, E., Lorson, C.L. and Ebert, A.D. (2017) Astrocyte-produced miR-146a as a mediator of motor neuron loss in spinal muscular atrophy. *Hum Mol Genet*, in press.

146 Aghamaleky Sarvestany, A., Hunter, G., Tavendale, A., Lamont, D.J., Llavero Hurtado, M., Graham, L.C., Wishart, T.M. and Gillingwater, T.H. (2014) Label-free quantitative proteomic profiling identifies disruption of ubiquitin homeostasis as a key driver of Schwann cell defects in spinal muscular atrophy. *J Proteome Res*, **13**, 4546-4557.

147 Hunter, G., Aghamaleky Sarvestany, A., Roche, S.L., Symes, R.C. and Gillingwater, T.H. (2014) SMN-dependent intrinsic defects in Schwann cells in mouse models of spinal muscular atrophy. *Hum Mol Genet*, **23**, 2235-2250.

148 Hunter, G., Powis, R.A., Jones, R.A., Groen, E.J., Shorrock, H.K., Lane, F.M., Zheng, Y., Sherman, D.L., Brophy, P.J. and Gillingwater, T.H. (2016) Restoration of SMN in

Schwann cells reverses myelination defects and improves neuromuscular function in spinal muscular atrophy. *Human molecular genetics*, in press.

149 O'Meara, R.W., Cummings, S.E., De Repentigny, Y., McFall, E., Michalski, J.P., Deguise, M.O., Gibeault, S. and Kothary, R. (2017) Oligodendrocyte development and CNS myelination are unaffected in a mouse model of severe spinal muscular atrophy. *Hum Mol Genet*, in press.

150 Deguise, M.O. and Kothary, R. (2017) New insights into SMA pathogenesis: immune dysfunction and neuroinflammation. *Ann Clin Transl Neurol*, **4**, 522-530.

151 McNally, E.M., Kaltman, J.R., Benson, D.W., Canter, C.E., Cripe, L.H., Duan, D., Finder, J.D., Groh, W.J., Hoffman, E.P., Judge, D.P. *et al.* (2015) Contemporary cardiac issues in Duchenne muscular dystrophy. Working Group of the National Heart, Lung, and Blood Institute in collaboration with Parent Project Muscular Dystrophy. *Circulation*, **131**, 1590-1598.

152 Burghes, A., DiDonato, C.J., McGovern, V.L. and Arnold, W.D. (2017) Sumner, C.J., Paushkin, S. and Ko, C.P. (eds.), In *Spinal Muscular Atrophy: Disease Mechanism and Therapy*. Elsevier, in press., pp. 241-260.

153 Monani, U.R., Sendtner, M., Coovert, D.D., Parsons, D.W., Andreassi, C., Le, T.T., Jablonka, S., Schrank, B., Rossoll, W., Rossol, W. *et al.* (2000) The human centromeric survival motor neuron gene (SMN2) rescues embryonic lethality in Smn(-/-) mice and results in a mouse with spinal muscular atrophy. *Human molecular genetics*, **9**, 333-339.

154 Hsieh-Li, H., Chang, J.-G., Jong, Y.-J., Wu, M.-H., Wang, N.M., Tsai, C. and Li, H. (2000) A mouse model for spinal muscular atrophy. *Nature Genetics*, **24**, 66-70.

155 Le, T.T., Pham, L.T., Butchbach, M.E., Zhang, H.L., Monani, U.R., Coovert, D.D., Gavrilina, T.O., Xing, L., Bassell, G.J. and Burghes, A.H. (2005) SMNDelta7, the major product of the centromeric survival motor neuron (SMN2) gene, extends survival in mice with spinal muscular atrophy and associates with full-length SMN. *Human molecular genetics*, **14**, 845-857.

156 Bowerman, M., Murray, L.M., Beauvais, A., Pinheiro, B. and Kothary, R. (2012) A critical smn threshold in mice dictates onset of an intermediate spinal muscular atrophy phenotype associated with a distinct neuromuscular junction pathology. *Neuromuscular disorders : NMD*, **22**, 263-276.

157 Eshraghi, M., McFall, E., Gibeault, S. and Kothary, R. (2016) Effect of genetic background on the phenotype of the Smn2B/- mouse model of spinal muscular atrophy. *Human molecular genetics*, in press.

158 Monani, U.R., Pastore, M.T., Gavrilina, T.O., Jablonka, S., Le, T.T., Andreassi, C., DiCocco, J.M., Lorson, C., Androphy, E.J., Sendtner, M. *et al.* (2003) A transgene carrying an A2G missense mutation in the SMN gene modulates phenotypic severity in mice with severe (type I) spinal muscular atrophy. *J Cell Biol*, **160**, 41-52.

159 Tsai, L.-K.K., Tsai, M.-S.S., Lin, T.-B.B., Hwu, W.-L.L. and Li, H. (2006) Establishing a standardized therapeutic testing protocol for spinal muscular atrophy. *Neurobiology of disease*, **24**, 286-295.

160 Workman, E., Saieva, L., Carrel, T.L., Crawford, T.O., Liu, D., Lutz, C., Beattie, C.E., Pellizzoni, L. and Burghes, A.H. (2009) A SMN missense mutation complements SMN2 restoring snRNPs and rescuing SMA mice. *Hum Mol Genet*, **18**, 2215-2229.

161 Osborne, M., Gomez, D., Feng, Z., McEwen, C., Beltran, J., Cirillo, K., El-Khodor, B., Lin, M.Y., Li, Y., Knowlton, W.M. *et al.* (2012) Characterization of behavioral and neuromuscular junction phenotypes in a novel allelic series of SMA mouse models. *Hum Mol Genet*, **21**, 4431-4447.

162 Deguise, M.-O.O., Boyer, J.G., McFall, E.R., Yazdani, A., De Repentigny, Y. and Kothary, R. (2016) Differential induction of muscle atrophy pathways in two mouse models of spinal muscular atrophy. *Scientific reports*, **6**, 28846.

163 Millino, C., Fanin, M., Vettori, A., Laveder, P., Mostacciuolo, M.L., Angelini, C. and Lanfranchi, G. (2009) Different atrophy-hypertrophy transcription pathways in muscles affected by severe and mild spinal muscular atrophy. *BMC medicine*, **7**, 14.

164 Pearn, J. (1978) Incidence, prevalence, and gene frequency studies of chronic childhood spinal muscular atrophy. *Journal of medical genetics*, **15**, 409-413.

165 Prior, T.W., Snyder, P.J., Rink, B.D., Pearl, D.K., Pyatt, R.E., Mihal, D.C., Conlan, T., Schmalz, B., Montgomery, L., Ziegler, K. *et al.* (2010) Newborn and carrier screening for spinal muscular atrophy. *American journal of medical genetics. Part A*, **152A**, 1608-1616.

166 Boyer, J.G., Bowerman, M. and Kothary, R. (2010) The many faces of SMN: deciphering the function critical to spinal muscular atrophy pathogenesis. *Future Neurology*, **5**.

167 Hammond, S.M., Gogliotti, R.G., Rao, V., Beauvais, A., Kothary, R. and DiDonato, C.J. (2010) Mouse survival motor neuron alleles that mimic SMN2 splicing and are inducible rescue embryonic lethality early in development but not late. *PloS one*, **5**.

168 Boyer, J.G., Deguise, M.-O.O., Murray, L.M., Yazdani, A., De Repentigny, Y., Boudreau-Larivière, C. and Kothary, R. (2014) Myogenic program dysregulation is contributory to disease pathogenesis in spinal muscular atrophy. *Human molecular genetics*, **23**, 4249-4259.

169 Bricceno, K.V., Martinez, T., Leikina, E., Duguez, S., Partridge, T.A., Chernomordik, L.V., Fischbeck, K.H., Sumner, C.J. and Burnett, B.G. (2014) Survival motor neuron protein deficiency impairs myotube formation by altering myogenic gene expression and focal adhesion dynamics. *Human molecular genetics*, **23**, 4745-4757.

170 Lecker, S.H., Jagoe, T.R., Gilbert, A., Gomes, M., Racos, V., Iley, J., Price, R.S., Mitch, W.E. and Goldberg, A.L. (2004) Multiple types of skeletal muscle atrophy involve a common program of changes in gene expression. *The FASEB Journal*, **18**, 39-51.

171 Sacheck, J.M., Hyatt, J.-P.K.P., Raffaello, A., Jagoe, R.T., Roy, R.R., Edgerton, V.R., Lecker, S.H. and Goldberg, A.L. (2007) Rapid disuse and denervation atrophy involve transcriptional changes similar to those of muscle wasting during systemic diseases. *FASEB journal : official publication of the Federation of American Societies for Experimental Biology*, **21**, 140-155.

172 Moresi, V., Williams, A.H., Meadows, E., Flynn, J.M., Potthoff, M.J., McAnally, J., Shelton, J.M., Backs, J., Klein, W.H., Richardson, J.A. *et al.* (2010) Myogenin and class II HDACs control neurogenic muscle atrophy by inducing E3 ubiquitin ligases. *Cell*, **143**, 35-45.

173 Macpherson, P.C., Wang, X. and Goldman, D. (2011) Myogenin regulates denervation-dependent muscle atrophy in mouse soleus muscle. *Journal of cellular biochemistry*, **112**, 2149-2159.

174 Bricceno, K.V., Sampognaro, P.J., Van Meerbeke, J.P., Sumner, C.J., Fischbeck, K.H. and Burnett, B.G. (2012) Histone deacetylase inhibition suppresses myogenin-dependent atrogene activation in spinal muscular atrophy mice. *Human molecular genetics*, **21**, 4448-4459.

175 Avila, A.M., Burnett, B.G., Taye, A.A., Gabanella, F., Knight, M.A., Hartenstein, P., Cizman, Z., Di Prospero, N.A., Pellizzoni, L., Fischbeck, K.H. *et al.* (2007) Trichostatin A increases SMN expression and survival in a mouse model of spinal muscular atrophy. *The Journal of clinical investigation*, **117**, 659-671.

176 Liu, H., Yazdani, A., Murray, L.M., Beauvais, A. and Kothary, R. (2014) The Smn-independent beneficial effects of trichostatin A on an intermediate mouse model of spinal muscular atrophy. *PloS one*, **9**.

177 Iyer, C.C., McGovern, V.L., Wise, D.O., Glass, D.J. and Burghes, A.H. (2014) Deletion of atrophy enhancing genes fails to ameliorate the phenotype in a mouse model of spinal muscular atrophy. *Neuromuscular disorders : NMD*, **24**, 436-444.

178 Milan, G., Romanello, V., Pescatore, F., Armani, A., Paik, J.-H.H., Frasson, L., Seydel, A., Zhao, J., Abraham, R., Goldberg, A.L. *et al.* (2015) Regulation of autophagy and the ubiquitin-proteasome system by the FoxO transcriptional network during muscle atrophy. *Nature communications*, **6**, 6670.

179 Sandri, M., Sandri, C., Gilbert, A., Skurk, C., Calabria, E., Picard, A., Walsh, K., Schiaffino, S., Lecker, S.H. and Goldberg, A.L. (2004) Foxo transcription factors induce the atrophy-related ubiquitin ligase atrogin-1 and cause skeletal muscle atrophy. *Cell*, **117**, 399-412.

180 Mammucari, C., Milan, G., Romanello, V., Masiero, E., Rudolf, R., Del Piccolo, P., Burden, S.J., Di Lisi, R., Sandri, C., Zhao, J. *et al.* (2007) FoxO3 controls autophagy in skeletal muscle in vivo. *Cell metabolism*, **6**, 458-471.

181 Bodine, S.C., Latres, E., Baumhueter, S., Lai, V.K., Nunez, L., Clarke, B.A., Poueymirou, W.T., Panaro, F.J., Na, E., Dharmarajan, K. *et al.* (2001) Identification of ubiquitin ligases required for skeletal muscle atrophy. *Science (New York, N.Y.)*, **294**, 1704-1708.

182 Schiaffino, S. and Mammucari, C. (2011) Regulation of skeletal muscle growth by the IGF1-Akt/PKB pathway: insights from genetic models. *Skeletal muscle*, **1**, 4.

183 Sandri, M. (2013) Protein breakdown in muscle wasting: role of autophagy-lysosome and ubiquitin-proteasome. *The international journal of biochemistry & cell biology*, **45**, 2121-2129.

184 Roy, S., Dubowitz, V. and Wolman, L. (1971) Ultrastructure of muscle in infantile spinal muscular atrophy. *Journal of the neurological sciences*, **12**, 219-232.

185 Szliwowski, H.B. and Drochmans, P. (1975) Ultrastructural aspects of muscle and nerve in Werdnig-Hoffmann disease. *Acta neuropathologica*, **31**, 281-296.

186 Klionsky, D.J., Abdalla, F.C., Abeliovich, H., Abraham, R.T., Acevedo-Arozena, A., Adeli, K., Agholme, L., Agnello, M., Agostinis, P., Aguirre-Ghiso, J.A. *et al.* (2012) Guidelines

for the use and interpretation of assays for monitoring autophagy. *Autophagy*, **8**, 445-544.

187 Weidberg, H., Shvets, E., Shpilka, T., Shimron, F., Shinder, V. and Elazar, Z. (2010) LC3 and GATE-16/GABARAP subfamilies are both essential yet act differently in autophagosome biogenesis. *The EMBO journal*, **29**, 1792-1802.

188 Bjørkøy, G., Lamark, T., Brech, A., Outzen, H., Perander, M., Overvatn, A., Stenmark, H. and Johansen, T. (2005) p62/SQSTM1 forms protein aggregates degraded by autophagy and has a protective effect on huntingtin-induced cell death. *The Journal of cell biology*, **171**, 603-614.

189 Bosma, M., Hesselink, M.K., Sparks, L.M., Timmers, S., Ferraz, M.J., Mattijssen, F., van Beurden, D., Schaart, G., de Baets, M.H., Verheyen, F.K. *et al.* (2012) Perilipin 2 improves insulin sensitivity in skeletal muscle despite elevated intramuscular lipid levels. *Diabetes*, **61**, 2679-2690.

190 Senf, S.M., Dodd, S.L. and Judge, A.R. (2010) FOXO signaling is required for disuse muscle atrophy and is directly regulated by Hsp70. *American journal of physiology. Cell physiology*, **298**, 45.

191 Senf, S.M., Sandesara, P.B., Reed, S.A. and Judge, A.R. (2011) p300 Acetyltransferase activity differentially regulates the localization and activity of the FOXO homologues in skeletal muscle. *American journal of physiology. Cell physiology*, **300**, 501.

192 Bertaggia, E., Coletto, L. and Sandri, M. (2012) Posttranslational modifications control FoxO3 activity during denervation. *American Journal of Physiology - Cell Physiology*, **302**.

193 Essaghir, A., Dif, N., Marbehant, C.Y., Coffer, P.J. and Demoulin, J.-B.B. (2009) The transcription of FOXO genes is stimulated by FOXO3 and repressed by growth factors. *The Journal of biological chemistry*, **284**, 10334-10342.

194 Skurk, C., Izumiya, Y., Maatz, H., Razeghi, P., Shiojima, I., Sandri, M., Sato, K., Zeng, L., Schiekofer, S., Pimentel, D. *et al.* (2005) The FOXO3a Transcription Factor Regulates Cardiac Myocyte Size Downstream of AKT Signaling. *Journal of Biological Chemistry*, **280**, 20814-20823.

195 Sengupta, A., Molkentin, J.D. and Yutzey, K.E. (2009) FoxO transcription factors promote autophagy in cardiomyocytes. *The Journal of biological chemistry*, **284**, 28319-28331.

196 Schips, T.G., Wietelmann, A., Höhn, K., Schimanski, S., Walther, P., Braun, T., Wirth, T. and Maier, H.J. (2011) FoxO3 induces reversible cardiac atrophy and autophagy in a transgenic mouse model. *Cardiovascular research*, **91**, 587-597.

197 Zhao, J., Brault, J.J., Schild, A., Cao, P., Sandri, M., Schiaffino, S., Lecker, S.H. and Goldberg, A.L. (2007) FoxO3 coordinately activates protein degradation by the autophagic/lysosomal and proteasomal pathways in atrophying muscle cells. *Cell metabolism*, **6**, 472-483.

198 Rose, F.F., Mattis, V.B., Rindt, H. and Lorson, C.L. (2009) Delivery of recombinant follistatin lessens disease severity in a mouse model of spinal muscular atrophy. *Human molecular genetics*, **18**, 997-1005.

199 Sumner, C.J., Wee, C.D., Warsing, L.C., Choe, D.W., Ng, A.S., Lutz, C. and Wagner, K.R. (2009) Inhibition of myostatin does not ameliorate disease features of severe spinal muscular atrophy mice. *Human molecular genetics*, **18**, 3145-3152.

200 Ling, K.K., Gibbs, R.M., Feng, Z. and Ko, C.-P.P. (2012) Severe neuromuscular denervation of clinically relevant muscles in a mouse model of spinal muscular atrophy. *Human molecular genetics*, **21**, 185-195.

201 Ting, C.-H.H., Lin, C.-W.W., Wen, S.-L.L., Hsieh-Li, H.-M.M. and Li, H. (2007) Stat5 constitutive activation rescues defects in spinal muscular atrophy. *Human molecular genetics*, **16**, 499-514.

202 Beharry, A.W., Sandesara, P.B. and Roberts, B.M. (2014) HDAC1 activates FoxO and is both sufficient and required for skeletal muscle atrophy. *HDAC1 activates FoxO and is both sufficient and required for skeletal muscle atrophy*, in press.

203 Moller, P., Moe, N., Saugstad, O.D., Skullerud, K., Velken, M., Berg, K., Nitter-Hauge, S. and Borresen, A.L. (1990) Spinal muscular atrophy type I combined with atrial septal defect in three sibs. *Clin Genet*, **38**, 81-83.

204 Foust, K.D., Wang, X., McGovern, V.L., Braun, L., Bevan, A.K., Haidet, A.M., Le, T.T., Morales, P.R., Rich, M.M., Burghes, A.H. *et al.* (2010) Rescue of the spinal muscular atrophy phenotype in a mouse model by early postnatal delivery of SMN. *Nature biotechnology*, **28**, 271-274.

205 Shafey, D., Boyer, J.G., Bhanot, K. and Kothary, R. (2010) Identification of novel interacting protein partners of SMN using tandem affinity purification. *Journal of proteome research*, **9**, 1659-1669.

206 Hamilton, G. and Gillingwater, T.H. (2013) Spinal muscular atrophy: going beyond the motor neuron. *Trends in molecular medicine*, **19**, 40-50.

207 Hua, Y., Liu, Y.H., Sahashi, K., Rigo, F., Bennett, C.F. and Krainer, A.R. (2015) Motor neuron cell-nonautonomous rescue of spinal muscular atrophy phenotypes in mild and severe transgenic mouse models. *Genes & development*, **29**, 288-297.

208 Shafey, D., Côté, P.D. and Kothary, R. (2005) Hypomorphic Smn knockdown C2C12 myoblasts reveal intrinsic defects in myoblast fusion and myotube morphology. *Experimental cell research*, **311**, 49-61.

209 Hayhurst, M., Wagner, A.K., Cerletti, M., Wagers, A.J. and Rubin, L.L. (2012) A cell-autonomous defect in skeletal muscle satellite cells expressing low levels of survival of motor neuron protein. *Developmental biology*, **368**, 323-334.

210 Bowerman, M., Michalski, J.-P.P., Beauvais, A., Murray, L.M., DeRepentigny, Y. and Kothary, R. (2014) Defects in pancreatic development and glucose metabolism in SMN-depleted mice independent of canonical spinal muscular atrophy neuromuscular pathology. *Human molecular genetics*, **23**, 3432-3444.

211 Bowerman, M., Swoboda, K.J., Michalski, J.-P.P., Wang, G.-S.S., Reeks, C., Beauvais, A., Murphy, K., Woulfe, J., Screaton, R.A., Scott, F.W. *et al.* (2012) Glucose metabolism and pancreatic defects in spinal muscular atrophy. *Annals of neurology*, **72**, 256-268.

212 Wang, C.H., Finkel, R.S., Bertini, E.S. and Schroth, M. (2007) Consensus statement for standard of care in spinal muscular atrophy. *Consensus statement for standard of care in spinal muscular atrophy*, in press.

213 Gombash, S.E., Cowley, C.J., Fitzgerald, J.A., Iyer, C.C., Fried, D., McGovern, V.L., Williams, K.C., Burghes, A.H., Christofi, F.L., Gulbransen, B.D. *et al.* (2015) SMN deficiency disrupts gastrointestinal and enteric nervous system function in mice. *Human molecular genetics*, **24**, 3847-3860.

214 Sintusek, P., Catapano, F., Angkathunkayul, N., Marrosu, E., Parson, S.H., Morgan, J.E., Muntoni, F. and Zhou, H. (2016) Histopathological Defects in Intestine in Severe Spinal Muscular Atrophy Mice Are Improved by Systemic Antisense Oligonucleotide Treatment. *PloS one*, **11**.

215 Bürglen, L., Spiegel, R., Ignatius, J., Cobben, J.M., Landrieu, P., Lefebvre, S., Munnich, A. and Melki, J. (1995) SMN gene deletion in variant of infantile spinal muscular atrophy. *The Lancet*, **346**.

216 Tein, I., Sloane, A.E., Donner, E.J., Lehotay, D.C., Millington, D.S. and Kelley, R.I. (1995) Fatty acid oxidation abnormalities in childhood-onset spinal muscular atrophy: primary or secondary defect(s)? *Pediatric neurology*, **12**, 21-30.

217 Delves, P.J. and Roitt, I.M. (2000) The immune system. First of two parts. *The New England journal of medicine*, **343**, 37-49.

218 Delves, P.J. and Roitt, I.M. (2000) The immune system. Second of two parts. *The New England journal of medicine*, **343**, 108-117.

219 Mebius, R.E. and Kraal, G. (2005) Structure and function of the spleen. *Nature reviews. Immunology*, **5**, 606-616.

220 Tarantino, G., Scalera, A. and Finelli, C. (2013) Liver-spleen axis: intersection between immunity, infections and metabolism. *World journal of gastroenterology : WJG*, **19**, 3534-3542.

221 Cesta, M.F. (2006) Normal structure, function, and histology of the spleen. *Toxicologic pathology*, **34**, 455-465.

222 Vacchio, M.S., Ciucci, T. and Bosselut, R. (2016) 200 Million Thymocytes and I: A Beginner's Survival Guide to T Cell Development. *Methods Mol Biol*, **1323**, 3-21.

223 Elmore, S.A. (2006) Enhanced histopathology of the thymus. *Toxicologic pathology*, **34**, 656-665.

224 Starr, T.K., Jameson, S.C. and Hogquist, K.A. (2003) Positive and negative selection of T cells. *Annual review of immunology*, **21**, 139-176.

225 Hogquist, K.A., Baldwin, T.A. and Jameson, S.C. (2005) Central tolerance: learning self-control in the thymus. *Nature reviews. Immunology*, **5**, 772-782.

226 Lee, J.Y. and Love, P.E. (2016) Assessment of T Cell Development by Flow Cytometry. *Methods Mol Biol*, **1323**, 47-64.

227 Hu, Q., Nicol, S.A., Suen, A.Y. and Baldwin, T.A. (2012) Examination of thymic positive and negative selection by flow cytometry. *Journal of visualized experiments : JoVE*, in press.

228 Ransohoff, R.M. (2016) How neuroinflammation contributes to neurodegeneration. *Science (New York, N.Y.)*, **353**, 777-783.

229 Banerjee, R., Mosley, R.L., Reynolds, A.D., Dhar, A., Jackson-Lewis, V., Gordon, P.H., Przedborski, S. and Gendelman, H.E. (2008) Adaptive immune neuroprotection in G93A-SOD1 amyotrophic lateral sclerosis mice. *PloS one*, **3**.

230 O'Rourke, J.G., Bogdanik, L., Yáñez, A., Lall, D., Wolf, A.J., Muhammad, A.K., Ho, R., Carmona, S., Vit, J.P., Zarrow, J. *et al.* (2016) C9orf72 is required for proper macrophage and microglial function in mice. *Science (New York, N.Y.)*, **351**, 1324-1329.

231 Beers, D.R., Henkel, J.S., Zhao, W., Wang, J. and Appel, S.H. (2008) CD4+ T cells support glial neuroprotection, slow disease progression, and modify glial morphology in an animal model of inherited ALS. *Proc Natl Acad Sci U S A*, **105**, 15558-15563.

232 Chiu, I.M., Chen, A., Zheng, Y., Kosaras, B., Tsiftsoglou, S.A., Vartanian, T.K., Brown, R.H., Jr. and Carroll, M.C. (2008) T lymphocytes potentiate endogenous neuroprotective inflammation in a mouse model of ALS. *Proc Natl Acad Sci U S A*, **105**, 17913-17918.

233 Hirahara, H., Ogawa, M., Kimura, M., Iiai, T., Tsuchida, M., Hanawa, H., Watanabe, H. and Abo, T. (1994) Glucocorticoid independence of acute thymic involution induced by lymphotoxin and estrogen. *Cellular immunology*, **153**, 401-411.

234 Screpanti, I., Morrone, S., Meco, D., Santoni, A., Gulino, A., Paolini, R., Crisanti, A., Mathieson, B.J. and Frati, L. (1989) Steroid sensitivity of thymocyte subpopulations during intrathymic differentiation. Effects of 17 beta-estradiol and dexamethasone on subsets expressing T cell antigen receptor or IL-2 receptor. *Journal of immunology (Baltimore, Md. : 1950)*, **142**, 3378-3383.

235 Savino, W. and Dardenne, M. (2000) Neuroendocrine control of thymus physiology. *Endocrine reviews*, **21**, 412-443.

236 Hachiya, Y., Arai, H., Hayashi, M., Kumada, S., Furushima, W., Ohtsuka, E., Ito, Y., Uchiyama, A. and Kurata, K. (2005) Autonomic dysfunction in cases of spinal muscular atrophy type 1 with long survival. *Brain Dev*, **27**, 574-578.

237 Araujo, A.p., Araujo, M. and Swoboda, K.J. (2009) Vascular perfusion abnormalities in infants with spinal muscular atrophy. *The Journal of pediatrics*, **155**, 292-294.

238 Rudnik-Schöneborn, S. and Vogelgesang, S. (2010) Digital necroses and vascular thrombosis in severe spinal muscular atrophy. *Digital necroses and vascular thrombosis in severe spinal muscular atrophy*, in press.

239 Ackerman, K.D., Felten, S.Y., Dijkstra, C.D., Livnat, S. and Felten, D.L. (1989) Parallel development of noradrenergic innervation and cellular compartmentation in the rat spleen. *Experimental Neurology*, **103**, 239255.

240 Bellinger, D.L., Lorton, D., Felten, S.Y. and Felten, D.L. (1992) Innervation of lymphoid organs and implications in development, aging, and autoimmunity. *International journal of immunopharmacology*, **14**, 329-344.

241 Baggiolini, M. (1998) Chemokines and leukocyte traffic. *Nature*, **392**, 565-568.

242 Rennert, P.D., Browning, J.L. and Mebius, R. (1996) Surface lymphotoxin alpha/beta complex is required for the development of peripheral lymphoid organs. *The Journal of …*, in press.

243 Matsumoto, M., Fu, Y.X., Molina, H. and Chaplin, D.D. (1997) Lymphotoxin-alpha-deficient and TNF receptor-I-deficient mice define developmental and functional characteristics of germinal centers. *Immunological reviews*, **156**, 137-144.

244 Fütterer, A., Mink, K., Luz, A., Kosco-Vilbois, M.H. and Pfeffer, K. (1998) The lymphotoxin beta receptor controls organogenesis and affinity maturation in peripheral lymphoid tissues. *Immunity*, **9**, 59-70.

245 Förster, R., Schubel, A., Breitfeld, D., Kremmer, E., Renner-Müller, I., Wolf, E. and Lipp, M. (1999) CCR7 coordinates the primary immune response by establishing functional microenvironments in secondary lymphoid organs. *Cell*, **99**, 23-33.

246 Ettinger, R., Browning, J.L., Michie, S.A., van Ewijk, W. and McDevitt, H.O. (1996) Disrupted splenic architecture, but normal lymph node development in mice expressing a soluble lymphotoxin-beta receptor-IgG1 fusion protein. *Proceedings of the National Academy of Sciences of the United States of America*, **93**, 13102-13107.

247 Ngo, V.N., Korner, H., Gunn, M.D., Schmidt, K.N., Riminton, D.S., Cooper, M.D., Browning, J.L., Sedgwick, J.D. and Cyster, J.G. (1999) Lymphotoxin alpha/beta and tumor necrosis factor are required for stromal cell expression of homing chemokines in B and T cell areas of the spleen. *The Journal of experimental medicine*, **189**, 403-412.

248 Gunn, M.D., Kyuwa, S., Tam, C., Kakiuchi, T., Matsuzawa, A., Williams, L.T. and Nakano, H. (1999) Mice lacking expression of secondary lymphoid organ chemokine have defects in lymphocyte homing and dendritic cell localization. *The Journal of experimental medicine*, **189**, 451-460.

249 Geijtenbeek, T.B., Groot, P.C., Nolte, M.A., van Vliet, S.J., Gangaram-Panday, S.T., van Duijnhoven, G.C., Kraal, G., van Oosterhout, A.J. and van Kooyk, Y. (2002) Marginal zone macrophages express a murine homologue of DC-SIGN that captures blood-borne antigens in vivo. *Blood*, **100**, 2908-2916.

250 Koppel, E.A., Ludwig, I.S., Hernandez, M.S., Lowary, T.L., Gadikota, R.R., Tuzikov, A.B., Vandenbroucke-Grauls, C.M., van Kooyk, Y., Appelmelk, B.J. and Geijtenbeek, T.B. (2004) Identification of the mycobacterial carbohydrate structure that binds the C-type lectins DC-SIGN, L-SIGN and SIGNR1. *Immunobiology*, **209**, 117-127.

251 Elomaa, O., Kangas, M., Sahlberg, C., Tuukkanen, J., Sormunen, R., Liakka, A., Thesleff, I., Kraal, G. and Tryggvason, K. (1995) Cloning of a novel bacteria-binding receptor structurally related to scavenger receptors and expressed in a subset of macrophages. *Cell*, **80**, 603-609.

252 Jones, C., Virji, M. and Crocker, P.R. (2003) Recognition of sialylated meningococcal lipopolysaccharide by siglecs expressed on myeloid cells leads to enhanced bacterial uptake. *Molecular microbiology*, **49**, 1213-1225.

253 Narver, H.L., Kong, L., Burnett, B.G., Choe, D.W., Bosch-Marcé, M., Taye, A.A., Eckhaus, M.A. and Sumner, C.J. (2008) Sustained improvement of spinal muscular atrophy mice treated with trichostatin A plus nutrition. *Annals of neurology*, **64**, 465-470.

254 Somers, E., Lees, R.D., Hoban, K., Sleigh, J.N., Zhou, H., Muntoni, F., Talbot, K., Gillingwater, T.H. and Parson, S.H. (2016) Vascular Defects and Spinal Cord Hypoxia in Spinal Muscular Atrophy. *Annals of neurology*, **79**, 217-230.

255 Somers, E., Stencel, Z., Wishart, T.M., Gillingwater, T.H. and Parson, S.H. (2012) Density, calibre and ramification of muscle capillaries are altered in a mouse model of severe spinal muscular atrophy. *Neuromuscular disorders : NMD*, **22**, 435-442.

256 Turner, M.D., Nedjai, B., Hurst, T. and Pennington, D.J. (2014) Cytokines and chemokines: At the crossroads of cell signalling and inflammatory disease. *Biochimica et biophysica acta*, **1843**, 2563-2582.

257 Randall, T.D. and Mebius, R.E. (2014) The development and function of mucosal lymphoid tissues: a balancing act with micro-organisms. *Mucosal Immunol*, **7**, 455-466.

258 Deguise, M.O., De Repentigny, Y., McFall, E., Auclair, N., Sad, S. and Kothary, R. (2017) Immune dysregulation may contribute to disease pathogenesis in spinal muscular atrophy mice. *Hum Mol Genet*, in press.

259 Thomson, A.K., Somers, E., Powis, R.A., Shorrock, H.K., Murphy, K., Swoboda, K.J., Gillingwater, T.H. and Parson, S.H. (2017) Survival of motor neurone protein is required for normal postnatal development of the spleen. *J Anat*, **230**, 337-346.

260 Khairallah, M.T., Astroski, J., Custer, S.K., Androphy, E.J., Franklin, C.L. and Lorson, C.L. (2017) SMN deficiency negatively impacts red pulp macrophages and spleen development in mouse models of Spinal Muscular Atrophy. *Hum Mol Genet*, in press.

261 Thomson, A.K., Somers, E., Powis, R.A., Shorrock, H.K., Murphy, K., Swoboda, K.J., Gillingwater, T.H. and Parson, S.H. (2016) Survival of motor neurone protein is required for normal postnatal development of the spleen. *J Anat*, in press.

262 Ransohoff, R.M. (2016) How neuroinflammation contributes to neurodegeneration. *Science*, **353**, 777-783.

263 Cappellano, G., Carecchio, M., Fleetwood, T., Magistrelli, L., Cantello, R., Dianzani, U. and Comi, C. (2013) Immunity and inflammation in neurodegenerative diseases. *Am J Neurodegener Dis*, **2**, 89-107.

264 Gertz, B., Wong, M. and Martin, L.J. (2012) Nuclear localization of human SOD1 and mutant SOD1-specific disruption of survival motor neuron protein complex in transgenic amyotrophic lateral sclerosis mice. *J Neuropathol Exp Neurol*, **71**, 162-177.

265 Kariya, S., Re, D.B., Jacquier, A., Nelson, K., Przedborski, S. and Monani, U.R. (2012) Mutant superoxide dismutase 1 (SOD1), a cause of amyotrophic lateral sclerosis, disrupts the recruitment of SMN, the spinal muscular atrophy protein to nuclear Cajal bodies. *Hum Mol Genet*, **21**, 3421-3434.

266 Perera, N.D., Sheean, R.K., Crouch, P.J., White, A.R., Horne, M.K. and Turner, B.J. (2016) Enhancing survival motor neuron expression extends lifespan and attenuates neurodegeneration in mutant TDP-43 mice. *Hum Mol Genet*, **25**, 4080-4093.

267 Turner, B.J., Alfazema, N., Sheean, R.K., Sleigh, J.N., Davies, K.E., Horne, M.K. and Talbot, K. (2014) Overexpression of survival motor neuron improves neuromuscular function and motor neuron survival in mutant SOD1 mice. *Neurobiol Aging*, **35**, 906-915.

268 Yamazaki, T., Chen, S., Yu, Y., Yan, B., Haertlein, T.C., Carrasco, M.A., Tapia, J.C., Zhai, B., Das, R., Lalancette-Hebert, M. *et al.* (2012) FUS-SMN protein interactions link the motor neuron diseases ALS and SMA. *Cell Rep*, **2**, 799-806.

269 Bowerman, M., Murray, L.M., Scamps, F., Schneider, B.L., Kothary, R. and Raoul, C. (2017) Pathogenic commonalities between spinal muscular atrophy and amyotrophic lateral sclerosis: a converging road to therapeutic development. *Eur J Med Gen*, in press., under revision.

270 McGivern, J.V., Patitucci, T.N., Nord, J.A., Barabas, M.A., Stucky, C.L. and Ebert, A.D. (2013) Spinal muscular atrophy astrocytes exhibit abnormal calcium regulation and reduced growth factor production. *Glia*, **61**, 1418-1428.

271 Deguise, M.O., De Repentigny, Y., McFall, E., Auclair, N., Sad, S. and Kothary, R. (2017) Immune dysregulation may contribute to disease pathogenesis in spinal muscular atrophy mice. *Hum Mol Genet*, **26**, 801-819.

272 Rindt, H., Feng, Z., Mazzasette, C., Glascock, J.J., Valdivia, D., Pyles, N., Crawford, T.O., Swoboda, K.J., Patitucci, T.N., Ebert, A.D. *et al.* (2015) Astrocytes influence the severity of spinal muscular atrophy. *Hum Mol Genet*, **24**, 4094-4102.

273 Zhang, S., Tang, M.B., Luo, H.Y., Shi, C.H. and Xu, Y.M. (2017) Necroptosis in neurodegenerative diseases: a potential therapeutic target. *Cell Death Dis*, **8**, e2905.

274 Ito, Y., Ofengeim, D., Najafov, A., Das, S., Saberi, S., Li, Y., Hitomi, J., Zhu, H., Chen, H., Mayo, L. *et al.* (2016) RIPK1 mediates axonal degeneration by promoting inflammation and necroptosis in ALS. *Science*, **353**, 603-608.

275 Shao, L., Yu, S., Ji, W., Li, H. and Gao, Y. (2017) The Contribution of Necroptosis in Neurodegenerative Diseases. *Neurochem Res*, **42**, 2117-2126.

276 Murray, L.M., Beauvais, A., Gibeault, S., Courtney, N.L. and Kothary, R. (2015) Transcriptional profiling of differentially vulnerable motor neurons at pre-symptomatic stage in the Smn (2b/-) mouse model of spinal muscular atrophy. *Acta Neuropathol Commun*, **3**, 55.

277 Simon, C.M., Dai, Y., Van Alstyne, M., Koutsioumpa, C., Pagiazitis, J.G., Chalif, J.I., Wang, X., Rabinowitz, J.E., Henderson, C.E., Pellizzoni, L. *et al.* (2017) Converging

Mechanisms of p53 Activation Drive Motor Neuron Degeneration in Spinal Muscular Atrophy. *Cell Rep*, **21**, 3767-3780.

278 Van Alstyne, M., Simon, C.M., Sardi, S.P., Shihabuddin, L.S., Mentis, G.Z. and Pellizzoni, L. (2018) Dysregulation of Mdm2 and Mdm4 alternative splicing underlies motor neuron death in spinal muscular atrophy. *Genes Dev*, **32**, 1045-1059.

279 Courtney, N.L., Mole, A.J., Thomson, A.K. and Murray, L.M. (2019) Reduced P53 levels ameliorate neuromuscular junction loss without affecting motor neuron pathology in a mouse model of spinal muscular atrophy. *Cell Death Dis*, **10**, 515.

280 Pasparakis, M. and Vandenabeele, P. (2015) Necroptosis and its role in inflammation. *Nature*, **517**, 311-320.

281 Rickard, J.A., O'Donnell, J.A., Evans, J.M., Lalaoui, N., Poh, A.R., Rogers, T., Vince, J.E., Lawlor, K.E., Ninnis, R.L., Anderton, H. *et al.* (2014) RIPK1 regulates RIPK3-MLKL-driven systemic inflammation and emergency hematopoiesis. *Cell*, **157**, 1175-1188.

282 Schroder, K. and Tschopp, J. (2010) The inflammasomes. *Cell*, **140**, 821-832.

283 Verhaart, I.E.C., Robertson, A., Wilson, I.J., Aartsma-Rus, A., Cameron, S., Jones, C.C., Cook, S.F. and Lochmuller, H. (2017) Prevalence, incidence and carrier frequency of 5q-linked spinal muscular atrophy - a literature review. *Orphanet J Rare Dis*, **12**, 124.

284 Chaytow, H., Huang, Y.T., Gillingwater, T.H. and Faller, K.M.E. (2018) The role of survival motor neuron protein (SMN) in protein homeostasis. *Cell Mol Life Sci*, **75**, 3877-3894.

285 Shanmugarajan, S., Tsuruga, E., Swoboda, K.J., Maria, B.L., Ries, W.L. and Reddy, S.V. (2009) Bone loss in survival motor neuron (Smn(-/-) SMN2) genetic mouse model of spinal muscular atrophy. *J Pathol*, **219**, 52-60.

286 Shanmugarajan, S., Swoboda, K.J., Iannaccone, S.T., Ries, W.L., Maria, B.L. and Reddy, S.V. (2007) Congenital bone fractures in spinal muscular atrophy: functional role for SMN protein in bone remodeling. *J Child Neurol*, **22**, 967-973.

287 Groen, E.J.N., Talbot, K. and Gillingwater, T.H. (2018) Advances in therapy for spinal muscular atrophy: promises and challenges. *Nat Rev Neurol*, **14**, 214-224.

288 Davis, R.H., Miller, E.A., Zhang, R.Z. and Swoboda, K.J. (2015) Responses to Fasting and Glucose Loading in a Cohort of Well Children with Spinal Muscular Atrophy Type II. *J Pediatr*, **167**, 1362-1368 e1361.

289 Walter, L.M., Deguise, M.O., Meijboom, K.E., Betts, C.A., Ahlskog, N., van Westering, T.L.E., Hazell, G., McFall, E., Kordala, A., Hammond, S.M. *et al.* (2018) Interventions Targeting Glucocorticoid-Kruppel-like Factor 15-Branched-Chain Amino Acid Signaling Improve Disease Phenotypes in Spinal Muscular Atrophy Mice. *EBioMedicine*, **31**, 226-242.

290 Trefts, E., Gannon, M. and Wasserman, D.H. (2017) The liver. *Curr Biol*, **27**, R1147-R1151.

291 Sendensky, A.D., Jean-François. (2011) al., P.G.e. (ed.), In *Clinical gastroenterology: Chronic liver failure*, in press.

292 Vitte, J.M.M., Davoult, B., Roblot, N., Mayer, M., Joshi, V., Courageot, S., Tronche, F., Vadrot, J., Moreau, M.H., Kemeny, F. *et al.* (2004) Deletion of murine Smn exon 7

directed to liver leads to severe defect of liver development associated with iron overload. *The American journal of pathology*, **165**, 1731-1741.

293 Li, J., Motsko, S.P., Goehring, E.L., Jr., Tave, A., Pezzullo, J.C. and Jones, J.K. (2010) Prevalence of pediatric dyslipidemia: comparison of a population-based claims database to national surveys. *Pharmacoepidemiol Drug Saf*, **19**, 1031-1040.

294 Ford, E.S., Li, C., Zhao, G. and Mokdad, A.H. (2009) Concentrations of low-density lipoprotein cholesterol and total cholesterol among children and adolescents in the United States. *Circulation*, **119**, 1108-1115.

295 Dathan-Stumpf, A., Vogel, M., Hiemisch, A., Thiery, J., Burkhardt, R., Kratzsch, J. and Kiess, W. (2016) Pediatric reference data of serum lipids and prevalence of dyslipidemia: Results from a population-based cohort in Germany. *Clin Biochem*, **49**, 740-749.

296 Kit, B.K., Kuklina, E., Carroll, M.D., Ostchega, Y., Freedman, D.S. and Ogden, C.L. (2015) Prevalence of and trends in dyslipidemia and blood pressure among US children and adolescents, 1999-2012. *JAMA Pediatr*, **169**, 272-279.

297 Johnson, W.D., Kroon, J.J., Greenway, F.L., Bouchard, C., Ryan, D. and Katzmarzyk, P.T. (2009) Prevalence of risk factors for metabolic syndrome in adolescents: National Health and Nutrition Examination Survey (NHANES), 2001-2006. *Arch Pediatr Adolesc Med*, **163**, 371-377.

298 Schwimmer, J.B., Deutsch, R., Kahen, T., Lavine, J.E., Stanley, C. and Behling, C. (2006) Prevalence of fatty liver in children and adolescents. *Pediatrics*, **118**, 1388-1393.

299 Pacifico, L., Poggiogalle, E., Cantisani, V., Menichini, G., Ricci, P., Ferraro, F. and Chiesa, C. (2010) Pediatric nonalcoholic fatty liver disease: A clinical and laboratory challenge. *World J Hepatol*, **2**, 275-288.

300 Nathan, D.M., Turgeon, H. and Regan, S. (2007) Relationship between glycated haemoglobin levels and mean glucose levels over time. *Diabetologia*, **50**, 2239-2244.

301 Muro, E., Atilla-Gokcumen, G.E. and Eggert, U.S. (2014) Lipids in cell biology: how can we understand them better? *Mol Biol Cell*, **25**, 1819-1823.

302 Storck, E.M., Ozbalci, C. and Eggert, U.S. (2018) Lipid Cell Biology: A Focus on Lipids in Cell Division. *Annu Rev Biochem*, **87**, 839-869.

303 Millan, J., Pinto, X., Munoz, A., Zuniga, M., Rubies-Prat, J., Pallardo, L.F., Masana, L., Mangas, A., Hernandez-Mijares, A., Gonzalez-Santos, P. *et al.* (2009) Lipoprotein ratios: Physiological significance and clinical usefulness in cardiovascular prevention. *Vasc Health Risk Manag*, **5**, 757-765.

304 Hardy, T., Oakley, F., Anstee, Q.M. and Day, C.P. (2016) Nonalcoholic Fatty Liver Disease: Pathogenesis and Disease Spectrum. *Annu Rev Pathol*, **11**, 451-496.

305 McMillan, H.J., Gregas, M., Darras, B.T. and Kang, P.B. (2011) Serum transaminase levels in boys with Duchenne and Becker muscular dystrophy. *Pediatrics*, **127**, e132-136.

306 DeZwaan-McCabe, D., Sheldon, R.D., Gorecki, M.C., Guo, D.F., Gansemer, E.R., Kaufman, R.J., Rahmouni, K., Gillum, M.P., Taylor, E.B., Teesch, L.M. *et al.* (2017) ER Stress Inhibits Liver Fatty Acid Oxidation while Unmitigated Stress Leads to Anorexia-Induced Lipolysis and Both Liver and Kidney Steatosis. *Cell Rep*, **19**, 1794-1806.

307 Pagliassotti, M.J. (2012) Endoplasmic reticulum stress in nonalcoholic fatty liver disease. *Annu Rev Nutr*, **32**, 17-33.

308 Shu, K.X., Li, B. and Wu, L.X. (2007) The p53 network: p53 and its downstream genes. *Colloids Surf B Biointerfaces*, **55**, 10-18.

309 Ohlsson, C., Mellstrom, D., Carlzon, D., Orwoll, E., Ljunggren, O., Karlsson, M.K. and Vandenput, L. (2011) Older men with low serum IGF-1 have an increased risk of incident fractures: the MrOS Sweden study. *J Bone Miner Res*, **26**, 865-872.

310 Murdocca, M., Malgieri, A., Luchetti, A., Saieva, L., Dobrowolny, G., de Leonibus, E., Filareto, A., Quitadamo, M.C., Novelli, G., Musaro, A. *et al.* (2012) IPLEX administration improves motor neuron survival and ameliorates motor functions in a severe mouse model of spinal muscular atrophy. *Mol Med*, **18**, 1076-1085.

311 Sahashi, K., Ling, K.K., Hua, Y., Wilkinson, J.E., Nomakuchi, T., Rigo, F., Hung, G., Xu, D., Jiang, Y.-P.P., Lin, R.Z. *et al.* (2013) Pathological impact of SMN2 mis-splicing in adult SMA mice. *EMBO molecular medicine*, **5**, 1586-1601.

312 Evstatiev, R. and Gasche, C. (2012) Iron sensing and signalling. *Gut*, **61**, 933-952.

313 Herzig, S., Long, F., Jhala, U.S., Hedrick, S., Quinn, R., Bauer, A., Rudolph, D., Schutz, G., Yoon, C., Puigserver, P. *et al.* (2001) CREB regulates hepatic gluconeogenesis through the coactivator PGC-1. *Nature*, **413**, 179-183.

314 Altarejos, J.Y. and Montminy, M. (2011) CREB and the CRTC co-activators: sensors for hormonal and metabolic signals. *Nat Rev Mol Cell Biol*, **12**, 141-151.

315 Campbell, J.E. and Drucker, D.J. (2015) Islet alpha cells and glucagon--critical regulators of energy homeostasis. *Nat Rev Endocrinol*, **11**, 329-338.

316 Larsen, S., Nielsen, J., Hansen, C.N., Nielsen, L.B., Wibrand, F., Stride, N., Schroder, H.D., Boushel, R., Helge, J.W., Dela, F. *et al.* (2012) Biomarkers of mitochondrial content in skeletal muscle of healthy young human subjects. *J Physiol*, **590**, 3349-3360.

317 Hardwick, J.P., Osei-Hyiaman, D., Wiland, H., Abdelmegeed, M.A. and Song, B.J. (2009) PPAR/RXR Regulation of Fatty Acid Metabolism and Fatty Acid omega-Hydroxylase (CYP4) Isozymes: Implications for Prevention of Lipotoxicity in Fatty Liver Disease. *PPAR Res*, **2009**, 952734.

318 Berlanga, A., Guiu-Jurado, E., Porras, J.A. and Auguet, T. (2014) Molecular pathways in non-alcoholic fatty liver disease. *Clin Exp Gastroenterol*, **7**, 221-239.

319 Bechmann, L.P., Hannivoort, R.A., Gerken, G., Hotamisligil, G.S., Trauner, M. and Canbay, A. (2012) The interaction of hepatic lipid and glucose metabolism in liver diseases. *J Hepatol*, **56**, 952-964.

320 Fan, J.G. and Cao, H.X. (2013) Role of diet and nutritional management in non-alcoholic fatty liver disease. *J Gastroenterol Hepatol*, **28 Suppl 4**, 81-87.

321 Sun, B., Purcell, R.H., Terrillion, C.E., Yan, J., Moran, T.H. and Tamashiro, K.L. (2012) Maternal high-fat diet during gestation or suckling differentially affects offspring leptin sensitivity and obesity. *Diabetes*, **61**, 2833-2841.

322 Chen, E., Tsai, T.H., Li, L., Saha, P., Chan, L. and Chang, B.H. (2017) PLIN2 is a Key Regulator of the Unfolded Protein Response and Endoplasmic Reticulum Stress Resolution in Pancreatic beta Cells. *Sci Rep*, **7**, 40855.

323 Carson, A.P., Fox, C.S., McGuire, D.K., Levitan, E.B., Laclaustra, M., Mann, D.M. and Muntner, P. (2010) Low hemoglobin A1c and risk of all-cause mortality among US adults without diabetes. *Circ Cardiovasc Qual Outcomes*, **3**, 661-667.

324 Wang, P. (2017) What Clinical Laboratorians Should Do in Response to Extremely Low Hemoglobin A1c Results. *Lab Med*, **48**, 89-92.

325 Aggarwal, V., Schneider, A.L. and Selvin, E. (2012) Low hemoglobin A(1c) in nondiabetic adults: an elevated risk state? *Diabetes Care*, **35**, 2055-2060.

326 Christman, A.L., Lazo, M., Clark, J.M. and Selvin, E. (2011) Low glycated hemoglobin and liver disease in the U.S. population. *Diabetes Care*, **34**, 2548-2550.

327 Finkelstein, A., Kunis, G., Seksenyan, A., Ronen, A., Berkutzki, T., Azoulay, D., Koronyo-Hamaoui, M. and Schwartz, M. (2011) Abnormal changes in NKT cells, the IGF-1 axis, and liver pathology in an animal model of ALS. *PLoS One*, **6**, e22374.

328 Neve, A., Trüb, J., Saxena, S. and Schümperli, D. (2016) Central and peripheral defects in motor units of the diaphragm of spinal muscular atrophy mice. *Molecular and cellular neurosciences*, **70**, 30-41.

329 Eshraghi, M., Gombar, R., De Repentigny, Y., Vacratsis, P.O. and Kothary, R. (2019) Pathologic Alterations in the Proteome of Synaptosomes from a Mouse Model of Spinal Muscular Atrophy. *J Proteome Res*, in press.

330 Wishart, T.M., Mutsaers, C.A., Riessland, M., Reimer, M.M., Hunter, G., Hannam, M.L., Eaton, S.L., Fuller, H.R., Roche, S.L., Somers, E. *et al.* (2014) Dysregulation of ubiquitin homeostasis and β-catenin signaling promote spinal muscular atrophy. *Journal of Clinical Investigation*, **124**.

331 Miller, N., Shi, H., Zelikovich, A.S. and Ma, Y.C. (2016) Motor neuron mitochondrial dysfunction in spinal muscular atrophy. *Hum Mol Genet*, **25**, 3395-3406.

332 Fuller, H.R., Mandefro, B., Shirran, S.L., Gross, A.R., Kaus, A.S., Botting, C.H., Morris, G.E. and Sareen, D. (2015) Spinal Muscular Atrophy Patient iPSC-Derived Motor Neurons Have Reduced Expression of Proteins Important in Neuronal Development. *Front Cell Neurosci*, **9**, 506.

333 Boyd, P.J., Tu, W.Y., Shorrock, H.K., Groen, E.J.N., Carter, R.N., Powis, R.A., Thomson, S.R., Thomson, D., Graham, L.C., Motyl, A.A.L. *et al.* (2017) Bioenergetic status modulates motor neuron vulnerability and pathogenesis in a zebrafish model of spinal muscular atrophy. *PLoS Genet*, **13**, e1006744.

334 Acsadi, G., Lee, I., Li, X., Khaidakov, M., Pecinova, A., Parker, G.C. and Huttemann, M. (2009) Mitochondrial dysfunction in a neural cell model of spinal muscular atrophy. *J Neurosci Res*, **87**, 2748-2756.

335 Berger, A., Mayr, J.A., Meierhofer, D., Fotschl, U., Bittner, R., Budka, H., Grethen, C., Huemer, M., Kofler, B. and Sperl, W. (2003) Severe depletion of mitochondrial DNA in spinal muscular atrophy. *Acta Neuropathol*, **105**, 245-251.

336 Ripolone, M., Ronchi, D., Violano, R., Vallejo, D., Fagiolari, G., Barca, E., Lucchini, V., Colombo, I., Villa, L., Berardinelli, A. *et al.* (2015) Impaired Muscle Mitochondrial Biogenesis and Myogenesis in Spinal Muscular Atrophy. *JAMA neurology*, **72**, 666-675.

337 Jongpiputvanich, S., Sueblinvong, T. and Norapucsunton, T. (2005) Mitochondrial respiratory chain dysfunction in various neuromuscular diseases. *J Clin Neurosci*, **12**, 426-428.

338 Sperl, W., Skladal, D., Gnaiger, E., Wyss, M., Mayr, U., Hager, J. and Gellerich, F.N. (1997) High resolution respirometry of permeabilized skeletal muscle fibers in the diagnosis of neuromuscular disorders. *Mol Cell Biochem*, **174**, 71-78.

339 Butchbach, M.E., Rose, F.F., Rhoades, S., Marston, J., McCrone, J.T., Sinnott, R. and Lorson, C.L. (2010) Effect of diet on the survival and phenotype of a mouse model for spinal muscular atrophy. *Biochemical and biophysical research communications*, **391**, 835-840.

340 Orngreen, M.C., Zacho, M., Hebert, A., Laub, M. and Vissing, J. (2003) Patients with severe muscle wasting are prone to develop hypoglycemia during fasting. *Neurology*, **61**, 997-1000.

341 Harpey, J.P., Charpentier, C., Paturneau-Jouas, M., Renault, F., Romero, N. and Fardeau, M. (1990) Secondary metabolic defects in spinal muscular atrophy type II. *Lancet*, **336**, 629-630.

342 (1992) National Cholesterol Education Program (NCEP): highlights of the report of the Expert Panel on Blood Cholesterol Levels in Children and Adolescents. *Pediatrics*, **89**, 495-501.

343 Expert Panel on Integrated Guidelines for Cardiovascular, H., Risk Reduction in, C., Adolescents, National Heart, L. and Blood, I. (2011) Expert panel on integrated guidelines for cardiovascular health and risk reduction in children and adolescents: summary report. *Pediatrics*, **128 Suppl 5**, S213-256.

344 Frezza, C., Cipolat, S. and Scorrano, L. (2007) Organelle isolation: functional mitochondria from mouse liver, muscle and cultured fibroblasts. *Nat Protoc*, **2**, 287-295.

345 Folch, J., Lees, M. and Sloane Stanley, G.H. (1957) A simple method for the isolation and purification of total lipides from animal tissues. *J Biol Chem*, **226**, 497-509.

346 Morrison, W.R. and Smith, L.M. (1964) Preparation of Fatty Acid Methyl Esters and Dimethylacetals from Lipids with Boron Fluoride--Methanol. *J Lipid Res*, **5**, 600-608.

347 Rudel, L.L., Kelley, K., Sawyer, J.K., Shah, R. and Wilson, M.D. (1998) Dietary monounsaturated fatty acids promote aortic atherosclerosis in LDL receptor-null, human ApoB100-overexpressing transgenic mice. *Arterioscler Thromb Vasc Biol*, **18**, 1818-1827.

348 Theocharidis, A., van Dongen, S., Enright, A.J. and Freeman, T.C. (2009) Network visualization and analysis of gene expression data using BioLayout Express(3D). *Nat Protoc*, **4**, 1535-1550.

349 Graham, L.C., Eaton, S.L., Brunton, P.J., Atrih, A., Smith, C., Lamont, D.J., Gillingwater, T.H., Pennetta, G., Skehel, P. and Wishart, T.M. (2017) Proteomic profiling of neuronal mitochondria reveals modulators of synaptic architecture. *Mol Neurodegener*, **12**, 77.

350 Jones, R.A., Harrison, C., Eaton, S.L., Llavero Hurtado, M., Graham, L.C., Alkhammash, L., Oladiran, O.A., Gale, A., Lamont, D.J., Simpson, H. *et al.* (2017) Cellular and Molecular Anatomy of the Human Neuromuscular Junction. *Cell Rep*, **21**, 2348-2356.

351 Llavero Hurtado, M., Fuller, H.R., Wong, A.M.S., Eaton, S.L., Gillingwater, T.H., Pennetta, G., Cooper, J.D. and Wishart, T.M. (2017) Proteomic mapping of differentially vulnerable pre-synaptic populations identifies regulators of neuronal stability in vivo. *Sci Rep*, **7**, 12412.

352 Huang da, W., Sherman, B.T. and Lempicki, R.A. (2009) Systematic and integrative analysis of large gene lists using DAVID bioinformatics resources. *Nat Protoc*, **4**, 44-57.

353 Huang da, W., Sherman, B.T. and Lempicki, R.A. (2009) Bioinformatics enrichment tools: paths toward the comprehensive functional analysis of large gene lists. *Nucleic Acids Res*, **37**, 1-13.

354 Mendell, J.R., Al-Zaidy, S., Shell, R., Arnold, W.D., Rodino-Klapac, L.R., Prior, T.W., Lowes, L., Alfano, L., Berry, K., Church, K. *et al.* (2017) Single-Dose Gene-Replacement Therapy for Spinal Muscular Atrophy. *N Engl J Med*, **377**, 1713-1722.

355 Gladman, J.T., Bebee, T.W., Edwards, C., Wang, X., Sahenk, Z., Rich, M.M. and Chandler, D.S. (2010) A humanized Smn gene containing the SMN2 nucleotide alteration in exon 7 mimics SMN2 splicing and the SMA disease phenotype. *Hum Mol Genet*, **19**, 4239-4252.

356 Cobb, M.S., Rose, F.F., Rindt, H., Glascock, J.J., Shababi, M., Miller, M.R., Osman, E.Y., Yen, P.F., Garcia, M.L., Martin, B.R. *et al.* (2013) Development and characterization of an SMN2-based intermediate mouse model of Spinal Muscular Atrophy. *Hum Mol Genet*, **22**, 1843-1855.

357 Bogdanik, L.P., Osborne, M.A., Davis, C., Martin, W.P., Austin, A., Rigo, F., Bennett, C.F. and Lutz, C.M. (2015) Systemic, postsymptomatic antisense oligonucleotide rescues motor unit maturation delay in a new mouse model for type II/III spinal muscular atrophy. *Proc Natl Acad Sci U S A*, **112**, E5863-5872.

358 Tsai, L.K., Tsai, M.S., Lin, T.B., Hwu, W.L. and Li, H. (2006) Establishing a standardized therapeutic testing protocol for spinal muscular atrophy. *Neurobiol Dis*, **24**, 286-295.

359 Jablonka, S., Schrank, B., Kralewski, M., Rossoll, W. and Sendtner, M. (2000) Reduced survival motor neuron (Smn) gene dose in mice leads to motor neuron degeneration: an animal model for spinal muscular atrophy type III. *Hum Mol Genet*, **9**, 341-346.

360 Simon, C.M., Jablonka, S., Ruiz, R., Tabares, L. and Sendtner, M. (2010) Ciliary neurotrophic factor-induced sprouting preserves motor function in a mouse model of mild spinal muscular atrophy. *Hum Mol Genet*, **19**, 973-986.

361 Deguise, M.O., Baranello, G., Mastella, C., Beauvais, A., Michaud, J., Leone, A., De Amicis, R., Battezzati, A., Dunham, C., Selby, K. *et al.* (2019) Abnormal fatty acid metabolism is a core component of spinal muscular atrophy. *Ann Clin Transl Neurol*, **6**, 1519-1532.

362 Gong, B., Legault, D., Miki, T., Seino, S. and Renaud, J.M. (2003) KATP channels depress force by reducing action potential amplitude in mouse EDL and soleus muscle. *Am J Physiol Cell Physiol*, **285**, C1464-1474.

363 Furukawa, T., Nakao, K., Sugita, H. and Tsukagoshi, H. (1968) Kugelberg-Welander disease with particular reference to sex-influenced manifestations. *Arch Neurol*, **19**, 156-162.

364 Hausmanowa-Petrusewicz, I., Zaremba, J., Borkowska, J. and Szirkowiec, W. (1984) Chronic proximal spinal muscular atrophy of childhood and adolescence: sex influence. *J Med Genet*, **21**, 447-450.

365 Hahnen, E., Forkert, R., Marke, C., Rudnik-Schoneborn, S., Schonling, J., Zerres, K. and Wirth, B. (1995) Molecular analysis of candidate genes on chromosome 5q13 in autosomal recessive spinal muscular atrophy: evidence of homozygous deletions of the SMN gene in unaffected individuals. *Hum Mol Genet*, **4**, 1927-1933.

366 Capon, F., Levato, C., Merlini, L., Angelini, C., Mostacciuolo, M.L., Politano, L., Novelli, G. and Dallapiccola, B. (1996) Discordant clinical outcome in type III spinal muscular atrophy sibships showing the same deletion pattern. *Neuromuscul Disord*, **6**, 261-264.

367 Zerres, K. and Rudnik-Schoneborn, S. (1995) Natural history in proximal spinal muscular atrophy. Clinical analysis of 445 patients and suggestions for a modification of existing classifications. *Arch Neurol*, **52**, 518-523.

368 Jedrzejowska, M., Milewski, M., Zimowski, J., Borkowska, J., Kostera-Pruszczyk, A., Sielska, D., Jurek, M. and Hausmanowa-Petrusewicz, I. (2009) Phenotype modifiers of spinal muscular atrophy: the number of SMN2 gene copies, deletion in the NAIP gene and probably gender influence the course of the disease. *Acta Biochim Pol*, **56**, 103-108.

369 Cobben, J.M., van der Steege, G., Grootscholten, P., de Visser, M., Scheffer, H. and Buys, C.H. (1995) Deletions of the survival motor neuron gene in unaffected siblings of patients with spinal muscular atrophy. *Am J Hum Genet*, **57**, 805-808.

370 Wang, C.H., Xu, J., Carter, T.A., Ross, B.M., Dominski, M.K., Bellcross, C.A., Penchaszadeh, G.K., Munsat, T.L. and Gilliam, T.C. (1996) Characterization of survival motor neuron (SMNT) gene deletions in asymptomatic carriers of spinal muscular atrophy. *Hum Mol Genet*, **5**, 359-365.

371 Helmken, C., Hofmann, Y., Schoenen, F., Oprea, G., Raschke, H., Rudnik-Schoneborn, S., Zerres, K. and Wirth, B. (2003) Evidence for a modifying pathway in SMA discordant families: reduced SMN level decreases the amount of its interacting partners and Htra2-beta1. *Hum Genet*, **114**, 11-21.

372 Cusco, I., Barcelo, M.J., Rojas-Garcia, R., Illa, I., Gamez, J., Cervera, C., Pou, A., Izquierdo, G., Baiget, M. and Tizzano, E.F. (2006) SMN2 copy number predicts acute or chronic spinal muscular atrophy but does not account for intrafamilial variability in siblings. *J Neurol*, **253**, 21-25.

373 Jedrzejowska, M., Borkowska, J., Zimowski, J., Kostera-Pruszczyk, A., Milewski, M., Jurek, M., Sielska, D., Kostyk, E., Nyka, W., Zaremba, J. *et al.* (2008) Unaffected patients with a homozygous absence of the SMN1 gene. *Eur J Hum Genet*, **16**, 930-934.

374 Oprea, G.E., Krober, S., McWhorter, M.L., Rossoll, W., Muller, S., Krawczak, M., Bassell, G.J., Beattie, C.E. and Wirth, B. (2008) Plastin 3 is a protective modifier of autosomal recessive spinal muscular atrophy. *Science*, **320**, 524-527.

375 Stratigopoulos, G., Lanzano, P., Deng, L., Guo, J., Kaufmann, P., Darras, B., Finkel, R., Tawil, R., McDermott, M.P., Martens, W. *et al.* (2010) Association of plastin 3 expression with disease severity in spinal muscular atrophy only in postpubertal females. *Arch Neurol*, **67**, 1252-1256.

376 Kariya, S., Obis, T., Garone, C., Akay, T., Sera, F., Iwata, S., Homma, S. and Monani, U.R. (2014) Requirement of enhanced Survival Motoneuron protein imposed during neuromuscular junction maturation. *The Journal of clinical investigation*, **124**, 785-800.

377 Pearn, J.H., Hudgson, P. and Walton, J.N. (1978) A clinical and genetic study of spinal muscular atrophy of adult onset: the autosomal recessive form as a discrete disease entity. *Brain*, **101**, 591-606.

378 Gavrilina, T.O., McGovern, V.L., Workman, E., Crawford, T.O., Gogliotti, R.G., DiDonato, C.J., Monani, U.R., Morris, G.E. and Burghes, A.H. (2008) Neuronal SMN expression corrects spinal muscular atrophy in severe SMA mice while muscle-specific SMN expression has no phenotypic effect. *Human molecular genetics*, **17**, 1063-1075.

379 Hellbach, N., Peterson, S., Haehnke, D., Shankar, A., LaBarge, S., Pivaroff, C., Saenger, S., Thomas, C., McCarthy, K., Ebeling, M. *et al.* (2018) Impaired myogenic development, differentiation and function in hESC-derived SMA myoblasts and myotubes. *PLoS One*, **13**, e0205589.

380 Riessland, M., Ackermann, B., Förster, A., Jakubik, M., Hauke, J., Garbes, L., Fritzsche, I., Mende, Y., Blumcke, I., Hahnen, E. *et al.* (2010) SAHA ameliorates the SMA phenotype in two mouse models for spinal muscular atrophy. *Human Molecular Genetics*, **19**, 1492-1506.

381 Somers, E., Riessland, M., Schreml, J., Wirth, B., Gillingwater, T.H. and Parson, S.H. (2013) Increasing SMN levels using the histone deacetylase inhibitor SAHA ameliorates defects in skeletal muscle microvasculature in a mouse model of severe spinal muscular atrophy. *Neurosci Lett*, **544**, 100-104.

382 Mutsaers, C.A., Wishart, T.M., Lamont, D.J., Riessland, M., Schreml, J., Comley, L.H., Murray, L.M., Parson, S.H., Lochmüller, H., Wirth, B. *et al.* (2011) Reversible molecular pathology of skeletal muscle in spinal muscular atrophy. *Human molecular genetics*, **20**, 4334-4344.

383 Kwon, D.Y., Motley, W.W., Fischbeck, K.H. and Burnett, B.G. (2011) Increasing expression and decreasing degradation of SMN ameliorate the spinal muscular atrophy phenotype in mice. *Human molecular genetics*, **20**, 3667-3677.

384 Deguise, M.O. and Kothary, R. (2019) Binda, O. (ed.), In *Chromatin Signaling and Neurological Disorders*. Elsevier, Vol. 7, pp. 27-52.

385 Brahe, C., Vitali, T., Tiziano, F.D., Angelozzi, C., Pinto, A.M., Borgo, F., Moscato, U., Bertini, E., Mercuri, E. and Neri, G. (2005) Phenylbutyrate increases SMN gene expression in spinal muscular atrophy patients. *Eur J Hum Genet*, **13**, 256-259.

386 Mercuri, E., Bertini, E., Messina, S., Pelliccioni, M., D'Amico, A., Colitto, F., Mirabella, M., Tiziano, F.D., Vitali, T., Angelozzi, C. *et al.* (2004) Pilot trial of phenylbutyrate in spinal muscular atrophy. *Neuromuscul Disord*, **14**, 130-135.

387 Brichta, L., Holker, I., Haug, K., Klockgether, T. and Wirth, B. (2006) In vivo activation of SMN in spinal muscular atrophy carriers and patients treated with valproate. *Ann Neurol*, **59**, 970-975.

388 Tsai, L.K., Yang, C.C., Hwu, W.L. and Li, H. (2007) Valproic acid treatment in six patients with spinal muscular atrophy. *Eur J Neurol*, **14**, e8-9.

389 Piepers, S., Cobben, J.M., Sodaar, P., Jansen, M.D., Wadman, R.I., Meester-Delver, A., Poll-The, B.T., Lemmink, H.H., Wokke, J.H., van der Pol, W.L. *et al.* (2011) Quantification

of SMN protein in leucocytes from spinal muscular atrophy patients: effects of treatment with valproic acid. *J Neurol Neurosurg Psychiatry*, **82**, 850-852.

390 Swoboda, K.J., Scott, C.B., Crawford, T.O., Simard, L.R., Reyna, S.P., Krosschell, K.J., Acsadi, G., Elsheik, B., Schroth, M.K., D'Anjou, G. *et al.* (2010) SMA CARNI-VAL trial part I: double-blind, randomized, placebo-controlled trial of L-carnitine and valproic acid in spinal muscular atrophy. *PLoS One*, **5**, e12140.

391 Swoboda, K.J., Scott, C.B., Reyna, S.P., Prior, T.W., LaSalle, B., Sorenson, S.L., Wood, J., Acsadi, G., Crawford, T.O., Kissel, J.T. *et al.* (2009) Phase II open label study of valproic acid in spinal muscular atrophy. *PLoS One*, **4**, e5268.

392 Kissel, J.T., Scott, C.B., Reyna, S.P., Crawford, T.O., Simard, L.R., Krosschell, K.J., Acsadi, G., Elsheik, B., Schroth, M.K., D'Anjou, G. *et al.* (2011) SMA CARNIVAL TRIAL PART II: a prospective, single-armed trial of L-carnitine and valproic acid in ambulatory children with spinal muscular atrophy. *PLoS One*, **6**, e21296.

393 Darbar, I.A., Plaggert, P.G., Resende, M.B., Zanoteli, E. and Reed, U.C. (2011) Evaluation of muscle strength and motor abilities in children with type II and III spinal muscle atrophy treated with valproic acid. *BMC Neurol*, **11**, 36.

394 Kissel, J.T., Elsheikh, B., King, W.M., Freimer, M., Scott, C.B., Kolb, S.J., Reyna, S.P., Crawford, T.O., Simard, L.R., Krosschell, K.J. *et al.* (2014) SMA valiant trial: a prospective, double-blind, placebo-controlled trial of valproic acid in ambulatory adults with spinal muscular atrophy. *Muscle Nerve*, **49**, 187-192.

395 Renusch, S.R., Harshman, S., Pi, H., Workman, E., Wehr, A., Li, X., Prior, T.W., Elsheikh, B.H., Swoboda, K.J., Simard, L.R. *et al.* (2015) Spinal Muscular Atrophy Biomarker

Measurements from Blood Samples in a Clinical Trial of Valproic Acid in Ambulatory Adults. *J Neuromuscul Dis*, **2**, 119-130.

396 Nadeau, A., D'Anjou, G., Debray, G., Robitaille, Y., Simard, L.R. and Vanasse, M. (2007) A newborn with spinal muscular atrophy type 0 presenting with a clinicopathological picture suggestive of myotubular myopathy. *J Child Neurol*, **22**, 1301-1304.

397 Harding, B.N., Kariya, S., Monani, U.R., Chung, W.K., Benton, M., Yum, S.W., Tennekoon, G. and Finkel, R.S. (2015) Spectrum of neuropathophysiology in spinal muscular atrophy type I. *J Neuropathol Exp Neurol*, **74**, 15-24.

398 Fidzianska, A. (1974) Ultrastructural changes in muscle in spinal muscular atrophy. Werding-Hoffmann's disease. *Acta Neuropathol*, **27**, 247-256.

399 Fidziańska, A., Goebel, H.H. and Warlo, I. (1990) Acute infantile spinal muscular atrophy. Muscle apoptosis as a proposed pathogenetic mechanism. *Brain : a journal of neurology*, **113 (Pt 2)**, 433-445.

400 Bohm, J., Biancalana, V., Malfatti, E., Dondaine, N., Koch, C., Vasli, N., Kress, W., Strittmatter, M., Taratuto, A.L., Gonorazky, H. *et al.* (2014) Adult-onset autosomal dominant centronuclear myopathy due to BIN1 mutations. *Brain*, **137**, 3160-3170.

401 Dowling, J.J., Vreede, A.P., Low, S.E., Gibbs, E.M., Kuwada, J.Y., Bonnemann, C.G. and Feldman, E.L. (2009) Loss of myotubularin function results in T-tubule disorganization in zebrafish and human myotubular myopathy. *PLoS Genet*, **5**, e1000372.

402 Al-Qusairi, L., Weiss, N., Toussaint, A., Berbey, C., Messaddeq, N., Kretz, C., Sanoudou, D., Beggs, A.H., Allard, B., Mandel, J.L. *et al.* (2009) T-tubule disorganization

and defective excitation-contraction coupling in muscle fibers lacking myotubularin lipid phosphatase. *Proc Natl Acad Sci U S A*, **106**, 18763-18768.

403 Lawlor, M.W., Alexander, M.S., Viola, M.G., Meng, H., Joubert, R., Gupta, V., Motohashi, N., Manfready, R.A., Hsu, C.P., Huang, P. *et al.* (2012) Myotubularin-deficient myoblasts display increased apoptosis, delayed proliferation, and poor cell engraftment. *Am J Pathol*, **181**, 961-968.

404 Hnia, K., Tronchere, H., Tomczak, K.K., Amoasii, L., Schultz, P., Beggs, A.H., Payrastre, B., Mandel, J.L. and Laporte, J. (2011) Myotubularin controls desmin intermediate filament architecture and mitochondrial dynamics in human and mouse skeletal muscle. *J Clin Invest*, **121**, 70-85.

405 Robb, S.A., Sewry, C.A., Dowling, J.J., Feng, L., Cullup, T., Lillis, S., Abbs, S., Lees, M.M., Laporte, J., Manzur, A.Y. *et al.* (2011) Impaired neuromuscular transmission and response to acetylcholinesterase inhibitors in centronuclear myopathies. *Neuromuscul Disord*, **21**, 379-386.

406 Dowling, J.J., Joubert, R., Low, S.E., Durban, A.N., Messaddeq, N., Li, X., Dulin-Smith, A.N., Snyder, A.D., Marshall, M.L., Marshall, J.T. *et al.* (2012) Myotubular myopathy and the neuromuscular junction: a novel therapeutic approach from mouse models. *Dis Model Mech*, **5**, 852-859.

407 Russell, A.J., Hartman, J.J., Hinken, A.C., Muci, A.R., Kawas, R., Driscoll, L., Godinez, G., Lee, K.H., Marquez, D., Browne, W.F.t. *et al.* (2012) Activation of fast skeletal muscle troponin as a potential therapeutic approach for treating neuromuscular diseases. *Nat Med*, **18**, 452-455.

408 Andrews, J.A., Miller, T.M., Vijayakumar, V., Stoltz, R., James, J.K., Meng, L., Wolff, A.A. and Malik, F.I. (2018) CK-2127107 amplifies skeletal muscle response to nerve activation in humans. *Muscle Nerve*, **57**, 729-734.

409 Kang, Y.S., Kim, J.Y., Bruening, S.A., Pack, M., Charalambous, A., Pritsker, A., Moran, T.M., Loeffler, J.M., Steinman, R.M. and Park, C.G. (2004) The C-type lectin SIGN-R1 mediates uptake of the capsular polysaccharide of Streptococcus pneumoniae in the marginal zone of mouse spleen. *Proc Natl Acad Sci U S A*, **101**, 215-220.

410 Kang, Y.-S.S., Yamazaki, S., Iyoda, T., Pack, M., Bruening, S.A., Kim, J.Y., Takahara, K., Inaba, K., Steinman, R.M. and Park, C.G. (2003) SIGN-R1, a novel C-type lectin expressed by marginal zone macrophages in spleen, mediates uptake of the polysaccharide dextran. *International immunology*, **15**, 177-186.

411 Amlot, P.L. and Hayes, A.E. (1985) Impaired human antibody response to the thymus-independent antigen, DNP-Ficoll, after splenectomy. Implications for post-splenectomy infections. *Lancet (London, England)*, **1**, 1008-1011.

412 Davies, J.M., Lewis, M.P., Wimperis, J., Rafi, I., Ladhani, S., Bolton-Maggs, P.H. and British Committee for Standards in, H. (2011) Review of guidelines for the prevention and treatment of infection in patients with an absent or dysfunctional spleen: prepared on behalf of the British Committee for Standards in Haematology by a working party of the Haemato-Oncology task force. *Br J Haematol*, **155**, 308-317.

413 Wan, B., Feng, P., Guan, Z., Sheng, L., Liu, Z. and Hua, Y. (2018) A severe mouse model of spinal muscular atrophy develops early systemic inflammation. *Hum Mol Genet*, in press.

414 Bach, J.R. (2007) Medical considerations of long-term survival of Werdnig-Hoffmann disease. *American journal of physical medicine & rehabilitation / Association of Academic Physiatrists*, **86**, 349-355.

415 Ge, X., Bai, J., Lu, Y., Qu, Y. and Song, F. (2012) The natural history of infant spinal muscular atrophy in China: a study of 237 patients. *J Child Neurol*, **27**, 471-477.

416 Cobben, J.M., Lemmink, H.H., Snoeck, I., Barth, P.A., van der Lee, J.H. and de Visser, M. (2008) Survival in SMA type I: a prospective analysis of 34 consecutive cases. *Neuromuscul Disord*, **18**, 541-544.

417 Mannaa, M.M., Kalra, M., Wong, B., Cohen, A.P. and Amin, R.S. (2009) Survival probabilities of patients with childhood spinal muscle atrophy. *J Clin Neuromuscul Dis*, **10**, 85-89.

418 Gormley, M.C. (2014) Respiratory management of spinal muscular atrophy type 2. *J Neurosci Nurs*, **46**, E33-41.

419 Ajmo, C.T., Jr., Vernon, D.O., Collier, L., Hall, A.A., Garbuzova-Davis, S., Willing, A. and Pennypacker, K.R. (2008) The spleen contributes to stroke-induced neurodegeneration. *J Neurosci Res*, **86**, 2227-2234.

420 Yamazaki, T., Chen, S., Yu, Y., Yan, B., Haertlein, T.C., Carrasco, M.A., Tapia, J.C., Zhai, B., Das, R., Lalancette-Hebert, M. *et al.* (2012) FUS-SMN protein interactions link the motor neuron diseases ALS and SMA. *Cell Reports*, **2**, 799-806.

421 Engelhardt, J.I. and Appel, S.H. (1990) IgG reactivity in the spinal cord and motor cortex in amyotrophic lateral sclerosis. *Arch Neurol*, **47**, 1210-1216.

422 Kawamata, T., Akiyama, H., Yamada, T. and McGeer, P.L. (1992) Immunologic reactions in amyotrophic lateral sclerosis brain and spinal cord tissue. *Am J Pathol*, **140**, 691-707.

423 Cervero, C., Blasco, A., Tarabal, O., Casanovas, A., Piedrafita, L., Navarro, X., Esquerda, J.E. and Caldero, J. (2018) Glial Activation and Central Synapse Loss, but Not Motoneuron Degeneration, Are Prevented by the Sigma-1 Receptor Agonist PRE-084 in the Smn2B/- Mouse Model of Spinal Muscular Atrophy. *J Neuropathol Exp Neurol*, **77**, 577-597.

424 Bresolin, N., Freddo, L., Tegazzin, V., Bet, L., Armani, M. and Angelini, C. (1984) Carnitine and acyltransferase in experimental neurogenic atrophies: changes with treatment. *J Neurol*, **231**, 170-175.

425 Sproule, D.M., Montes, J., Montgomery, M. and Battista, V. (2009) Increased fat mass and high incidence of overweight despite low body mass index in patients with spinal muscular atrophy. *Neuromuscular …*, in press.

426 Poruk, K.E., Davis, R., Smart, A.L., Chisum, B.S., LaSalle, B.A., Chan, G.M., Gill, G., Reyna, S.P. and Swoboda, K.J. (2012) Observational study of caloric and nutrient intake, bone density, and body composition in infants and children with spinal muscular atrophy type I. *Neuromuscular Disorders*, **22**, 966-973.

427 Bertoli, S., De Amicis, R., Mastella, C., Pieri, G., Giaquinto, E., Battezzati, A., Leone, A. and Baranello, G. (2016) Spinal Muscular Atrophy, types I and II: What are the differences in body composition and resting energy expenditure? *Clin Nutr*, in press.

428 Zeng, M.D., Fan, J.G., Lu, L.G., Li, Y.M., Chen, C.W., Wang, B.Y. and Mao, Y.M. (2008) Guidelines for the diagnosis and treatment of nonalcoholic fatty liver diseases. *J Dig Dis*, **9**, 108-112.

429 Fergani, A., Oudart, H., Gonzalez De Aguilar, J.L., Fricker, B., Rene, F., Hocquette, J.F., Meininger, V., Dupuis, L. and Loeffler, J.P. (2007) Increased peripheral lipid clearance in an animal model of amyotrophic lateral sclerosis. *J Lipid Res*, **48**, 1571-1580.

430 Mulroy, E., Gleeson, S. and Furlong, M.J. (2016) Stress-Induced Ketoacidosis in Spinal Muscular Atrophy: An Under-Recognized Complication. *J Neuromuscul Dis*, **3**, 419-423.

431 Lakkis, B., El Chediak, A., Hashash, J.G. and Koubar, S.H. (2018) Severe ketoacidosis in a patient with spinal muscular atrophy. *CEN Case Rep*, in press.

432 Stoimenis, D., Spyridonidou, C., Theofanidou, S., Petridis, N., Papaioannou, N., Iasonidou, C. and Kapravelos, N. (2019) Euglycemic Ketoacidosis in Spinal Muscular Atrophy. *Case Rep Pediatr*, **2019**, 2862916.

433 LaMarca, N.H., Golden, L., John, R.M. and Naini, A. (2013) Diabetic Ketoacidosis in an Adult Patient With Spinal Muscular Atrophy Type II Further Evidence of Extraneural Pathology Due to Survival Motor Neuron 1 Mutation? *Diabetic Ketoacidosis in an Adult Patient With Spinal Muscular Atrophy Type II Further Evidence of Extraneural Pathology Due to Survival Motor Neuron 1 Mutation?*, in press.

434 Kolbel, H., Hauffa, B.P., Wudy, S.A., Bouikidis, A., Della Marina, A. and Schara, U. (2017) Hyperleptinemia in children with autosomal recessive spinal muscular atrophy type I-III. *PLoS One*, **12**, e0173144.

435 Finkel, R.S., Sejersen, T., Mercuri, E. and Group, E.S.W.S. (2017) 218th ENMC International Workshop:: Revisiting the consensus on standards of care in SMA Naarden, The Netherlands, 19-21 February 2016. *Neuromuscul Disord*, **27**, 596-605.

436 Mehta, N.M., Newman, H., Tarrant, S. and Graham, R.J. (2016) Nutritional Status and Nutrient Intake Challenges in Children With Spinal Muscular Atrophy. *Pediatr Neurol*, **57**, 80-83.

437 Lau, J.K., Zhang, X. and Yu, J. (2017) Animal models of non-alcoholic fatty liver disease: current perspectives and recent advances. *J Pathol*, **241**, 36-44.

438 Ibrahim, S.H., Hirsova, P., Malhi, H. and Gores, G.J. (2016) Animal Models of Nonalcoholic Steatohepatitis: Eat, Delete, and Inflame. *Dig Dis Sci*, **61**, 1325-1336.

439 Van Herck, M.A., Vonghia, L. and Francque, S.M. (2017) Animal Models of Nonalcoholic Fatty Liver Disease-A Starter's Guide. *Nutrients*, **9**.

440 Tandra, S., Yeh, M.M., Brunt, E.M., Vuppalanchi, R., Cummings, O.W., Unalp-Arida, A., Wilson, L.A. and Chalasani, N. (2011) Presence and significance of microvesicular steatosis in nonalcoholic fatty liver disease. *J Hepatol*, **55**, 654-659.

441 Rinella, M.E. and Green, R.M. (2004) The methionine-choline deficient dietary model of steatohepatitis does not exhibit insulin resistance. *J Hepatol*, **40**, 47-51.

442 Sahai, A., Malladi, P., Pan, X., Paul, R., Melin-Aldana, H., Green, R.M. and Whitington, P.F. (2004) Obese and diabetic db/db mice develop marked liver fibrosis in a model of nonalcoholic steatohepatitis: role of short-form leptin receptors and osteopontin. *Am J Physiol Gastrointest Liver Physiol*, **287**, G1035-1043.

443 Ito, M., Suzuki, J., Tsujioka, S., Sasaki, M., Gomori, A., Shirakura, T., Hirose, H., Ito, M., Ishihara, A., Iwaasa, H. *et al.* (2007) Longitudinal analysis of murine steatohepatitis model induced by chronic exposure to high-fat diet. *Hepatol Res*, **37**, 50-57.

444 Sheng, L., Wan, B., Feng, P., Sun, J., Rigo, F., Bennett, C.F., Akerman, M., Krainer, A.R. and Hua, Y. (2018) Downregulation of Survivin contributes to cell-cycle arrest during postnatal cardiac development in a severe spinal muscular atrophy mouse model. *Hum Mol Genet*, **27**, 486-498.

445 Ottesen, E.W., Howell, M.D., Singh, N.N., Seo, J., Whitley, E.M. and Singh, R.N. (2016) Severe impairment of male reproductive organ development in a low SMN expressing mouse model of spinal muscular atrophy. *Sci Rep*, **6**, 20193.

446 Doktor, T.K., Hua, Y., Andersen, H.S., Broner, S., Liu, Y.H., Wieckowska, A., Dembic, M., Bruun, G.H., Krainer, A.R. and Andresen, B.S. (2017) RNA-sequencing of a mouse-model of spinal muscular atrophy reveals tissue-wide changes in splicing of U12-dependent introns. *Nucleic Acids Res*, **45**, 395-416.

447 Lipnick, S.L., Agniel, D.M., Aggarwal, R., Makhortova, N.R., Finlayson, S.G., Brocato, A., Palmer, N., Darras, B.T., Kohane, I. and Rubin, L.L. (2019) Systemic nature of spinal muscular atrophy revealed by studying insurance claims. *PLoS One*, **14**, e0213680.

448 Wasserman, H.M., Hornung, L.N., Stenger, P.J., Rutter, M.M., Wong, B.L., Rybalsky, I., Khoury, J.C. and Kalkwarf, H.J. (2017) Low bone mineral density and fractures are highly prevalent in pediatric patients with spinal muscular atrophy regardless of disease severity. *Neuromuscul Disord*, **27**, 331-337.

449 Vai, S., Bianchi, M.L., Moroni, I., Mastella, C., Broggi, F., Morandi, L., Arnoldi, M.T., Bussolino, C. and Baranello, G. (2015) Bone and Spinal Muscular Atrophy. *Bone*, **79**, 116-120.